



**HAL**  
open science

# Contribution to the Design and Implementation of Portable Tactile Displays for the Visually Impaired

Ramiro Velazquez

► **To cite this version:**

Ramiro Velazquez. Contribution to the Design and Implementation of Portable Tactile Displays for the Visually Impaired. Automatic. Université Pierre et Marie Curie - Paris VI, 2006. English. NNT : . tel-00085703

**HAL Id: tel-00085703**

**<https://theses.hal.science/tel-00085703>**

Submitted on 13 Jul 2006

**HAL** is a multi-disciplinary open access archive for the deposit and dissemination of scientific research documents, whether they are published or not. The documents may come from teaching and research institutions in France or abroad, or from public or private research centers.

L'archive ouverte pluridisciplinaire **HAL**, est destinée au dépôt et à la diffusion de documents scientifiques de niveau recherche, publiés ou non, émanant des établissements d'enseignement et de recherche français ou étrangers, des laboratoires publics ou privés.

# THESE de DOCTORAT

*de*

l'UNIVERSITE PARIS 6  
- Pierre et Marie Curie -

*Spécialité MECANIQUE - ROBOTIQUE*

*présentée par*

**Ramiro VELAZQUEZ**

*pour obtenir le titre de*

DOCTEUR de l'UNIVERSITE PARIS 6

*Sujet de la thèse :*

---

## Contribution à la Conception et à la Réalisation d'Interfaces Tactiles Portables pour les Déficients Visuels

---

*Soutenue le 28 Juin 2006*

*devant le jury composé de :*

N.	CHAILLET	Professeur à l'Université de Franche-Comté	<i>Rapporteur</i>
B.	SEMAIL	Professeur à l'Université de Lille I	<i>Rapporteur</i>
J.C.	GUINOT	Professeur à l'Université de Paris VI	<i>Co-directeur de thèse</i>
E.	PISSALOUX	Professeur à l'Université de Rouen	<i>Co-directrice de thèse</i>
M.	SIEGEL	Professeur à l'Université Carnegie Mellon	<i>Examineur</i>
V.	PERDEREAU	Professeur à l'Université de Paris VI	<i>Examineur</i>
M.	HAFEZ	Ingénieur de Recherche au CEA/LIST	<i>Examineur</i>
F.	VIDAL	Professeur à l'Université de Malaga	<i>Examineur</i>
J.	SZEWCZYK	Maître de Conférences à l'Université de Versailles	<i>Examineur</i>



# Remerciements

Ce travail de thèse a été réalisé au sein du Laboratoire de Robotique de Paris (LRP) de l'Université Paris 6 en collaboration avec le Commissariat à l'Énergie Atomique (CEA, Fontenay aux Roses) dans le cadre d'une bourse franco-mexicaine SFERE-CONACYT.

Je tiens tout d'abord à remercier M. **Jean-Claude Guinot** pour m'avoir accueilli dans l'école doctorale de Sciences Mécaniques de Paris 6, ainsi que M. **Philippe Bidaud** pour m'avoir donné l'opportunité de travailler au Laboratoire de Robotique de Paris.

J'adresse mes plus vifs remerciements à ma directrice de thèse Mme **Edwige Pissaloux** qui m'a proposé un sujet de recherche original et passionnant. Je voudrais que vous sachiez combien votre encadrement a été pédagogique pendant ces quatre années. Merci pour votre confiance et pour tout ce que vous avez fait pour un mexicain en France. Je vous exprime ici ma plus profonde gratitude.

Je veux également exprimer toute ma reconnaissance à M. **Moustapha Hafez** et à M. **Jérôme Szewczyk** pour leur aide, leurs conseils et pour le suivi scientifique et technique de ces travaux.

Je voudrais remercier Mme **Betty Semail** et M. **Nicolas Chaillet** qui m'ont fait l'honneur d'être rapporteurs de ce mémoire et à Mme **Véronique Perdereau** pour avoir présidé le jury de thèse. Je voudrais remercier particulièrement M. **Mel Siegel** et M. **Fernando Vidal** pour les remarques, les corrections et les critiques apportées.

Je remercie très sincèrement **Vincent de Sars**, **Michael Wiertlewski** et **Eléonor Fontaine**, votre aide a été très précieuse pour la réussite de cette thèse.

Je voudrais également transmettre mes remerciements à **Mehdi Boukallel** et **Maxime Girot** pour leur patience dans la correction de ce manuscrit.

Que tous les **permanents** et **doctorants** du Laboratoire de Robotique de Paris soient assurés de ma gratitude. Chacun d'entre eux a contribué à l'aboutissement de mon travail. Je les remercie de leur amitié et de leur soutien durant ces années.

Finalmente quiero agradecer a mi **familia**. Muchas gracias por su apoyo a lo largo de estos años de ausencia y de aventuras al otro lado del mundo. Sin ustedes nada de esto hubiera sido posible.

**Ramiro Velázquez-Guerrero**



# Contents

Table of contents	i
Table of figures	iii
Introduction	1
<b>1 Toward a New Electronic Travel Aid for the Blind</b>	<b>3</b>
1.1 Blind mobility aids . . . . .	4
1.1.1 Classic aids . . . . .	4
1.1.2 Electronic travel aids . . . . .	4
1.1.3 Synthesis and discussion . . . . .	10
1.2 Intelligent Glasses: a visuo-tactile ETA for the blind . . . . .	11
1.2.1 Vision system . . . . .	12
1.2.2 Tactile display . . . . .	13
1.3 Criteria for the design of the IG tactile display . . . . .	21
1.3.1 Guidelines for tactile displays: a psychophysiology approach . . . . .	21
1.3.2 Choice of actuation technology . . . . .	24
1.4 Essential features of shape memory alloys . . . . .	25
1.5 Conclusion . . . . .	28
<b>2 Design and Characterization of SMA Helical Springs</b>	<b>29</b>
2.1 Modeling of shape memory alloys . . . . .	30
2.2 The thermal dynamics of SMAs . . . . .	31
2.2.1 Heat transfer analysis . . . . .	31
2.2.2 Heat-exchange coefficient $h$ . . . . .	32
2.2.3 Parameter determination through an example . . . . .	33
2.2.4 Phase transformation . . . . .	36
2.3 SMA mechanical behavior . . . . .	40
2.3.1 Strain-deflection behavior . . . . .	40
2.3.2 Temperature dependence . . . . .	41
2.3.3 Load-deflection-temperature relation . . . . .	43
2.3.4 Behavior of the plastic region: evolution of $r_b$ . . . . .	43
2.3.5 Material constants . . . . .	44
2.3.6 Deformation behavior of an SMA helical spring . . . . .	45
2.4 Experimental procedure . . . . .	47

---

2.4.1	Material . . . . .	47
2.4.2	Parameter identification . . . . .	47
2.4.3	Phase transformation parameters . . . . .	48
2.4.4	Resistivity/Electrical resistance . . . . .	50
2.5	Experimental evaluation of SMA thermomechanical properties . . . . .	52
2.5.1	Thermal behavior of the NiTi spring . . . . .	52
2.5.2	Mechanical behavior of the NiTi spring . . . . .	56
2.5.3	Micro-structural observations on the NiTi specimens . . . . .	61
2.6	Conclusion . . . . .	62
<b>3</b>	<b>Miniature SMA Actuator for Tactile Binary Information Display</b>	<b>65</b>
3.1	SMA based actuators . . . . .	66
3.1.1	Two-way actuator using a mass . . . . .	68
3.1.2	Biased actuator . . . . .	69
3.1.3	SMA antagonist actuator . . . . .	70
3.1.4	Bistable mechanisms . . . . .	72
3.2	An SMA based actuator for touch stimulation . . . . .	74
3.2.1	Proposed solutions . . . . .	74
3.3	Prototype and performance . . . . .	80
3.4	Conclusion . . . . .	83
<b>4</b>	<b>A Low-Cost Highly-Portable Tactile Display with SMAs</b>	<b>85</b>
4.1	Tactile display . . . . .	86
4.1.1	Design and implementation . . . . .	86
4.1.2	Prototype . . . . .	89
4.2	Drive system . . . . .	90
4.2.1	Electronic drive . . . . .	91
4.2.2	Crossbar circuit analysis and control method . . . . .	94
4.2.3	Software . . . . .	99
4.3	A thermal array structure . . . . .	100
4.4	Conclusion . . . . .	104
<b>5</b>	<b>Preliminary Psychophysical Evaluation of the Tactile Display</b>	<b>105</b>
5.1	First evaluation of the tactile display . . . . .	106
5.1.1	Experimental procedure . . . . .	106
5.2	Experiment 1: tactile acuity and Braille . . . . .	106
5.2.1	Session 1 - Location of a tactile stimulus . . . . .	107
5.2.2	Session 2 - Location of tactile stimuli . . . . .	108
5.2.3	Session 3 - Bimodal perception . . . . .	109
5.3	Experiment 2: shape recognition . . . . .	110
5.3.1	Session 1 - Primitive shapes . . . . .	110
5.3.2	Session 2 - Various shapes . . . . .	112
5.4	Experiment 3: space interaction and navigation . . . . .	113
5.4.1	Session 1 - Direction recognition . . . . .	113
5.4.2	Session 2 - Environment structure . . . . .	115

---

5.4.3	Session 3 - Navigation and tactile maps . . . . .	117
5.5	Conclusion . . . . .	122
<b>Conclusions</b>		<b>123</b>
<b>Bibliography</b>		<b>127</b>
<b>Publications</b>		<b>135</b>
<b>Appendixes</b>		<b>137</b>
<b>A</b>	<b>SMA Helical Spring Design Parameters</b>	<b>137</b>
<b>B</b>	<b>Experimental Platforms</b>	<b>141</b>
B.1	Measurement of electrical resistance . . . . .	141
B.2	Measurement of SMA thermal properties . . . . .	142
B.3	Measurement of SMA mechanical properties . . . . .	143
<b>C</b>	<b>Cooling Flow Rate</b>	<b>145</b>
<b>D</b>	<b>Résumé des travaux</b>	<b>147</b>
D.1	Le système Lunettes Intelligentes . . . . .	147
D.1.1	Interface tactile . . . . .	148
D.1.2	Critères de conception d'une interface tactile pour le système LI . . . . .	149
D.2	Les alliages à mémoire de forme . . . . .	151
D.2.1	Élément actif en AMF . . . . .	152
D.3	Actionneur tactile . . . . .	154
D.4	Interface tactile . . . . .	158
D.4.1	Surface à stimulation tactile . . . . .	158
D.4.2	Système électronique de commande . . . . .	160
D.5	Évaluation expérimentale de l'interface tactile et du concept de représentation de l'espace des LI . . . . .	161
D.6	Conclusion . . . . .	165





# List of Figures

1.1	Classic travel aids for the blind: (a) white cane and (b) guide dog. . . . .	4
1.2	Hand held sonars: (a) the Kay Sonic Torch (1964), (b) the Mowat Sensor (1977) and (c) the Miniguide (2005). . . . .	5
1.3	(a) The SonicGuide (1974) and (b) its latest version, the KASPA system (2002). . . . .	6
1.4	The University of Michigan ETAs: (a) the Navbelt and (b) the GuideCane. . . . .	7
1.5	Ultrasonic based canes: (a) The Bat "K" Sonar-Cane and (b) the Ultra-Cane. Note that the user is able to detect obstacles and take decisions before making contact with the white cane. . . . .	7
1.6	Laser based ETAs: (a) the C-5 Laser Cane concept and (b) the Téléact. . . . .	8
1.7	(a) The vOICe system and (b) an example of its image-to-sound rendering. . . . .	9
1.8	The TDU system. . . . .	9
1.9	The Dobelle eye: a prosthetic device surgically implanted to stimulate the brain's visual cortex. . . . .	10
1.10	Navigation using the IG system. . . . .	11
1.11	The IG operation principle: translation of visual data onto a tactile representation. . . . .	12
1.12	The image acquisition/processing performed by the IG vision system. . . . .	13
1.13	(a) Braille cell, (b) Braille cells only possible vertical arrangement and (c) portable Braille display [HumanWare]. . . . .	15
1.14	Piezoelectric based tactile displays. Prototypes of (a) the University of Exeter, (b) the University of Heidelberg and (c) McGill University. . . . .	16
1.15	Pneumatic based devices. (a) Berkeley's tactile display and (b) touch stimulation devices: the University of Salford's (1) Teletact and (2) palmar pad and (3) Toshiba's glove. . . . .	17
1.16	SMA based tactile displays. Prototypes of (a) the TiNi Alloy Company, (b) the University of Newcastle, (c) the University of Tokyo and (d) Harvard University. . . . .	18
1.17	Electromagnetic based tactile displays. Prototypes of (a) Harvard University, (b) NIBH, (c) Exo Inc. (d) the University of Karlsruhe and (e) CEA/LIST. . . . .	20
1.18	(a) The University of Hull ER fluids based tactile display and (b) EAP based ciliary device from Kobe University. . . . .	20
1.19	Cross-section of the glabrous skin of the hand schematically representing the location of the four types of mechanoreceptors, after [Johansson83]. . . . .	22

1.20	Skin indentation minimal detection thresholds as function of frequency, after [Sekuler02]. . . . .	23
1.21	The SME in SMAs at macroscopic and crystallographic levels. . . . .	25
1.22	Schematic of M→A and A→M transformations, after [Liang90]. . . . .	26
1.23	Stress-temperature dependence in SMAs. . . . .	26
1.24	(a) The shape memory effect (SME) and (b) superelasticity in SMAs. . . .	27
2.1	SMA block diagram model. . . . .	30
2.2	Heat exchange model. . . . .	31
2.3	Calculated thermal relationships for SMAs using equations (2.6) to (2.9): (a) effect of diameter $d$ on coefficient $h$ , (b) time response of a set of wire's diameter to a fixed heating current (500 mA), (c) time response of a 200 $\mu\text{m}$ wire at different heating electric currents (400 to 800 mA), comparison of (d) actuating, (e) resetting and (f) total time responses under free and forced convection conditions. . . . .	35
2.4	Effect of dimensionless heat of transformation $H$ on the cooling time. . . .	38
2.5	Temperature-time curves of the SMA: with and without phase transformation. . . . .	39
2.6	Torsional stress and torsional strain distribution in an SMA wire. . . . .	40
2.7	Schematic stress-strain curves under constant temperature. . . . .	42
2.8	Evolution of the boundary radius $r_b$ and torsional stress distribution during the (a), (b) loading and (c)-(e) unloading processes ( $T > A_s$ ). . . . .	43
2.9	Material constants: (a) temperature dependent SMA modulus of elasticity, after [Birman97] and (b) influence of $c_m$ and $c_a$ in the SMA phase diagram. . . .	44
2.10	Analytical load-deflection relations of the SMA spring under constant temperatures (20, 78 and 98°C). . . . .	45
2.11	Relation between load and boundary radius of transformation. . . . .	46
2.12	(a) Calculated SMA behavior in the load-deflection-temperature space and (b) SMA deflection-temperature behavior at constant stress. . . . .	46
2.13	Fabrication procedure of an SMA helical spring: (a) constrained Flexinol wire on a mandrel and (b) helical shape after heat treatment. . . . .	47
2.14	DSC results: (a) comparison of the DSCs of NiTi wire and spring, (b) DSCs of the spring Pre and Post 40 thermal cycles, (c) temperature stabilization during the A→R transformation and (d) DSC showing heat of transformation $\Delta H$ . . . . .	49
2.15	The spring's measured electrical resistance $R$ as a function of (a) deflection and (b) temperature. (c) Comparison of the evolution of $R$ as a function of temperature for different pre-deformations values. (d) Experimental data fitted by empiric equation (2.30). . . . .	51
2.16	Comparison of the experimental temperature-time response with the corresponding simulation. . . . .	53
2.17	Time response using a displacement relation: (a) response to a set of input currents (7 mm pre-deformed spring) and (b) analytical/experimental comparison of actuation times. . . . .	54
2.18	Time response at constant stress (6.2 MPa). . . . .	55

---

2.19	Experimental time response as a function of the applied stress. . . . .	55
2.20	Deformation behavior of the SMA spring: (a) load-deflection relations at constant temperatures (20, 85 and 105°C) and (b) hysteresis due to R-phase. . . . .	56
2.21	Experimentally based computational SMA behavior in the load-deflection-temperature space. . . . .	57
2.22	Comparison of experimental stress-strain curves: (a) helical spring and (b) straight wire. . . . .	58
2.23	Load/stress-deflection/strain experimental results for austenitic plastic strain developed. . . . .	59
2.24	Computational stress-deflection-temperature behavior for martensitic/austenitic plastic deformation in loading. . . . .	59
2.25	Strain amplitude versus number of cycles. . . . .	60
2.26	Comparison between the micro-structures of a NiTi wire and helical spring before and after fatigue induced by plastic strain. . . . .	62
3.1	Main SMA actuator configurations using one-way effect SMAs: (a) linear and (b) rotational motion. . . . .	66
3.2	Examples of existing actuators using the basic types of SMA configurations: (a), (b) antagonistic and (c), (d) biased actuators. . . . .	67
3.3	Dead weight load as biasing force: (a) the actuator's conceptual representation and its load-deflection behavior. (b) Thermomechanical path performed by the actuator in the load-deflection-temperature space. . . . .	68
3.4	Biased actuator: (a) the actuator's conceptual representation and its load-deflection behavior. (b) Thermomechanical path performed by the actuator in the load-deflection-temperature space. . . . .	69
3.5	Influence of the bias spring stiffness $k$ on the load-deflection characteristic of the actuator. . . . .	70
3.6	SMA antagonist principle: (a) the actuator's conceptual representation and load-deflection relations for a complete operating cycle. (b) Thermomechanical path performed by the actuator in the load-deflection-temperature space. . . . .	71
3.7	Antagonist operation with a passive austenitic spring: active spring's behavior at (a) set and (b) reset points. . . . .	72
3.8	Bistable actuator: biased configuration using a blocking mechanism to achieve two stable positions. . . . .	73
3.9	Principle and prototype of an SMA based taxel with a pen-like latching mechanism. . . . .	75
3.10	Principle of taxel based on an SMA antagonist arrangement and a clamping/latching mechanism. . . . .	76
3.11	Optimized principle of the SMA taxel. . . . .	77
3.12	The upper spring's behavior face to an external force during its austenitic state. . . . .	78
3.13	The upper spring's behavior face to an external force: martensitic case. . . . .	79
3.14	Miniature SMA based actuator: implementation and prototype. . . . .	80

---

3.15	Effect of external force on the taxel's displacement: upper spring in (a) austenite and (b) martensite state. . . . .	81
3.16	The taxel's performance: bistable concept with no blocking structures. . .	82
3.17	(a) The antagonist controller and position tracking responses of the actuator to 0.27 and 0.37 Hz square power signals. (b) Tracking responses to 0.5, 1 and 1.5 Hz square power signals under forced-air convection conditions. . . . .	83
4.1	Conceptual representation of a 8 x 8 SMA based tactile display. . . . .	86
4.2	Water-jet cut PVC structure. . . . .	87
4.3	(a) Structure of the tactile display and (b) configuration of one row of taxels. . . . .	87
4.4	The actuator's electromechanical connector. . . . .	88
4.5	(a) High-density compact actuator array and (b) contact area. . . . .	88
4.6	Low-cost highly-portable tactile display with SMAs. . . . .	89
4.7	Examples of 2D shapes displayed using the tactile device. . . . .	90
4.8	Drive components of the tactile display. . . . .	90
4.9	2N <sup>2</sup> controller's architecture. . . . .	91
4.10	(a) 3N crossbar matrix switch control method: a half SMA spring is actuated by placing its row to <i>V</i> and the corresponding column to <i>GND</i> . (b) The controller's crossbar-based architecture. . . . .	92
4.11	Scalability of the electronic controllers: crossbar vs traditional (independent control) architecture. . . . .	93
4.12	(a) The actuator's crossbar-driven circuit model and (b) bipolar, (c) MosFet transistor arrays proposed to drive the taxel from a TTL input. . . . .	94
4.13	(a) Parasitic parallel resistors in the tactile display and (b) SMA-diode array implemented to eliminate parasitic resistors and current losses. . . . .	95
4.14	Crossbar correspondence with vectors and matrices. . . . .	96
4.15	The mirror effect in the crossbar-based tactile display. . . . .	96
4.16	User interfaces. . . . .	100
4.17	The SMA's heat flow distribution as a function of distance. . . . .	101
4.18	Superposition used to simulate the impact of several heat sources. . . . .	101
4.19	Steady-state solution of the 3 x 3 array (surface and contour plots) with (a) one, (b) two, (c) four and (d) eight heat sources. . . . .	102
4.20	Simulated temperature-time responses for the 1, 2, 4 and 8-adjacency configurations: (a) passive and (b) active SMA. . . . .	103
5.1	The experimental platform. . . . .	107
5.2	Single stimulus point configurations to evaluate the subjects' tactile acuity (location of a tactile stimulus). . . . .	107
5.3	The subjects' performance for each of the nine configurations (passive touch). . . . .	108
5.4	Braille characters to evaluate the subjects' tactile acuity (location of simultaneous tactile stimuli). . . . .	108
5.5	The subjects' performance in the Braille character recognition task (active touch): touch (black bars) and vision+touch (yellow bars). Bimodal perception led to a better recognition performance. . . . .	109

---

5.6	The six basic shapes used in experiment 2. All shapes were displayed in a 5 x 5 taxel area (40% of the active space on the display). The black dot represents the subject's related position to the shape. . . . .	110
5.7	The mean percent correct discrimination performance for each of the six basic shapes (active touch). . . . .	111
5.8	Exploration times by shape. Filled shapes appear to be more difficult to identify. . . . .	111
5.9	Results of the 5 subjects in the 2D tactile shape recognition task. . . . .	112
5.10	Exploration time by shape (drawing session). . . . .	113
5.11	Configurations used in the direction recognition task. The four basic directions (North, South, Est, West) were presented to the subjects as straight lines. The number inside the contact pin indicates its schedule of activation and the black dot the subject's related position to the moving sequence. . . . .	114
5.12	The second set of configurations used in the direction recognition task. . . . .	114
5.13	Comparison between trial-1/trial-2 direction recognition times. The broken line represents the end of sequence display (8 s). . . . .	115
5.14	(a) Configurations used in the environment structure understanding task and (b) the subject in the environment. . . . .	116
5.15	Comparison between the subjects' average recognition performance in trials 1 and 2. . . . .	116
5.16	Exploration times per subject in the environment structure understanding task: (a) trial 1 and (b) trial 2. . . . .	117
5.17	(a) The virtual environment used in session 3. The subject progresses in the environment according to the schedule indicated. (b) The subject's views and the corresponding tactile representations. The subject's position in the environment/tactile display is represented by the black dot. . . . .	118
5.18	The four environments proposed to the subjects. The correct answer is <b>B</b> . Note that shape recognition (square/rectangle, triangle and straight lines) and spatial sense (dimension and location) abilities are evaluated as well. . . . .	118
5.19	The four views recognized by subject-1. . . . .	119
5.20	The four views recognized by subject-2. . . . .	119
5.21	The four views recognized by subject-3. . . . .	120
5.22	The four views recognized by subject-4. . . . .	120
5.23	The four views recognized by subject-5. . . . .	121
5.24	Exploration times per subject in the tactile map task. . . . .	122
5.25	Evolution of DSC thermograms of NiTi alloy at 500°C. . . . .	125
5.26	Heating drive methods among rows in the matrix. Signals and temporal evolution of temperature using a (a) one by one (currently used) and (b) PWM method. . . . .	125
A.1	(a) Tensile force exerted as a function of geometrical parameters $D$ and $d$ and (b) 2D representation of the region of interest. . . . .	139
B.1	Schematic representation of the experimental setups used to measure the spring's electrical resistance. . . . .	141

---

B.2	Experimental setup used to measure the spring's thermal behavior: (a) photo and (b) schematic representation. . . . .	142
B.3	Experimental platform used to measure the spring's tensile behavior: (a) photo and (b) schematic representation. . . . .	143
C.1	Fan in a rectangular duct. . . . .	145
D.1	(a) Concept de navigation avec le système Lunettes Intelligentes et (b) son mode opératoire: (1) l'image mosaïque obtenue avec le système de stéréovision, représentant l'environnement immédiat, (2) les obstacles dans la scène sont localisés par l'intermédiaire des algorithmes de vision et sont affichés via leur contour (3) sur l'interface tactile, l'identification de leur position permet alors d'en déduire la trajectoire à suivre. . . . .	148
D.2	Seuil de détection minimal de déformation de la peau en fonction de la fréquence dans les corpuscules de Meissner, d'après [Sekuler02]. . . . .	150
D.3	Effet mémoire de forme. . . . .	151
D.4	(a) Ressort NiTi et (b) températures de transition déterminées par analyse DSC. . . . .	152
D.5	Relations force-déformation du ressort NiTi : (a) Confrontation des mesures expérimentales et de simulation à températures constantes (20, 85 et 105°C) et (b) représentation dans l'espace force-déformation-température du comportement en charge. . . . .	154
D.6	Actionneur miniature basé sur le principe de montage antagoniste de deux ressorts en AMF. . . . .	154
D.7	Principe d'opération du taxel proposé. . . . .	155
D.8	Principe de fonctionnement antagoniste des AMF: représentation conceptuelle et relations force-déformation pour un cycle d'opération. . . . .	156
D.9	Principe de fonctionnement antagoniste des AMF: trajectoire thermomécanique dans l'espace force-déformation-température. . . . .	157
D.10	Performance du taxel lors de l'application d'une force externe $F_e$ : concept bistable sans structures additionnelles de blocage. . . . .	157
D.11	(a) Le contrôleur antagoniste et ses réponses en position aux fréquences d'entrée de 0,27 et 0,37 Hz. (b) Réponses en position aux fréquences de 0,5, 1 et 1,5 Hz sous conditions de convection forcée. . . . .	158
D.12	(a) Concept de l'interface tactile et (b) prototype (64 taxels). . . . .	159
D.13	Première version d'une interface tactile portable à bas coût pour les déficients visuels basée sur des micro-actionneurs en alliages à mémoire de forme (AMF). . . . .	159
D.14	Système électronique de commande. . . . .	160
D.15	Contrôleur électronique 3N. . . . .	161
D.16	La plate-forme expérimentale. . . . .	162
D.17	(a) L'environnement virtuel proposé aux sujets. Le sujet progresse dans l'environnement selon la numérotation indiquée. (b) Les vues du sujet et les représentations tactiles correspondantes. La position du sujet dans l'environnement et sur la surface tactile est indiquée par le point noir. . . . .	162

D.18 Les 4 environnements proposés aux sujets. La réponse correcte est la <b>B</b> . Deux capacités sont simultanément testées: la reconnaissance de formes (carré/rectangle, triangle et ligne droite) et la spatialisation (dimension et placement). . . . .	163
D.19 Les quatre vues dessinées par les 5 sujets et leur décision finale. . . . .	164





# Introduction

Advances of technology and better knowledge in human psycho-physiological 3D world perception permit the design and development of new powerful and fast interfaces assisting humans in the execution of complex and difficult tasks. Since their beginning, haptic interfaces (force and tactile displays) have been mainly associated with virtual reality environments. However, integrated with vision, they present a potential solution to the problem of systems applied to situations where vision is limited or absent, and where concise and high speed information is required. Intelligent mobile robotics systems, highly reactive interfaces, medical instrumentation and electronic aids for mobility of the blind are some potential examples. The last application is perhaps one of the most challenging.

Indeed, according to the 2002 monitoring report of the World Health Organization (WHO)<sup>1</sup>, there are currently close to 180 million people worldwide suffering from severe visual disability, 45 million of whom are totally blind. This census indicates that 7.4 million live in Europe and estimates that this number will double in the next twenty years as Europe becomes an aging society [WHO02]. As a significant part of our society, the issue of the blind/visually impaired represents a very important problem in terms of health and social security.

Research on supportive systems for the blind has focused on two main areas: information transmission and mobility assistance.

Problems related to information transmission concern reading, character recognition and rendering graphic information about 2D and 3D scenes. The most successful reading tool is the Braille dot code. Introduced by Louis Braille in the 19<sup>th</sup> century, it has now become a standard worldwide. Inventions addressing the problems of character recognition and pictorial representation mostly consist of tactile interfaces. They permit character and graphic recognition by feeling a tactile version of them.

Of all sensations perceived through our senses, those received through sight have by far the greatest influence on perception. Sight combined with the other senses, mainly hearing, allow us to have a world global perception. For the blind, the lack of sight and its "substitution" by hearing and touch provide unfortunately a world with only limited perception. Undoubtedly, most of the information required for mobility tasks is gathered

---

<sup>1</sup>The 2002 WHO report is considered the best achievable scientific estimate of the global burden of visual impairment since the early 1990s. The next report is expected in 2020.

through sight. Confronting a blind person to mobility is a challenging issue. Many sighted do not fully realize the problems involved when moving about. Things that the sighted take for granted may be major constraints for the blind. Human mobility seems then to be more than traveling from a starting to a destination point: spatial information of the immediate environment, orientation and obstacle avoidance are essential to offer the blind autonomy and most of all, safety.

Many electronic aids for mobility of the blind have been proposed. However, none of them has met the demanding criteria of enabling independent, efficient and safe travel in unfamiliar and non-cooperating environments. Therefore, there is an urgent need to determine how and by which technology is possible to best compensate the blind for deficiencies in spatial mobility.

The work presented in this dissertation was developed within the *Intelligent Glasses (IG)* project, whose goal is to design and prototype a novel improved electronic system for mobility assistance of the blind.

The dissertation is organized as follows:

Chapter 1 justifies the reason for the design and implementation of new travel aids for the blind through a survey and evaluation of existing aids. The chapter introduces then the *Intelligent Glasses*, a system that codes the visual environment into the tactile domain using stereoscopic vision and a tactile display. The chapter focuses next on the design of a tactile display. A survey of existing tactile displays is presented to identify the different actuation technologies used. An evaluation of their characteristics suggests retaining the shape memory alloy (SMA) technology, particularly the helical spring shape.

Chapter 2 focuses on the design and implementation of an SMA helical spring that is optimal in time response, fatigue and force performance for touch stimulation applications. Existing constitutive models are used to predict its thermomechanical behavior and experimental results are presented to validate it.

Based on these results, chapter 3 presents the design, implementation and experimental evaluation of a miniature actuator for touch stimulation. After an evaluation of different SMA based actuator configurations, several prototypes are envisaged and implemented. A comparison of their performances suggests retaining an antagonist configuration.

Chapter 4 presents the design and implementation of an SMA based tactile display device. A technical description of the tactile display, electronic drive and control method is presented in detail.

Chapter 5 evaluates the performance of the tactile display and the effectiveness of the information displayed through a set of tactile perception tests.

Finally, the dissertation concludes with a summary of the achievements of the present work and future work perspectives.

---

# Chapter 1

## Toward a New Electronic Travel Aid for the Blind

---

This introductory chapter addresses the issue of blind mobility aids, particularly of electronic travel aids (ETAs). A review of the literature is first presented to illustrate the most relevant work and progresses done in this area. Then, an evaluation of the characteristics of existing ETAs is performed to identify their shortcomings and to formulate the key points for a new improved ETA: the *Intelligent Glasses*. Within this framework, the research goals of the dissertation will be defined, followed by a general overview of the entire work.

## 1.1 Blind mobility aids

Several devices have been developed for mobility and navigation assistance of the blind and are typically known as travel aids or blind mobility aids. Two kinds of mobility aids can be identified in the literature: classic and electronic aids.

### 1.1.1 Classic aids

The most successful and widely used are the white cane (also called walking cane) and the guide dog.

The white cane (Figure 1.1(a)), a simple and purely mechanical device, is a dedicated tool to detect static obstacles on the ground, uneven surfaces, holes and steps via simple tactile-force feedback. It is inexpensive (about 50 €), lightweight and portable. However, its "scan" range is limited (1-2 m and neither overhanging nor dynamic obstacle detection) and the user must be trained in its use for more than one hundred hours with no guarantee to master the technique [RNIB].

Guide dogs (Figure 1.1(b)) are very capable travel aids. However, they require extensive training, constant care (estimated in 6200 €/year), they have a relative short useful life-time (7 to 8 years) and their price is far to be affordable (about 15,000 €) [GDA]. Furthermore, a dog is not capable of taking a decision in situations beyond its training.



(a)



(b)

Figure 1.1: Classic travel aids for the blind: (a) white cane and (b) guide dog.

### 1.1.2 Electronic travel aids

Since the 1960s, the technology progresses have made possible the development of electronic travel aids (ETAs). Technologically, two groups of ETAs can be distinguished: the traditional and the new generation of ETAs.

Traditional ETAs are similar to radar systems: a laser or ultrasonic beam is emitted in a certain direction in space and the beam is reflected back from objects that it confronts on its way. A sensor detects the reflected beam, measures the distance to the object and indicates that information to the user through audio or tactile signals.

A new generation of ETAs aims to provide a sensory substitution/supplementation more than merely obstacle detection. These ETAs intend to transform stimuli characteristic of visual modality into stimuli of another sensory modality (mostly hearing and touch). The information is acquired using video cameras and its processing is more at cognitive level (brain plasticity, perception, intentionality, etc.) [Lenay03].

A brief non-exhaustive review of ETAs is presented below.

### 1.1.2.1 First generation/Traditional ETAs

#### *Ultrasonic ETAs*

Many ETAs of varying types and ergonomics have been developed.

In the early years, the most sophisticated device that first became commercially available was the *Kay Sonic Torch* (Figure 1.2(a)), a hand held device that used an FM sonar with an auditory feedback presented to the user via an earphone. The distance to an object was indicated by a frequency and its nature by a timbre [Kay64a].

Since then, hand held type devices continued to be developed: the *Mowat Sensor* (Figure 1.2(b)) displays the distance to an object (up to 4 m) by means of tactile vibrations. The intensity of vibration is inversely proportional to the distance between the sensor and the object [Pressey77].

The *Nottingham Obstacle Detector (NOD)* provides an auditory feedback proportional to the distance user-object via eight different musical tones [Bissit80].

The most recent hand held device is the *Miniguide* (Figure 1.2(c)) which is able to detect obstacles up to 8 m and provides both vibrotactile and auditory feedbacks [GDP].



(a)



(b)



(c)

Figure 1.2: Hand held sonars: (a) the Kay Sonic Torch (1964), (b) the Mowat Sensor (1977) and (c) the Miniguide (2005).

Other ETAs attempt to be wearable to replace the active manual scanning of the environment by body (torso/head) movement:

The *Russell Pathsounder* [Russell66a], the first wearable ETA (no longer available), consisted of two ultrasonic sensors worn around the neck and provided vibrotactile and auditory feedbacks to indicate a binary "path clear" or "path not clear".

The *Binaural Sonic Aid (SonicGuide)* [Kay74b] consists of an ultrasonic wide-beam equipment mounted on spectacle lenses (Figure 1.3(a)). Signals reflected from the 3D world are presented to the user as audio indicating the presence of an obstacle and its approximate distance to the user.

The SonicGuide has undergone continuous improvements and its latest version is the system called *KASPA* [SonicVision]. Unlike the SonicGuide, KASPA is worn as a headband (Figure 1.3(b)). KASPA creates an auditory representation of the objects ahead of the user, and, with sufficient training, allows users to distinguish different objects and even different surfaces in the environment.

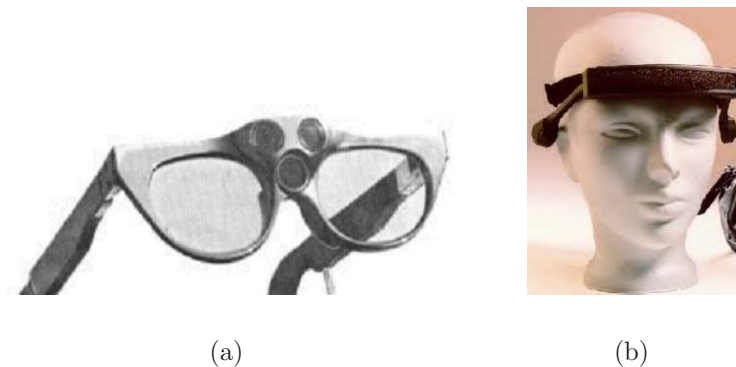


Figure 1.3: (a) The SonicGuide (1974) and (b) its latest version, the KASPA system (2002).

The *NavBelt* [Borenstein90], another wearable ETA proposed by the University of Michigan, provides acoustical feedback from an array of ultrasonic sensors mounted on a belt around the abdomen (Figure 1.4(a)). These sensors provide information on very local obstacles placed in a  $120^\circ$  wide sector ahead of the user.

Later on, the same team conceived the *GuideCane* [Ulrich01], which is the Navbelt concept in a wheeled white cane-like device (Figure 1.4(b)). Similarly, the ultrasonic sensors provide a total scan range of  $120^\circ$  and are able to detect obstacles placed on the walking surface.

Since the GuideCane, the concept of ultrasonic canes quickly improved to fully incorporate the sensors in the traditional white cane. Two products are nowadays commercially available: the *Bat "K" Sonar-Cane* and the *UltraCane*.

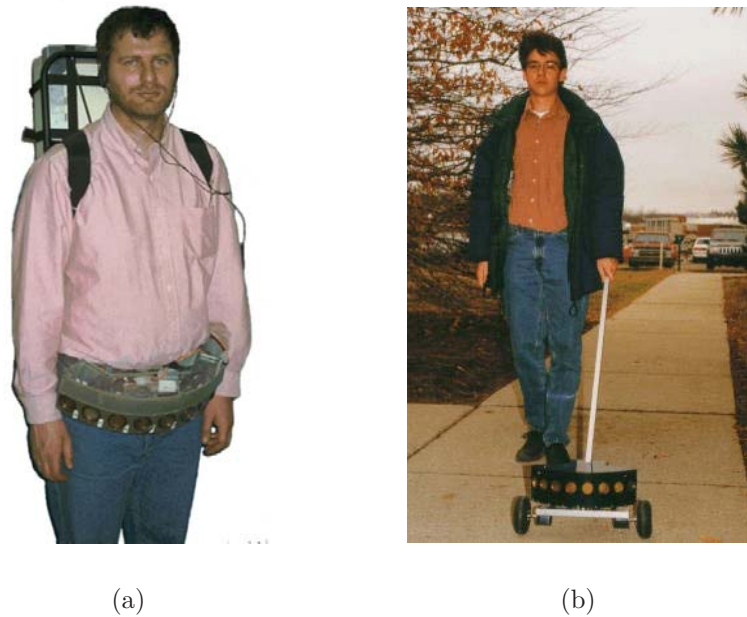


Figure 1.4: The University of Michigan ETAs: (a) the Navbelt and (b) the GuideCane.

While the Bat "K" Sonar-Cane (Figure 1.5(a)) provides acoustical feedback (the frequency of the sound is proportional to distance) [BAT], the Ultracane (Figure 1.5(b)) provides a vibration type feedback through the handle (vibrations become faster as the user moves closer to the object) [SFS]. Both offer a detection range of 5 m and provide information on obstacles located ahead of the user and at head height.

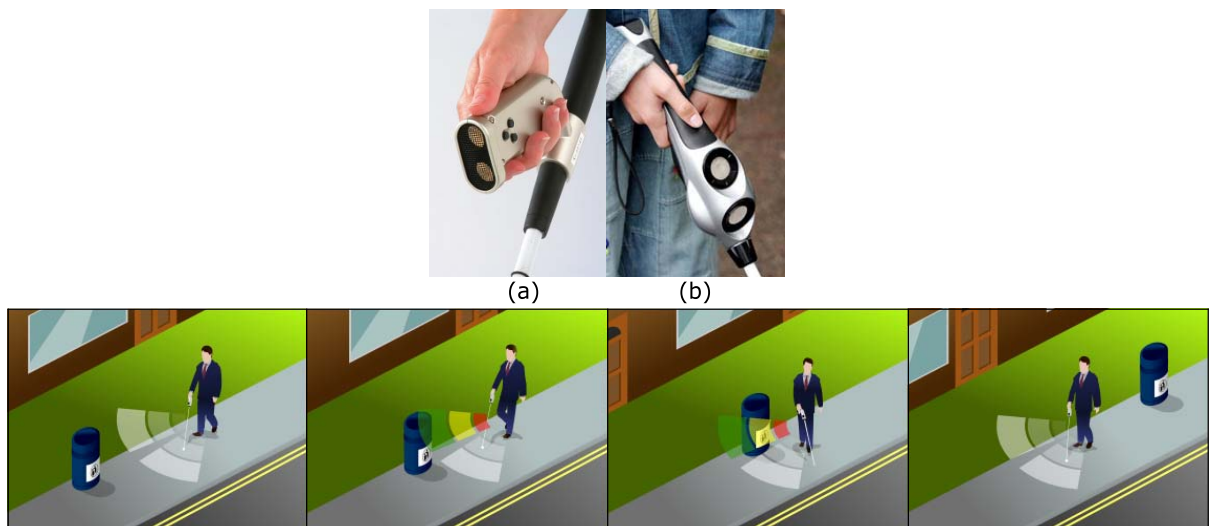


Figure 1.5: Ultrasonic based canes: (a) The Bat "K" Sonar-Cane and (b) the UltraCane. Note that the user is able to detect obstacles and take decisions before making contact with the white cane.

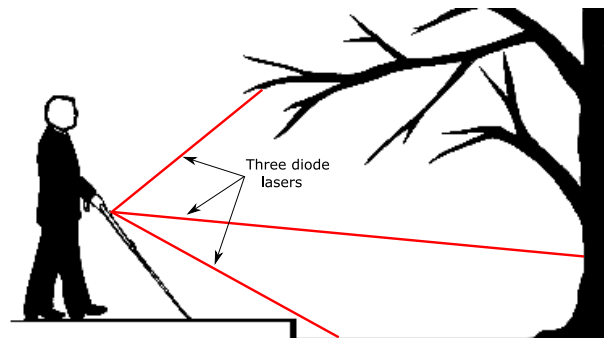


### *Laser ETAs*

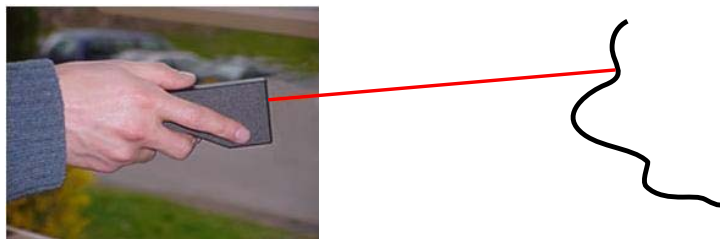
One of the best known and early laser based ETAs is the *C-5 Laser Cane* [Benjamin73] which is based on optical triangulation to detect drop-offs, obstacles at head height and overhanging obstacles in front of the user up to a range of 3.5 m ahead (Figure 1.6(a)). It requires environment scanning and provides information on one nearest obstacle at a time by means of acoustic feedback.

This system developed in the 70s is the precursor of a large series of laser based devices incorporated in the cane, such as the *LaserCane* [Nurion-Raycal].

The *Télé tact* [Farcy97], designed at Paris 11 University, is a pistol-like system detecting obstacles and calculating their user-related position by means of a laser beam (Figure 1.6(b)). Two feedback modes are handled: acoustic and tactile.



(a)



(b)

Figure 1.6: Laser based ETAs: (a) the C-5 Laser Cane concept and (b) the *Télé tact*.

### 1.1.2.2 New generation of ETAs

The *vOICe* system (Figure 1.7(a)), patented by Philips Co., converts visual depth information into an auditory representation [Meijer92]. This is the first device that successfully uses a camera as an input source. An image is translated to sounds where frequency and loudness represents different scene information parameters such as position, elevation and brightness (Figure 1.7(b)). Simple things like finding an object may be mastered in minutes but fully mastering the *vOICe*'s visual-to-auditory language may well take years.



Figure 1.7: (a) The *vOICe* system and (b) an example of its image-to-sound rendering.

The *TDU* (Tongue Display Unit), proposed in [Bach-Rita98], translates optical images picked up by a camera into electro-tactile stimuli which are delivered to the dorsum of the tongue via a 12 x 12 flexible electrode array placed in the mouth (Figure 1.8). After sufficient training (15 h), the user loses awareness of on-the-tongue sensations and perceive the stimulation as shapes and features in space.

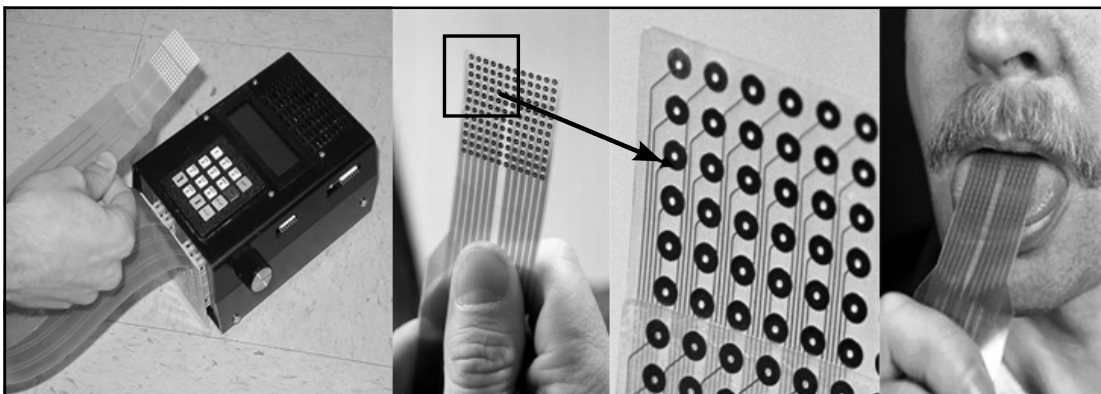


Figure 1.8: The *TDU* system.

The ultimately goal of the *TDU* is to develop a compact, cosmetically acceptable, wireless system for blind people, with a miniature TV camera, microelectronics and FM transmitter built into a pair of glasses, and the electro-tactile array fitted in a dental orthodontic retainer.

Another approach, much more invasive, proposes to stimulate directly the brain zones concerned with visual perception. The *Dobelle eye* (Figure 1.9) consists of a miniature camera and an ultrasonic distance sensor, both mounted on a pair of eyeglasses. The sensors connect through a cable to a miniature computer, which is worn in a pack on the user's belt. After processing the video and distance signals, the computer uses a sophisticated computer-imaging technology to simplify the image. The computer transmits then the image as pulses to an array of 68 platinum electrodes implanted on the surface of the brain's visual cortex [Dobelle00].

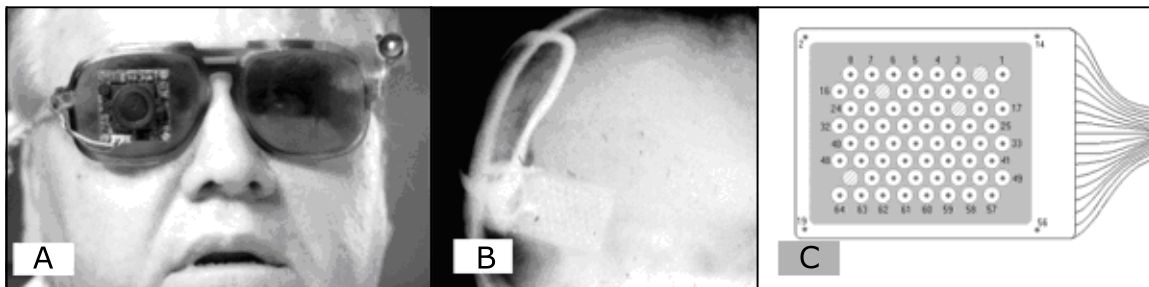


Figure 1.9: The Dobelle eye: a prosthetic device surgically implanted to stimulate the brain's visual cortex.

These kind of devices need to be surgically implanted and intend to partially restore lost vision to people who are blind using the brain's plasticity, i.e. the brain's ability to reorganize neural pathways based on new sensory experiences.

### 1.1.3 Synthesis and discussion

Despite 40 years of efforts and the great variety of ETAs available, none of these devices is widely used and user acceptance is low. One of the main reasons of this rejection seems to be the quite small improvement achieved in comparison to classic travel aids (cane and dog).

Five fundamental shortcomings are identified in these ETAs:

1. Active scanning. Traditional ETAs obtain a 3D world perception via complex, sequential and time-consuming operations: environment scanning using sonar-wave or laser-beam requires the user to actively scan the environment, to memorize the gathered information, to analyze it and to take a decision: constant activity and conscious (cognitive) effort that reduce walking speed and quickly fatigue the user.
2. Acoustic feedback, in both traditional and new ETAs, interferes with the blind person's ability to pick up environmental cues through hearing. Additional related problems are the degradation and overload of the hearing sense. Recent studies [Hakkinen02] have shown that a 20-30 minute usage of acoustic feedback devices causes serious problems to human sensors information registration, reduces human capacity to perform usual tasks and affects the posture and equilibrium.

3. Long learning/training time. New generation ETAs require long training times to learn and master the visual-to-another-sensory-modality new language: a non-negligible hidden cost.
4. Invasive technologies. Traditional ETAs are invasive. They are intrusive and disturb the environment with their scanning and feedback technologies.
5. Burdensome devices. While traditional ETAs have accomplished to be lightweight and inconspicuous, the new ones are still too burdensome and visually noticeable to be portable devices, which is an essential need for people with visual impairments.

A fact is that until now, no ETA has been built that can meet the demanding criteria of enabling independent, efficient, effective and safe travel in unfamiliar and non-cooperating environments.

## 1.2 Intelligent Glasses: a visuo-tactile ETA for the blind

The *Intelligent Glasses (IG)* is a new sensory substitution/supplementation ETA that proposes a vision-like 3D world "quite" global perception concept that overcomes the drawbacks of sequential, time-consuming and environmental intrusive scanning.

As feedback, active touch, never used before in ETAs, could provide a significant improvement: quick interpretation and non-aggressive feedback using lightweight highly-portable devices.

The IG system is basically composed of 2 main modules: vision module and tactile display [Pissaloux02]. Figure 1.10 shows the navigation concept proposed by the IG.

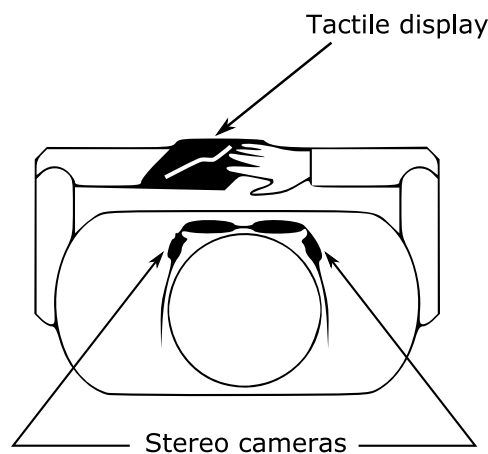


Figure 1.10: Navigation using the IG system.

The IG-ETA intends to provide a simplified representation of the obstacles present in a 3D environment. Figure 1.11 shows its operation principle: (a) a pair of stereo cameras acquire the environment's representation. (b) Vision algorithms are then applied in order to identify the obstacles in the scene and their user-related position. (c) Finally, this information is displayed on a tactile display for fast exploration by the user (active touch). Note that the resulting tactile map is a simple edge-like representation of the obstacles' locations in the scene and that all obstacles are considered and displayed in tactile domain as binary data: presence or absence of an obstacle.

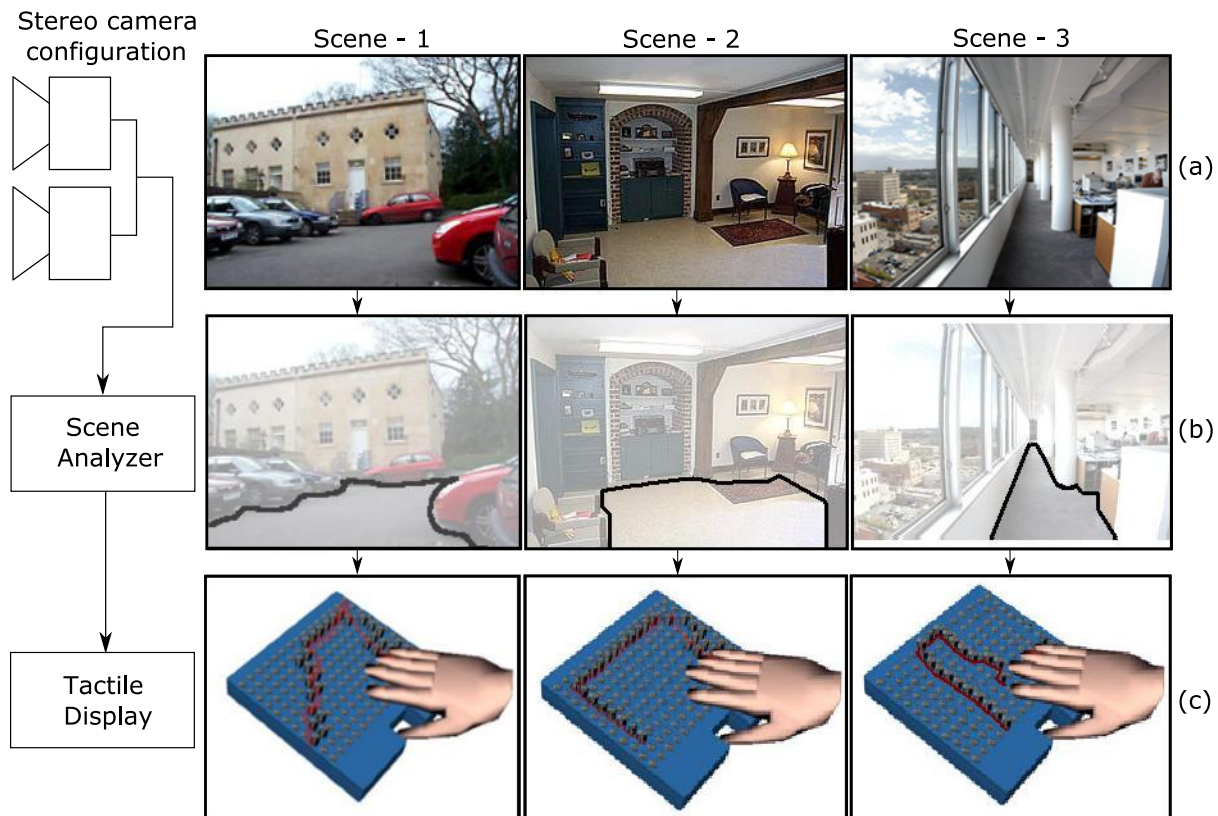


Figure 1.11: The IG operation principle: translation of visual data onto a tactile representation.

This dissertation will focus on the design and implementation of the tactile system. However, a brief overview of the image acquisition/processing unit is presented to illustrate its operation principle. Full details of the IG vision system can be found in [Maingreud05].

### 1.2.1 Vision system

It is widely known that orthogonal mapping of a 3D scene onto an image plane produces a 2D scene in which depth information is missing. The choice of binocular or stereoscopic vision seems then to be mandatory for obstacle detection as depth is directly related to the object's location in the scene.

Using two cameras, the IG vision module obtains two separate and different image views of a scene. Using an original biologically inspired method, homologous points in both images are found to recover the third dimension and to establish a depth map. Next, a reprojection of these points in the 3D space is performed (Figure 1.12). Finally, inertial information obtained from an inertial sensor transforms the camera referenced data to gravity referenced data related to the user's body.

The fact that the cameras are mounted on the glasses frame allows the user to obtain a quasi-global representation of the environment while exploring comfortably with different view points and with wide freedom as the cameras move with the head.

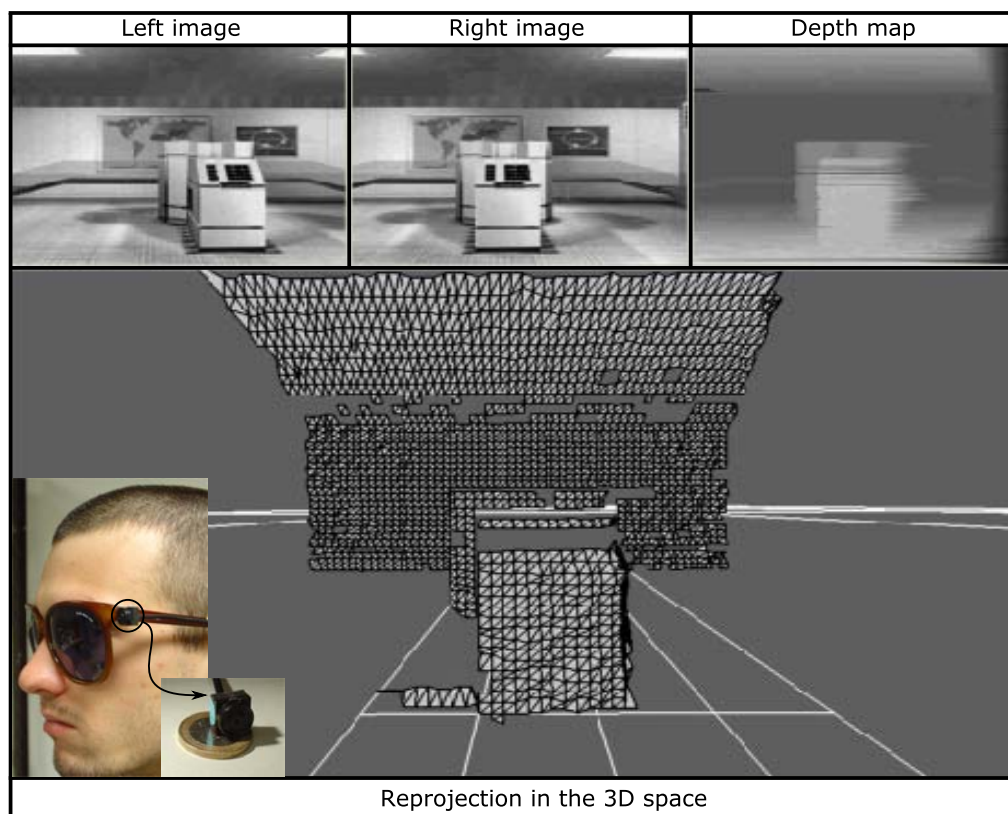


Figure 1.12: The image acquisition/processing performed by the IG vision system.

## 1.2.2 Tactile display

Tactile displays are devices meant to stimulate the skin, particularly on fingertips, to create sensations of contact. Typical displays involve arrays of vibrators or upward/downward moveable pins as skin indentation mechanisms.

Tactile stimulation can be achieved in a number of different actuation technologies. Those already explored include electromagnetic (solenoids and voice coils<sup>1</sup>), piezoelectric ce-

<sup>1</sup>A voice coil or buzzer is the actuator of an audio speaker.

ramic, pneumatic, shape memory alloys (SMAs), electroactive polymers (EAPs) and electrorheological (ER) fluids. An overview of these different technologies is summarized in table 1.1. Each of these approaches has its own advantages/disadvantages and, due to the tradeoffs between bandwidth, delivered force, integration capacity and cost, none of them has been found optimal for tactile displays.

Technology	Principle	Advantages	Disadvantages
Piezoelectric crystals	Changing electric field causes expansion and contraction of crystals	- High spatial resolution - High bandwidth	- Small strokes
Pneumatic	Uses a pressurized gas (air) as the medium for energy transmission	- Low moving mass	- Poor spatial resolution - Limited bandwidth
Shape memory alloys (SMAs)	SMAs contract when heated and expand again as they cool under stress	- Good power/mass ratio	- Low efficiency - Low bandwidth
Solenoid	Magnetic coil applies force to ferrous plunger	- High steady-state forces - Simple to control - Better bandwidth than other materials (except for piezoelectric crystals and voice coils)	- Relatively heavy and bulky
Voice coil	Voice coil vibrates to transmit low amplitude, high frequency vibrations to the skin	- High temporal resolution - Relatively small and lightweight	- Poor spatial resolution
Electrorheological (ER) fluids	Change viscosity and yield stress in the presence of an electric field	- High bandwidth - Small size - Relatively high forces - Lightweight	- Difficult to control - Large voltages (KV) - Only used to emulate stiffness (reactive forces, no "push" forces)
Electroactive polymers (EAPs)	EAPs change in size and shape in response to electrical stimulation	- Ultra lightweight - Better bandwidth and resilience than SMAs - Small voltages and currents (1-2 V, $\mu$ A-mA) - Large strokes	- Low actuation forces (mostly bending actuation) - Poor robustness - Low mechanical energy density

Table 1.1: Actuation technologies used in tactile displays.

A brief non-exhaustive survey of tactile displays organized by technology is presented to illustrate the most representative work done in this area.

### 1.2.2.1 Piezoelectric based displays

Most tactile devices commercially available are piezoelectric Braille displays. A Braille cell, which represents a single character, consists of eight contact pins. In the standard Braille configuration, pins are spaced 2.54 mm apart and are capable of producing vertical strokes of 0.7 mm. Each pin produces a 0.17 N pull force at 6 Hz.

Each cell costs around 40 € and about 80 cells are typically used for displaying a line of text. Cost is not the only drawback when further applications of a significant number of Braille cells are envisaged:

(1) As piezoelectric technology is limited in stroke, mechanical amplifiers are needed. These are implemented as an additional burdensome module attached to the contact pins (Figure 1.13(a)). Displaying more than 2 lines of text at a time or 2D graphics becomes practically impossible: only two cells can be arranged vertically (Figure 1.13(b)).

(2) Portability in Braille text displays is quite relative. Nowadays it is defined by 1 kg weight devices of dimensions: 25 x 15.5 x 5 cm (Figure 1.13(c)).

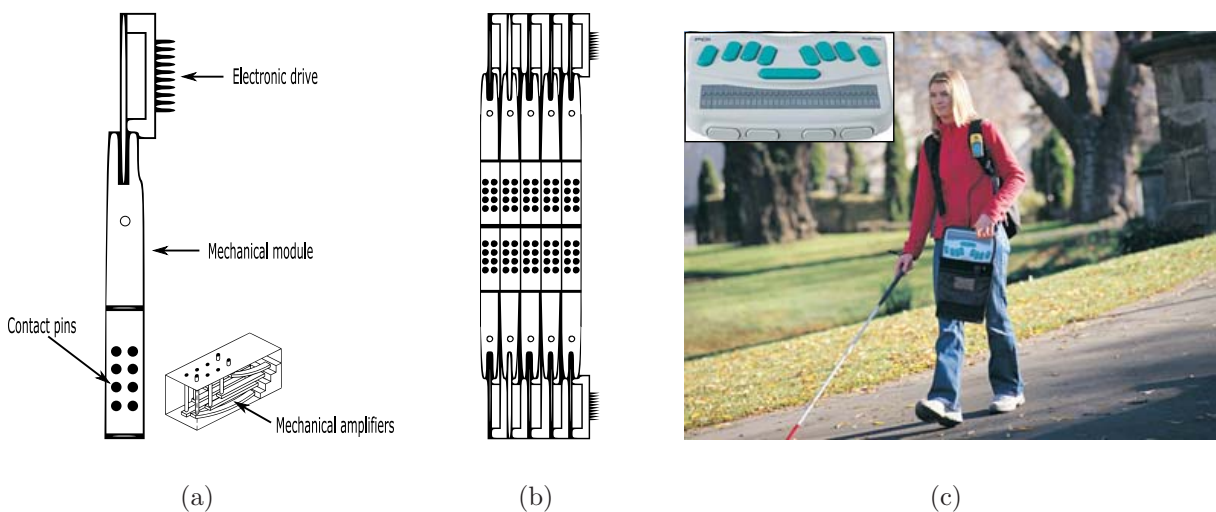


Figure 1.13: (a) Braille cell, (b) Braille cells only possible vertical arrangement and (c) portable Braille display [HumanWare].

Another example of piezoelectric based tactile display is the one designed and implemented at the University of Exeter (UK) (Figure 1.14(a)). This array consists of 100 independently addressed pins spaced 1 mm apart (an effective tactile area of 1 cm<sup>2</sup>, which covers the fingertip). This display produces vertical excursions of 50 μm and has a working bandwidth of 25-400 Hz [Summers02].



The University of Heidelberg (Germany) has developed the *Virtual Tactile Display (VTD)* (Figure 1.14(b)), a tactile display for interactive tactile graphics. It consists of 6 Braille cells (48 piezoelectric actuators) assembled in a movable tactile unit that slides across an area of 220 mm x 220 mm providing access to approximately 4000 "virtual" actuators. The maximum refresh rate is 50 Hz [Maucher00].

McGill University (Canada) has been working on the development of a tactile display called the *Stimulator of Tactile Receptors by Skin Stretch (STReSS)* (Figure 1.14(c)), a novel device that stimulates the fingertip by lateral skin stretch. It is composed of a miniature array of 100 piezoelectric based actuators distributed in ten packs of 10 "combs". The combs are packed one next to another to form a matrix with 1 mm spatial resolution. Its refresh rate is 700 Hz [Pasquero03].

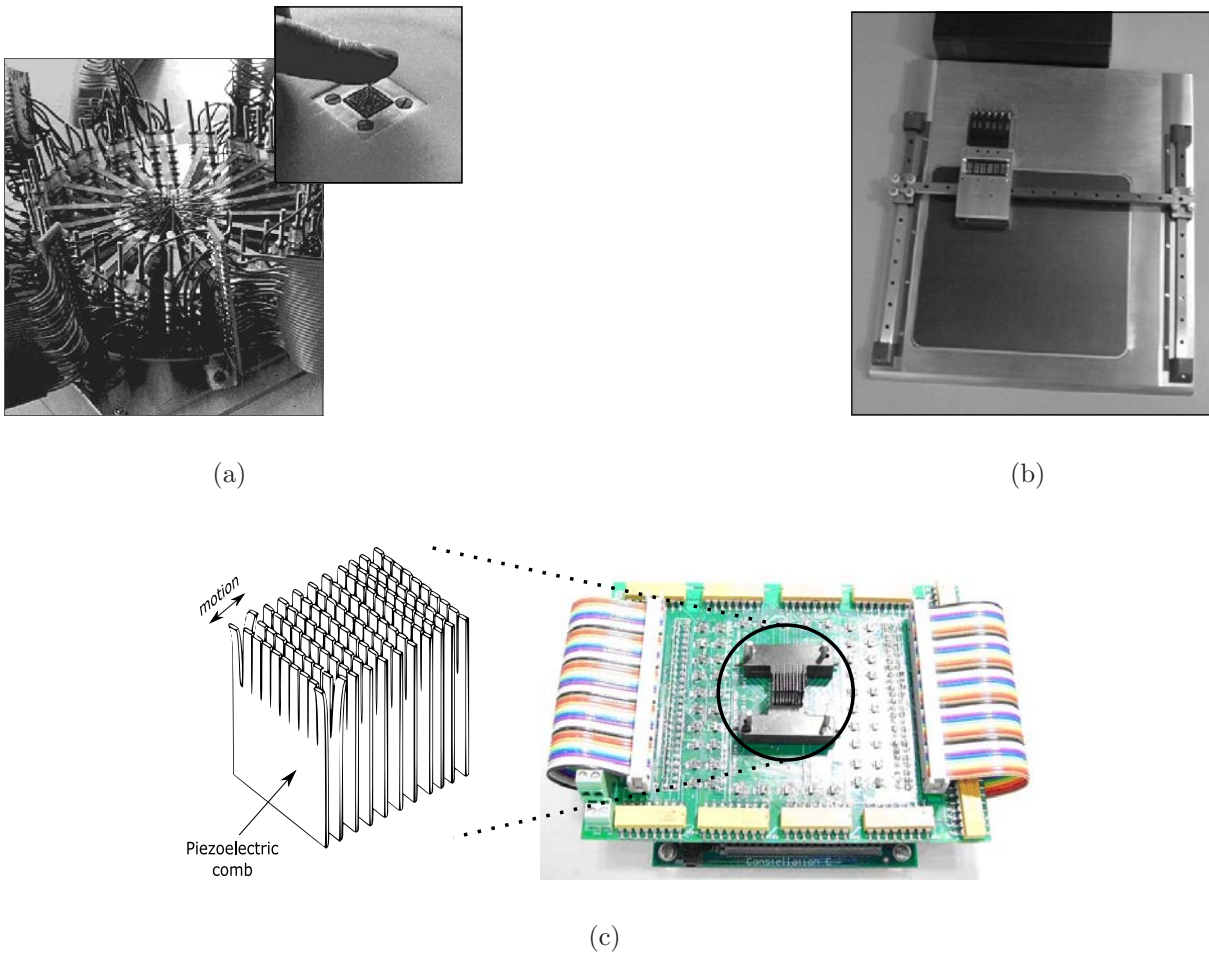


Figure 1.14: Piezoelectric based tactile displays. Prototypes of (a) the University of Exeter, (b) the University of Heidelberg and (c) McGill University.

### 1.2.2.2 Pneumatic based displays

Until now, it seems that the University of California at Berkeley (USA) has proposed the only pneumatic based tactile display (Figure 1.15(a)). This prototype is a 5 x 5 array spaced 2.5 mm apart and has a maximum pull force of 0.3 N per element, with a frequency response of 8 Hz. It uses individually machined pins driven by air at 0.5 MPa pressure. The tactile display is one piece and it is molded from silicone rubber [Moy00].

Other pneumatic based touch stimulation devices do exist such as gloves (passive touch) mainly for teletaction and teleoperation applications [Stone00]. Some examples are the *Teletact* (Figure 1.15(b.1)), developed by the University of Salford (UK), which provides contact forces by inflating miniature air pockets mounted on the glove. The *Teletact* contains thirty air pockets distributed along the glove, which cover the fingers and palm. The same team has developed a pneumatic based palmar pad for virtual reality applications (Figure 1.15(b.2)). Three *Teletact*-like air pockets are attached to the outer surface of the hand to provide simple tactile feedback when the user's virtual hand makes contact with a virtual object.

Similarly, the glove developed by the Toshiba Nuclear Engineering Laboratory (Japan) integrates five inflatable air pockets to apply a pressure on the user's fingertips (Figure 1.15(b.3)).

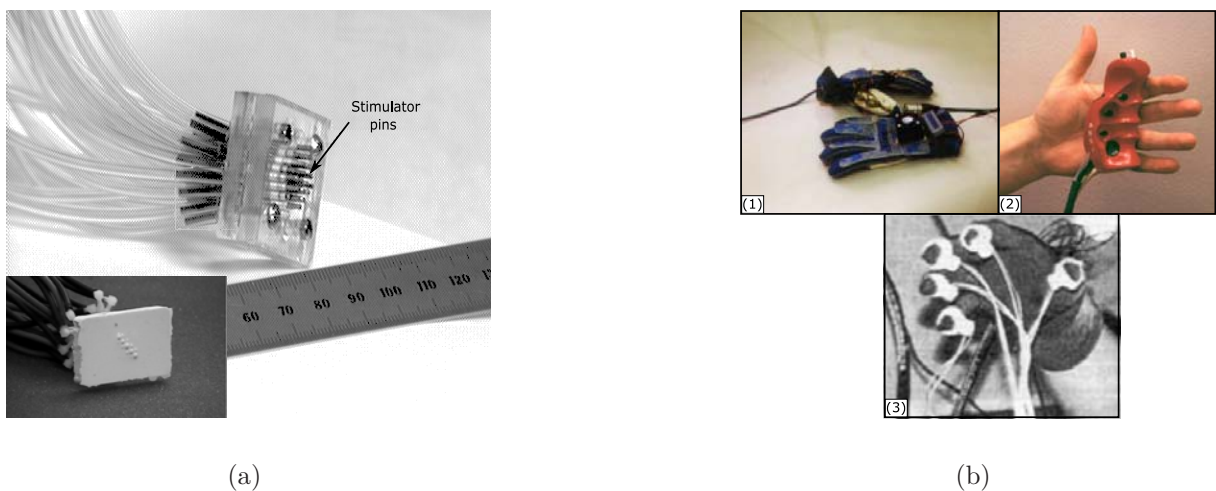


Figure 1.15: Pneumatic based devices. (a) Berkeley's tactile display and (b) touch stimulation devices: the University of Salford's (1) *Teletact* and (2) palmar pad and (3) Toshiba's glove.

### 1.2.2.3 SMA based displays

The TiNi Alloy Company has developed a tactile display consisting of a 5 x 6 array of pins actuated by SMA wires with 1.5 mm spatial resolution and 1 mm vertical excursion (Figure 1.16(a)). Each wire is capable of developing a 60 mN pull force. The maximum bandwidth achieved is 0.9 Hz [TiNi-Alloy90].

The University of Newcastle (UK) has also proposed a tactile display actuated by SMA wires. Their prototype (Figure 1.16(b)) consists of 64 pins spaced 2.54 mm apart. Each actuator uses an SMA wire of 120 mm length and 0.1 mm in diameter to vertically actuate the pin to a height range of 1.7 mm. The refreshable rate is reported as 0.5 Hz upon the use of a fan. The entire tactile display is driven by a 12 V, 6 A power source [Taylor97a].

The University of Tokyo (Japan) has been working on a tactile display for presenting 3D shapes. They built a 4 x 4 array of pins actuated by SMA helical springs (Figure 1.16(c)). Pins are spaced 12 mm apart and are capable of producing vertical strokes of 120 mm. Each actuator produces a 30 mN pull force at 0.35 Hz bandwidth when driven at 12V, 200 mA [Nakatani03].

Harvard University (USA) has designed and implemented a tactile display that consists of a line of 10 pins actuated by SMA wires. The actuator in figure 1.16(d) is the basis of this display. Note that it exhibits a "V shape" to compensate the limited strains of SMA wires. Pin spacing is 2 mm and each actuator is capable of delivering a 3 mm stroke and 2 N pull forces. One of the key points of the display is that the actuator is immersed in a fluid (a water-copper solution) in order to accelerate the SMA cooling rate. The resulting bandwidth achieves the 40 Hz [Wellman97].

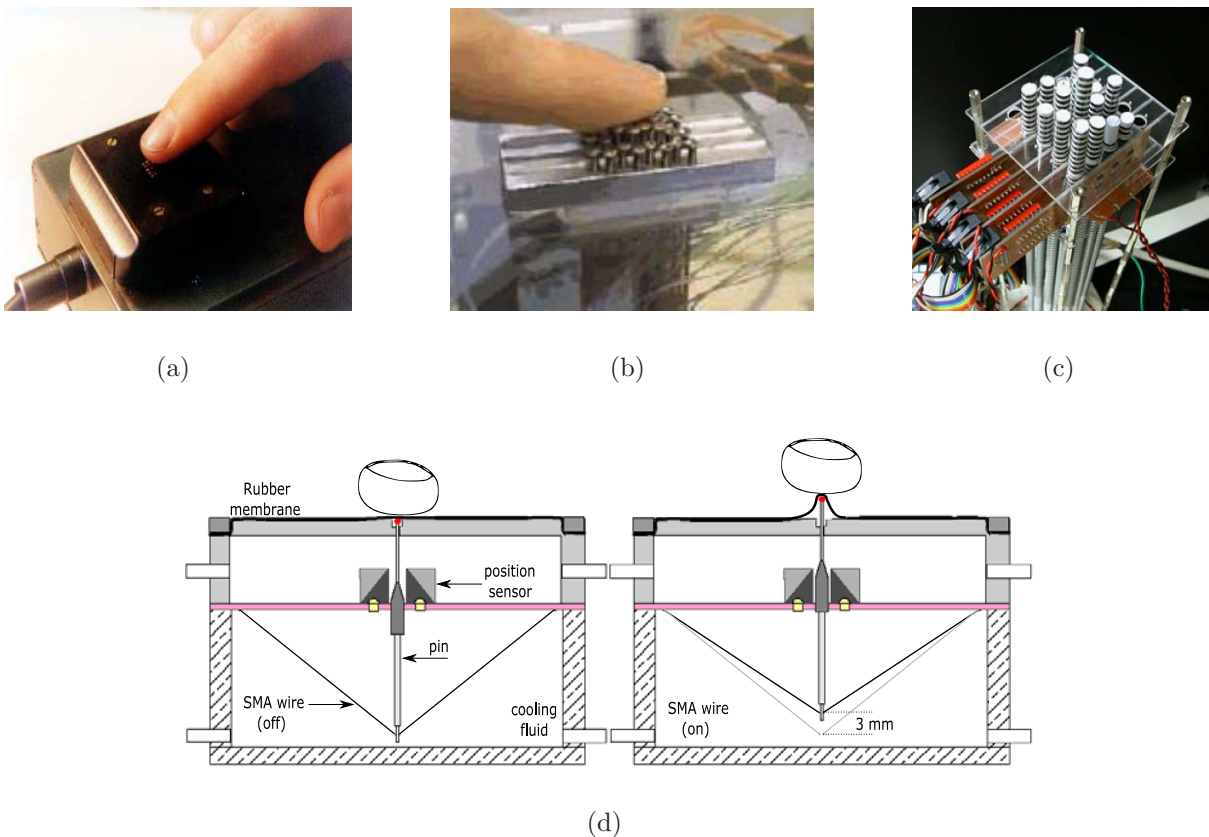


Figure 1.16: SMA based tactile displays. Prototypes of (a) the TiNi Alloy Company, (b) the University of Newcastle, (c) the University of Tokyo and (d) Harvard University.

#### 1.2.2.4 Electromagnetic based displays

Harvard University (USA) has proposed another tactile display. This one actuated by commercial RC servomotors. Their prototype (Figure 1.17(a)) consists of a 6 x 6 array of pins spaced 2 mm apart that provides vertical excursions of 2 mm and 10 N forces. The display can accurately represent frequencies up to 25 Hz [Wagner02].

Another servomotor based tactile display is the one proposed by NIBH (Japan) (Figure 1.17(b)). Their display presents 3D shapes in a 64 x 64 array. Pin spacing is 3 mm upon a 3-layer servo arrangement and vertical excursion achieves the 10 mm in steps of 0.1 mm. Each servomotor is capable of withstanding a 3 N contact force [Shinohara98].

An example of voice coil based touch stimulation device is the *Touchmaster* by Exo Inc. The Touchmaster stimulates all four fingers and the thumb with micrometer vibrations provided by voice coil actuators (Figure 1.17(c)). Bandwidth can be fixed between 210 and 240 Hz.

Researchers at the University of Karlsruhe (Germany) have developed a tactile display (Figure 1.17(d)) that consists of three 24-needle printing heads thus providing a total of 72 actuators, although only 64 are actually used. Each needle is electromagnetically triggered by a miniature solenoid and vibrates at a maximum frequency of 600 Hz [Fischer95].

CEA/LIST (France) has been working on a vibratory tactile display called *VITAL* (Figure 1.17(e)), which consists of an 8 x 8 array of electromagnetic microcoils that can vibrate up to 800 Hz. Pin spacing is 5 mm, vertical excursion is 100  $\mu\text{m}$  and the maximum force delivered by each microcoil is about 13 mN [Benali-Khoudja04].

#### 1.2.2.5 ER fluids and EAP based displays

ER fluids and EAPs technologies are relatively new and have not been yet widely used in applications of tactile displays. However, two pilot examples can be found in the literature:

The University of Hull (UK) has developed a tactile display based on ER fluids to create sensations of texture. Their prototype (Figure 1.18(a)) consists of two parallel surfaces separated by a 2.5 mm gap filled with ER fluids. The upper surface is a flexible rubber sheet while the bottom one is a 5 x 5 array of aluminum pins spaced 2 mm apart. When the pins are connected to a high voltage source (3.5 KV), the ER fluid layer above changes its viscoelasticity in few milliseconds and gives a tactile sensation of stiffness [Taylor98b].

Researchers from Kobe University (Japan) have been working toward reproducing the human tactile sensation of fine touch of cloth. With this purpose, they developed a ciliary-like tactile device using ionic EAPs actuators immersed in water (Figure 1.18(b)). Each cilium is 2 mm wide by 5 mm long. High frequency drives (up to 50 Hz) generate

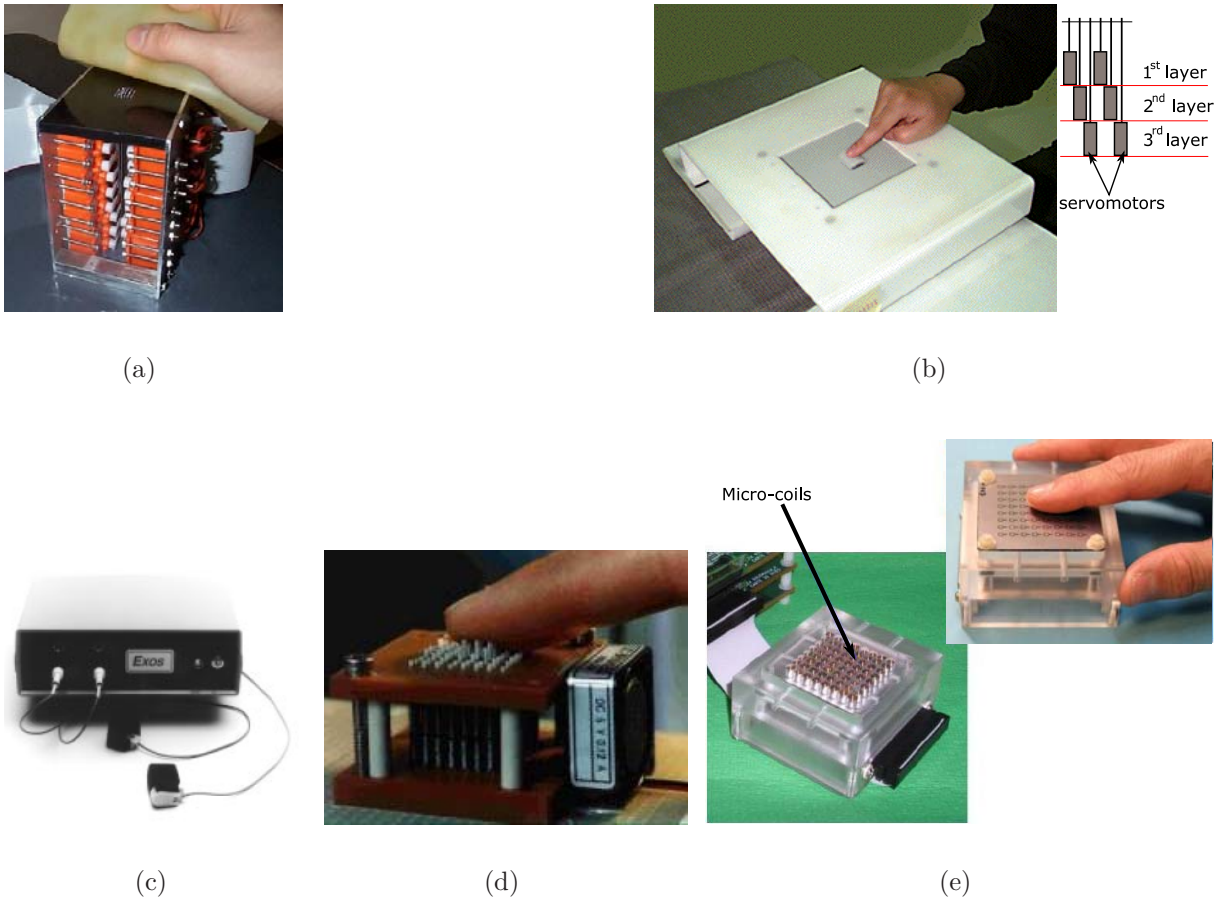


Figure 1.17: Electromagnetic based tactile displays. Prototypes of (a) Harvard University, (b) NIBH, (c) Exo Inc. (d) the University of Karlsruhe and (e) CEA/LIST.

fast vibration of the EAP and short motions of the cilia while low frequency drives induce slow vibrations in the EAP and large motion strokes of the cilia [Konyo00].

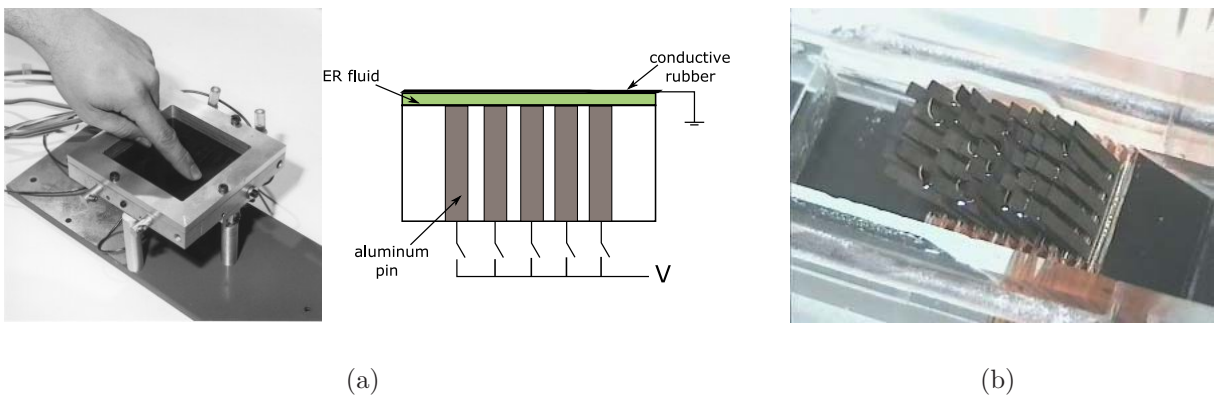


Figure 1.18: (a) The University of Hull ER fluids based tactile display and (b) EAP based ciliary device from Kobe University.

## 1.3 Criteria for the design of the IG tactile display

The basic idea behind the IG output's device framework is to design an implement an interface that accurately presents the nearby 3D environment to the user by means of touch stimulation. According to the IG information representation concept, the tactile display will consist of a 2D array of tactile stimulator actuators.

Interaction with the user is one of our major concerns. User acceptance will mainly depend on the tactile display; if the user finds it easy to use, comfortable and reliable, then the IG-ETA will be accepted. An optimal tactile display for the IG-ETA should accomplish the following global design criteria [Velazquez04f]:

1. It should be easy to use and require little or no training. The user should be able to use the device and understand the information displayed in almost an intuitive way.
2. It should be portable but not wearable. It is desirable that the tactile display is as lightweight and small as possible and can easily fit into a jacket pocket or small pack. Furthermore, it suggests an unobtrusive and inconspicuous device, which are essential for people with visual impairments. A device worn on the body is not desirable: a permanent contact between the device and the user hardly ensures comfort over long periods of time and, sooner or later, annoys the user. It must be the user's choice whether to use the display or not.
3. It should be low-power consumption. The power source faces two constraints: supply considerable lasting energy to the tactile display for a regular walking journey and be lightweight as it must respect the portability criterion.
4. It should be low-cost to represent a significant advantage over commercially available devices and for future industrial production.

Technological parameters such as pin spacing, stroke, force and bandwidth are discussed below.

### 1.3.1 Guidelines for tactile displays: a psychophysiology approach

Touch is one of the human senses that allow interaction with the environment. It is emphasized to be an active modality in which world information is obtained by exploratory contact movements between the body and the object. The skin is the sense organ that contains the essential biological sensors of touch. It encompasses 3 main groups of sensors organized by biological function: the *thermoreceptors*, responsible for thermal sensing, the

*nociceptors*, responsible for pain sensing and the *mechanoreceptors*, sensitive to mechanical stimulus and skin deformation.

Our interest focuses on the mechanoreceptors as they are responsible for sensing and transmission of physical deformations by external forces to the nervous system. Figure 1.19 shows the cross-section of the human glabrous skin. Four kinds of mechanoreceptors can be found:

1. *Pacini corpuscles* sensitive to high frequency vibrations.
2. *Ruffini endings*, which respond to lateral extension of the skin. It is said to be the responsible for feeling articular movement.
3. *Merkel cells* perceive pressure.
4. *Meissner corpuscles* sensitive to low frequency vibration. They are considered to be sensitive to fine-touch stimuli since they provide the best reception of movement across the skin.

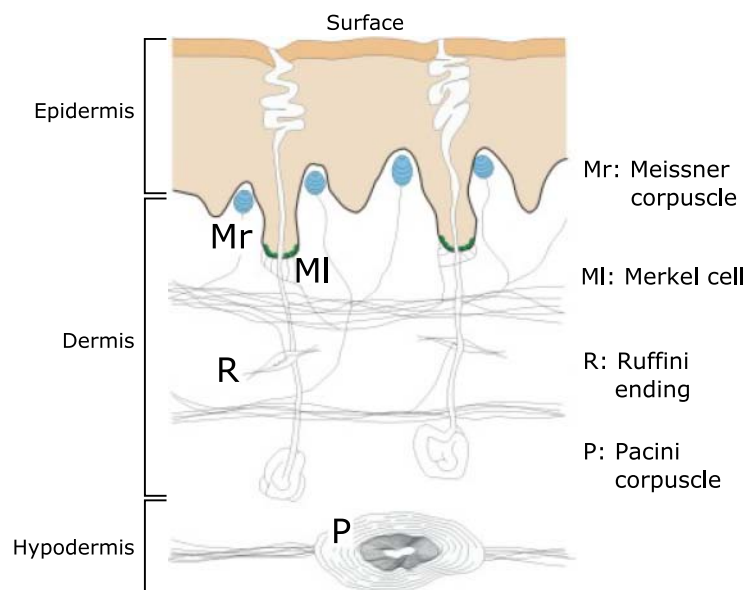


Figure 1.19: Cross-section of the glabrous skin of the hand schematically representing the location of the four types of mechanoreceptors, after [Johansson83].

Our interest mainly focuses on Meissner and Pacini skin mechanoreceptors since they are involved in hand feeling during object exploration. Figure 1.20(b) shows the relation between the amount of skin indentation and frequency for stimuli detection in these mechanoreceptors. Note that while Pacini corpuscles are sensitive to low amplitude-high frequency stimuli, Meissner ones are sensitive to high amplitude-low frequency stimuli.

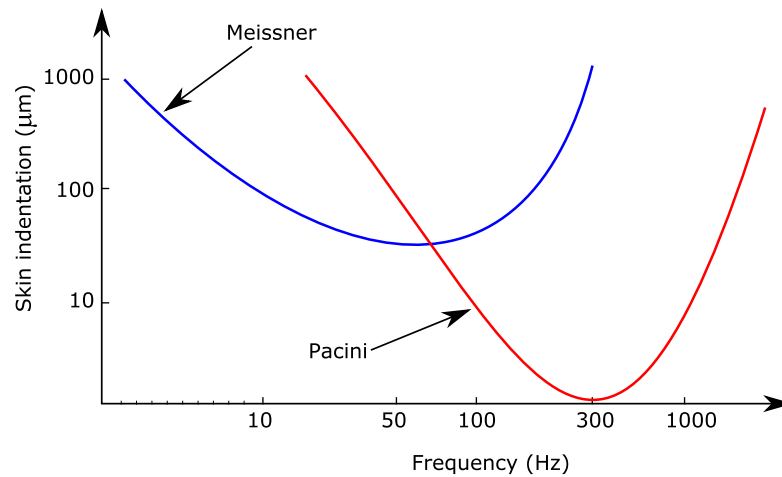


Figure 1.20: Skin indentation minimal detection thresholds as function of frequency, after [Sekuler02].

The IG intends to display information that represents a significant gradient in the skin surface and that remains static during exploration more than vibrating information. It seems then that stimulation of Meissner corpuscles is more suitable for the application.

Concerning spatial discrimination of Meissner cells, a density of 140 per  $\text{cm}^2$  is usually found in fingertips. This corresponds to a 0.9 mm center-to-center spacing. However, this does not mean that we can actually perceive with this resolution. Human touch cannot perform discretely below a resolution suggested by a two-point discrimination threshold (TPDT). The TPDT is the minimum distance with which we can identify 2 points given in a simultaneous two-point contact [Geiger84]. The TPDT on fingertips is 2 to 3 mm, being 2.54 mm the standard TPDT adopted by Braille devices.

Concerning object exploration, a survey of psychophysical experimental data indicates that a 50 to 100 mN force is applied during fine-touch exploration [Loomis81].

From this first general study, we conclude that design goals for a Meissner stimulation device should integrate a large number of actuators with a 2.54 mm interspacing, an effective skin indentation of 0.7 to 1 mm, stimuli frequencies of 1 to 3 Hz and a minimum delivered force of 100 mN.



### 1.3.2 Choice of actuation technology

From the existing tactile displays presented in the state of the art, it is possible to identify and summarize the key points of the different actuation technologies for implementing a tactile display (Table 1.2).

Technology	Frequency (Hz)				Potential drawbacks to consider (spatial resolution, stroke, force and external burden)
	1	10	50	250	
Piezoelectric	X	X	X	X	Limited strokes, need burdensome amplifiers at expenses of spatial resolution. Power source must provide approx. 200 V, 50 $\mu$ A per pin
Pneumatic	X	X	-	-	External burden (valves, tubes, air cylinder, etc.)
SMAs	X	-	-	-	Limited bandwidth (may be improved with coolants). Wires are limited in stroke. Power source must provide approx. 5-12 V, 200 mA per pin
Servomotors	X	X	X	-	Burdensome, not so lightweight, spatial resolution can be achieved upon layers at expense of increasing the device's dimension
Microcoils & voice coils	X	X	X	X	Small strokes and low forces
ER fluids	X	X	X	X	No actuation. Power source must provide approx. 3.5 kV, 20 mA per pin
EAPs (ionic)	X	X	X	-	Low forces (mostly bending actuation), traction mechanisms can be constructed at expenses of spatial resolution. Needs an aqueous medium

Table 1.2: Key points for the choice of an actuation technology.

Note that all the described technologies fail to match at least one of the requirements for an ideal tactile display: piezoelectric, pneumatic, servomotors and EAPs seriously constraint the portability criterion. ER fluids do not provide actuation and microcoils and voice coils are more suitable for vibratory tactile displays and Pacinian stimulation.

It seemed to us that SMAs could provide the best tradeoff and performance for the IG tactile display. In the course of this dissertation we will try to demonstrate the feasibility of SMAs as actuation technology for a low-cost highly-portable compliant tactile display.

## 1.4 Essential features of shape memory alloys

Shape memory alloys (SMAs) have several characteristics that make them attractive over other materials, especially for actuation applications: compact size, high power/weight ratio, high fatigue resistance to cyclic motion and spark-free, clean and noiseless operation. Additionally, they have unique properties based on superelasticity and shape memory effect (SME) [Ikuta90].

The shape memory effect (SME) is the ability of a certain group of materials to "memorize" a specific shape when subjected to the appropriate thermal process. Materials exhibiting this effect are metallic alloys such as AgCd, AuCd, CuAlNi, CuSn, InTi, NiAl and the popular NiTi.

The SME occurs as a result of a temperature dependent transformation between two solid phases: high temperature austenite ( $A$ ) phase and low temperature martensite ( $M$ ) phase. Austenite phase contains the memorized or predefined shape of the material. When cooled to martensite, the material presents very low stiffness and yield strength. It is quite malleable and can be easily deformed into a new shape, which it retains. Upon heating, the material returns to its austenitic original and pre-deformed shape (Figure 1.21).

At microscopic level, the SMA's austenitic crystalline structure is highly symmetric and well ordered. Upon cooling, the crystalline structure collapses leaning in opposite directions along subsequent layers that are self-accommodating (or twinned) so that no macroscopic deformation results. Applying an external stress on the SMA will cause the twinned martensite layers to begin to lean in the same direction. When all the layers are leaning the same way, the SMA is said to be oriented (or detwinned). Upon heating, the crystal layers line up to recover their original symmetry (Figure 1.21).

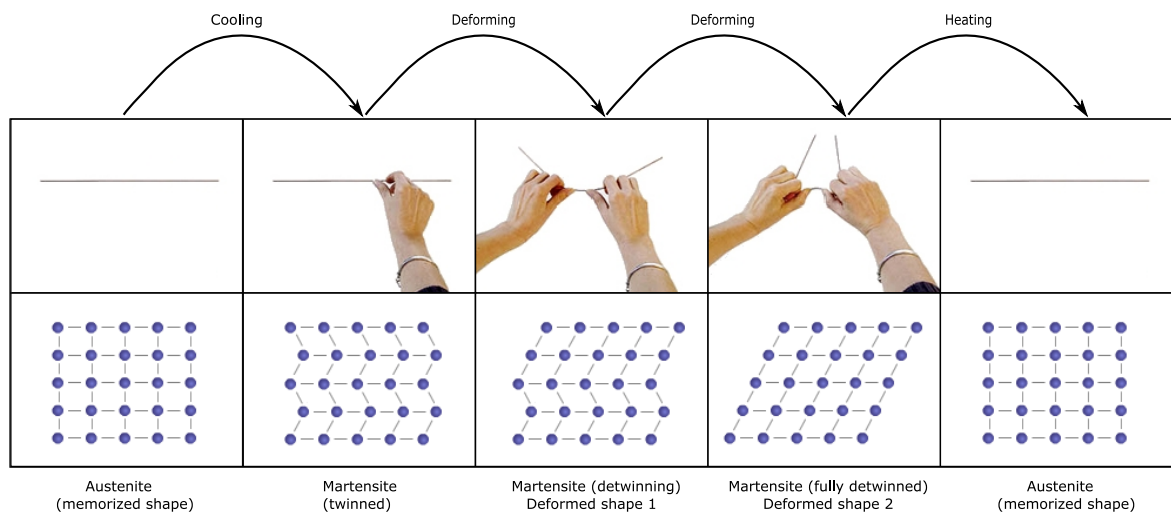


Figure 1.21: The SME in SMAs at macroscopic and crystallographic levels.

A typical SME schematic is shown in figure 1.22. The  $M \rightarrow A$  and  $A \rightarrow M$  transformations are essentially characterized by four temperatures:  $A_s$  and  $A_f$  are the start and finish temperatures for the  $A$  phase, respectively, while  $M_s$  and  $M_f$  are the start and finish temperatures for the  $M$  phase, respectively. As seen, SMAs show a significant hysteresis during both transformations.

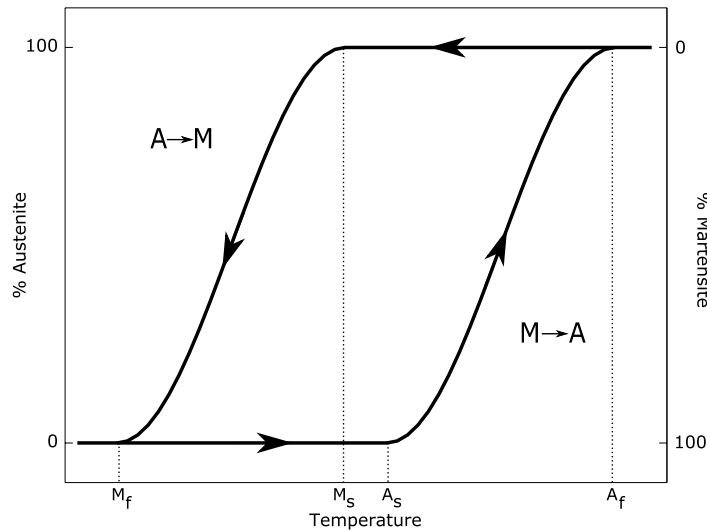


Figure 1.22: Schematic of  $M \rightarrow A$  and  $A \rightarrow M$  transformations, after [Liang90].

External stress on the material also causes the four phase transition temperatures to increase. Figure 1.23 presents the typical SMA phase diagram showing the fairly linear relationship between stress ( $\sigma$ ), temperature ( $T$ ) and phase. For example, consider an SMA in its  $A_f$  temperature. When an external stress  $\sigma_1$  is applied, all four transition temperatures increase. Note that upon sufficient loading, the SMA reaches its  $M_f$  temperature. Since the SMA is now in the martensite phase, it is malleable for a determined percent strain. When the stress  $\sigma_1$  is removed, all transition temperatures again decrease and the SMA reverts back to its original point ( $A_f$ ).

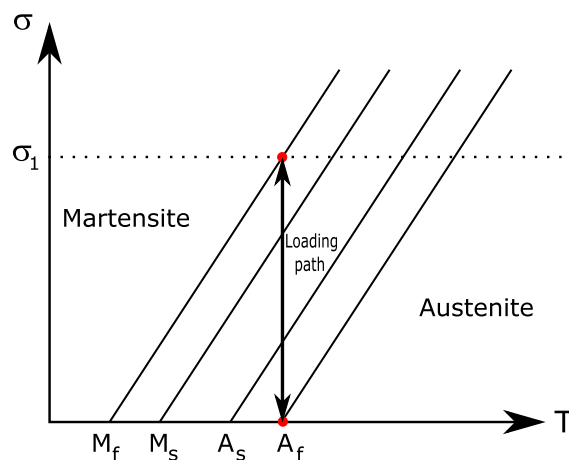


Figure 1.23: Stress-temperature dependence in SMAs.

The  $M \rightarrow A$  and  $A \rightarrow M$  transformations are the key to explain the SME and the super-elasticity.

Figure 1.24(a) illustrates the SME in the stress-strain-temperature ( $\sigma$ ,  $\epsilon$ ,  $T$ ) space, where  $\epsilon$  is the SMA's strain. Consider an SMA in martensite state at zero-stress ( $A$ ). In this point the SMA's crystalline structure is twinned martensite. During loading ( $AB$ ), the behavior is first elastic. When stress goes over a certain critical value, a large strain in the SMA suddenly occurs upon a small increase in stress. This is called plastic behavior. In this process, the crystal layers transform to detwinned martensite. On unloading, a period of pure elastic recovery is observed ( $BC$ ). This is due to a small portion of the detwinned martensite that transforms back to twinned martensite. The only way to fully recover the original shape is to heat the SMA to its austenite phase ( $CD$ ). Finally, upon cooling the austenite is converted back into twinned martensite ( $DA$ ).

Figure 1.24(b) illustrates the superelasticity in the stress-strain ( $\sigma$ ,  $\epsilon$ ) space. Consider an SMA in the austenite state at a temperature  $T > A_f$ . As the SMA is loaded from the stress-free initial stage ( $A$ ), it presents an elastic ( $AB$ ), a superelastic ( $BC$ ) and once again elastic behavior ( $CD$ ) due to a stress-induced conversion of austenite into detwinned martensite. Upon unloading ( $DCA$ ), a reverse transformation from detwinned martensite to austenite occurs. At the end of the loading-unloading process no permanent strain is present and the stress-strain path is a closed hysteresis loop.

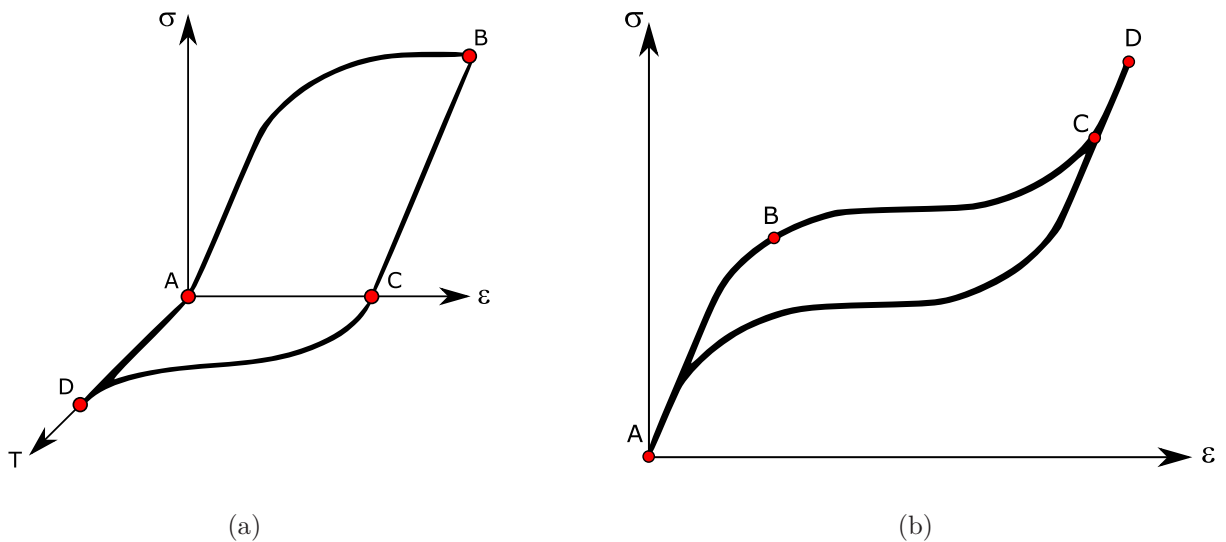


Figure 1.24: (a) The shape memory effect (SME) and (b) superelasticity in SMAs.

### *Limitations of SMAs*

Despite all the advantages of SMAs, there are three major drawbacks to be considered when designing actuators: low bandwidth, non-linearity and limited strain.

First, the actuation frequency of an SMA is basically defined by the speed with which it can be heated to  $A_f$  and then cooled to  $M_f$ . As it can be deduced, the limiting factors on the speed of SMAs are the heating and cooling rates. The resulting bandwidth is generally low, typically less than 0.1 Hz and it is mostly dictated by the achievable cooling rate. This limitation will be addressed in chapter 3.

Second, since the SME implies a phase transformation with significant hysteresis, SMAs are highly non-linear and difficult to control accurately. The non-linear properties of SMAs will be addressed in chapter 2 and the control strategy in chapter 3.

Third, experimental testing of SMA straight wires has revealed that strain is limited to approximately 8%, with practical strains restricted to around 4 to 5 % of their original length (a detailed review of mechanics of SMA straight wires can be found in [Chaillet99]). However, SMAs can be formed into almost any shaped actuator. Most popular shapes are wire, spring, tubing, sheet and ribbon. Compared to wires, springs do have a significantly higher recoverable strain. Impressive 300% strokes can easily be obtained using helical springs. However, as they perform in torsion instead of tension, they cannot develop the same force.

This work suggests that SMA springs can be designed to exert significant forces for tactile applications having at the same time, stroke and compactness not offered by long straight wires.

## 1.5 Conclusion

This introductory chapter has discussed the issue of blind mobility aids. A survey of electronic travel aids (ETAs) has permitted the identification of the main drawbacks that cause low user acceptance.

Considering (and with the goal of improving) all these drawbacks, a new visuo-tactile ETA called the *Intelligent Glasses (IG)* has been introduced. Using a pair of video cameras and a tactile display, the IG-ETA proposes a simplified tactile representation of the obstacles present in the visual environment.

The chapter focused then on the design and implementation of a tactile display. A brief review of tactile displays existing in the literature permitted the identification of the different actuation technologies as well as their advantages and limitations. Based on the project's criteria, the shape memory alloy (SMA) technology has been finally selected as the actuation technology of choice.

Finally, the essential features of SMAs were presented. To overcome the limited strokes of SMA straight wires, an SMA helical spring has been envisaged to be used as the basis of the tactile display. The next chapter will concern its modeling, implementation and experimental characterization and evaluation.

---

## Chapter 2

# Design and Characterization of SMA Helical Springs

---

This chapter presents the design, modeling and implementation of a NiTi SMA helical spring intended to be the active element of a miniature actuator for tactile stimulation. Existing constitutive models are used to predict its thermomechanical behavior. Following an experimental re-identification of the parameters involved in modeling, actuation speed and force-displacement experimental results are presented to validate simulation. The cyclic performance is then evaluated through a fatigue life analysis. Finally, some microstructural observations on the effects of heat treatment and fatigue are presented and discussed.

## 2.1 Modeling of shape memory alloys

Extensive work has been devoted to model the SMA thermomechanical behavior. Approaches range from atomic interactions ([Patoor87], [Falk89], [Kafka94], [Lexcelent96], [Nae03]) and thermodynamic formulations ([Ortin89a], [Ortin91b], [Berveiller91], [Boyd96a], [Boyd96b]) to phenomenological models based on experimental data ([Tanaka86], [Liang90], [Brinson93], [Graesser94], [Ivshin94]). A comprehensive review of work done in SMA modeling can be found in [Birman97] (195 references in 1997).

Models agree, regardless of their approach, that an SMA element can be considered as a three-element system in which thermal energy is converted into mechanical work. Figure 2.1 illustrates the SMA block diagram model.

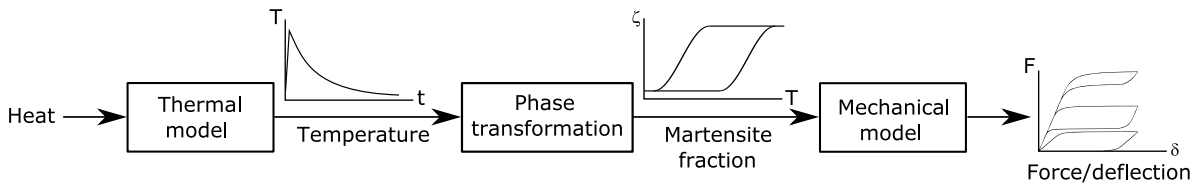


Figure 2.1: SMA block diagram model.

In spite of their high quality, most of these models are difficult to use in practice: they lead to quite complex mathematical equations that require burdensome numerical solution. Moreover, they involve parameters not clearly identified and depend on previously determined experimental data.

This chapter discusses the main features associated with SMA modeling through existing constitutive models suitable for easy analytical prediction of the SMA behavior: they use only the geometry of the SMA element and few material properties extracted from the manufacturer's data sheets or from the literature. The models here presented can be applied to design SMA helical springs that are optimal in time response and force performance.

Modeling in this chapter starts developing the thermal dynamics of SMAs through a classic heat transfer analysis, then it integrates Liang-Rogers kinetic law to take into account the phase transformation phenomenon. Finally, the mechanical behavior is predicted using a Tanaka based model.

## 2.2 The thermal dynamics of SMAs

### 2.2.1 Heat transfer analysis

Let us start analyzing the SMA thermal behavior considering a system in thermal equilibrium (Figure 2.2) where  $Q_s$  is the heat generated by an external source and  $Q_{conduction}$ ,  $Q_{convection}$  and  $Q_{radiation}$  are the different dissipation forms of heat.

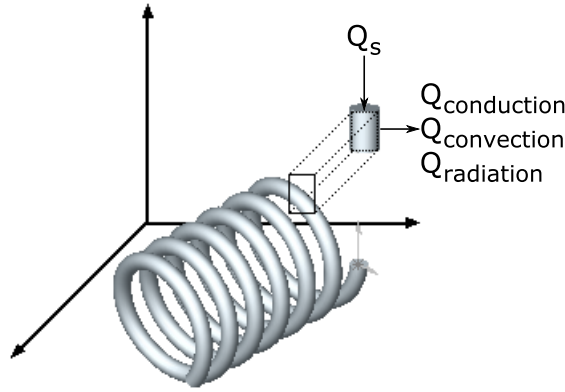


Figure 2.2: Heat exchange model.

From this thermal balance, the heat stored in the SMA can be expressed using the classical differential equation of heat transfer as follows:

$$\rho CV \frac{dT}{dt} = Q_s - Q_{conduction} - Q_{convection} - Q_{radiation} \quad (2.1)$$

where  $\rho$  is the density of the SMA,  $C$  is its specific heat,  $V$  is the volume of the SMA material and  $T$  is the temperature of the SMA at a time  $t$ .

Practically, any source of heat producing a temperature change in the material and/or its surrounding medium can be used: electrical current, Peltier effect, laser, hot air, hot fluid, etc.

For most applications (those within the atmosphere),  $Q_{radiation}$  can be neglected. Concerning  $Q_{convection}$ , it can be expressed as:

$$Q_{convection} = hS(T - T_e) \quad (2.2)$$

where  $h$  is the heat-exchange coefficient between the SMA and the surrounding medium,  $S$  is the surface area of the SMA and  $T_e$  is the environment's temperature.

Being a metallic alloy,  $Q_{conduction}$  is usually neglected by assuming that the temperature is uniform in the material at all times due to its low internal resistance to heat conduction. A fast method to evaluate when  $Q_{conduction}$  can be neglected is the Biot number defined by:

$$B_i = \frac{hl}{k} \quad (2.3)$$



where  $l$  is the characteristic length of the SMA material and  $k$  is its thermal conductivity. If  $B_i$  is less than 0.01, then this assumption is considered valid.

Once the Biot number has been validated, equation (2.1) becomes:

$$\rho CV \frac{dT}{dt} = Q_s - hS(T - T_e) \quad (2.4)$$

Solution of equation (2.4) yields to an expression describing the temporal evolution of temperature:

$$T(t) = \begin{cases} T_e + \frac{Q_s}{hS}(1 - e^{-at}) & \text{(heating)} \\ T_e + (T_o - T_e)e^{-at} & \text{(cooling)} \end{cases} \quad \text{with } a = \frac{hS}{\rho CV} \quad (2.5)$$

where  $a$  is the thermal time constant and  $T_o$  the temperature of the SMA at the beginning of the cooling process.

### 2.2.2 Heat-exchange coefficient $h$

Recall that, in classical theory of convective heat transfer, the heat-exchange coefficient  $h$  is defined by:

$$h = \frac{\lambda N_u}{l} \quad (2.6)$$

where  $\lambda$  is the thermal conductivity of the convective medium (gas or fluid) and  $N_u$  is the Nusselt number which defines the heat-exchange ratio given the conditions of convection (free or forced). For both cases,  $N_u$  is typically expressed as [Dubbelt95]:

$$N_u = \begin{cases} \left( 0.6 + \frac{0.387(GrPr)^{\frac{1}{4}}}{[1 + (0.559/Pr)^{\frac{9}{16}}]^{\frac{8}{27}}} \right)^2 & \text{(free convection)} \\ 0.664 \left( \frac{\omega l}{\nu} \right)^{\frac{1}{2}} Pr^{\frac{1}{3}} & \text{(forced convection)} \end{cases} \quad \text{with } Gr = \frac{g\psi\Delta T l^3}{\nu^2} \quad (2.7)$$

where  $g$  is the acceleration due to gravity,  $\Delta T$  is the maximum temperature difference between the material and the surrounding medium,  $\omega$  is the flow rate and  $\psi$ ,  $\nu$ ,  $Pr$  and  $Gr$  are the thermal expansion coefficient, the kinematic viscosity and the Prandtl and Grashof numbers for the convective medium, respectively.

Concerning the characteristic length  $l$ , it is commonly defined as the volume of the material divided by its surface area ( $l=V/S$ ). However, in the case of thin metallic cylinders or wires (a particularly popular shape in SMAs), it is more pertinent to consider the characteristic length equal to the cylinder's diameter ( $l=d$ ) when the element is placed perpendicularly to the flow and equal to its length ( $l=L$ ) when placed parallel to the flow.

### 2.2.3 Parameter determination through an example

Now that equation (2.5) relates temperature to an input heat source, let us analyze the thermal behavior of an SMA at this point to highlight the basic concepts of its actuation.

Consider a NiTi SMA helical spring of wire diameter  $d$ , mean diameter  $D$  and  $N$  active coils to be electrically actuated at standard conditions (air at room temperature).

For electrically driven SMAs, heat is generated in accordance with the Lenz-Joule law:

$$Q_s = i^2 R \quad , \text{ with: } R = \rho_e \frac{L}{\phi} \quad (2.8)$$

where  $i$  is the electrical current applied and  $R$  is the element's electrical resistance, which can be calculated from the material's resistivity  $\rho_e$ , the element's length  $L$  and its cross sectional area  $\phi$ .

Thus, if the Biot number is valid, equation (2.8) together with classical geometry of a helical spring can further reduce equation (2.5) to:

$$T(t) = \begin{cases} T_e + \frac{4\rho_e i^2}{\pi^2 d^3 h} (1 - e^{-at}) & \text{(heating)} \\ T_e + (T_o - T_e)e^{-at} & \text{(cooling)} \end{cases} \quad \text{with } a = \frac{4h}{\rho C d} \quad (2.9)$$

Note that the only geometrical parameter that influences the thermal response of the SMA spring is the wire diameter  $d$ , which is evident if we consider that a spring is essentially a wire wound into a helix.

Consider a set of NiTi wires of diameter: 100, 150, 200 and 250  $\mu\text{m}$ . The thermal properties of NiTi, directly extracted from the manufacturer's data sheets ([Dynalloy]), as well as the air properties of interest for this study are given in table 2.1.

Figure 2.3(a) shows the evolution of heat-exchange coefficient  $h$  for this set of wires. Note that natural convection becomes more efficient as the diameter decreases.

Being the Biot number valid for all cases, equation (2.9) can be used. Figure 2.3(b) shows the time response of this set of wires to a step current of 500 mA. The duration of the pulse varies according to the time in which the SMA achieves its final temperature of transformation ( $A_f$ ). Note that the actuation time increases with the diameter.

NiTi Flexinol properties		
Property	Value	Unit
Density $\rho$	6450	$\text{kg}\cdot\text{m}^{-3}$
Specific heat $C$	320	$\text{J}\cdot\text{kg}^{-1}\cdot\text{K}^{-1}$
Thermal conductivity $k$	8	$\text{W}\cdot\text{m}^{-1}\cdot\text{K}^{-1}$
Resistivity $\rho_e$	76 to 82 $\times 10^{-8}$	$\Omega\cdot\text{m}$
Transformation Temperatures $A_f, A_s, M_s, M_f$	78, 68, 52, 42	$^{\circ}\text{C}$
Air properties (20°C)		
Thermal conductivity $\lambda$	0.0257	$\text{W}\cdot\text{m}^{-1}\cdot\text{K}^{-1}$
Thermal expansion coefficient $\psi$	$3.43 \times 10^{-3}$	$\text{K}^{-1}$
Kinematic viscosity $\nu$	$15.11 \times 10^{-6}$	$\text{m}^2\cdot\text{s}^{-1}$
Prandtl number $Pr$	0.713	-

Table 2.1: Thermal properties of the NiTi SMA spring and its surrounding medium.

Figure 2.3(c) shows the time response to a set of step currents applied to the 200  $\mu\text{m}$  diameter wire. The amplitude is varied from 400 to 800 mA. Note that the greater the current, the faster the SMA heats.

Figure 2.3(d) shows the effect of coefficient  $h$  during the heating process. Note that the greater the current, the less the influence of convection. Figure 2.3(e) shows the corresponding cooling response under conditions of free and forced convection with the environment. Note the acceleration effect of forced air convection on cooling.

A simple method to induce forced convection is by flowing air from an external fan. Compared to free convection, forced convection decreases the cooling time, for example, by a factor of 2 when using a 1 m/s air flow rate.

Thus, the total time response is composed of the time required for heating up and cooling down the SMA. Figure 2.3(f) shows the importance of using forced convection on cooling, mostly for continuous cyclic operation. Note that the SMA can be actuated 2 times during a free convection period by using forced convection.

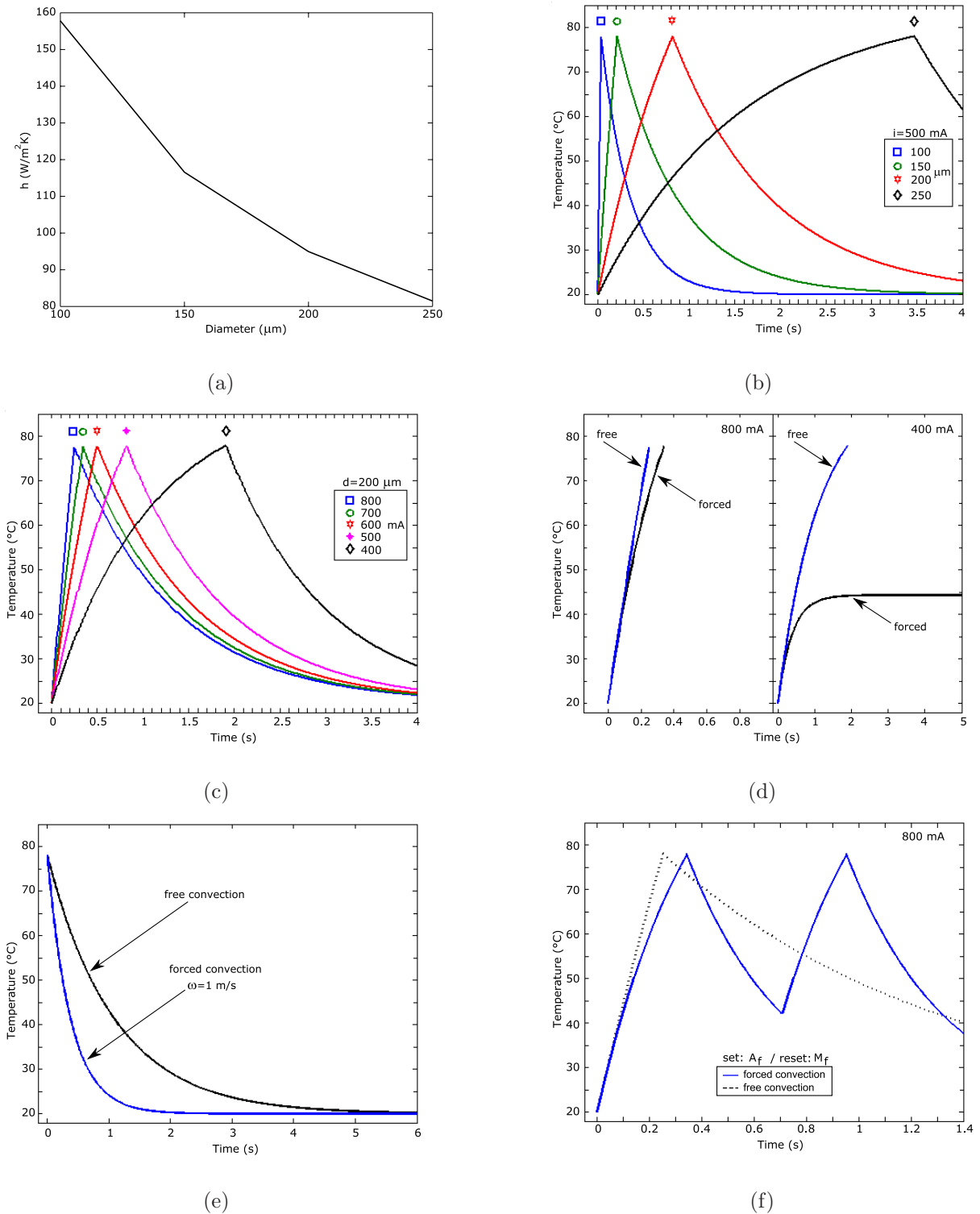


Figure 2.3: Calculated thermal relationships for SMAs using equations (2.6) to (2.9): (a) effect of diameter  $d$  on coefficient  $h$ , (b) time response of a set of wire's diameter to a fixed heating current (500 mA), (c) time response of a 200 μm wire at different heating electric currents (400 to 800 mA), comparison of (d) actuating, (e) resetting and (f) total time responses under free and forced convection conditions.

### 2.2.4 Phase transformation

Unfortunately, actual SMA thermal behavior is more complex. As seen in chapter 1, SMAs, unlike traditional materials, show hysteresis during both M→A and A→M transformations. Physically, these hystereses are a dissipation and assimilation of latent heat due to phase transformation that tend to slow down both heating and cooling processes. Consequently, it is necessary to include this effect in the thermal analysis.

A successful empirical relation has been proposed by Liang and Rogers [Liang90], which describes the amount of martensite fraction  $\xi$  transformed on a temperature  $T$ . For constant load conditions,  $\xi$  can be written for cooling as:

$$\xi(T) = \begin{cases} 0 & \text{at } T > M_s \\ \frac{1}{2} \left[ \cos \left( \pi \frac{T-M_f}{M_s-M_f} \right) + 1 \right] & \text{at } M_f < T < M_s \\ 1 & \text{at } T < M_f \end{cases} \quad (2.10)$$

The analogous dependence can be expressed for heating by replacing  $M_s$  and  $M_f$  temperatures with  $A_f$  and  $A_s$  temperatures correspondingly.

Equation (2.10) completes the energy balance equation (2.4) with the phase transformation parameter as follows:

$$\rho V \left[ C \frac{dT}{dt} + \Delta H \frac{d\xi}{dt} \right] = \begin{cases} Q_s - hS(T - T_e) & \text{(heating)} \\ -hS(T - T_e) & \text{(cooling)} \end{cases} \quad (2.11)$$

where  $\Delta H$  is the latent heat defined on the transformation interval.

Solution of equation (2.11) can be easily obtained using any scientific computing software such as *Maple*<sup>1</sup> or *Mathematica*<sup>2</sup>. For example, the analytical solution for cooling in  $M_f < T < M_s$  obtained using *Maple* can be expressed as:

$$t = t_0 + \frac{\pi}{2} \frac{\rho V \Delta H}{hS\Gamma} \{ \cos(\pi X) [Si(\pi Y) - Si(\pi Z)] - \sin(\pi X) [Ci(\pi Y) - Ci(\pi Z)] \}$$

with:  $X = \frac{M_f - T_e}{\Gamma}$ ,  $Y = \frac{T - T_e}{\Gamma}$ ,  $Z = \frac{M_s - T_e}{\Gamma}$ ,  $\Gamma = M_s - M_f$  (2.12)

$$\text{and: } Si(x) = \int_0^x \frac{\sin(y)}{y} dy, \quad Ci(x) = \int_0^x \frac{\cos(y)}{y} dy$$

where  $t_0$  is the time to reach  $M_s$  (i.e. before transformation starts) defined by equation (2.5).

---

<sup>1</sup>Maplesoft Corporation

<sup>2</sup>Wolfram Research

Simplified analytical methods for solving equation (2.11) do exist in the literature and might be more practical, faster and easier to implement. A successful example is the algorithm developed and validated experimentally by Potapov and da Silva [Potapov00]. This method can be summarized as follows. Consider the dimensionless variables:

$$\begin{aligned}
T' &= \frac{T - M_f}{M_s - M_f} && \text{(dimensionless temperature)} \\
U &= \frac{M_f - T_e}{M_s - M_f} && \text{(dimensionless difference between the transformation} \\
&&& \text{and the surrounding medium)} \\
J &= \frac{A_f - M_s}{M_s - M_f} && \text{(dimensionless transformation hysteresis)} \\
H &= \frac{\Delta H}{C(M_s - M_f)} && \text{(dimensionless heat of phase transformation)} \\
t' &= \frac{hS}{\rho CV} t && \text{(dimensionless time)}
\end{aligned} \tag{2.13}$$

### Cooling process:

Once the heating process is over, the SMA starts to cool down by natural convection. During  $1 < T' < 1 + J$  (equivalent in dimensionless terms to  $M_s < T < A_f$ ), the temperature-time curve is simply defined by:

$$t' = -\ln(T' + U) + \ln(1 + J + U) \tag{2.14}$$

At  $t'_1 = -\ln(1 + U) + \ln(1 + J + U)$  the temperature reaches  $M_s$  and phase transformation starts. In the regime  $0 < T' < 1$  (equivalent to  $M_f < T < M_s$ ), the temperature-time response is governed by:

$$\begin{aligned}
t' &= t'_1 - \ln(T' + U) + \ln(1 + U) + \\
&+ \frac{H}{2(0.5 + U)^2} \left[ (1 + U - T') \cos(\pi T') + \frac{1}{\pi} \sin(\pi T') + U \right]
\end{aligned} \tag{2.15}$$

Figure 2.4 shows the calculated dimensionless cooling curve as a function of dimensionless heat of phase transformation  $H$ . As seen,  $H$  strongly influences the cooling response. Typical  $H$  values for NiTi SMAs of 1 to 2.5 result in a 2 to 3 times increase of the cooling time without phase transformation.

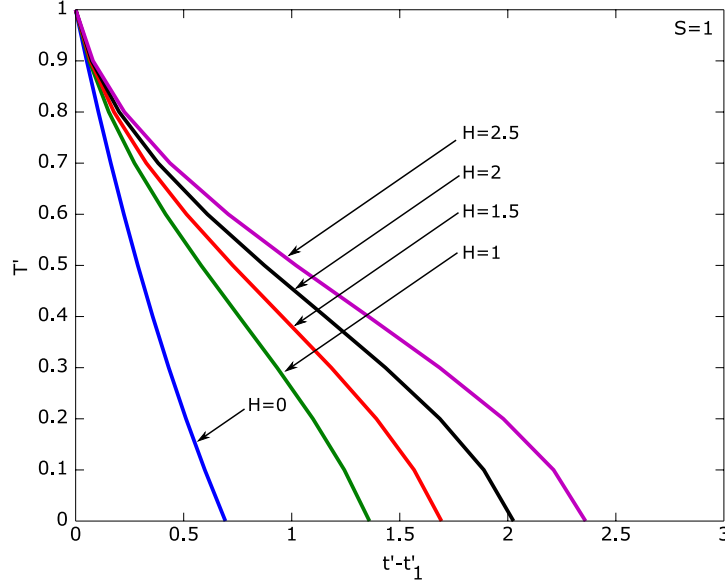


Figure 2.4: Effect of dimensionless heat of transformation  $H$  on the cooling time.

At  $t'_2 = t'_1 - \ln(U) + \ln(1 + U) + H/(0.5 + U)$  the transformation finishes and the evolution of temperature is defined for  $T' < 0$  (i.e.  $T < M_f$ ) as:

$$t' = t'_2 - \ln(T' + U) + \ln(U) \quad (2.16)$$

### Heating process:

Analogously for the heating process, the dimensionless power  $Q'$  can be defined as:

$$Q' = \frac{Q_s}{hS(M_s - M_f)} \quad (2.17)$$

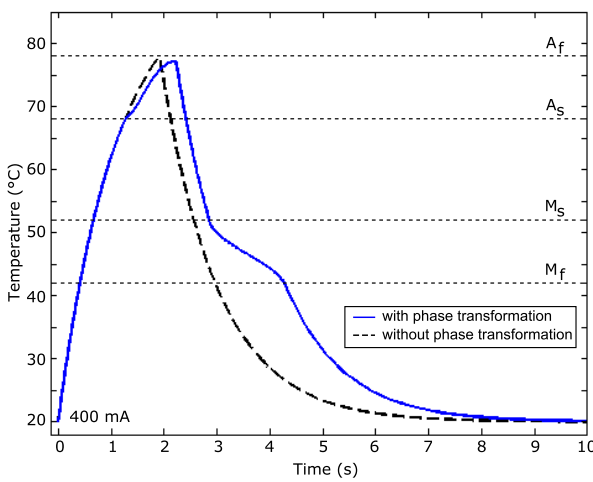
At  $J < T' < 1 + J$  (i.e.  $A_s < T < A_f$ ), the temperature-time relation is defined by:

$$t' = -\ln(Q' - U - T') + \ln(Q' - U - J - 1) + \frac{H}{2(0.5 + U + J - Q')^2} \left[ (1 + U - Q' + 2J - T') \cos(\pi(T' - J)) + \frac{1}{\pi} \sin(\pi(T' - J)) + U + J - Q' \right] \quad (2.18)$$

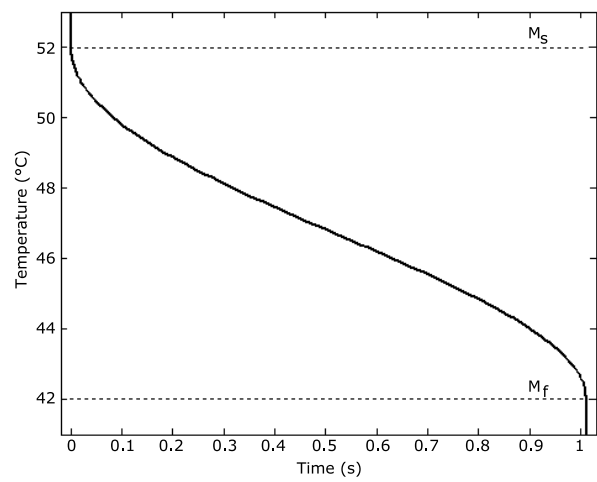
Equation (2.18) permits us to perceive the heat required to complete phase transformation and equation (2.15) the heat released during the reverse transformation.

Figure 2.5(a) shows the delay effect due to phase transformation on the thermal response of a 200  $\mu\text{m}$  diameter wire. The latent heat of transformation  $\Delta H$  was assumed to be 14 J/g, a typical value in NiTi SMAs. Note that the effect of phase transformation moderately extends the heating time, but significantly increases the cooling one. It can then be considered that its influence on heating is negligible but on cooling, it should always be taken into account.

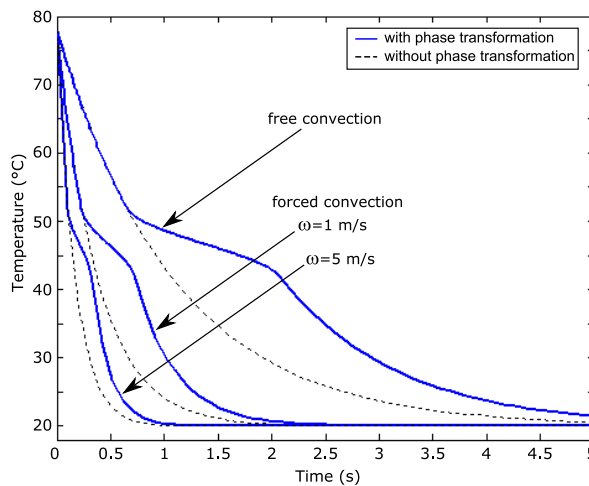
Figure 2.5(b) shows the delay evolution on cooling due to phase transformation while figure 2.5(c) compares the cooling response under free and forced convection conditions. Note that the effect of phase transformation decreases with more efficient convections.



(a)



(b)



(c)

Figure 2.5: Temperature-time curves of the SMA: with and without phase transformation.



## 2.3 SMA mechanical behavior

Considering the simple geometry of a helical spring, Tobushi and Tanaka [Tobushi91b] have proposed and experimentally validated a simple elastoplastic constitutive relation to predict its SMA load-deflection behavior. This relation suggests a stress-strain-temperature dependence that is summarized in this section.

### 2.3.1 Strain-deflection behavior

The mechanical problem consists of a simple uniaxial tension exerted along the helical spring. The helical spring is mainly defined by its mean diameter  $D$ , the wire's diameter  $d$  and the number of active coils  $N$ . Assuming that  $d$  is small in comparison to  $D$ , it can be considered that the cross section of the wire is only submitted to pure torsion.

Suppose then that only pure torsional stress  $\tau$  acts in the cross section  $\phi$  of the wire. Therefore, the deformation in  $\phi$  is only torsional strain  $\gamma$ .

Recall from classical theory of torsional elements, that the distribution of  $\tau$  along  $\phi$  is not uniform: a higher stress is observed in the outer diameter where the fibers are the most loaded (Figure 2.6(a)). Analogously for an SMA helical spring, during the loading process, the elastic to plastic transformation proceeds from the outer diameter to the center of the circular section. Due to the geometry of the section, the transformed zones are concentric rings (Figure 2.6(b)).

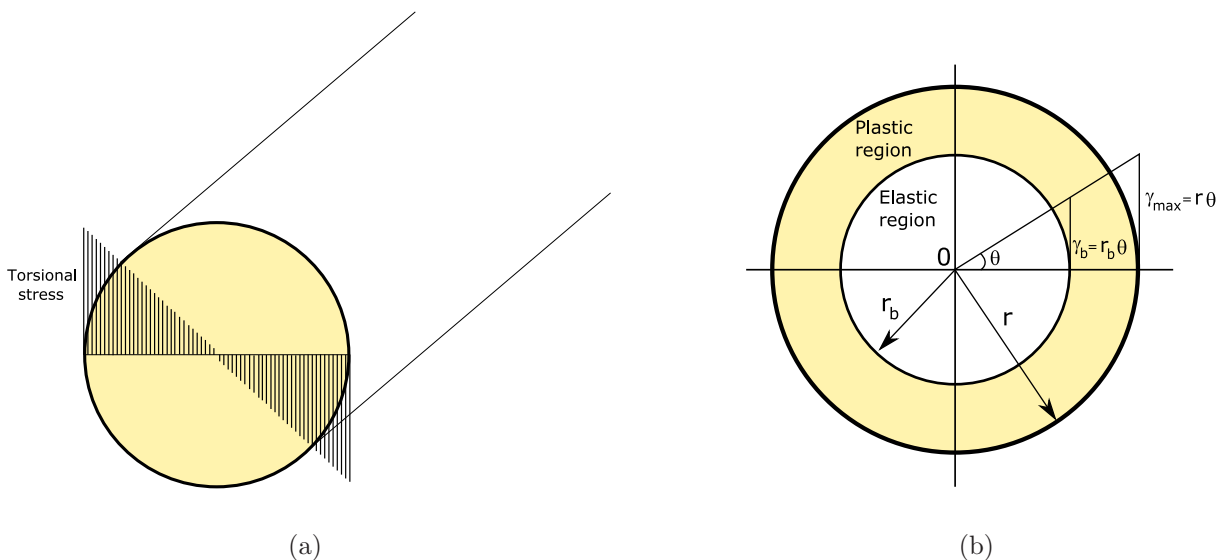


Figure 2.6: Torsional stress and torsional strain distribution in an SMA wire.

At the surface, torsional strain  $\gamma$  can be related to the wire radius  $r$  as follows:

$$\gamma_{max} = r\theta \quad (2.19)$$

where  $\theta$  is the twist angle per unit length of the wire. When the loading conditions reach a critical stress  $\tau_p$ , plasticity starts at  $r$  and progresses into the radius  $r_b$ . Torsional strain  $\gamma_b$  at the boundary of both regions is then defined as:

$$\gamma_b = r_b\theta = \frac{\tau_p}{G} \quad (2.20)$$

where  $G$  is the shear modulus of elasticity. Deflection  $\delta$  can be obtained along the wire as:

$$\delta = \int_0^{\pi DN} \frac{D\theta ds}{2} = \frac{\pi D^2 N \theta}{2} = \frac{\pi D^2 N \tau_p}{2Gr_b} \quad (2.21)$$

Thus, the relation between the deflection  $\delta$  and the boundary radius of transformation  $r_b$  is given by:

$$r_b = \frac{\pi D^2 N \tau_p}{2G\delta} \quad (2.22)$$

### 2.3.2 Temperature dependence

Tanaka considers in his extensively used constitutive laws [Tanaka86] based on the second law of thermodynamics, that the thermomechanical process of biphasic materials, such as SMAs, is entirely described by the state variables stress ( $\sigma$ ), strain( $\epsilon$ ), martensite fraction ( $\xi$ ) and temperature ( $T$ ) and can be generally expressed as:

$$\sigma - \sigma_0 = G(\xi)\epsilon - G(\xi_0)\epsilon_0 + \Omega(\xi)\xi - \Omega(\xi_0)\xi_0 + \Theta(T - T_0) \quad (2.23)$$

where  $\Omega(\xi)$  and  $\Theta$  are the transformation tensor and the thermoelastic coefficient respectively. The "0" subscripts denote the initial conditions that describe the state of the SMA prior to the thermomechanical process.

Using Tanaka's model, torsional stress  $\tau$  can be expressed for all initial conditions equal to zero as:

$$\tau = G(\xi)\gamma + \Omega(\xi)\xi + \Theta(T) \quad (2.24)$$

The following assumptions are made:

- (i) The influence of thermoelasticity is negligible for the range of actuation temperature considered, so  $\Theta=0$ .
- (ii) The transformation starts and finishes at constant stress, so  $\Omega(\xi)=0$ .

Consequently, equation (2.24) further reduces to:

$$\tau = G(\xi)\gamma \quad (2.25)$$

Equation (2.25) is governed by the evolution of  $\xi$  for a stress induced martensitic (SIM) transformation upon loading or for a reverse transformation upon unloading. For both cases, the following expressions describe the transformation kinetics:

$$\xi = \begin{cases} 1 - e^{[b_a c_m (M_s - T) + b_m \tau]} & \text{(SIM transformation)} \\ e^{[b_a c_a (A_s - T) + b_a \tau]} & \text{(Reverse transformation)} \end{cases} \quad (2.26)$$

where  $b_a$ ,  $b_m$ ,  $c_m$  and  $c_a$  are the material constants that describe the transformation conditions. Thus, transformation starts when the stress  $\tau$  reaches a critical value  $\tau_p$  defined by:

$$\tau_p = \begin{cases} \tau_m = c_m (T - M_s) & \text{(SIM transformation)} \\ \tau_a = c_a (T - A_s) & \text{(Reverse transformation)} \end{cases} \quad (2.27)$$

Figure 2.7 shows the schematic representation of equation (2.25) governed by equation (2.27). Figure 2.7(a) shows the SMA behavior in the martensitic state below  $A_s$  while figure 2.7(b) shows the one in the austenitic state above  $A_s$ . Typical values of  $\tau_m$  for NiTi SMAs are 120 and 55 MPa for the austenite (at  $A_f$ ) and martensite (at room temperature) phases, respectively [Otsuka99].

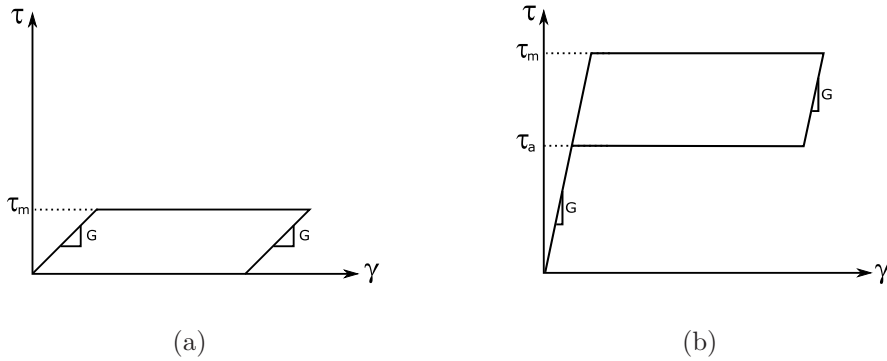


Figure 2.7: Schematic stress-strain curves under constant temperature.

### 2.3.3 Load-deflection-temperature relation

Using equations (2.22) and (2.27), the load-deflection-temperature relation for an SMA helical spring can be written as:

$$P = \begin{cases} \frac{Gd^4}{8ND^3}\delta & \text{(elastic region)} \\ \frac{\pi\tau_p d^3}{6D} \left[ 1 - \frac{1}{4} \left( \frac{\pi ND^2 \tau_p}{dG\delta} \right)^3 \right] & \text{(plastic region)} \end{cases} \quad (2.28)$$

where  $P$  is the extensive load applied to the SMA spring. Note that in the elastic region, the SMA spring behavior is identical to the one observed in a regular spring.

### 2.3.4 Behavior of the plastic region: evolution of $r_b$

When an SMA helical spring is loaded and unloaded at a constant temperature above  $A_s$ , the torsional stress  $\tau$  induced in the cross section of the wire varies as shown schematically in figure 2.8 [Tobushi91b].

In the loading process, an elastic behavior is first observed. In this region  $\tau$  is proportional to the radius  $r$  (Figure 2.8(a)). When  $\tau$  reaches the critical stress  $\tau_m$ , the SIM transformation starts. Upon an increase of load, the plastic region expands from the surface into the center and reaches the boundary of the elastic region at radius  $r_b$  (Figure 2.8(b)).

In the unloading process,  $\tau$  first decreases proportionally to  $r$  following an elastic behavior (Figure 2.8(c)). When  $\tau$  reaches the critical stress  $\tau_a$ , the reverse transformation starts and proceeds into the center upon a decrease of load (Figure 2.8(d)). When the reverse transformation is over, the original configuration is recovered following once again an elastic behavior (Figure 2.8(e)).

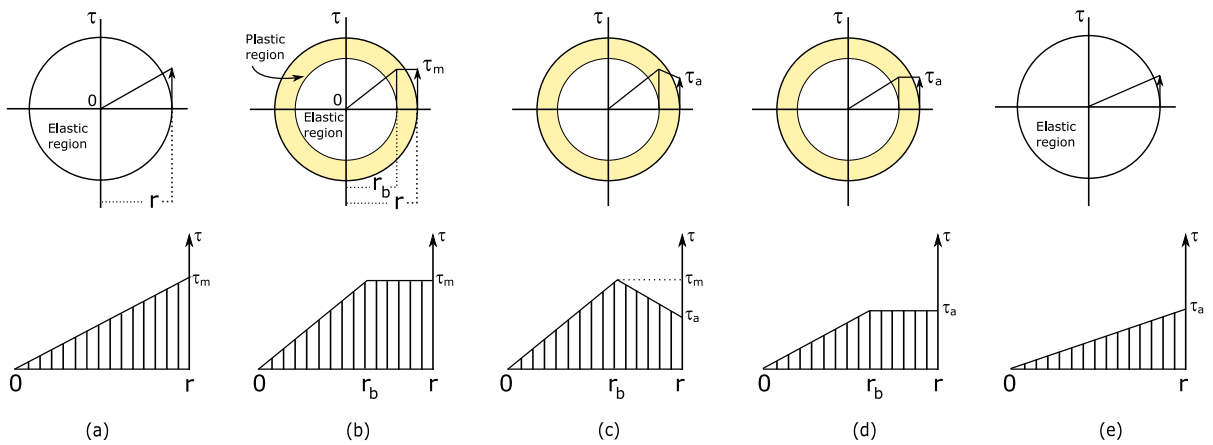


Figure 2.8: Evolution of the boundary radius  $r_b$  and torsional stress distribution during the (a), (b) loading and (c)-(e) unloading processes ( $T > A_s$ ).

### 2.3.5 Material constants

Concerning the material constants  $G$ ,  $c_m$  and  $c_a$ , it can be considered:

(i) The shear modulus of elasticity  $G$  is defined by:

$$G = \frac{E}{2(1 + \nu)} \quad (2.29)$$

where  $E$  is the Young's modulus of elasticity and  $\nu$  is the Poisson's ratio. SMAs are characterized by having a temperature dependent Young's modulus: low in martensitic state that completely changes to a high one in austenitic state (Figure 2.9(a)). Both  $E$  and  $\nu$  can be directly extracted from the manufacturer's data sheets.

(ii) In the stress-temperature phase diagram, the material constant's  $c_m$  and  $c_a$  describe the influence of stress on the phase transformation (Figure 2.9(b)). For helical springs, the values of  $c_m$  and  $c_a$  are estimated by the relationship between the torsional stress, torsional strain and temperature at the surface of the wire in torsion. Both values are commonly found in the literature for NiTi alloys.

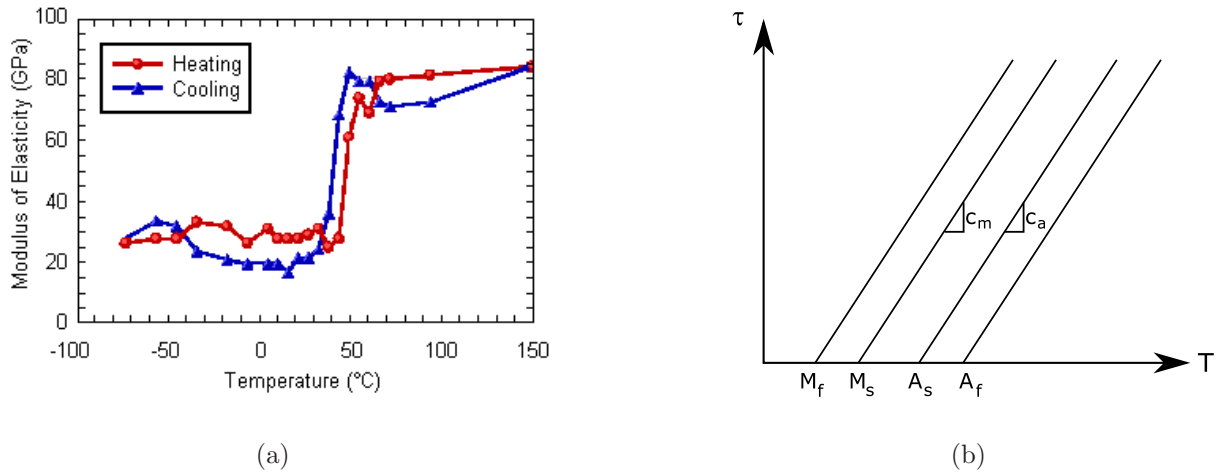


Figure 2.9: Material constants: (a) temperature dependent SMA modulus of elasticity, after [Birman97] and (b) influence of  $c_m$  and  $c_a$  in the SMA phase diagram.

Table 2.2 summarizes the values of the material constants used in the numerical analysis.

$E_a$	$E_m$	$\nu$	$c_m$	$c_a$
75 GPa	28 GPa	0.33	4.9 MPa·K <sup>-1</sup>	6.3 MPa·K <sup>-1</sup>

Table 2.2: Material constants (NiTi alloy).

### 2.3.6 Deformation behavior of an SMA helical spring

Let us analyze the mechanical behavior of an SMA helical spring by using equation (2.28). Consider an SMA helical spring of dimensions: wire diameter  $d=200 \mu\text{m}$ , mean spring diameter  $D=1.3 \text{ mm}$  and the number of active coils  $N=12$ .

Figure 2.10 shows the simulated relations between load  $P$  and deflection  $\delta$  in the loading-unloading processes at different constant temperatures for a maximum deflection of  $\delta_{max}=10 \text{ mm}$ .

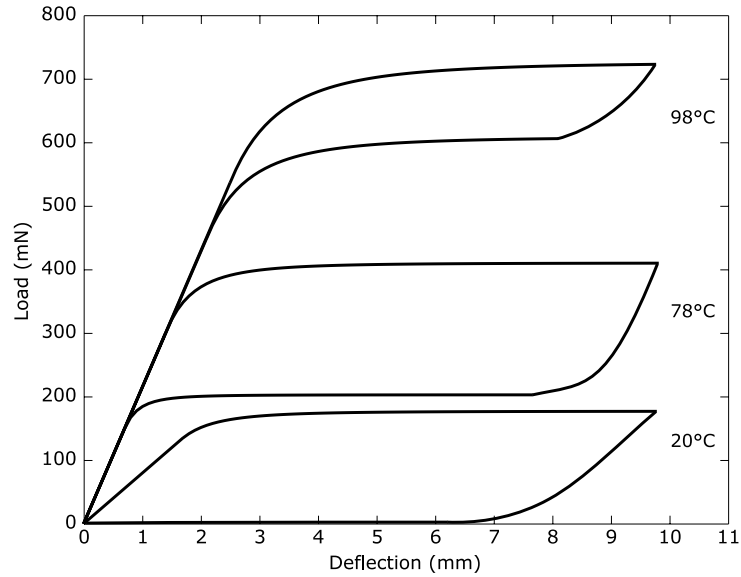


Figure 2.10: Analytical load-deflection relations of the SMA spring under constant temperatures (20, 78 and 98°C).

The simulated loading curves indicate that, in order to induce a 10 mm deflection to the SMA spring, the necessary load to be applied is approximately 180 mN at 20°C, 410 mN at 78°C and 720 mN at 98°C. On the other hand, the unloading curves indicate the expected mechanical hysteresis of the SMA when the original configuration is being recovered. Note that for temperatures at or above the austenite state, the memory shape is perfectly recovered but for martensite ones, it does not.

Figure 2.11 shows the relation between load  $P$  and the boundary radius  $r_b$  for the three constant temperatures considered. As mentioned in section 2.3.4, during the loading process, the SIM transformation starts at a point  $S_m$  on the surface of the wire and expands into the center. Upon an increase of  $P$ , the SIM transformation will reach a point  $B_m$  at  $\delta_{max}$ . During the unloading process, a point  $B_a$  is first reached following an elastic behavior. A further decrease of  $P$  triggers the reverse transformation, which contracts toward the surface until it reaches point  $F_a$ . Note that no reverse transformation starts for martensitic temperatures.

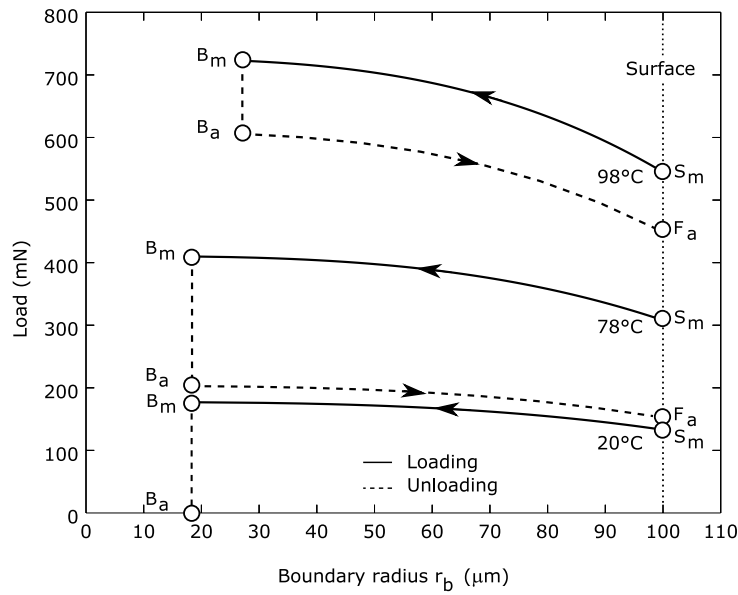


Figure 2.11: Relation between load and boundary radius of transformation.

As previously mentioned, equation (2.28) permits to establish a relationship between load, deflection and temperature. Thus, an operational zone can be defined for an SMA element [Bellouard00]. Figure 2.12(a) shows the phenomenological representation of the spring’s SMA behavior in this 3D space. Note that, as introduced in figure 2.10, the tensile force developed by the spring against a load increases with temperature.

From figure 2.12(a) it is also possible to obtain the spring’s behavior at constant stress. Figure 2.12(b) shows the analytical behavior in the deflection-temperature space at different stress constant values.

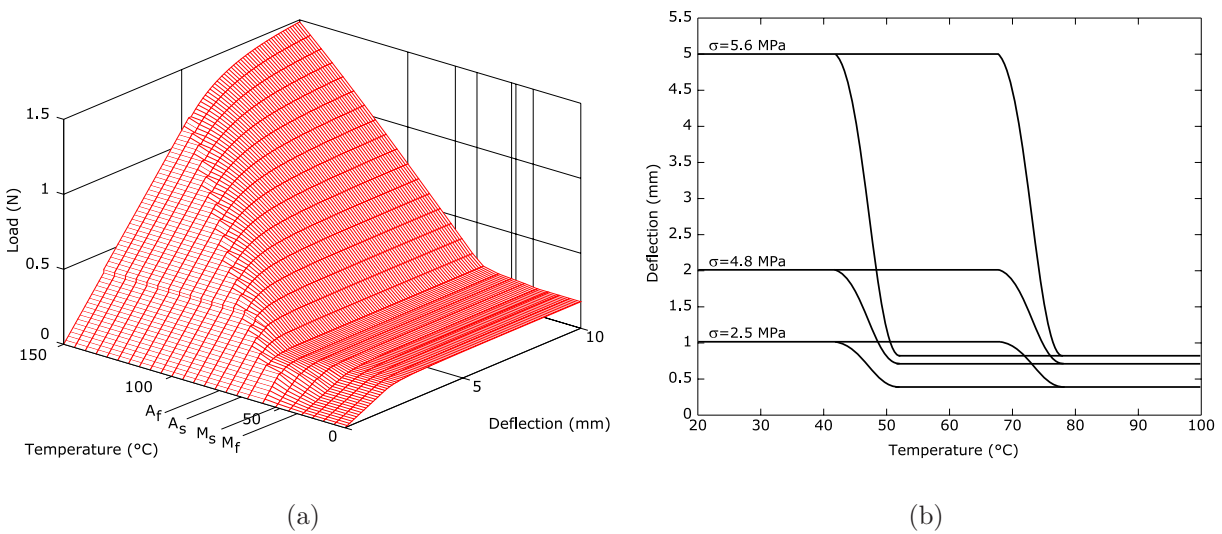


Figure 2.12: (a) Calculated SMA behavior in the load-deflection-temperature space and (b) SMA deflection-temperature behavior at constant stress.

## 2.4 Experimental procedure

### 2.4.1 Material

A NiTi helical spring was fabricated with trademark Flexinol<sup>3</sup> wire (Ni<sub>52</sub>Ti<sub>48</sub>) with the following geometric characteristics: 200  $\mu\text{m}$  of wire diameter, 1.3 mm of mean spring diameter, 12 active coils and 7 mm of free length. Its mass is 30 mg. The length of wire needed to make the spring was 58 mm (For further details on these parameters, refer to Appendix A).

The helical spring shape was set by winding the wire tightly on a cylindrical mandrel (screw-like) and then heat-treating both wire and mandrel at 500°C for 5 minutes. Rapid cooling via water quench concluded the process (Figure 2.13).

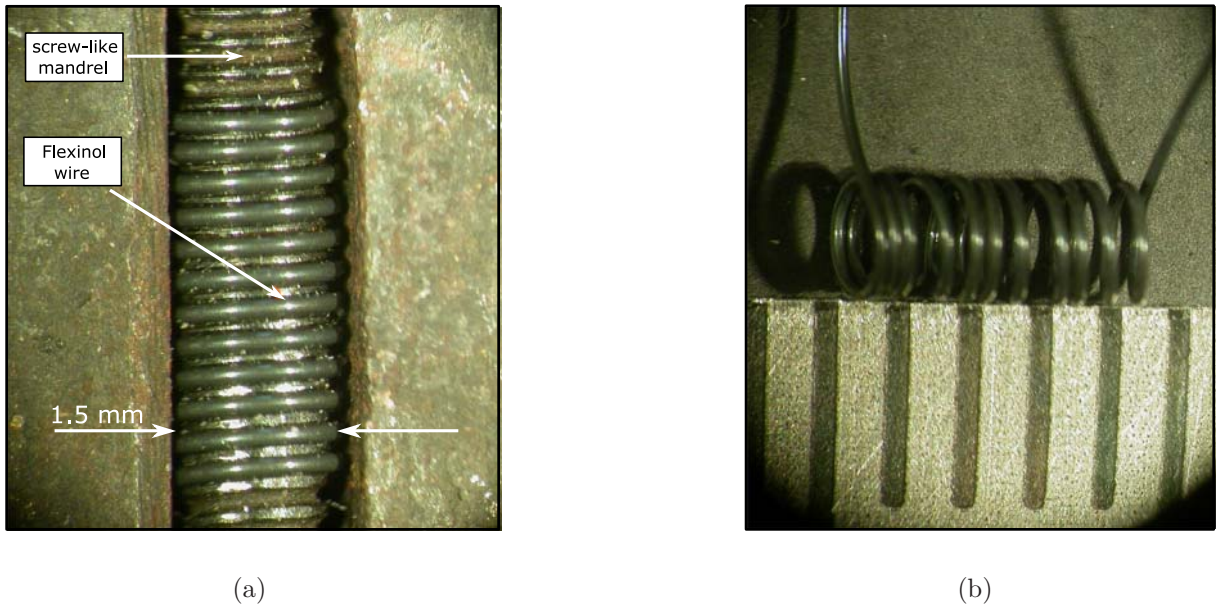


Figure 2.13: Fabrication procedure of an SMA helical spring: (a) constrained Flexinol wire on a mandrel and (b) helical shape after heat treatment.

### 2.4.2 Parameter identification

From the first experiments, it was easy to realize that numeric values for non-geometric parameters found in the literature or provided by the SMA manufacturers are usually very approximative, even inaccurate.

The reason is that most SMA properties depend on several fabrication factors such as chemical composition, thermomechanical history and experimental testing conditions that

---

<sup>3</sup>From Mondotronics.



certainly vary from manufacturer to manufacturer. Moreover, a manufacturer itself cannot guarantee standard constant values in the properties of their own SMAs.

In this section, experimental procedures are developed and used to determine the SMA properties of the spring specimen, especially to find those involved in SMA actuation, such as: transformation temperatures, latent heat of transformation and resistivity/electrical resistance.

### 2.4.3 Phase transformation parameters

Measurement of the transformation temperatures and the latent heat of transformation can be performed using a Differential Scanning Calorimeter (DSC).

DSC results obtained using a Perkin Elmer DSC 7 system are shown in Figure 2.14. All tests were performed as complete thermal cycles (from  $-40$  to  $120^{\circ}\text{C}$ ) on  $12.2$  mg NiTi samples heated and cooled at a constant rate of  $10^{\circ}\text{C min}^{-1}$  [Velazquez06a].

Figure 2.14(a) compares the DSCs of the Flexinol NiTi as a wire and spring. In addition to martensite and austenite, the analysis revealed that the material also exhibits an intermediate phase known as the rhombohedral or R-phase. Note that the transformation temperatures decrease (a different amount for each phase) once the wire undergoes the heat treatment process to set the helical shape.

Once a new shape has been fixed to an SMA, the transformation temperatures are unstable. To stabilize them, it is necessary to perform a series of thermal cycles with repeated heating and cooling. Forty cycles appeared to be enough for this purpose. Figure 2.14(b) compares the DSCs of the spring before and after the 40 thermal cycles test. Note that all transformation temperatures slightly decrease once stabilization. Figure 2.14(c) presents a zoom of the  $A \rightarrow R$  transformation.

The latent heat of transformation is usually determined by measuring the total area under the curve during the heating and cooling cycle. Figure 2.14(d) shows the  $M \rightarrow A$  and  $A \rightarrow R$  curves delineating the area used for the calculation of  $\Delta H$ .

Main results of the DSC analysis are summarized in table 2.3.

$M_f$	$M_s$	$R_f$	$R_s$	$A_s$	$A_f$	$\Delta H_{M \rightarrow A}$	$\Delta H_{A \rightarrow R}$
$-37^{\circ}\text{C}$	$-3^{\circ}\text{C}$	$36^{\circ}\text{C}$	$59^{\circ}\text{C}$	$28^{\circ}\text{C}$	$65^{\circ}\text{C}$	$14.38 \text{ J/g}$	$5.03 \text{ J/g}$

Table 2.3: Stable phase transformation parameters of the Flexinol NiTi spring specimen.

According to the DSC analysis, martensite phase takes place within the range  $-37$  to  $-3^{\circ}\text{C}$ . This means that, for actuation at room temperature, the M-transformation will never occur. The use of the R-phase instead of the M-phase will be evaluated in section 2.5.2.

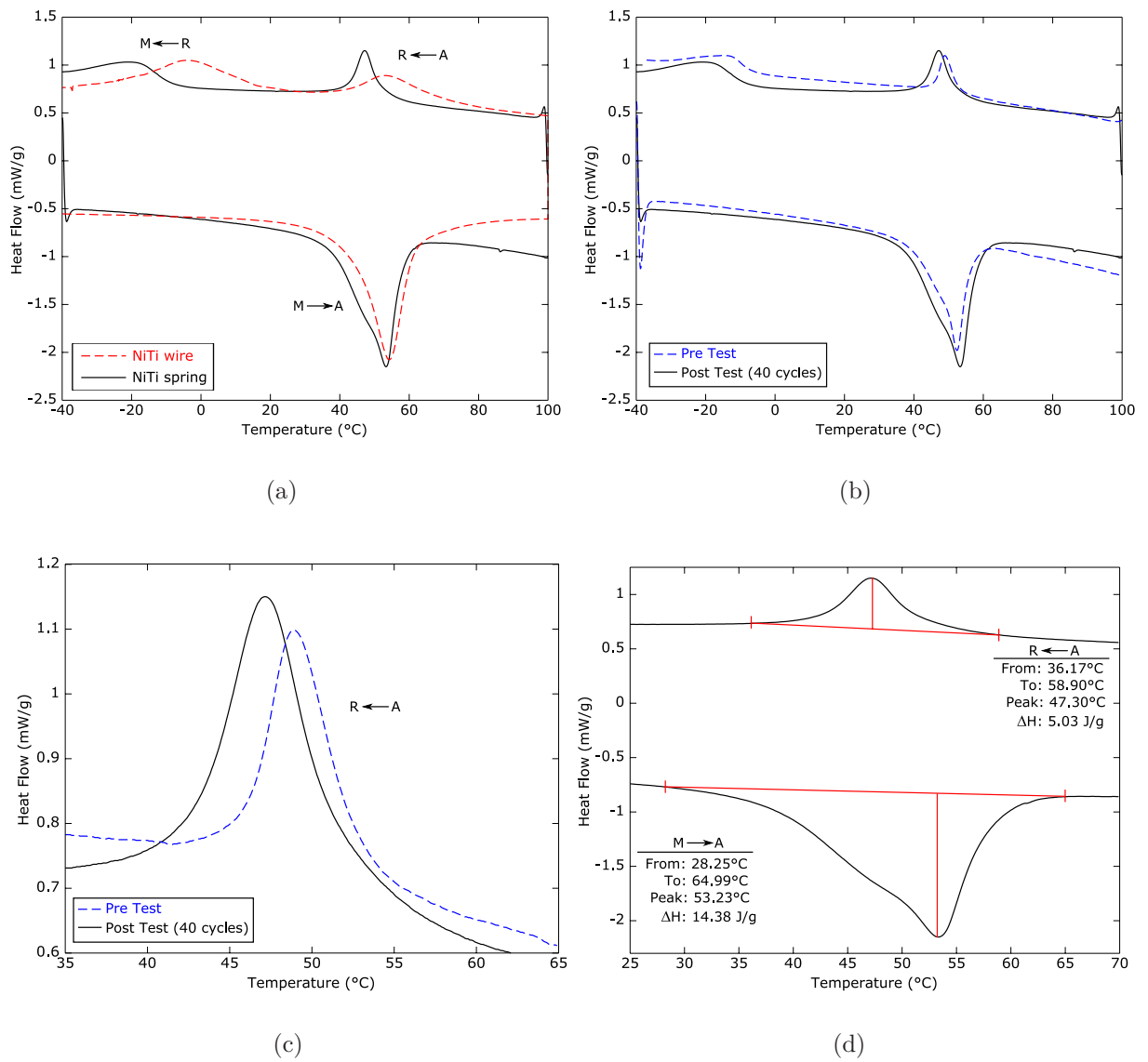


Figure 2.14: DSC results: (a) comparison of the DSCs of NiTi wire and spring, (b) DSCs of the spring Pre and Post 40 thermal cycles, (c) temperature stabilization during the A  $\rightarrow$  R transformation and (d) DSC showing heat of transformation  $\Delta H$ .

### 2.4.4 Resistivity/Electrical resistance

One of the major problems when SMAs are electrically heated is the non-linearity of their electrical resistance  $R$ . It is widely known that resistivity in NiTi alloys changes its value from martensite to austenite. In addition to this temperature dependence,  $R$  in SMAs is also strain-dependent.

Measurement of the spring's electrical resistance was performed using the experimental setup in Appendix B section B.1.

Figure 2.15(a) shows the spring's measured  $R$  as a function of deflection. Tests were conducted at room temperature for a maximum deflection of 10 mm. Note that  $R$  increases with deflection.

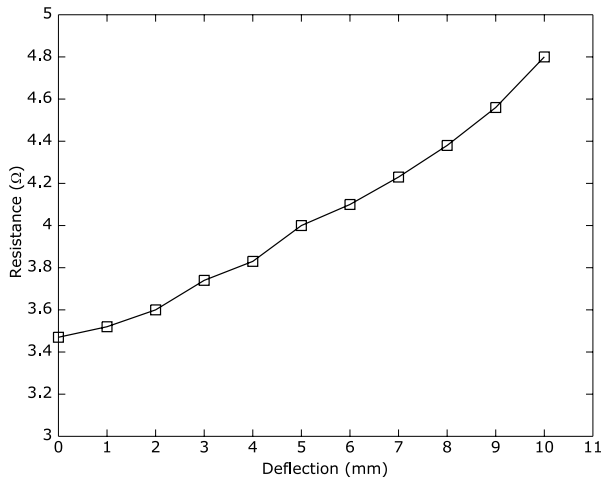
Figure 2.15(b) shows the evolution of  $R$  as a function of temperature. Tests were performed at zero deformation of the spring. The observed change between phases is about 12.5%. From this curve, calculation of the spring's resistivity is immediate:  $18.9 \times 10^{-7}$  and  $16.5 \times 10^{-7} \Omega \cdot \text{m}$  for the low and high temperature phase, respectively.

Figure 2.15(c) shows the evolution of  $R$  as a function of temperature for different pre-deflection values. Note that practically a homogeneous behavior is observed. The measured change between phases remains almost constant: from 12.5 to 14%.

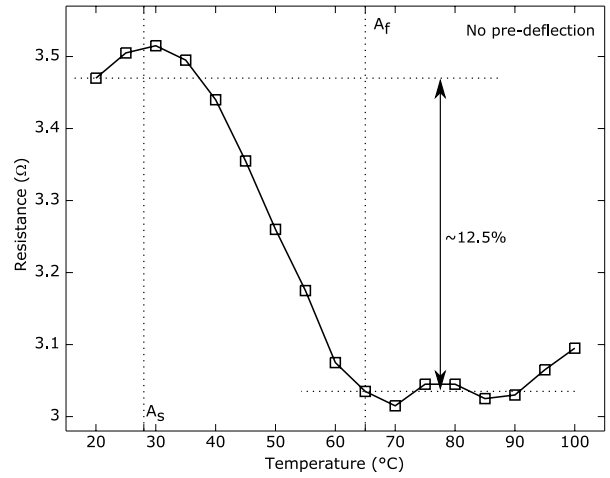
As demonstrated,  $R$  can neither be considered as a single value nor as a pair of constant values during the actuation process due to the large hysteresis that takes place between  $A_s$  and  $A_f$ . In order to model a closer behavior, an empirical approximation valid for  $0 \leq \delta \leq 10$  mm can be established by fitting the experimental data as follows:

$$R(\delta, T) = \begin{cases} 2.97 + \frac{1}{2}e^{0.13\delta} & \text{for } T < A_s \\ 1.97 + \frac{1}{2}e^{0.13\delta} + \cos \left[ \left(1 + \frac{\delta}{65}\right) \left(\frac{T-A_s}{A_f-A_s}\right) \right] & \text{for } A_s < T < A_f \\ 0.87 \left(2.97 + \frac{1}{2}e^{0.13\delta}\right) & \text{for } T > A_f \end{cases} \quad (2.30)$$

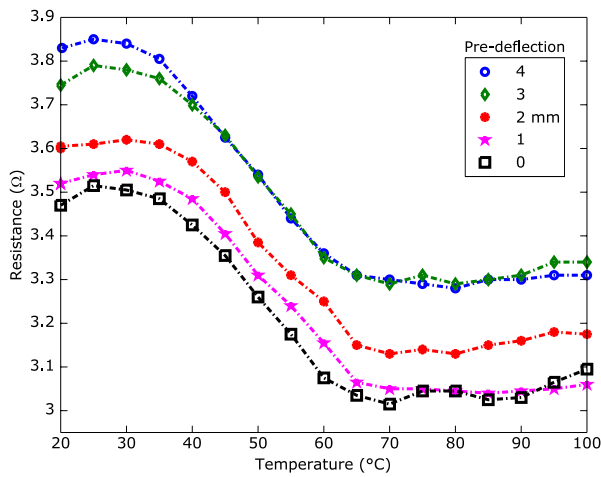
Figure 2.15(d) shows the experimental data fitted by equation (2.30).



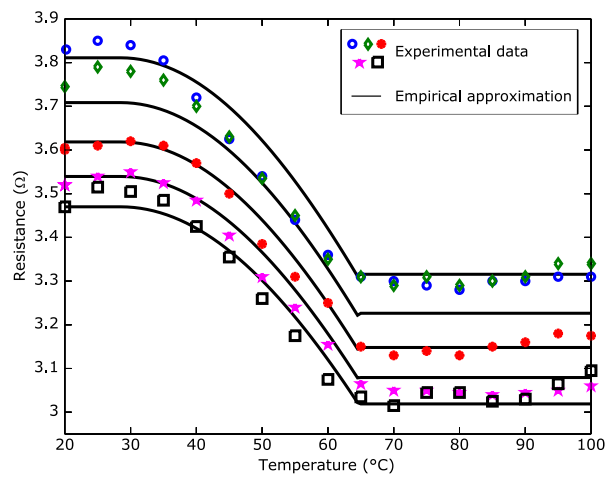
(a)



(b)



(c)



(d)

Figure 2.15: The spring's measured electrical resistance  $R$  as a function of (a) deflection and (b) temperature. (c) Comparison of the evolution of  $R$  as a function of temperature for different pre-deformations values. (d) Experimental data fitted by empiric equation (2.30).

## 2.5 Experimental evaluation of SMA thermomechanical properties

### 2.5.1 Thermal behavior of the NiTi spring

The experimentation presented in this section was performed using the platform described in Appendix B section B.2.

#### 2.5.1.1 Stress-free thermal behavior

The experimental conditions are as follows: The SMA spring is pre-deformed 7 mm at room temperature and it is slowly heated with a constant current of 200 mA and cooled using free-convection. No load is imposed.

Table 2.4 regroups the numerical values used for the simulation.

Property	Value	Reference
$\rho$ ( $\text{kg}\cdot\text{m}^{-3}$ )	6450	manufacturer's data sheets
$C$ ( $\text{J}\cdot\text{kg}^{-1}\cdot\text{K}^{-1}$ )	320	manufacturer's data sheets
$h$ ( $\text{W}\cdot\text{m}^{-2}\cdot\text{K}^{-1}$ )	94.96	calculated (eq. 2.6)
$A_f, A_s, R_s, R_f$ ( $^{\circ}\text{C}$ )	65, 28, 59, 36	experimentation
$\Delta H_{M\rightarrow A}$ ( $\text{J}\cdot\text{g}^{-1}$ )	14.38	experimentation
$\Delta H_{A\rightarrow R}$ ( $\text{J}\cdot\text{g}^{-1}$ )	5.03	experimentation
$R$ ( $\Omega$ )	governed by eq. 2.30	experimentation

Table 2.4: Summary of theoretical/experimental parameters for the NiTi spring.

Figure 2.16 compares the experimental and simulated temperature-time responses of the NiTi spring. Note that simulation using the experimentally determined properties reproduces sufficiently close the overall physical behavior.

Note also that the analytical cooling time is slightly underestimated in comparison to the experimental one. This is certainly related to the theoretical value of the heat-exchange coefficient  $h$ . In fact, as demonstrated by Polidori et al. in [Polidori98],  $h$  can show a highly unsteady behavior during the temperature-time evolution. Unfortunately, the unsteady problem of  $h$  is too complex to be solved and equations (2.6) and (2.7) permit us to obtain only a stationary value of  $h$ . Under these conditions, a close empirical value of  $h=55 \text{ W}\cdot\text{m}^{-2}\cdot\text{K}^{-1}$  best fits both heating and cooling curves.

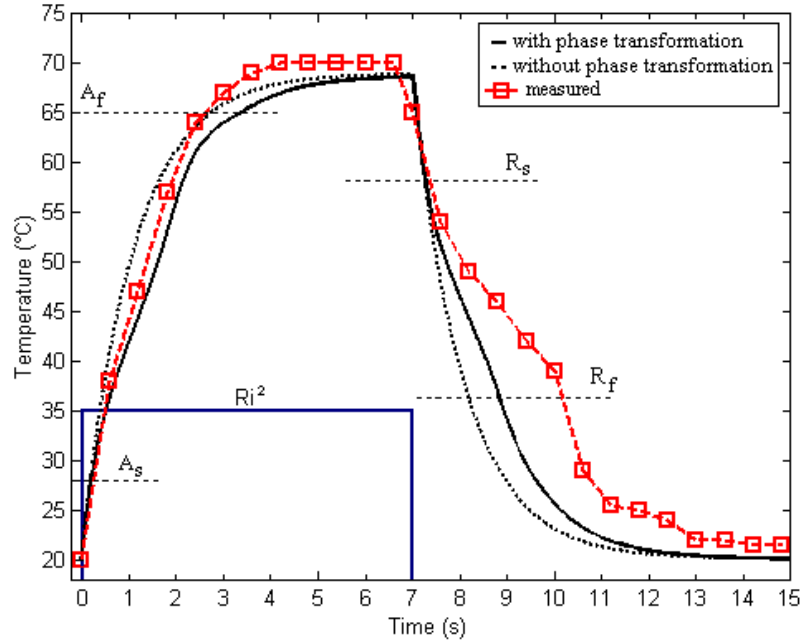


Figure 2.16: Comparison of the experimental temperature-time response with the corresponding simulation.

### 2.5.1.2 Thermal behavior at constant stress: the deflection point of view

Experimental results on the spring's thermal behavior could not be obtained for faster responses using the temperature sensor: the thermocouple, as most typical commercially available ones, offer sample rates up to 0.6 s; too low for measuring a rapid evolution of temperature. Instead, a relation between displacement and temperature was performed using the 20 ms sample rate linear variable differential transformer (LVDT). As described in Appendix B section B.2, the use of the LVDT implies that a 4 g mass (or a 1.24 MPa stress) is by default applied to the spring.

As seen in figure 2.17(a), a set of heating currents is applied to a 7 mm pre-deformed spring. The amplitude is varied from 200 to 500 mA. Recall from chapter 1 that an SMA heated from cold begins to transform into the austenite phase at  $A_s$ , and its transformation is essentially complete at  $A_f$ . Consequently, the time in which the SMA starts to present deformation is exactly the time that it needs to be heated enough to reach  $A_f$ .

Figure 2.17(b) bottom presents a zoom of the region of interest while the top section shows the analytical temperature evolution calculated using again the experimental values in table 2.4. Results are compared in table 2.5.

Note that the predicted time response reproduces reasonably close the experimental one and that the 1.24 MPa stress of the measurement instrumentation seems not to affect the time response significantly.

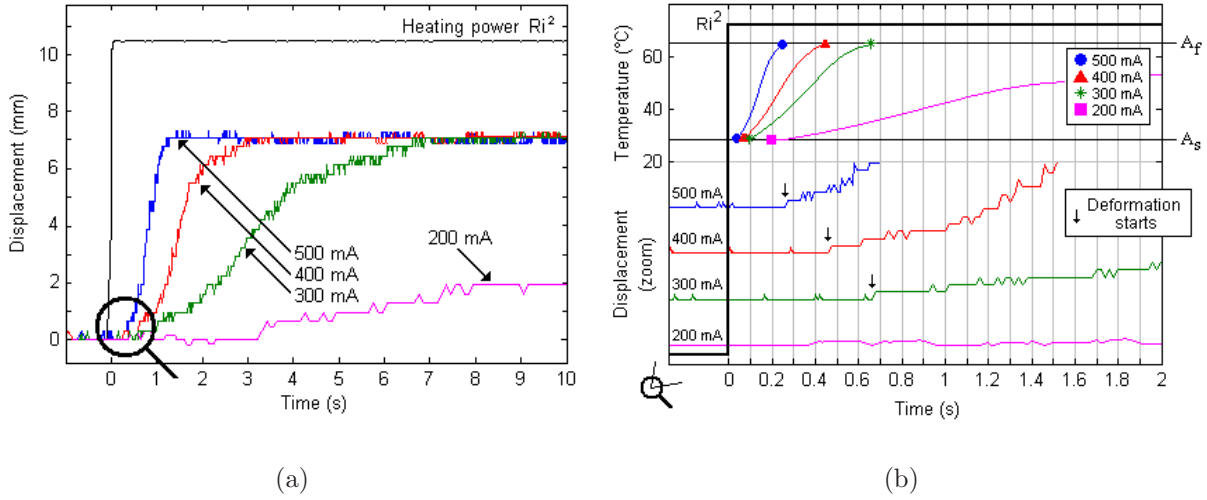


Figure 2.17: Time response using a displacement relation: (a) response to a set of input currents (7 mm pre-deformed spring) and (b) analytical/experimental comparison of actuation times.

Heating current (mA)	Time (s)		Experimental
	$A_s$	$A_f$	
500	0.0289	0.2387	0.26
400	0.0455	0.44	0.46
300	0.0822	0.6536	0.66
200	0.1945	3.315	3.2

Table 2.5: Comparison of analytical/experimental actuation times.

Experiments were also conducted at higher constant stress conditions: 3.1, 6.2, 9.4 and 12.5 MPa (10, 20, 30 and 40 g, respectively). Figure 2.18 shows, for example, the results of the same experiment when a constant stress of 6.2 MPa is applied to the spring. Table 2.6 compares the results with those obtained at 1.24 MPa.

As seen, time response is also influenced by the applied stress. If a stress is imposed during the heating process, then the SME, which normally occurs at given time, can only occur after enough extra heat energy to move the sample against the imposed stress is supplied. This evidently implies that the time response will increase. Figure 2.19 shows the evolution of the observed time at which the SME starts as a function of the applied stress for a constant input current of 300 mA.

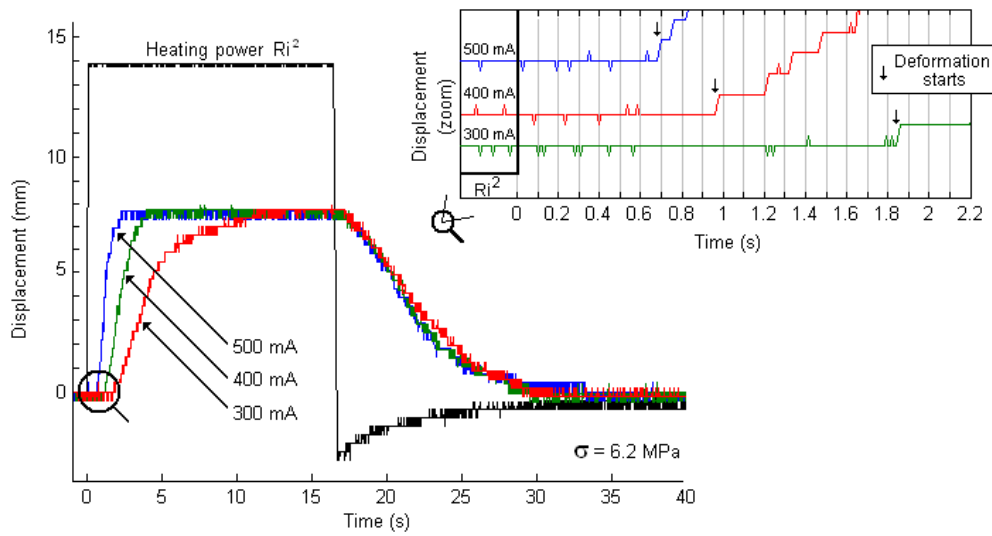


Figure 2.18: Time response at constant stress (6.2 MPa).

Heating current (mA)	Experimental time (s)	
	$\sigma=1.24$ MPa	$\sigma=6.2$ MPa
500	0.26	0.68
400	0.46	0.96
300	0.66	1.84

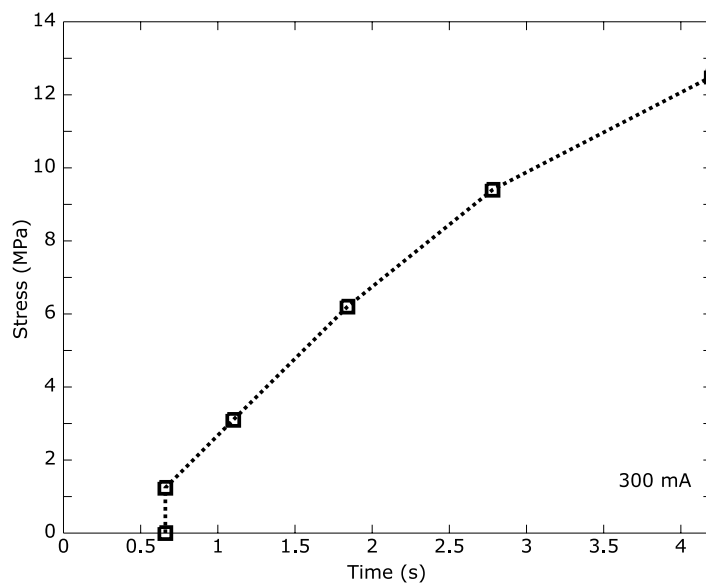
Table 2.6: Comparison of experimental actuation times for  $\sigma=1.24$  and  $\sigma=6.2$  MPa.

Figure 2.19: Experimental time response as a function of the applied stress.



## 2.5.2 Mechanical behavior of the NiTi spring

The experimentation presented in this section was performed using the platform described in Appendix B section B.3.

Figure 2.20(a) compares the calculated and experimental load-deflection curves of the NiTi spring for a maximum deflection of 10 mm. Experimentation was performed for each material phase independently, i.e., pure austenitic and pure R-phase loading/unloading under isothermal conditions (20, 85 and 105 °C).

As seen, numerical results well explain the spring's overall deformation behavior. However, a problem is observed in the model: plastic behavior is considered constant in both low and high temperature phases as figure 2.7 suggested. Note in figure 2.20(a) that experimental plasticity progresses in both phases while the analytical one tends to a constant value. It can be concluded that this model keeps its accuracy for regions close to the elastic-to-plastic transformation point and early plastic zones.

Figure 2.20(b) confirms the presence of the R-phase in the SMA spring. Recall from the DSC analysis in section 2.4.3, that martensite phase takes place within the range -37 to -3 °C. This means that, for actuation at room temperature, the M-transformation will never occur: the thermal cycle will be defined by A→R and R→A. The R-phase has similar macroscopic properties as the martensite phase and, as the DSC test revealed, the R-phase offers the advantage of a shorter temperature hysteresis. However, the use of the R-phase instead of the M-phase will not be considered for this work as the experimentally observed R-hysteresis is as small as 0.5 mm.

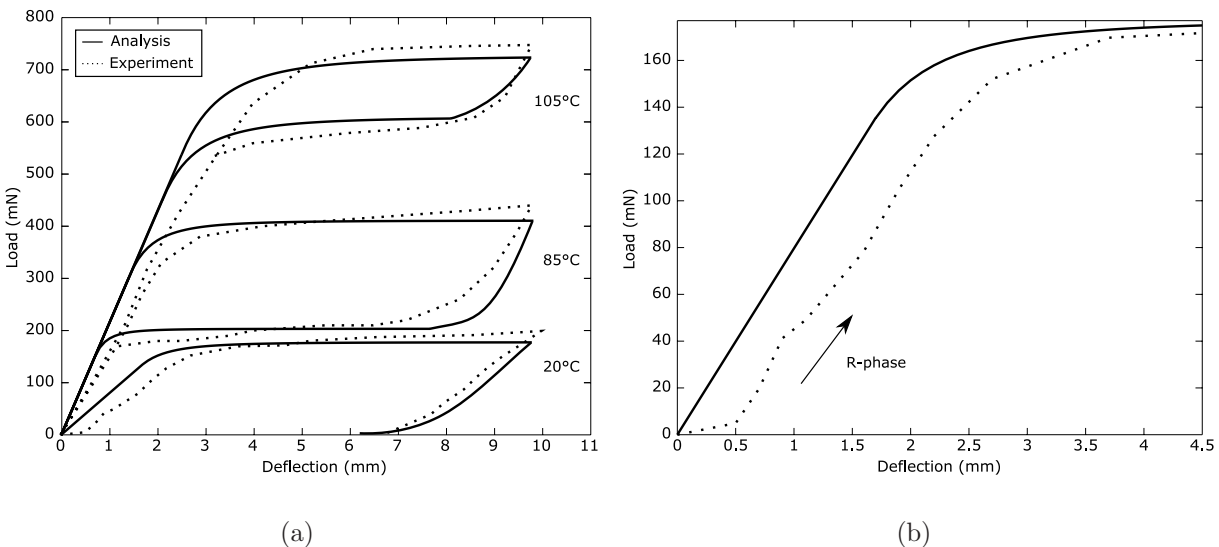


Figure 2.20: Deformation behavior of the SMA spring: (a) load-deflection relations at constant temperatures (20, 85 and 105°C) and (b) hysteresis due to R-phase.

Figure 2.21 proposes the new phenomenological representation of the spring's SMA behavior in the load-deflection-temperature space. Experimental observations during the tensile tests revealed that beyond  $105^{\circ}\text{C}$ , the load-deflection behavior was practically the same. These observations are integrated in the 3D representation.

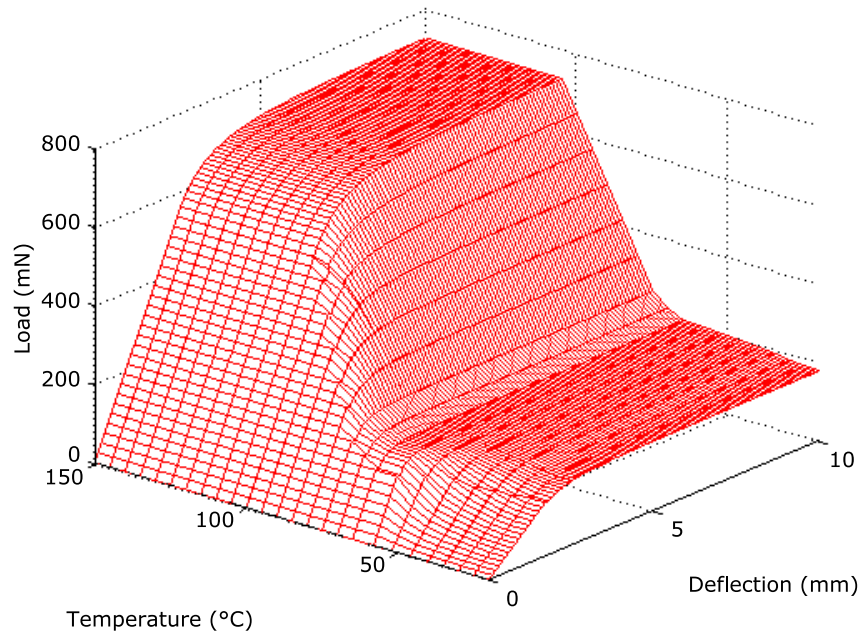


Figure 2.21: Experimentally based computational SMA behavior in the load-deflection-temperature space.

### 2.5.2.1 Comparison with straight wire

Figure 2.22 compares the experimental austenitic stress-strain SMA behavior of the helical spring and straight wire.

Experimental testing of the straight wire has revealed that useful stroke is limited to approximately 4 to 5 % of its original length.

The spring has a significantly higher recoverable strain compared to the wire. Impressive 300-400% strokes can easily be obtained. However, as it performs in torsion instead of tension, it cannot develop the same force.

Note that, while the rupture point in the straight wire is 1080 MPa at 14.6% strain, the spring's failure point is 22 MPa at 714%.

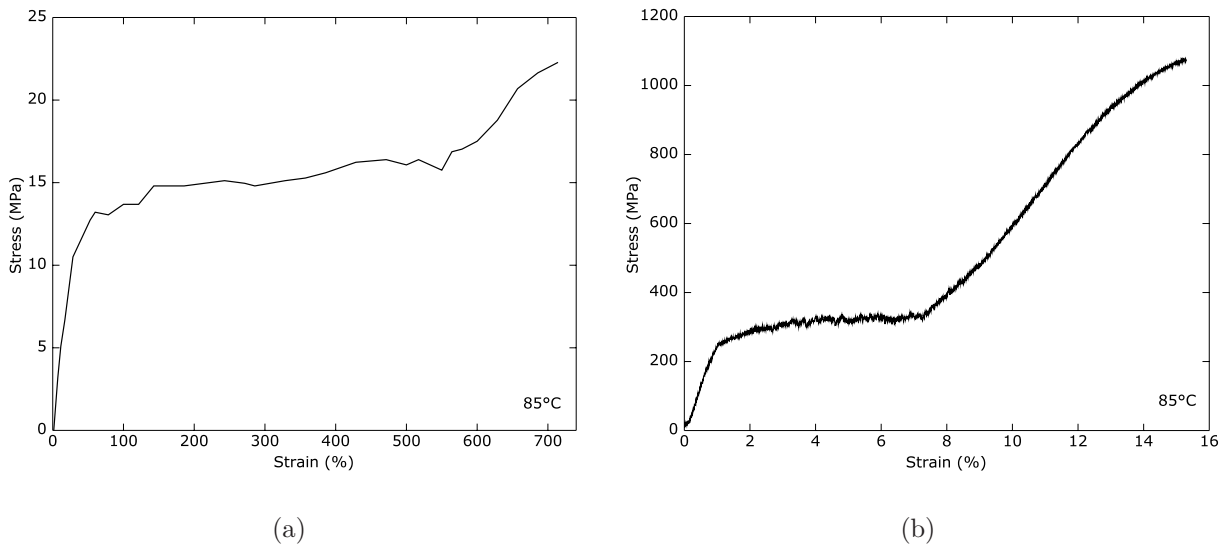


Figure 2.22: Comparison of experimental stress-strain curves: (a) helical spring and (b) straight wire.

### 2.5.2.2 Fatigue

In practice, SMAs are required to perform in cyclic motion. This implies that SMAs are subjected to both mechanical and thermal cycling with repeated loading/unloading and heating/cooling.

When subjected to thermomechanical cycling, the shape memory properties are affected, in particular the SME. From a material point of view, fatigue introduces defects such as dislocations that tend to soften and create fissures in the alloy eventually ending in the rupture of the material [Miller00].

To avoid or delay this degradation, it is convenient to study the fatigue properties of the material. This section evaluates the relationship between deformation and fatigue.

When an SMA is repeatedly loaded in the austenite phase, with a gradual increase of the total applied strain, the effect of accumulated plastic strain affects the phase transformation characteristics at some point. It becomes essential to determine this point in order to limit the strain amplitude applied to the SMA.

Figure 2.23 shows the load/stress-deflection/strain relationship of the SMA spring. Tests were performed at 85°C as complete loading/unloading cycles. Each cycle is repeated several times, incrementing the total strain by 142% (a 10 mm deflection step) for each loading. The effects of plastic strain on the transformation characteristics of the spring are quantified by measurement of the recoverable strain under zero applied stress for each mechanical cycle. Experimental results show that the memory shape is perfectly recovered for plastic deflections at 10, 20 and 30 mm. However at 40 mm, the spring slightly begins to lose its SME. 50 mm elongations produce a complete loss of actuation and a significant irrecoverable elongation appears even in the early cycles [Velazquez05b].

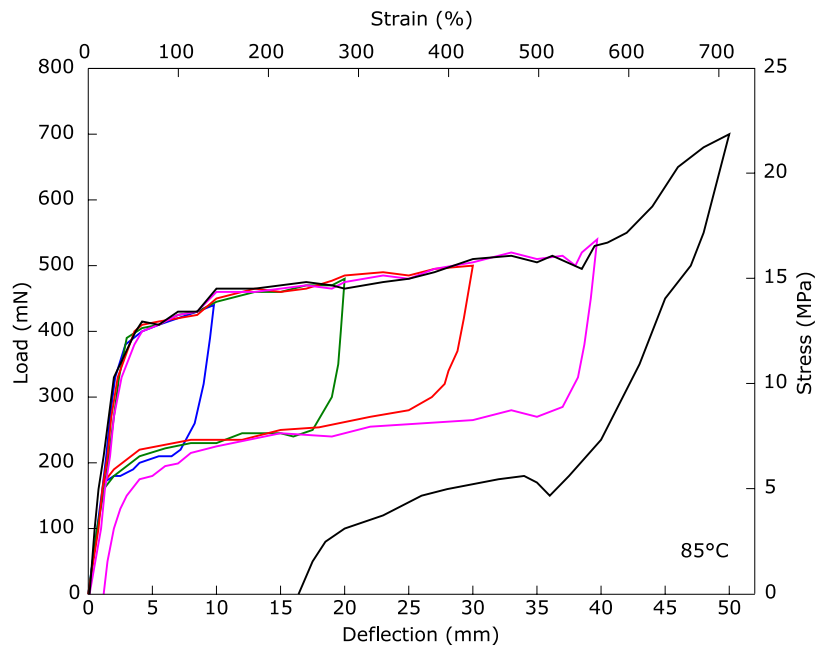


Figure 2.23: Load/stress-deflection/strain experimental results for austenitic plastic strain developed.

Figure 2.24 proposes a computational behavior of the spring's plasticity in the stress-deflection-temperature space. Note that, although stress-deflections curves are different at various temperatures, plastic strain limit is almost the same [Tobushi00a].

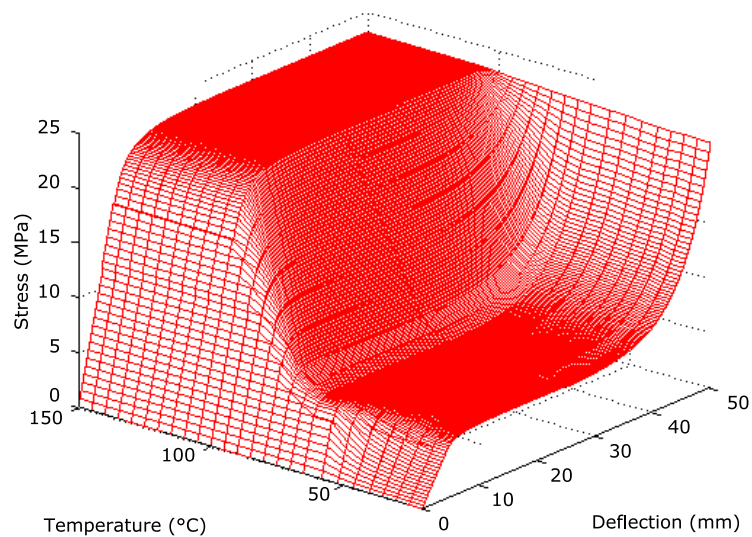


Figure 2.24: Computational stress-deflection-temperature behavior for martensitic/austenitic plastic deformation in loading.

### 2.5.2.3 Formulation of Fatigue Life

As seen from figure 2.23, there is an influence of the applied stress and developed strain on fatigue life. The issue now is to determine the number of cycles before failure.

In uniaxial isothermal fatigue, the Mason-Coffin relation relating plastic strain amplitude  $\epsilon_a$  to lifetime  $N_f$  is representative of classic low-cycle fatigue. This relationship can be expressed as follows:

$$N_f = (\alpha/\epsilon_a)^{(1/\beta)} \quad (2.31)$$

where  $\alpha$  and  $\beta$  represent  $\epsilon_a$  when  $N_f=1$  and the slope of the  $\log(\epsilon_a)$ - $\log(N_f)$  curve, respectively. According to the results obtained in figure 2.23,  $\alpha$  can be considered as 567% (a 40 mm elongation). Concerning  $\beta$ , a typical value of 0.5 is valid for metals.

However Flexinol is well known for its outstandingly high fatigue resistance. Flexinol is a specifically manufactured NiTi alloy optimized for high cycle multiple repetition use. The number of cycles to failure associated with plastic strain are typically quoted as follows: 1 cycle for strains of 8%,  $10^2$  cycles for strains of 4%,  $10^4$  cycles for strains of 2% and more than  $10^5$  cycles for strains of 1% [Dynalloy]. Fitting Flexinol's data with equation (2.31), indicates  $\beta=0.143$ .

Figure 2.25 shows the relation between deflection and number of cycles to failure (this last in logarithmic scale) for the helical spring. Note that for higher plastic strain levels, fewer cycles are needed to cause the specimen to fail and subsequently as the strain level decreases, the number of cycles to failure increases substantially.

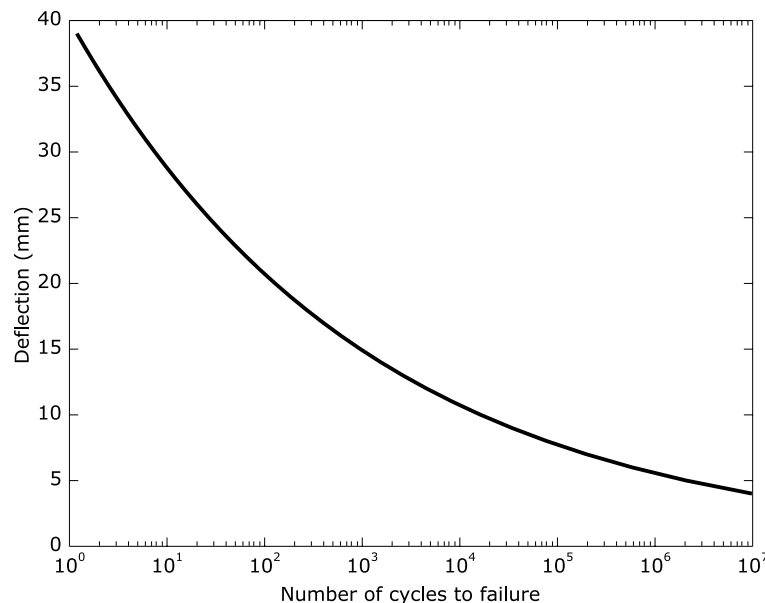


Figure 2.25: Strain amplitude versus number of cycles.

Analogously, the expected number of cycles to failure are: 1 cycle for elongations of 40 to 50 mm, 10 cycles for elongations of 30 mm,  $10^2$  cycles for 20 mm elongations and around  $10^4$  cycles for deformations of 10 mm. In order to obtain the maximum fatigue life (more than  $10^5$  cycles), the spring should be actuated with no more than a 5 mm deflection.

### 2.5.3 Micro-structural observations on the NiTi specimens

NiTi SMAs are very sensitive to thermomechanical treatments. In order to evaluate the effects of these treatments in the samples, a micro-structural analysis using a Scanning Electronic Microscope (SEM) was performed [Velazquez06a].

Figure 2.26 compares the micro-structures of the NiTi wire and spring before and after fatigue. Figure 2.26(a) shows the non-polished samples at room temperature. Note the evident effects of fatigue on the surface of the spring (bottom figure).

Figure 2.26(b) top shows the as-received surface of the wire. Note that the material presents a very inhomogeneous structure as well as a number of cracks. Figure 2.26(b) center shows the NiTi surface after the heat treatment process applied to set the spring shape. Note that irregularities eventually appear on the spring's surface. This is believed to be due to a local stress applied when setting the helical shape. Figure 2.26(b) bottom shows the spring's surface after the fatigue test. Note the severe damages on the surface that are finally responsible for the failure of the specimen.

Figure 2.26(c) top shows in detail the surface of the wire. Different micro-cracks are observed by which rupture starts. Figure 2.26(c) center shows in detail the surface of the spring. Note that the heat treatment process actually induces micro-structural modifications. A new granular order is observed that corresponds to the new crystallization. Figure 2.26(c) bottom shows in detail the surface of the spring after plastic fatigue. Note that the granular distribution becomes more accentuated with bigger and more defined grains. As suggested in [Sutou05], SMAs exhibit a strong dependence between grain size and mechanical behavior: as the grain size increases, the plastic behavior increases and the strength of the material decreases. Current research in this field concerns grain size reduction to the nanoscale to improve the mechanical and fatigue properties of SMAs.

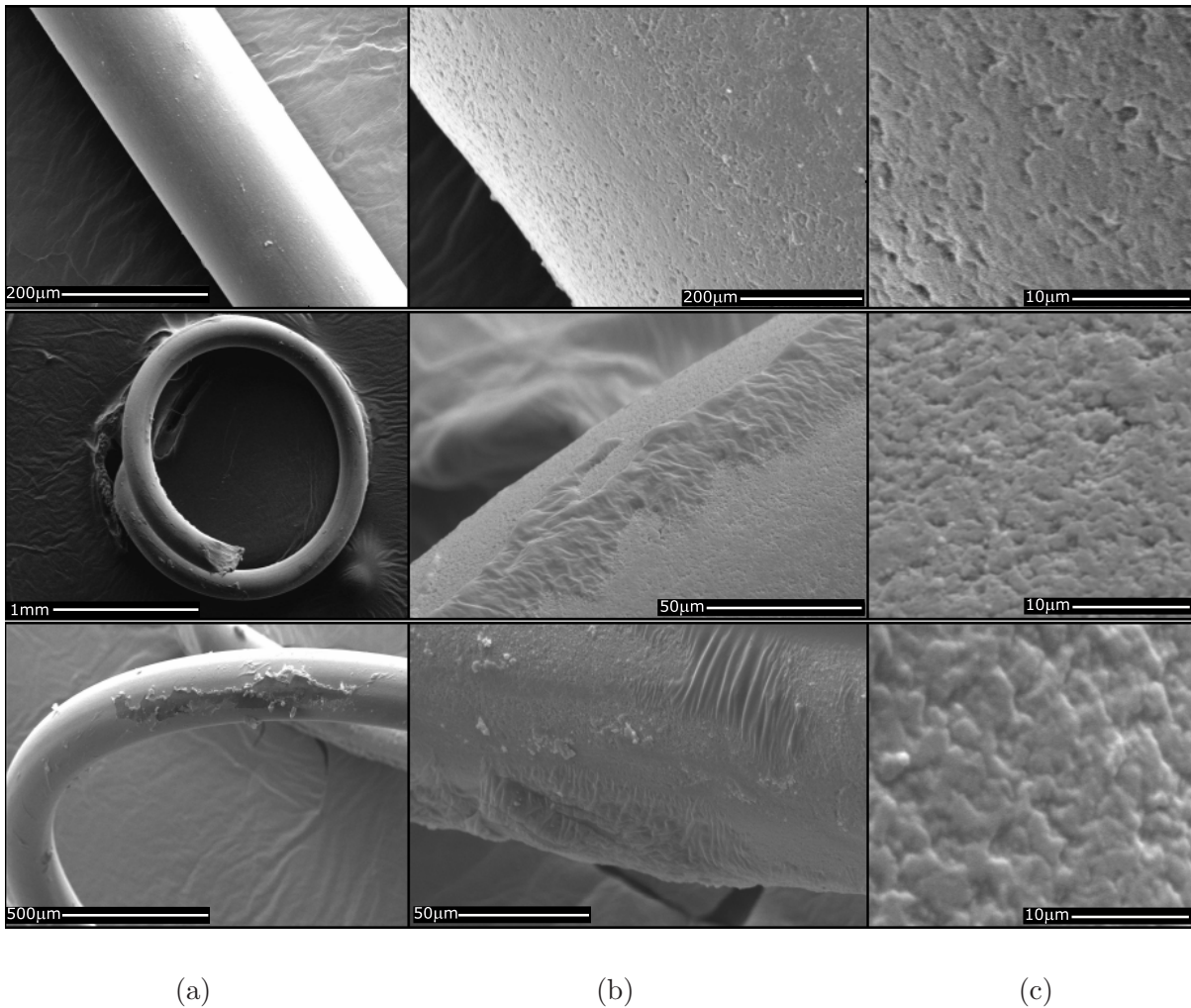


Figure 2.26: Comparison between the micro-structures of a NiTi wire and helical spring before and after fatigue induced by plastic strain.

## 2.6 Conclusion

This chapter has presented an analytical/experimental study of the thermomechanical characteristics of a NiTi SMA helical spring. Main results are summarized as follows:

1. The proposed analytical models are simple to use and represent sufficiently well both thermal and mechanical behaviors of SMA helical springs.
2. Time response of SMAs is mainly governed by the cooling time. The actuation frequency can be improved by using forced air convection methods (on cooling), increasing the input power (on heating) and/or decreasing the wire's diameter.
3. Thermal hystereses due to latent heat must be taken into account mostly when cooling by free convection.

- 
4. The tensile force developed by an SMA spring is a dependent function of its deflection and its temperature. The spring's geometrical parameters  $d$ ,  $D$  and  $N$  must be optimized to obtain a desired force and stroke.
  5. An experimental re-identification of parameters is usually needed to determine the exact value of the specimen's SMA properties involved in actuation.
  6. The analysis of the influence of plastic strain permits establishing the spring's operating stroke limit in order to obtain an acceptable number of cycles before fatigue failure.
  7. From these tests, it is possible to formulate a thermomechanical behavior useful to design SMA helical springs optimal in actuation speed, force and fatigue performance.





---

## Chapter 3

# Miniature SMA Actuator for Tactile Binary Information Display

---

This chapter presents a miniature SMA based actuator intended to be used to design and develop high-resolution, lightweight and compact interfaces for tactile binary information representation such as Braille. Since the main drawback of these devices is their high cost, the proposed actuator exploits the simplicity of its design and implementation to provide a low-cost actuation alternative. The actuator consists of an antagonist arranged pair of NiTi helical springs, which thermomechanical properties introduced in the previous chapter will be used to characterize its behavior. The actuator of 1.5 mm diameter and 150 mg mass is capable of developing a 300 mN pull force and 1.5 Hz bandwidth by using simple forced-air convection. The prototype and performance results are presented and discussed.

### 3.1 SMA based actuators

As discussed in chapter 1, SMAs achieve their actuation through the phenomenon of the shape memory effect (SME), which is non-reversible. This implies that, an SMA itself cannot be considered as an actuator since it does not provide reversible motion.

Two general approaches are used to exploit SMA materials in actuator applications: the one-way and the two-way effect.

*The one-way effect* describes the ability of SMAs to recover a memorized shape when heated up to austenite, but retains this shape when cooled down to martensite. To be used in cyclic actuation, it is necessary to provide a biasing force to induce the initial deformed shape in the martensite phase.

*The two-way effect* describes a memory process with two stable shapes: one in austenite and the other one in martensite. Therefore, the two-way effect does not require any external mechanisms for cyclic actuation.

While using the two-way effect provides simpler and compacter actuators with many fewer elements involved, it certainly requires extra manufacturing processes, it is difficult to achieve correctly and its strain is only half of that observed in one-way SMAs [Gill02]. This chapter focuses on one-way SMA based actuators.

Although a one-way effect SMA could be designed such that it exerts a force in three dimensions (when deformed in 3 directions from the memory configuration), the great majority apply a one-directional tensile force and cannot directly apply a compressive force. In many robotic applications, this is accomplished by using a mass, an elastic element or a second SMA arranged in antagonist mode [Waram93].

The simple mechanisms in figure 3.1 show how these configurations can be used to design actuators that create linear and rotational motion.

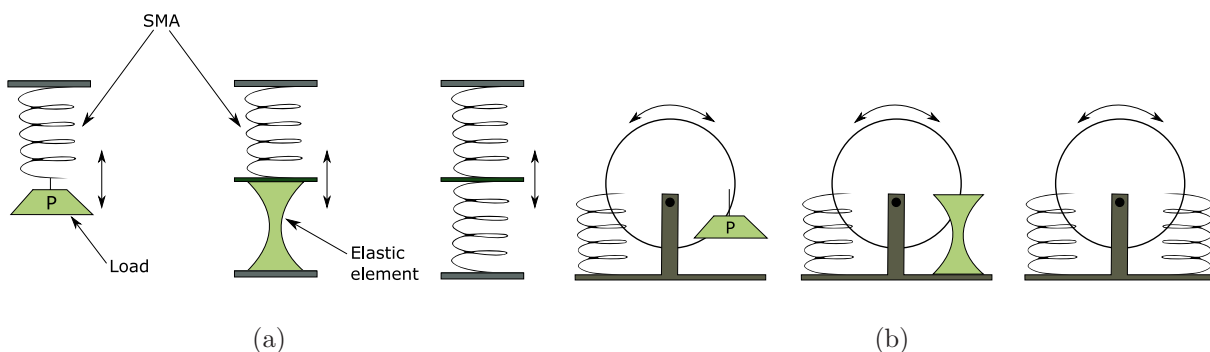


Figure 3.1: Main SMA actuator configurations using one-way effect SMAs: (a) linear and (b) rotational motion.

Some representative examples and applications of SMA based actuators can be found in the literature:

Ikuta in [Ikuta90] proposed a miniature gripper based on the antagonist arrangement of SMA helical springs to actuate two mechanical fingers (Figure 3.2(a)). Similarly, de Sars in [de Sars05] proposed the actuation of a high mobility endoscope using the antagonistic arrangement of SMA flat springs (Figure 3.2(b)).

Peirs in [Peirs98] proposed an SMA and elastic element configuration to actuate the tip of a 2-DOF endoscope (Figure 3.2(c)), while the actuator developed by Grant [Grant99] exploits the same configuration: several disks separated by SMA fibers and a bias spring move back and forth when heated and cooled (Figure 3.2(d)).

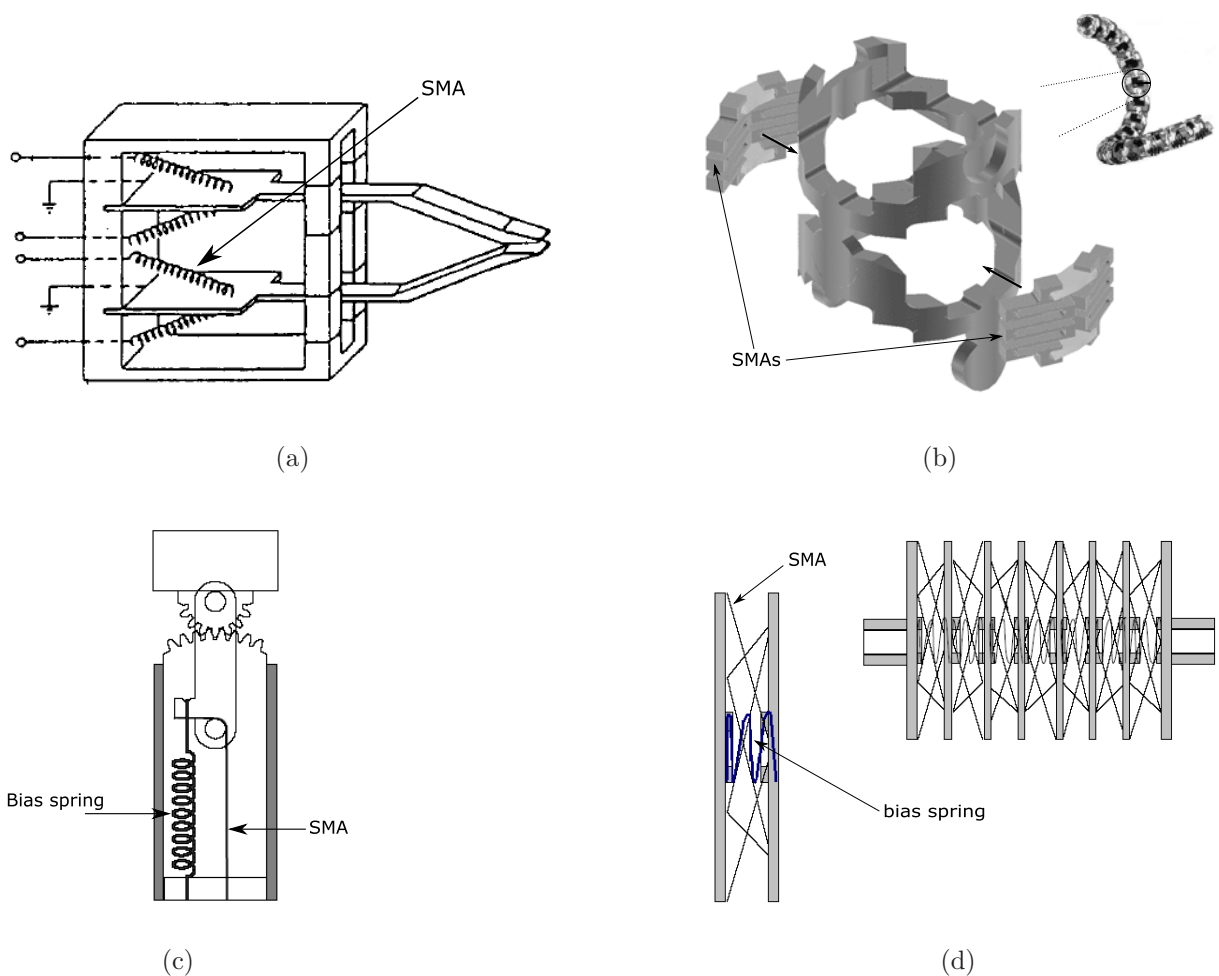


Figure 3.2: Examples of existing actuators using the basic types of SMA configurations: (a), (b) antagonistic and (c), (d) biased actuators.

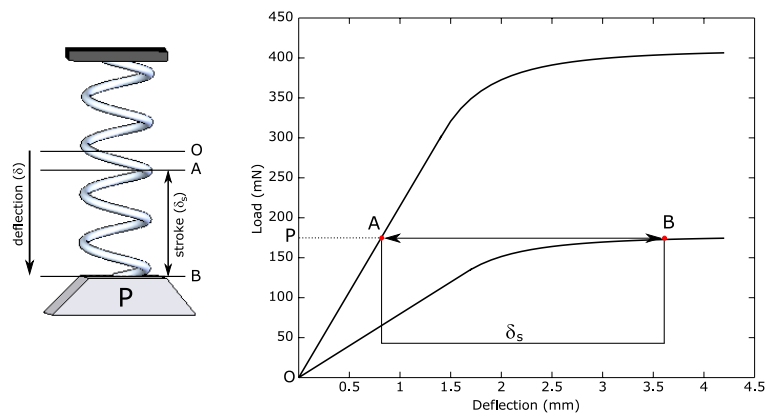
To understand the behavior behind the 3 basic SMA actuator configurations, let us consider the SMA NiTi helical spring of geometric and thermomechanical characteristics described in chapter 2.

### 3.1.1 Two-way actuator using a mass

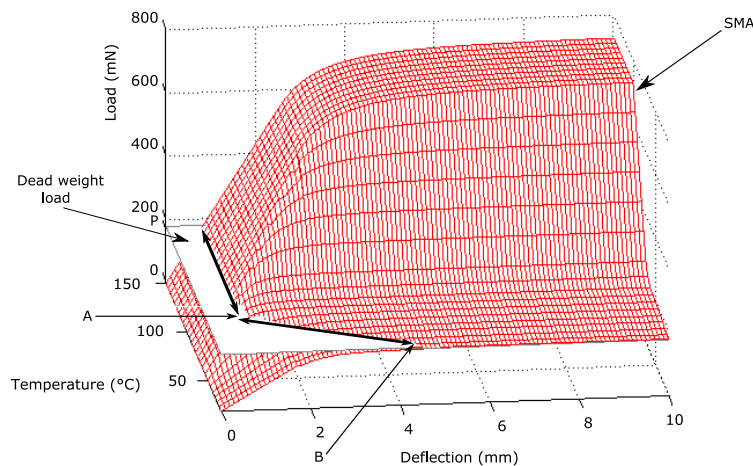
The most basic concept of SMA based actuator is shown in figure 3.3. It consists simply of a dead weight load acting as a biasing force.

Figure 3.3(a) shows the load-deflection behavior of this actuator. The SMA spring is deformed in martensite state to point  $B$  as a result of the load applied. Upon heating and cooling, the equilibrium point will be alternatively defined by  $A$  and  $B$ . Note that the path to be followed is a straight line of amplitude equal to the load applied.

Figure 3.3(b) shows the thermomechanical path performed by the actuator in the load-deflection-temperature space. Note that the actuator's behavior can be defined by the intersection of the surfaces characterizing both elements [Bellouard00].



(a)



(b)

Figure 3.3: Dead weight load as biasing force: (a) the actuator's conceptual representation and its load-deflection behavior. (b) Thermomechanical path performed by the actuator in the load-deflection-temperature space.

As seen, this actuator is very simple to implement. However there are some important drawbacks to consider:

The risk of plastic fatigue development is high: the value of  $P$  must be chosen to work within an appropriate elastoplastic zone. This implies limited tensile forces and strokes. Otherwise, the number of cycles to failure will decrease substantially.

Since a dead weight load is not easily incorporated into a device, this kind of actuator is completely impractical and a poor choice.

### 3.1.2 Biased actuator

One of the most popular SMA actuator configurations consists of an SMA arranged together with an elastic element or bias spring so that they oppose each other's motion (Figure 3.4(a)). Any element with a linear load-deflection behavior can be considered as a bias spring.

Consider the SMA spring pre-strained in martensite state to point  $B$  as a result of the compressive force applied by the bias spring. During the actuation cycle, the SMA tends to recover its austenitic characteristic translating the central mass to a new equilibrium point  $A$  and storing potential energy within the bias spring. Upon cooling, the potential energy in the bias spring will be expended in stretching the SMA back to point  $B$  obtaining this way the reversible motion (Figure 3.4(a)).

Figure 3.4(b) shows the thermomechanical path performed by the actuator in the load-deflection-temperature space. Note that the actuator's behavior is completely linear and elastic.

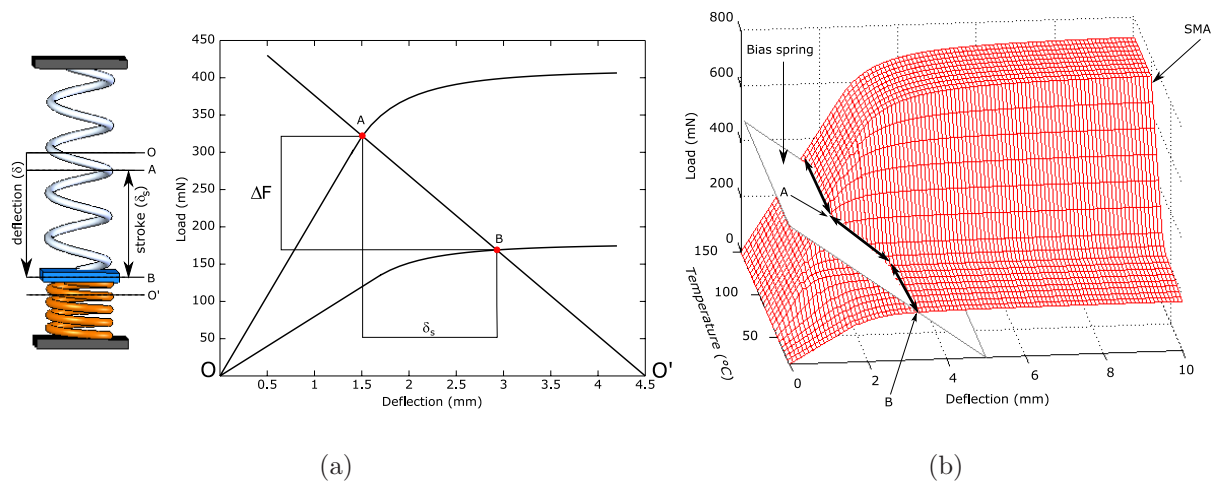


Figure 3.4: Biased actuator: (a) the actuator's conceptual representation and its load-deflection behavior. (b) Thermomechanical path performed by the actuator in the load-deflection-temperature space.

An important remark on this actuator is that its operating characteristics (available force and stroke) are directly affected by the bias spring stiffness  $k$ . Figure 3.5 shows the load-deflection curves for several actuators with bias springs of different stiffness in which  $k_1 > k_2 > k_3$ . Note that the influence of  $k$  results in actuators of different forces and strokes.

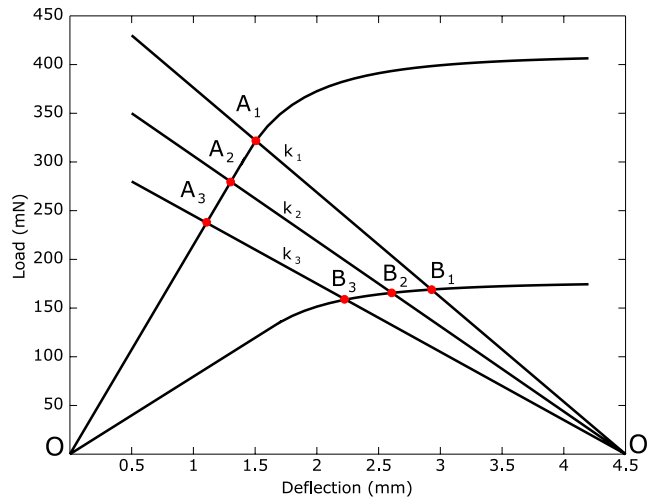


Figure 3.5: Influence of the bias spring stiffness  $k$  on the load-deflection characteristic of the actuator.

### 3.1.3 SMA antagonist actuator

Another technique to obtain reversible motion of an SMA is a second SMA element arranged in antagonist mode. The antagonist principle is based on heating one SMA element at a time, so that its austenitic state produces a force and displacement over the second martensitic SMA.

Consider both SMA springs identically pre-strained (distance  $O-\delta_0$  and  $O'-\delta_0$  in figure 3.6(a)) in martensitic equilibrium point  $\delta_0$  (Figure 3.6(a.1)). When the lower spring is heated, the new equilibrium point  $B$  is defined by the intersection of its austenite curve and the upper spring's martensite one (Figure 3.6(a.2)). When cooling, the lower spring tends to recover its martensite characteristic at the same time that the upper one mechanically unloads.

As seen, the equilibrium point does not follow the  $B-\delta_0$  trajectory but the  $B-D$  one (Figure 3.6(a.3)). The same phenomenon is observed when the upper spring is heated; it follows  $\delta_0/D-A-C$  instead of  $\delta_0/D-A-\delta_0$  (Figures 3.6(a.4) and 3.6(a.5)).

A more complete representation of the thermomechanical path followed by the equilibrium point is shown in figure 3.6(b). Note that the initial position  $\delta_0$  is not recovered due to the mechanic unloading characteristic of martensite.

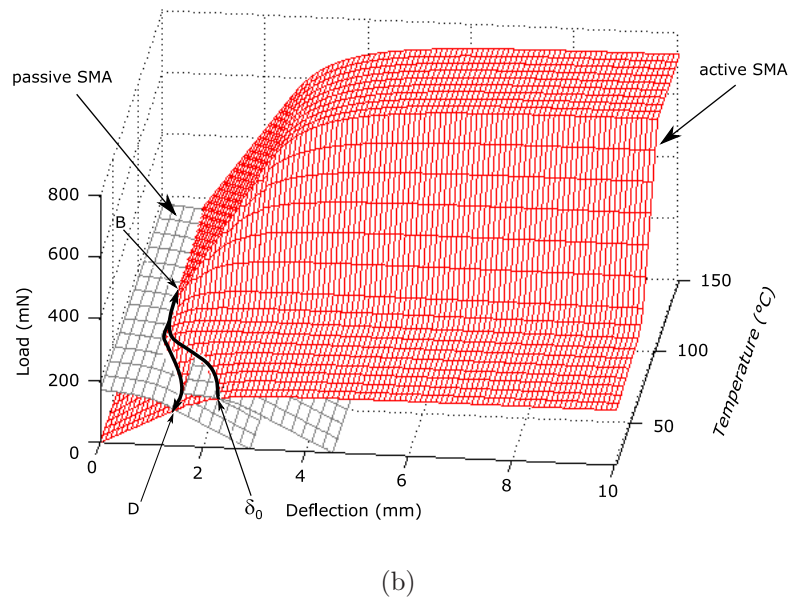
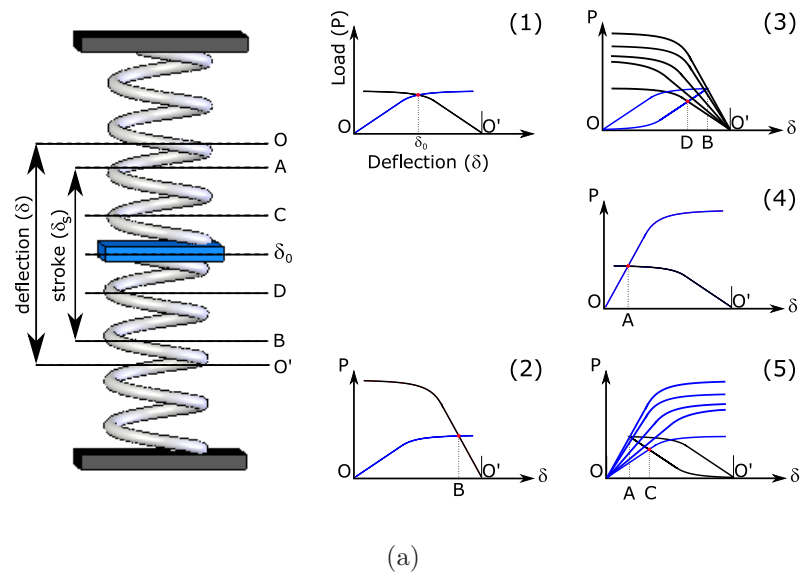
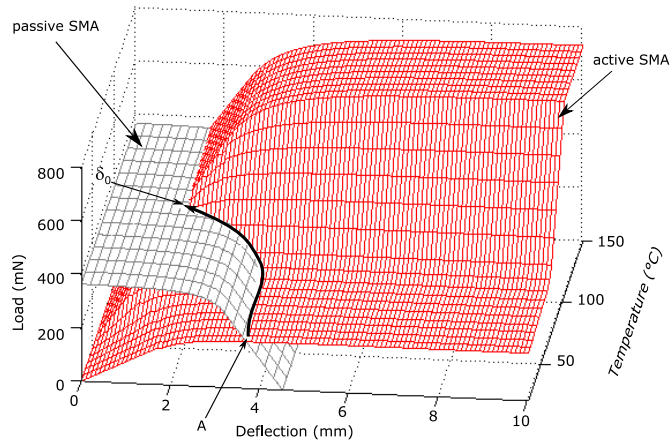


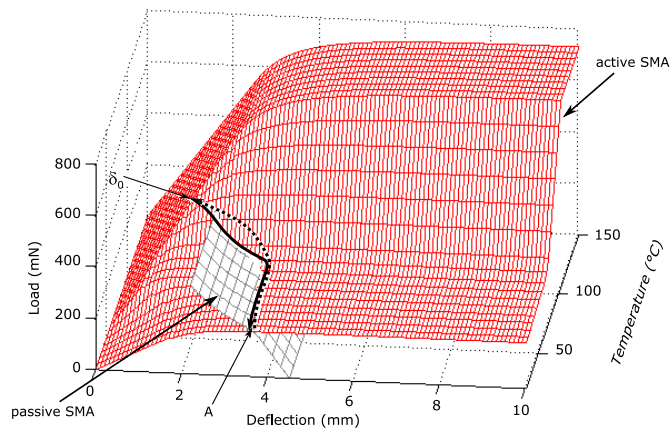
Figure 3.6: SMA antagonist principle: (a) the actuator’s conceptual representation and load-deflection relations for a complete operating cycle. (b) Thermomechanical path performed by the actuator in the load-deflection-temperature space.

A second possible case is when one of the springs is kept passive in the austenite state while the other one is activated from martensite to austenite (Figure 3.7(a)). Note that the superelasticity property appears in both active and passive springs in order to reach point  $\delta_0$ . When cooled, the passive spring mechanically unloads by following its austenite characteristic (Figure 3.7(b)). Note that the initial position  $A$  is recovered in this case even though a non-reversible path is observed between  $A$ - $\delta_0$ .





(a)



(b)

Figure 3.7: Antagonist operation with a passive austenitic spring: active spring's behavior at (a) set and (b) reset points.

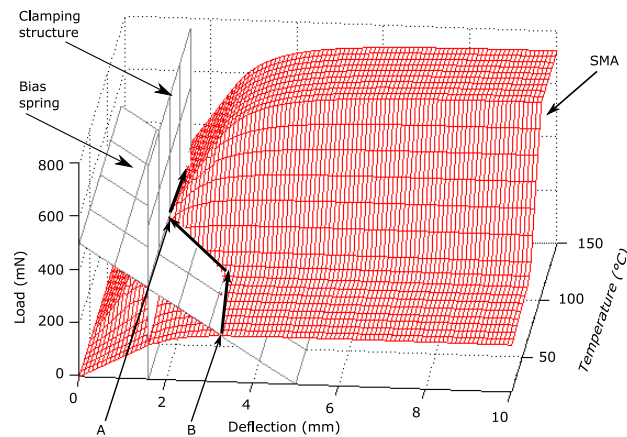
### 3.1.4 Bistable mechanisms

Note that all of the above configurations provide motion essentially between two points defined by the active and passive states of the SMA. However, only the passive state can be considered stable since no power is needed to sustain it.

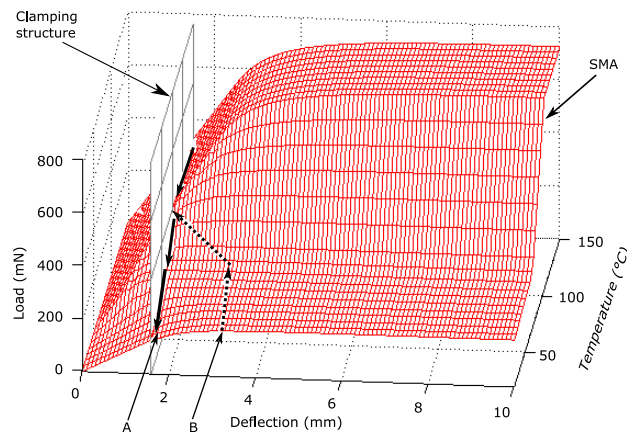
In contrast, the active state not only requires energy to be achieved but also to be retained; the SMA must be kept active, which not only leads to poor efficiency, but also implies serious drawbacks mostly when electrically heated. In principle, an SMA can be heated arbitrarily quickly by passing a sufficiently large current through it. However, excessive electrical power has the capacity to overheat the SMA, causing thermal stress fatigue and a gradual degradation of its performance.

A strategy for retaining the active position in the martensite state of the SMA is then required to avoid power consumption, useless output work and overheating. One method to achieve two stable positions is the use of clamping/latching mechanisms. Thus, the actuator would need energy only when changing from one state to the other and in neither of the two end positions power would be needed.

A 3D representation permits better understanding of the concept of the bistable actuator. Figure 3.8 shows, for example, the biased actuator with a clamping structure represented by a plane perpendicularly disposed to those representing the SMA and bias spring. Upon heating (Figure 3.8(a)), the thermomechanical path followed by the actuator is as defined in section 3.1.2. When position *A* is achieved, the blocking structure retains the SMA's deflection even when the SMA transforms back into its martensitic state (Figure 3.8(b)). Note that two stable states can now be reached.



(a)



(b)

Figure 3.8: Bistable actuator: biased configuration using a blocking mechanism to achieve two stable positions.

## 3.2 An SMA based actuator for touch stimulation

Actuators are irreplaceable constituents of mechatronic systems. Tactile displays are no exception. These devices essentially consist of an array of actuators or *taxels*<sup>1</sup> that are raised and lowered against the fingertips. Our goal is to stimulate the sense of touch through skin deformations to represent binary information patterns.

If we consider that exploring the contact pins for obtaining and understanding tactile information can take several seconds, it can be concluded that, actuators that spend a great deal of energy maintaining their active state are not acceptable. Bistable actuators are more suitable for touch stimulation.

Recall from the section "Guidelines for tactile displays: a psychophysiology approach" in chapter 1, that the challenge is to integrate a large number of actuators with a 2.54 mm interspacing, a delivered force of about 100 mN and a minimum reaction time of 1 s at indentation amplitudes of 1 mm. In this context, let us consider the SMA helical spring introduced in chapter 2 as the active element of a tactile actuator.

Several bistable taxel designs were envisaged. Three of them are presented here. These designs were implemented and evaluated in order to arrive at a specific design that seemed to be optimal in terms of implementation, cost and performance.

### 3.2.1 Proposed solutions

#### 3.2.1.1 Concept 1 - A pen-like tactile actuator

The first idea developed consists of an SMA spring, a bias steel compression spring and a pen-like blocking structure [Velazquez04e]. Inspired by a simple retractable ballpoint pen-like mechanism, the actuator's operating principle is shown in figure 3.9.

(1) At the initial position, the taxel's contact pin is raised. The SMA spring is pre-strained in the martensite phase while the bias spring is unstressed, (2) when the SMA spring is electrically heated, it recovers a compressed memorized shape that compresses the bias spring and retracts the contact pin, (3) the electrical current is then disconnected. The temperature of the SMA starts to decrease and so its yield strength. The bias spring tends to extend the SMA spring, fully latching the pen-like blocking structure. The taxel is now in the lower position and no further energy is required until a change is necessary. (4) To raise the pin again, the SMA spring is once more activated. The bias spring compresses and the blocking structure unlatches, (5) the electrical current is again disconnected. The bias spring is now able to fully recover its original shape. It extends the SMA spring completely, raising the pin and reaching in this way the initial position.

---

<sup>1</sup>Taxel (from tactile-pixel): Term used for a tactile element.

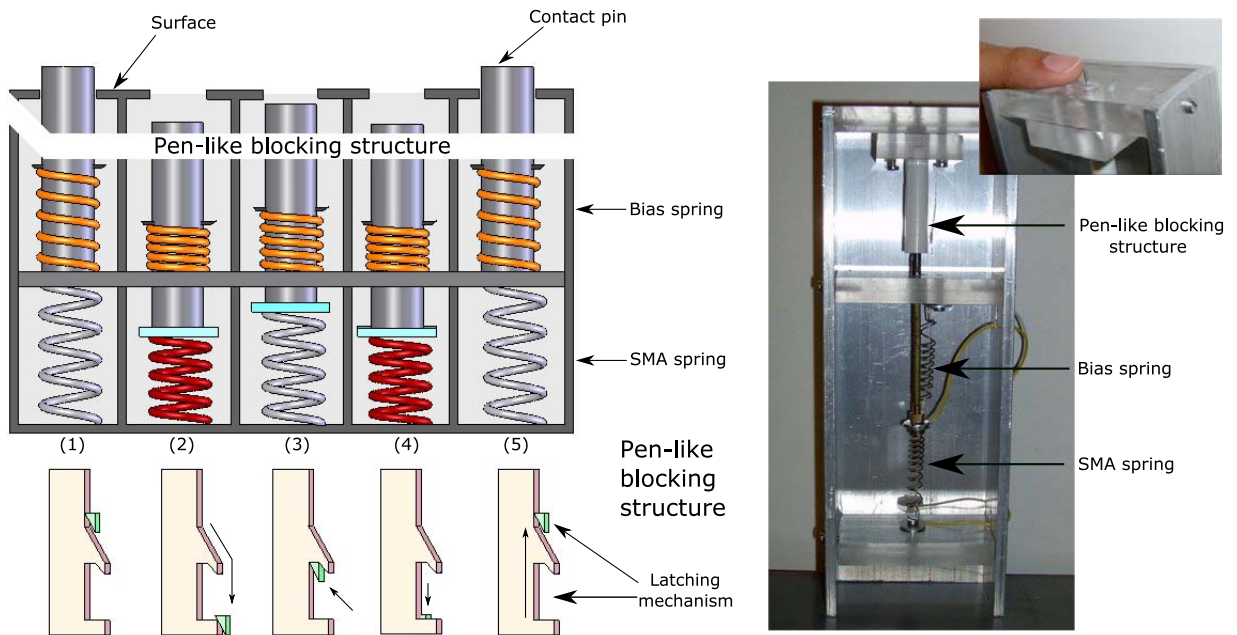


Figure 3.9: Principle and prototype of an SMA based taxel with a pen-like latching mechanism.

The main advantage of this concept is that one single SMA element is needed per actuator. A one-directional force is applied and optimized, through the pen-like bistable concept, to work as a tensile and compressive force.

A prototype was developed using this concept. The major drawback that appeared during the first tests was the frequency achieved: 0.1 Hz. The SMA needs to be heated and cooled to latch the mechanism and ensure the pin's lower position and then heated and cooled again to unlatch and raise the pin. Moreover, an additional non-negligible delay on the recovery effect of the bias spring was observed. Although the design seems attractive, the bandwidth limitation was considered enough to discard it.

### 3.2.1.2 Concept 2 - Antagonist pair and blocking structure

Further development of the pen-like concept is the actuator shown in figure 3.10. The idea consists of a pair of SMA springs configured in antagonist mode and a blocking structure [Velazquez04h]. The purpose of replacing the passive bias spring for an active SMA spring is to achieve a faster and controllable reversible movement to latch/unlatch or clamp/unclamp the blocking structure.

At the initial position (1), both SMA springs are pre-strained and in martensite phase, (2) when the SMA spring-1 is electrically heated, it recovers an austenitic compressed memorized shape that extends the SMA spring-2 and retracts the contact pin. Note that

upon this action, the blocking structure fully clamps/latches. The taxel is now in the lower position and no further energy is required until a change is necessary. (3) Similarly, to raise the pin, the SMA spring-2 is activated. Its austenite shape extends the spring-1 and unclamps/unlatches the lower blocking structure; the pin raises and clamps/latches in the upper blocking structure.

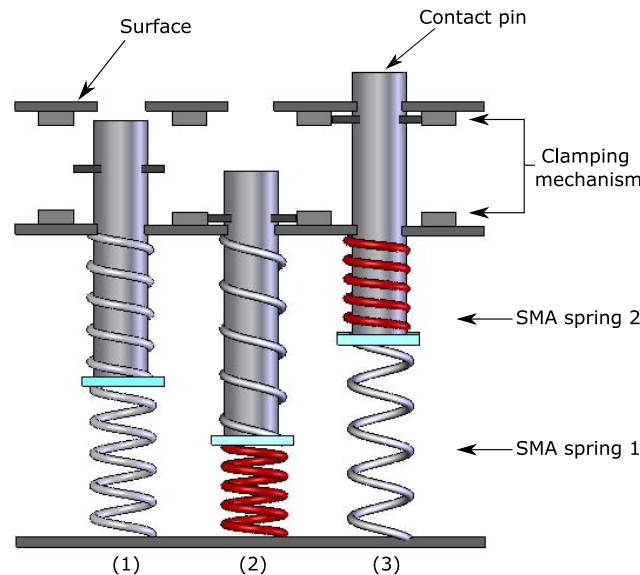


Figure 3.10: Principle of taxel based on an SMA antagonist arrangement and a clamping/latching mechanism.

Latching/clamping structures envisaged included rigid beams, magnets [Velazquez04h] and flexible structures [Hafez04].

If we consider that an external disturbance is applied to the actuator during the process of surface exploration with the fingertips, then the blocking structure has to be able to withstand the magnitude of this force. As aforementioned, a 50 to 100 mN force is considered to be applied during a normal haptic exploration. Consequently, the blocking structure has to ensure the upper position at least within this range.

However, an excess in this axial force will bring the binary system to a critical value in which bi-stability will no longer be ensured. This means that an intentionally violent touch, or external forces beyond a certain magnitude, will inevitably unlatch/unclamp the blocking mechanism. In this case, blocking mechanisms result completely useless.

To overcome this problem, let us formulate the following hypothesis:

**Hypothesis** - It is possible to configure the SMA antagonist arrangement with a pre-strained stable equilibrium in order to (1) ensure an acceptable bi-stability and (2) withstand normal haptic exploration contact forces without any blocking structure.

### 3.2.1.3 Concept 3 - Antagonist pair with no blocking structure

To validate this hypothesis, let us propose an actuator simply consisting of a pair of SMA springs configured in antagonist mode [Velazquez05d]. The operating principle is shown in figure 3.11.

At the initial position (1), the taxel's contact pin is raised. Both SMA springs are pre-stained and in martensite phase, (2) when the SMA spring-1 is electrically heated, it recovers an austenitic compressed memorized shape that extends the SMA spring-2 and retracts the contact pin. The taxel is now in the lower position. (3) When the electrical current is disconnected, the temperature of the spring-1 starts to decrease and so its rigidity. In consequence, the contact pin tends to rise. However, it does not return to the initial position (pin raised); the lower position is still ensured. (4) To raise the pin again, the SMA spring-2 is activated. Upon cooling, the initial position will be reached.

Based on the analysis presented in section 3.1.3, it can be considered that the actuator's equilibrium point is located in (1) *C*, (2) *B*, (3) *D* and (4) *A*.

Consider now the case when the surface is explored with the fingertips; (5) as seen in (1), the taxel's default configuration is when both SMA springs are in martensite phase and the contact pin is raised. This configuration must be able to withstand at least normal haptic exploration contact forces (100 mN). (6) If the user applies a higher force (an intentionally violent touch), the contact pin will be retracted to surface level. (7) When the force is released, the contact pin naturally rises to recover its original configuration.

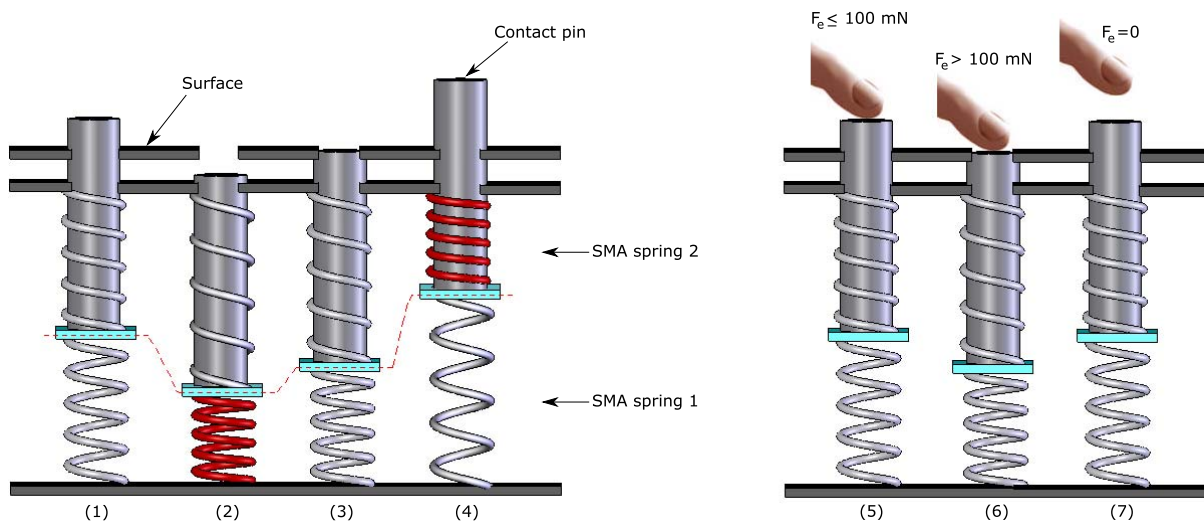


Figure 3.11: Optimized principle of the SMA taxel.

Let us analyze the case when an external force is applied to the system. Two situations can be predicted:

1. The force is applied during the austenitic state of the upper spring (Figure 3.12(a)). The superelasticity property appears in the active spring while the passive one follows an unloading behavior. Note that a 320 mN force is needed to reach point  $\delta_0$  (Figure 3.12(b)). When the external force is released, the active spring unloads by following its austenite characteristic as the passive one mechanically loads (Figure 3.12(c)).

Figure 3.12(d) shows this thermomechanical path in the load-deflection-temperature space. Note that the initial position  $A$  is recovered in this case even though a non-reversible path is observed between  $A$ - $\delta_0$ .

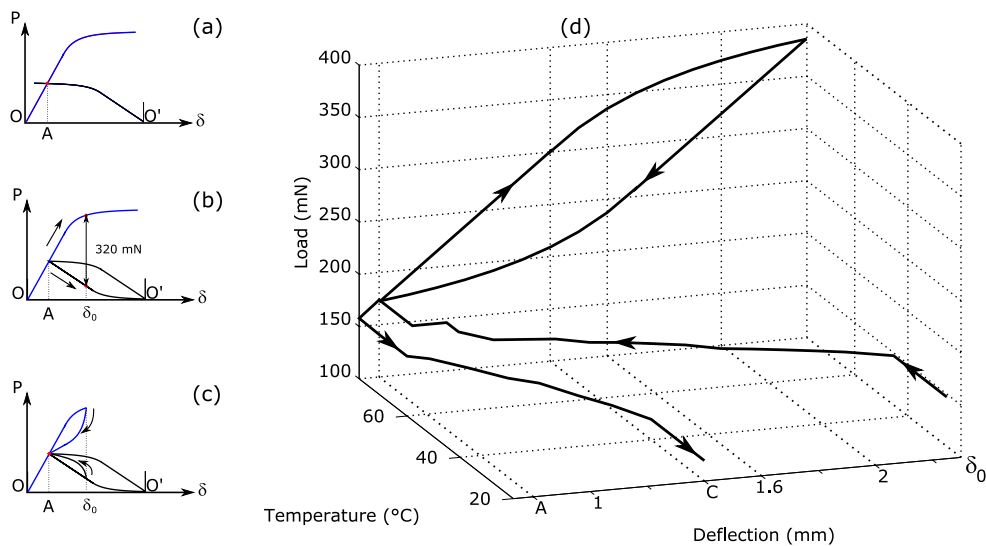


Figure 3.12: The upper spring's behavior face to an external force during its austenitic state.

2. The force is applied during the martensitic state of the upper spring (Figure 3.13(a)). Note that while the upper spring follows a loading behavior, the passive one follows an unloading path. A 120 mN force is required in this case to reach point  $\delta_0$  (Figure 3.13(b)). When the external force is released, both springs mechanically unload by following their martensite characteristic (Figure 3.13(c)). Note that point  $C$  is not recovered.

Figure 3.13(d) shows the load-deflection path performed for martensitic temperatures. Note that a new point  $E$  appears after the force is released. For subsequent cycles, a 60 mN force is required to reach  $\delta_0$  from point  $E$ .

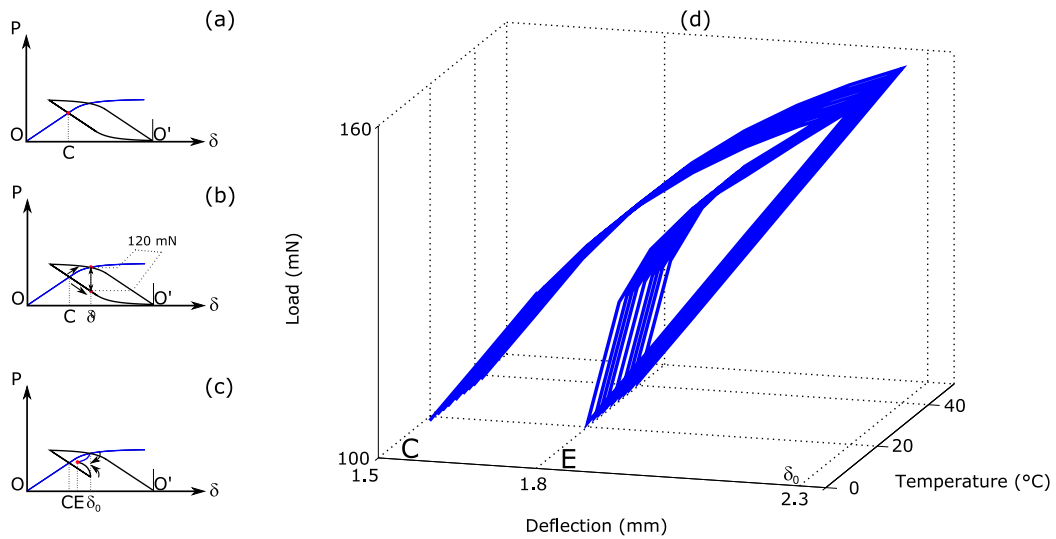


Figure 3.13: The upper spring's behavior face to an external force: martensitic case.

In conclusion, pre-strain  $\delta_0$  must be carefully determined in order to calibrate the system and ensure that  $B$  and  $D$  positions will provide a lower taxel position while  $A$ ,  $C$  and  $E$  will provide an upper one. Pre-straining both springs 2.3 mm at installation satisfies these requirements.

Note that the appropriate pre-straining not only ensures an acceptable bistability for touch applications but also reduces the control problem to a binary operation: taxel totally raised (position  $A$ ) or totally retracted (position  $B$ ). Therefore, each spring may take either the austenite (high temperature and contracted) state or the martensite (low temperature and stretched) state, and nothing in between.

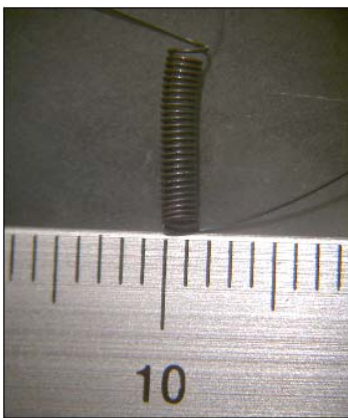


### 3.3 Prototype and performance

Figure 3.14 shows the taxel's implementation: Figure 3.14(a) shows the NiTi helical spring. It consists of 25 coils: 12 active coils for the upper actuator, 12 active coils for the lower one and an extra dead coil for fixing the spring to a movable central mass. The antagonist arrangement is achieved by grounding the SMA spring at the middle so that electrical current can flow independently in the upper or lower half.

Figure 3.14(b) shows the mechanical structures that compose the taxel: two 1.5 mm diameter steel supports for the central mass and a 0.5 mm diameter steel wire for the contact pin. Figure 3.14(c) shows the final assembly: The pin is thermo-electrically insulated and inserted into the SMA spring. Both are fixed using the miniature structures in figure 3.14(b) and an epoxy adhesive.

The prototype taxel is shown in figures 3.14(d) and (e). This miniature actuator is 1.5 mm diameter, 45 mm length and weights 150 mg. Its laboratory cost is 2 € [Velazquez05d].



(a)



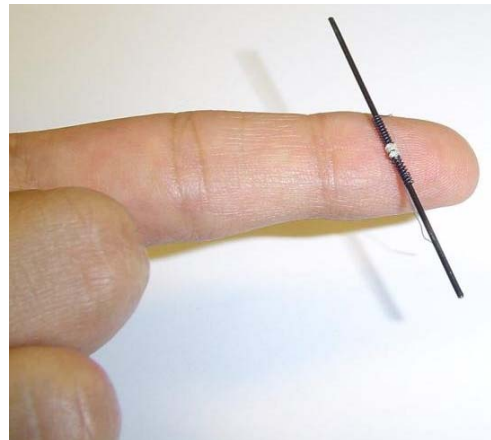
(b)



(c)



(d)



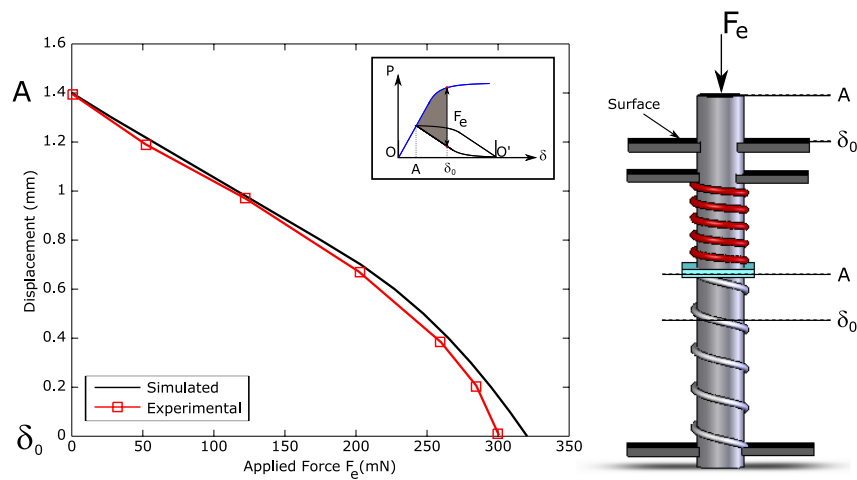
(e)

Figure 3.14: Miniature SMA based actuator: implementation and prototype.

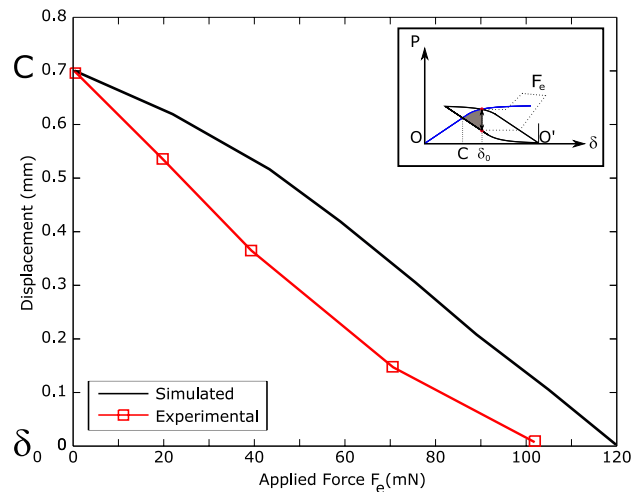
Figure 3.15 compares the simulated and experimental relationships between force applied and taxel displacement during the process of surface exploration with the fingertips.

The theoretical modeling and experimentation show that the force response of the SMA antagonistic taxel when an external force  $F_e$  is applied is actually defined by the difference between the curves characterizing the mechanical behavior of the springs.

Note that, while a 300 mN force is needed to retract the taxel to surface level during the austenitic state of the upper spring (Figure 3.15(a)), a 102 mN force is needed during its martensitic state (Figure 3.15(b)).



(a)



(b)

Figure 3.15: Effect of external force on the taxel's displacement: upper spring in (a) austenite and (b) martensite state.

The sequence in figure 3.16 demonstrates the taxel's main concept and performance. It shows a set of eight taxels and their behavior in response to an external force. (1) The taxels' default configuration is pin raised and the antagonistic pair of SMAs in martensite phase. During exploration, (2) the taxels withstand normal contact forces but (3) higher ones may retract the pins to surface level. (4) When the force is released, the contact pins naturally rise to recover the original configuration. A broken line is drawn to better appreciate the position of the central mass.

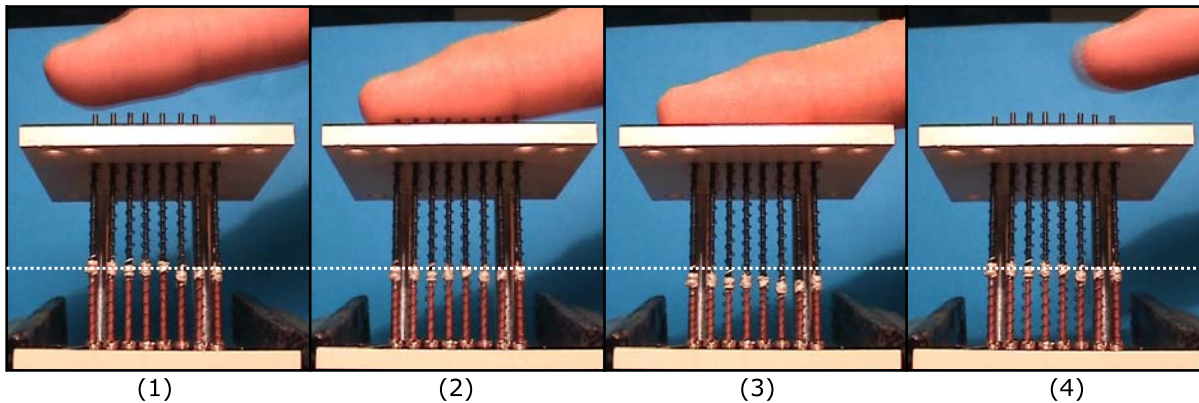


Figure 3.16: The taxel's performance: bistable concept with no blocking structures.

A service life of at least  $10^5$  cycles can be expected according to the fatigue analysis based on the spring's deflection value presented in chapter 2, section "Formulation of fatigue life".

To evaluate the taxel's bandwidth performance, an experimental setup was implemented as shown in figure 3.17(a). Note that one of the constraints of the antagonist actuator is that at no time should both SMA springs be driving the system. For this purpose, an inverse switch was used to route the input and alternatively activate springs 1 and 2.

Plots 3.17(a.1) and (a.2) show the position tracking response of the taxel, under no-load conditions, to 0.27 and 0.37 Hz square wave power signals, respectively. Note that, as frequency increases, the actuator's response becomes problematic: the cooling rate decreases significantly enough to produce no effect on both SMA springs. Soon, the actuator goes into saturation.

As table 2.5 in chapter 2 suggests, it is always possible to apply more electrical current to produce a faster response, but cooling is due exclusively to convective heat transfer to the surrounding medium. This limitation requires the use of different strategies for increasing the cooling rate.

Several approaches [Wellman97], [Russell95b] have suggested the use of water and heat sinking mechanisms as coolants. It has to be recognized that these methods have shown the most promising results. However, an actuator immersed in constant recirculating water and additional mechanisms complicate the actuator's design and hardly imply a fully portable, lightweight and compact tactile display.

To keep the actuator simple, forced-air convection provided by a simple inexpensive computer mini-fan was used as cooling system (Figure 3.17(b)). Plots 3.17(b.1), (b.2) and (b.3) show the modified experimental set-up and tracking response of the antagonist actuator, under no load conditions, to 0.5, 1 and 1.5 Hz square power signals, respectively.

Note that the actuator's bandwidth increases up to 1.5 Hz without saturation using forced-air convection. However, power demand increases as well in order to accelerate the heating rate and ensure the taxel's complete stroke (distance  $A-B$  in figure 3.17(a)).

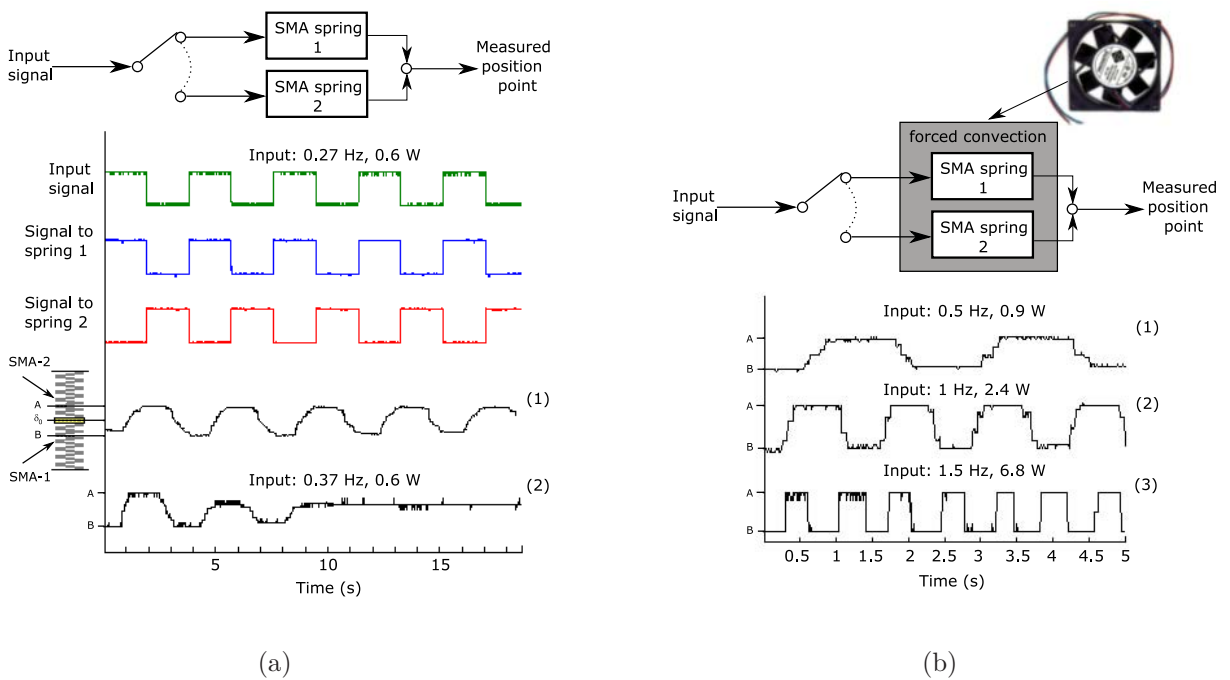


Figure 3.17: (a) The antagonist controller and position tracking responses of the actuator to 0.27 and 0.37 Hz square power signals. (b) Tracking responses to 0.5, 1 and 1.5 Hz square power signals under forced-air convection conditions.

## 3.4 Conclusion

This chapter has presented an SMA based electrically driven miniature actuator intended for touch stimulation. This actuator uses an antagonist arranged pair of SMA NiTi helical springs whose thermomechanical properties have been used to characterize its antagonist type behavior and performance.

The taxel of 1.5 mm diameter, 45 mm length, 150 mg mass and 3 mm total excursion is capable of producing an effective 0.7 mm skin deformation with a 300 mN pull force at 1.5 Hz bandwidth.

Main advantages of this concept of actuator are:

- The simplicity of design and ease of implementation.
- The simplicity of a binary control: taxel totally raised or totally retracted.
- A symmetric dynamic behavior as both SMA springs are identical.
- The actuator needs power only when changing from one state to the other and no miniature mechanical latching/clamping structures are needed to keep the taxel active. Lower and upper positions are ensured by the mechanical characteristics of the SMA springs. The active position is always ensured by at least a 60 mN pull force.
- Its overall performance: The actuator is capable of developing a 300 mN pull force at 1.5 Hz bandwidth when using forced-air convection provided by a simple and inexpensive mini-fan. A service life of more than  $10^5$  cycles can be expected.
- Its low cost (2 €).

Next chapter will focus on its application to the design and development of a high-resolution, lightweight, low-cost and portable tactile display.

---

## Chapter 4

# A Low-Cost Highly-Portable Tactile Display with SMAs

---

This chapter presents the design and implementation of a novel tactile display device that exhibits some advantageous features for the blind: low-cost, lightweight, compactness and high portability. The prototype consists of an 8 x 8 array of tactile pins actuated by SMAs with 2.6 mm spatial resolution (Braille-like). Unlike existing devices, the full display weights only 200 g and its compact dimensions make it easily carried by the user. A technical description of the tactile display, electronic drive and control method is presented in detail.

## 4.1 Tactile display

### 4.1.1 Design and implementation

A conceptual representation of the tactile display is proposed in figure 4.1. A first prototype of 8 x 8 tactile elements was envisaged. It consists of 3 plates that assemble the 64 taxels. The taxels are to be independently addressed, electrically heated and cooled using forced-air convection provided by a mini-fan placed right next to the plates [Velazquez05c].

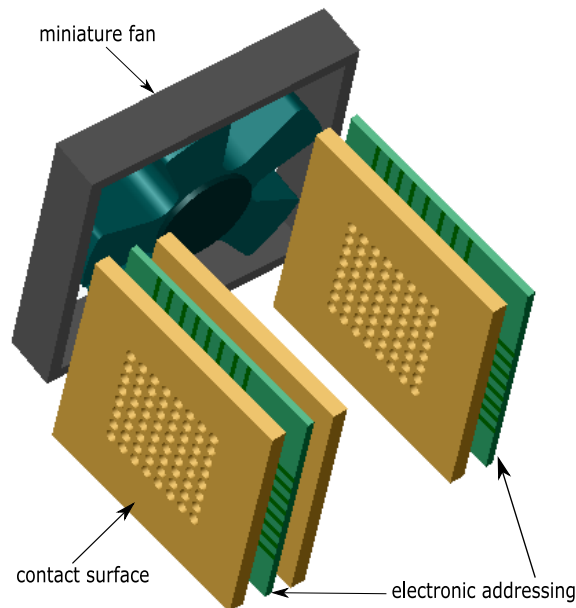


Figure 4.1: Conceptual representation of a 8 x 8 SMA based tactile display.

The three plates are made from PVC. Precise water-jet cutting of the pin holes allows a perfect vertical alignment and assembling between them. Figure 4.2 shows the plate with a dot spacing cut of 2.6 mm, within Braille standard. Note that 64 SMA based taxels can be integrated in a space equivalent to the surface of a one-euro coin.

Figure 4.3(a) shows the structure of the tactile display. Recall from chapter 3 that each taxel consists of a one-way effect NiTi SMA helical spring and a thermo-electrically insulated metallic pin, both fixed by a central mass. To operate in symmetric antagonist mode, the SMA spring has to be grounded in the central mass (its middle), so that electrical current can flow independently in the upper or lower half.

However, actually grounding the SMA in the central mass complicates the whole assembling process: the space between taxels is too small to install bendable wires and as both wire and central mass are movable, the risk of jamming between taxels is high. To simplify the assembling, the SMA's ground wire was installed at the bottom of the taxel. As the pin is metallic, this point can be fixed to be electrically the same as the central mass.

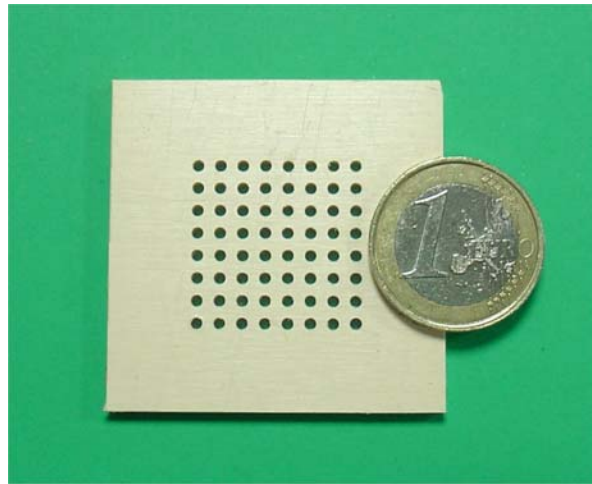
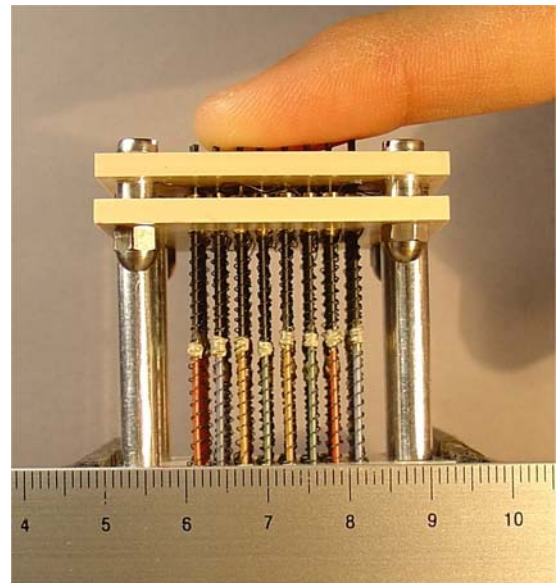
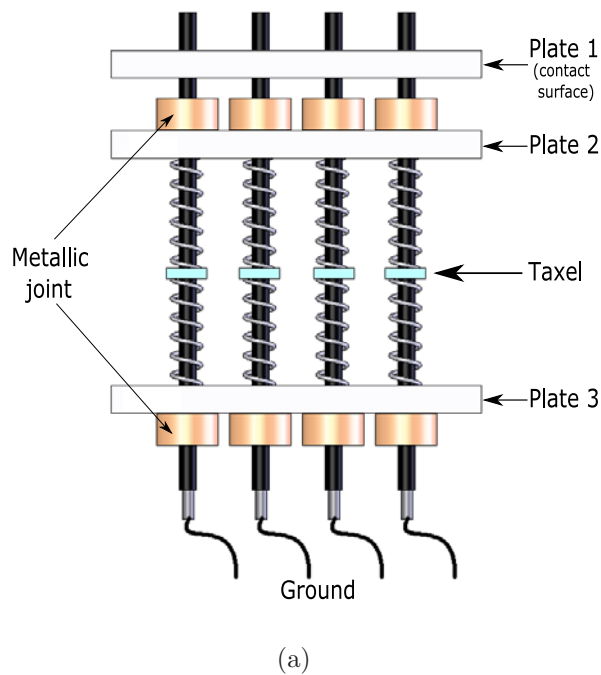


Figure 4.2: Water-jet cut PVC structure.

Figure 4.3(b) shows one row of 8 actuators. The desired Braille-like pin spacing is easily achieved using the proposed micro-actuator. Note that the entire taxel is still tightly packed in its original 1.5 mm diameter.



(a)

(b)

Figure 4.3: (a) Structure of the tactile display and (b) configuration of one row of taxels.

Both ends of the taxel's SMA spring are fixed to the plates using the metallic joint in figure 4.4. This joint is a -3 in 1- mechanical structure: (1) it fastens the SMA spring to the plate, (2) it electrically connects the taxel for its electronic drive and (3) it provides precise pin guidance through the plates' pin holes minimizing the friction level. Note that this joint avoids the widely known welding problem of SMAs and eases the taxel



replacement task if necessary: the top and bottom joints are simply unscrewed from the plates and the taxel can then be lifted out.

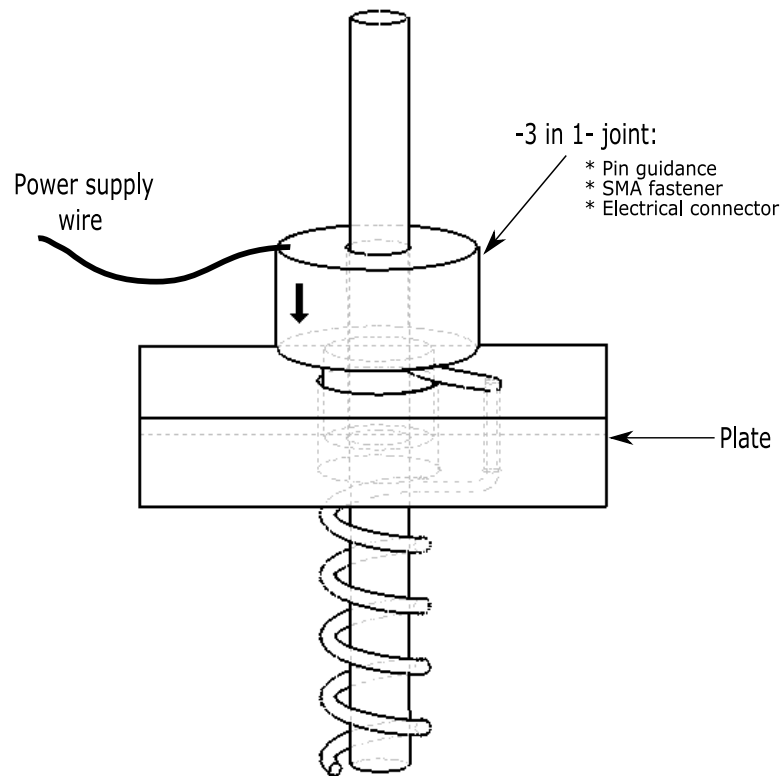
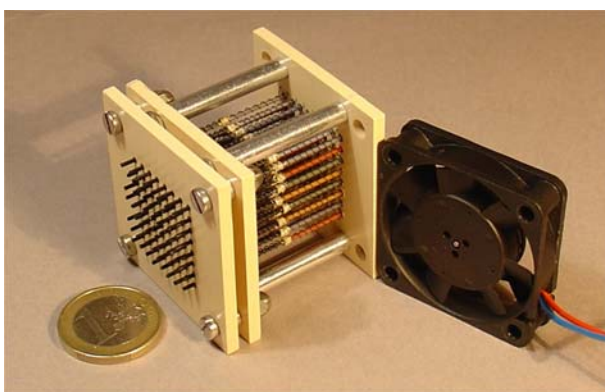
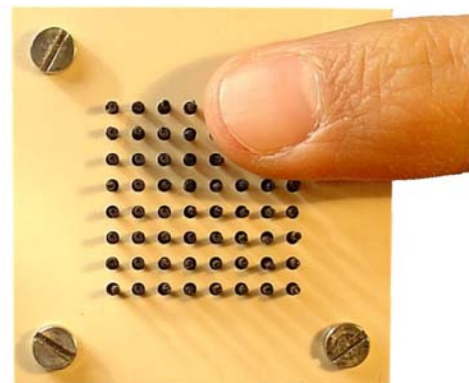


Figure 4.4: The actuator's electromechanical connector.

Figure 4.5(a) shows the taxel array fully assembled. The effective contact area is  $4.32 \text{ cm}^2$  in a  $2.08 \text{ cm} \times 2.08 \text{ cm}$  area, which can be conveniently covered with 2 fingertips (Figure 4.5(b)). Note that the design offers high spatial resolution in addition to being robust, maintainable and simple to fabricate.



(a)



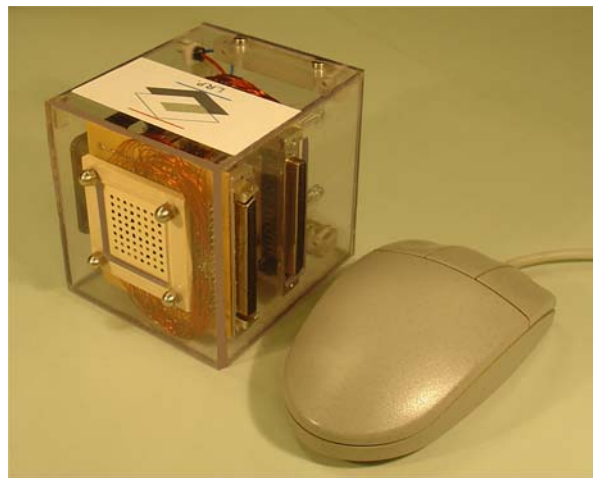
(b)

Figure 4.5: (a) High-density compact actuator array and (b) contact area.

### 4.1.2 Prototype

Figure 4.6(a) shows the final tactile display in a plexiglass enclosure. Summarizing its key features, this first prototype consists of a 64 element array spaced 2.6 mm apart that vertically actuates SMA based miniature actuators of 1.5 mm diameter to a height range of 1.4 mm with a pull force of 300 mN up to a 1.5 Hz bandwidth.

The full display weights 200 g and its compact dimensions (a cube of 8 cm side-length) make it easily carried by the user (Figure 4.6(b)).



(a)



(b)

Figure 4.6: Low-cost highly-portable tactile display with SMAs.

Its laboratory cost is only 200 € [Velazquez05c] and with industrial mass production, a much lower price can definitively be expected. A wide range of applications can then be envisaged: from an affordable-to-everyone tactile display to a disposable device.

Furthermore, its design is easily scalable with respect to the number of taxels while still being price attractive.

Figure 4.7 shows different examples of 2D tactile shapes displayed using this prototype.

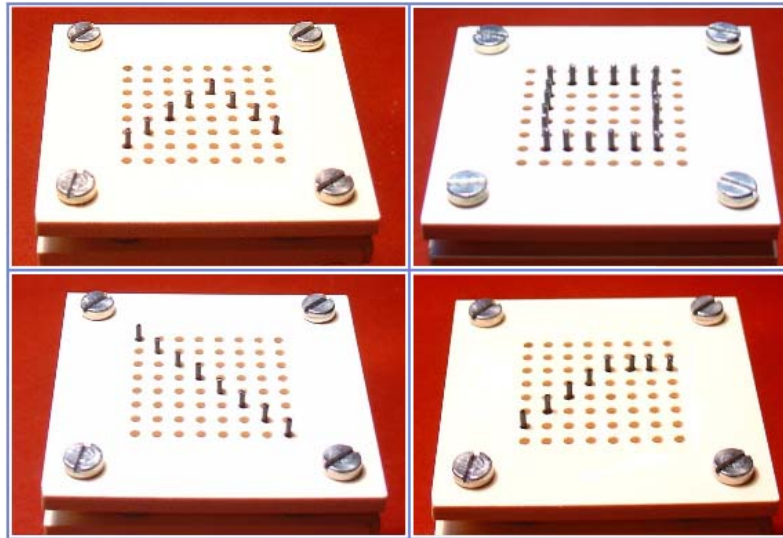


Figure 4.7: Examples of 2D shapes displayed using the tactile device.

## 4.2 Drive system

Figure 4.8 shows a schematic representation of the electronic system used to drive the tactile display [Velazquez06g]. The system consists of a user friendly software interface that generates tactile data (such as shapes, pictures, patterns, sequences, etc.). Using RS232 protocol, the computer transmits this information to an electronic module, where a controller interprets the command strings and sets the position (up or down) of each taxel of the display.

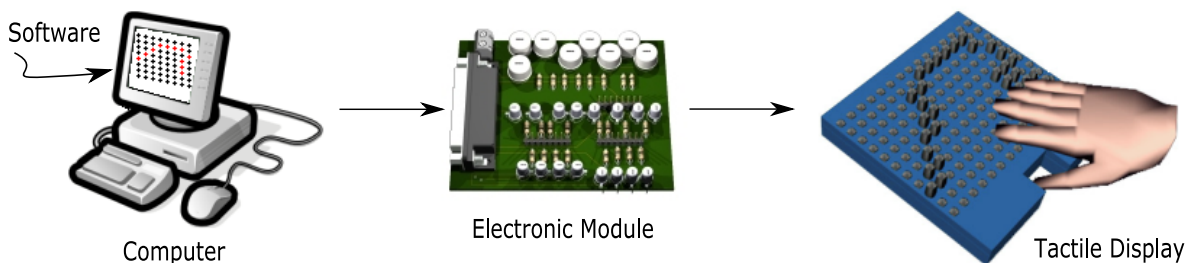


Figure 4.8: Drive components of the tactile display.

Both electronic drive and software are presented in the following subsections.

### 4.2.1 Electronic drive

Since the tactile display consists of 64 taxels, 128 SMA half-springs are needed to be controlled independently. Given the great number of actuators, a traditional electronic architecture, like the one in figure 4.9, can be proposed.

This architecture consists of a microcontroller along with multiplexers (Mux) to generate more digital outputs and demultiplexers (Dmux) to address them. For example, the architecture in figure 4.9 can be simply implemented with common off-the-shelf chips: any 8-bit 3-port microcontroller and a 74HC154 decoder can drive sixteen 8-bit 74HC374 multiplexers for a total of 128 bits. After power stage, the 128 SMA half-springs can be independently addressed.

An important issue that must be addressed in electronic control systems for matrix displays is the scalability problem: A typical  $N \times N$  matrix in which each element is controlled independently requires an amount of  $N^2$  control circuitry. In the case of the tactile display, a burdensome control scheme of  $2N^2$  is required to activate the 64 antagonist taxels independently.

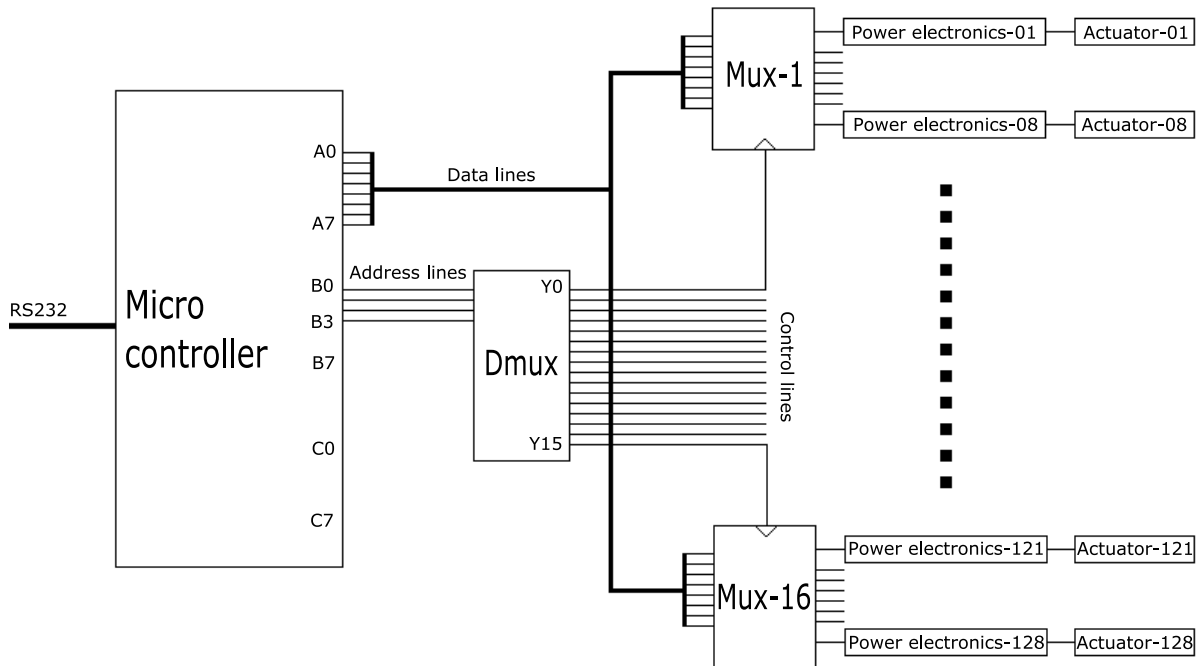
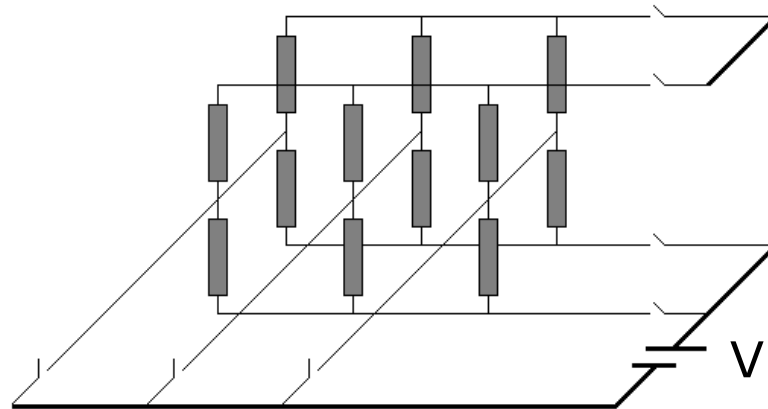


Figure 4.9:  $2N^2$  controller's architecture.

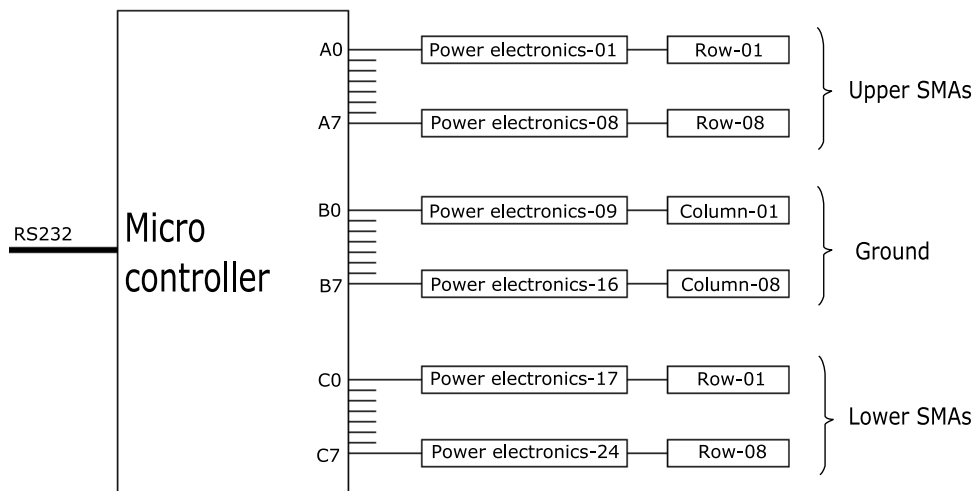
These kind of controllers work perfectly well if  $N$  is small. However, as the size of the matrix increases, the number of control elements quickly becomes very large [Nakatani03].

A more convenient and cost-effective method of implementing an electronic drive for large-scale matrix displays is the *crossbar method*.

Figure 4.10(a) shows the crossbar method adopted to drive the tactile display. Closing the switches at the appropriate crosspoint actuates the desired SMA half-spring. Figure 4.10(b) shows the controller's crossbar-based architecture still using the same 8-bit 3-port microcontroller. Note that all the output expansion circuitry is no longer needed and that the control scheme reduces from  $2N^2$  to  $3N$  [Velazquez06g].



(a)



(b)

Figure 4.10: (a)  $3N$  crossbar matrix switch control method: a half SMA spring is actuated by placing its row to  $V$  and the corresponding column to  $GND$ . (b) The controller's crossbar-based architecture.

Figure 4.11 compares the scalability of both traditional and crossbar controllers for higher-density displays. Note the outstanding scalability capabilities of the crossbar architecture. For example, a  $20 \times 20$  matrix would require 800 control elements under the traditional architecture while only 60 using the crossbar method.

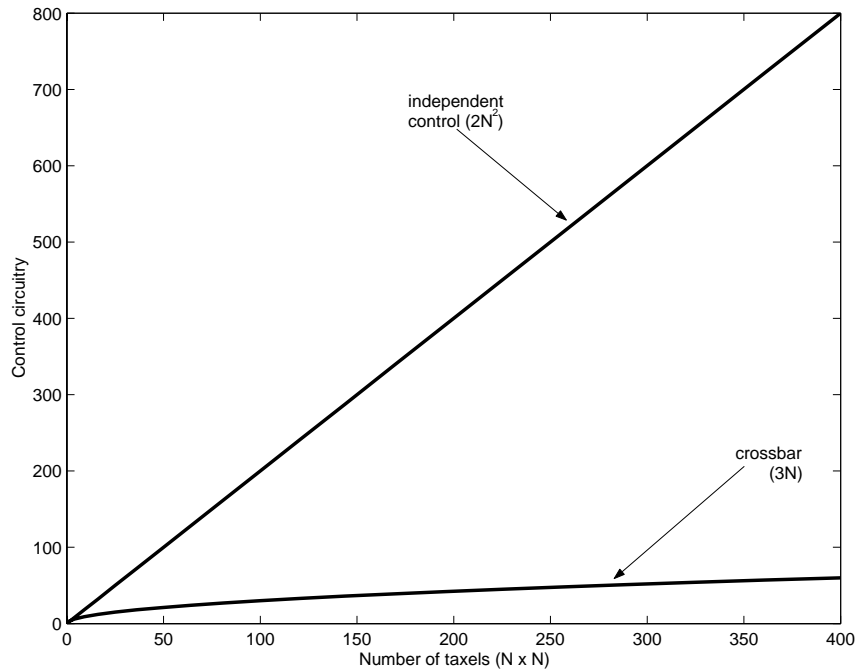


Figure 4.11: Scalability of the electronic controllers: crossbar vs traditional (independent control) architecture.

#### 4.2.1.1 Power electronics

Figure 4.12(a) shows the antagonist actuator crossbar circuit model while figures 4.12(b) and 4.12(c) translate it into circuits.

Figure 4.12(b) shows an early version of the power stage. Note that only three electrical resistances and three NPN/PNP bipolar transistors are used to drive a row of eight taxels (16 SMA springs) from a digital input. The values of  $R_1$  and  $R_2$  were fixed to limit the output current to 500 mA. Its main drawback is that the whole row of taxels is limited to 500 mA. Thus, if  $n$  taxels in a row are set at the same time, each one would be heated with  $500/n$  mA.

In order to provide 500 mA to each taxel, it is necessary to control the row's current according to the number of taxels set. This cannot be achieved using standard bipolar transistors but it is possible with MosFet technology. Figure 4.12(c) shows the modified version of the power stage using a power MosFet transistor.

Note that both transistor arrays are simple, fast and inexpensive to implement. They also intend to produce compact electronic boards so that they could be embedded in the same tactile display structure.

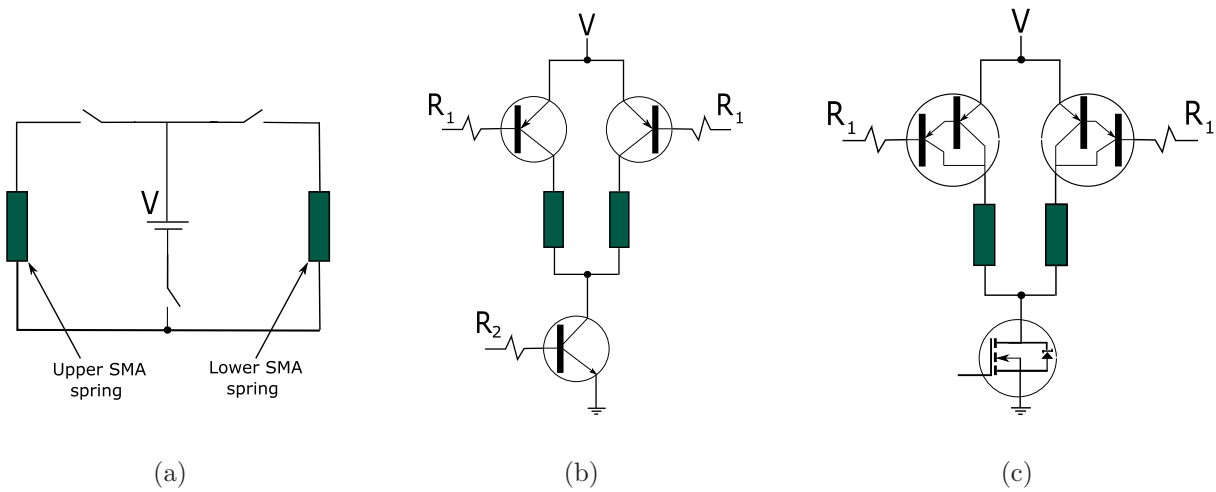


Figure 4.12: (a) The actuator's crossbar-driven circuit model and (b) bipolar, (c) MosFet transistor arrays proposed to drive the taxel from a TTL input.

#### 4.2.1.2 Power supply

A regular PC linear power supply (4 A,  $\pm 5$ ,  $\pm 12$  V) was temporarily used to drive the whole tactile system. Both tactile display and electronics use +5 V while the mini-fan uses +12 V. Future work must concern the design and implementation of an on-board lightweight power supply.

### 4.2.2 Crossbar circuit analysis and control method

In general, crossbar-based architectures offer several advantages for electronic controllers such as simplicity, compactness, programmability (less burdensome and faster executing driving programs), scalability and the potential for low-cost fabrication [Ziegler02].

However, there are also two main drawbacks associated with most crossbars systems: the mirror effect and parasitics signal losses along the structure. Furthermore, self-assembled crossbars may also have a high propensity for defects.

Before focusing on the mirror effect, it might be helpful for those implementing a crossbar structure to briefly discuss the second drawback: Since the elements are not addressed individually, the current may have various additional paths to flow aside from the branch of the circuit containing the element being addressed. Figure 4.13(a) shows this concept in the tactile display. Recall that the SMA electrically behaves as a resistance. So, current flowing through the desired SMA also finds a series of nodes of parasitic parallel resistors through which it splits. The consequence is that the desired SMA will receive only a part of the source current and it would take more time to actuate it.

The use of diodes or other two-terminal devices can improve the crossbar behavior. Figure 4.13(b) shows the SMA array together with diodes to restrict the flow path. Note that the current has now only one path to travel to ground.

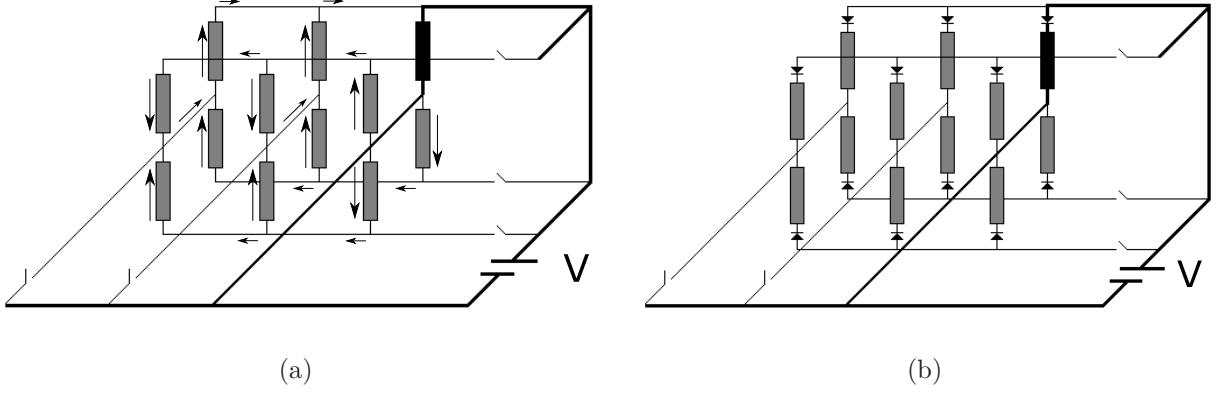


Figure 4.13: (a) Parasitic parallel resistors in the tactile display and (b) SMA-diode array implemented to eliminate parasitic resistors and current losses.

Concerning the mirror effect, the control strategy must be formulated accordingly. To state the problem mathematically, let us consider an  $N \times N$  matrix driven by three  $n$ -bit control signals:  $u$ ,  $b$  and  $g$ .

The upper SMA springs rows are denoted as:

$$\vec{u} = (u_1, u_2, \dots, u_n)$$

The lower SMA springs rows are denoted as:

$$\vec{b} = (b_1, b_2, \dots, b_n)$$

The ground rows are denoted as:

$$\vec{g} = (g_1, g_2, \dots, g_n)$$

The components  $u_i$ ,  $b_i$  and  $g_i$  of these vectors are constrained to be binary (0,1) and describe the switch state: open and closed, respectively. According to the crossbar principle in figure 4.14, the products  $\mathbf{U}$  and  $\mathbf{B}$ :

$$\mathbf{U} = \vec{u}^T \vec{g} = \begin{pmatrix} u_1 g_1 & u_1 g_2 & \dots & u_1 g_n \\ u_2 g_1 & u_2 g_2 & \dots & u_2 g_n \\ \vdots & \vdots & \ddots & \vdots \\ u_n g_1 & u_n g_2 & \dots & u_n g_n \end{pmatrix} \quad \text{and} \quad \mathbf{B} = \vec{b}^T \vec{g} = \begin{pmatrix} b_1 g_1 & b_1 g_2 & \dots & b_1 g_n \\ b_2 g_1 & b_2 g_2 & \dots & b_2 g_n \\ \vdots & \vdots & \ddots & \vdots \\ b_n g_1 & b_n g_2 & \dots & b_n g_n \end{pmatrix}$$

represent which SMA springs are actuated by a given control signal pair.



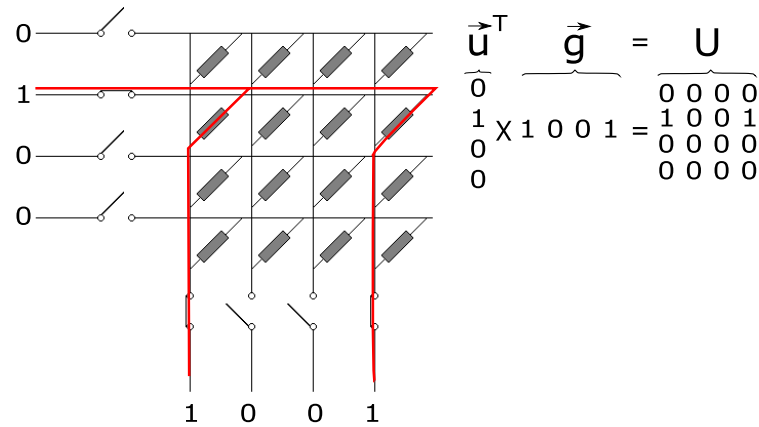


Figure 4.14: Crossbar correspondence with vectors and matrices.

However, the crossbar operation is not that simple: the  $u_i g_j$  or  $b_i g_j$  pair can match other  $u_k g_m$ ,  $b_k g_m$  pairs and produce a mirror effect.

To illustrate this concept, let us consider the examples in figure 4.15. Figure 4.15(a) shows the simultaneous activation of  $u_1 g_1$  and  $u_2 g_3$ . Note that closing the corresponding switches also activates  $u_2 g_1$  and  $u_1 g_3$ . Similarly, the activation of  $u_1 g_4$  and  $u_4 g_1$  triggers  $u_1 g_1$  and  $u_4 g_4$  (Figure 4.15(b)) and setting  $u_1 g_1$ ,  $u_2 g_2$ ,  $u_3 g_3$  and  $u_4 g_4$  in figure 4.15(c) creates 12 mirror pairs that switch the entire matrix on. Less evident undesired crosspoints can appear once both  $\mathbf{U}$  and  $\mathbf{B}$  matrices interact. Figure 4.15(d) shows that triggering simultaneously  $u_1 g_1$  and  $b_1 g_2$  also triggers  $u_1 g_2$ .

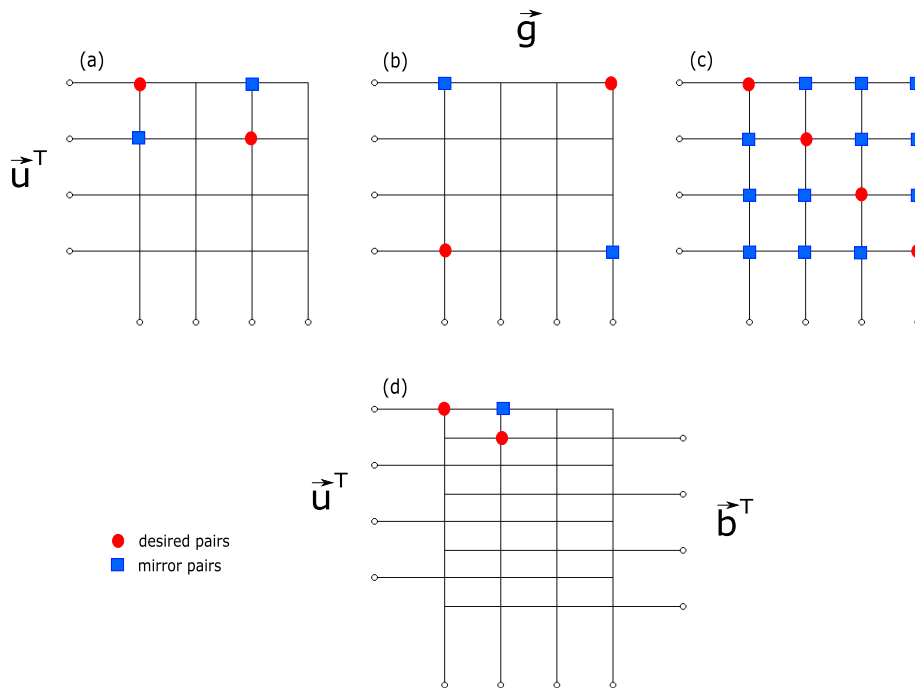


Figure 4.15: The mirror effect in the crossbar-based tactile display.

In general,  $M$  number of pair signals can create up to  $M(M - 1)$  mirror pairs. To avoid the mirror effect, each component  $u_i$ ,  $b_i$  must be matched with  $\vec{g}$  at a particular time slice.

Let us define two time vectors  $\vec{t}_u = (t_1, t_2, \dots, t_n)$  and  $\vec{t}_b = (t_{n+1}, t_{n+2}, \dots, t_{2n})$ . The new matrices subjected to a switch scheduling between rows can be defined as:

$$\mathbf{U}_t = \text{diag}(\vec{t}_u)\mathbf{U} = \begin{pmatrix} u_1g_1t_1 & u_1g_2t_1 & \dots & u_1g_nt_1 \\ u_2g_1t_2 & u_2g_2t_2 & \dots & u_2g_nt_2 \\ \vdots & \vdots & \ddots & \vdots \\ u_ng_1t_n & u_ng_2t_n & \dots & u_ng_nt_n \end{pmatrix} \quad \text{and}$$

$$\mathbf{B}_t = \text{diag}(\vec{t}_b)\mathbf{B} = \begin{pmatrix} b_1g_1t_{n+1} & b_1g_2t_{n+1} & \dots & b_1g_nt_{n+1} \\ b_2g_1t_{n+2} & b_2g_2t_{n+2} & \dots & b_2g_nt_{n+2} \\ \vdots & \vdots & \ddots & \vdots \\ b_ng_1t_{2n} & b_ng_2t_{2n} & \dots & b_ng_nt_{2n} \end{pmatrix}$$

Thus, the total time  $t_t$  to display a shape is defined by:

$$t_t = t_1u_1 + t_2u_2 + \dots + t_nu_n + t_{n+1}b_1 + t_{n+2}b_2 + \dots + t_{2n}b_n$$

Let us consider the 8 x 8 tactile display described so far. Recall from chapter 2 that an SMA is triggered once it reaches its  $A_f$  temperature. In the same chapter, it has been modeled and experimentally demonstrated for the SMA spring used in the display that  $A_f$  can be reached in 0.26 s using a 500 mA heating current (Table 2.5). However, once in  $A_f$ , the SMA does not contract instantaneously to its memorized shape. This effect together with the opposite force that implies the antagonist arrangement make that the taxel takes about 1 s to achieve either of its stable positions.

Using the switch scheduling method that iterates over each and every row of the matrix would take up to 16 s to display a shape.

We propose a simple crossbar scheduling optimized algorithm that minimizes  $t_t$  by maximizing the number of SMAs springs actuated at a time.

Its operating principle is as follows: (1) The algorithm first scans the matrix columns for set pairs, (2) it detects and matches identical columns in the matrix, (3) the remaining unmatched pairs are matched by rows. (4) Finally, it assigns a scheduling time slice for activation to each match.

Two representative examples are presented to illustrate the algorithm's optimization.

Example 1 represents a circle. The algorithm first scans for set elements in the matrix, then it detects and matches the columns that have exactly the same set elements. As no element remains unmatched, the algorithm establishes a schedule between the matched pairs. As seen, the algorithm’s optimization is able to display the circle in 4 switching states (4 s) while the conventional one-by-one row switching method would take 8 (8 s). Note that the mirror effect never appears during the switching process.

Example-1	Set pairs	Column match	Row match
$U = \begin{pmatrix} 0 & 0 & 0 & 1 & 1 & 0 & 0 & 0 \\ 0 & 0 & 1 & 0 & 0 & 1 & 0 & 0 \\ 0 & 1 & 0 & 0 & 0 & 0 & 1 & 0 \\ 1 & 0 & 0 & 0 & 0 & 0 & 0 & 1 \\ 1 & 0 & 0 & 0 & 0 & 0 & 0 & 1 \\ 0 & 1 & 0 & 0 & 0 & 0 & 1 & 0 \\ 0 & 0 & 1 & 0 & 0 & 1 & 0 & 0 \\ 0 & 0 & 0 & 1 & 1 & 0 & 0 & 0 \end{pmatrix}$	$g_1 \rightarrow U_4, U_5$ $g_2 \rightarrow U_3, U_6$ $g_3 \rightarrow U_2, U_7$ $g_4 \rightarrow U_1, U_8$ $g_5 \rightarrow U_1, U_8$ $g_6 \rightarrow U_2, U_7$ $g_7 \rightarrow U_3, U_6$ $g_8 \rightarrow U_4, U_5$	$g_1, g_8 \rightarrow U_4, U_5$ $g_2, g_7 \rightarrow U_3, U_6$ $g_3, g_6 \rightarrow U_2, U_7$ $g_4, g_5 \rightarrow U_1, U_8$	No matches found

Schedule	Final sequence
<ol style="list-style-type: none"> <li><b>1</b> <math>g_1, g_8 \rightarrow U_4, U_5</math></li> <li><b>2</b> <math>g_2, g_7 \rightarrow U_3, U_6</math></li> <li><b>3</b> <math>g_3, g_6 \rightarrow U_2, U_7</math></li> <li><b>4</b> <math>g_4, g_5 \rightarrow U_1, U_8</math></li> </ol>	$U_t = \begin{pmatrix} 0 & 0 & 0 & 4 & 4 & 0 & 0 & 0 \\ 0 & 0 & 3 & 0 & 0 & 3 & 0 & 0 \\ 0 & 2 & 0 & 0 & 0 & 0 & 2 & 0 \\ 1 & 0 & 0 & 0 & 0 & 0 & 0 & 1 \\ 1 & 0 & 0 & 0 & 0 & 0 & 0 & 1 \\ 0 & 2 & 0 & 0 & 0 & 0 & 2 & 0 \\ 0 & 0 & 3 & 0 & 0 & 3 & 0 & 0 \\ 0 & 0 & 0 & 4 & 4 & 0 & 0 & 0 \end{pmatrix}$

A more complex matrix to optimize is the one in the example 2. The same procedure is followed: some set elements are matched by columns, some by rows and a final schedule is established among them. Note that the algorithm is able to decompose columns into smaller columns and match them elsewhere (schedule 2). In this case, it would take 6 s to display the matrix contrary to 8 s using the traditional switching method.

Example-2	Set pairs	Column match	Row match
$U = \begin{pmatrix} 1 & 0 & 0 & 0 & 1 & 0 & 0 & 1 \\ 1 & 0 & 0 & 0 & 0 & 0 & 0 & 1 \\ 0 & 1 & 1 & 0 & 0 & 1 & 1 & 0 \\ 0 & 0 & 0 & 1 & 0 & 0 & 0 & 0 \\ 0 & 1 & 0 & 0 & 0 & 0 & 0 & 1 \\ 0 & 0 & 0 & 0 & 1 & 0 & 0 & 0 \\ 0 & 1 & 0 & 0 & 0 & 0 & 0 & 1 \\ 1 & 0 & 0 & 0 & 0 & 1 & 1 & 1 \end{pmatrix}$	$g_1 \rightarrow U_1, U_2, U_8$ $g_2 \rightarrow U_3, U_5, U_7$ $g_3 \rightarrow U_3$ $g_4 \rightarrow U_4$ $g_5 \rightarrow U_1, U_6$ $g_6 \rightarrow U_3, U_8$ $g_7 \rightarrow U_3, U_8$ $g_8 \rightarrow U_1, U_2, U_5, U_7, U_8$	$g_1, g_8 \rightarrow U_1, U_2, U_8$ $g_2, g_8 \rightarrow U_5, U_7$ $g_6, g_7 \rightarrow U_3, U_8$ $g_3, g_2 \rightarrow U_3$	$g_5 \rightarrow U_1, U_6$ $g_4 \rightarrow U_4$

Schedule	Final sequence
<b>1</b> $g_1, g_8 \rightarrow U_1, U_2, U_8$ <b>2</b> $g_2, g_8 \rightarrow U_5, U_7$ <b>3</b> $g_6, g_7 \rightarrow U_3, U_8$ <b>4</b> $g_3, g_2 \rightarrow U_3$ <b>5</b> $g_5 \rightarrow U_1, U_6$ <b>6</b> $g_4 \rightarrow U_4$	$U_t = \begin{pmatrix} \mathbf{1} & 0 & 0 & 0 & \mathbf{5} & 0 & 0 & \mathbf{1} \\ \mathbf{1} & 0 & 0 & 0 & 0 & 0 & 0 & \mathbf{1} \\ 0 & \mathbf{4} & \mathbf{4} & 0 & 0 & \mathbf{3} & \mathbf{3} & 0 \\ 0 & 0 & 0 & \mathbf{6} & 0 & 0 & 0 & 0 \\ 0 & \mathbf{2} & 0 & 0 & 0 & 0 & 0 & \mathbf{2} \\ 0 & 0 & 0 & 0 & \mathbf{5} & 0 & 0 & 0 \\ 0 & \mathbf{2} & 0 & 0 & 0 & 0 & 0 & \mathbf{2} \\ \mathbf{1} & 0 & 0 & 0 & 0 & \mathbf{3} & \mathbf{3} & \mathbf{1} \end{pmatrix}$

For matrices that cannot be optimized a one-by-one row switching method is adopted (8 switching states, 8 s). For example, setting a diagonal line along the display does not allow the algorithm to match any common element.

### 4.2.3 Software

In order to interact with the electronic drive and thus control the tactile display, a user friendly software graphic interface was implemented.

Its architecture and operational code were developed in C++ using the open source library *wxWidget*<sup>1</sup> to offer great flexibility in its execution platform: the tactile display is operational in Windows, GNU/Linux and MacOSX.

Two interactive modes were developed:

1. Figure 4.16(a) simulates the 8 x 8 matrix with buttons representing the 64 taxels. An active taxel (taxel up) is represented by a red button while an inactive one (taxel down) by a black button. The user chooses the taxels to activate/deactivate by clicking the corresponding buttons. When ready, the software sends the configuration to the electronic drive.
2. The second mode is a freehand painting tool (Figure 4.16(b)). As in commercially available paint software, the user simply draws a figure in a window. To obtain the closest matrix, the software segments the drawing area in 64 identical rectangles and quantifies the black pixels for each rectangle. If their number reaches a defined threshold, the rectangle is considered an active taxel.

Additionally, the software includes several features that simplify the use of the tactile display: it permits data storage/retrieval in/from hard disk or floppy drive, it allows concatenation of the data stored to establish sequences, it permits resetting the whole display (all taxels down) in one-step and it permits configuring the set/reset step current times applied to the taxels and the PC output port (serial port 1, 2, 3 or 4) [Wiertlewski06].

<sup>1</sup><http://www.wxwidget.org>

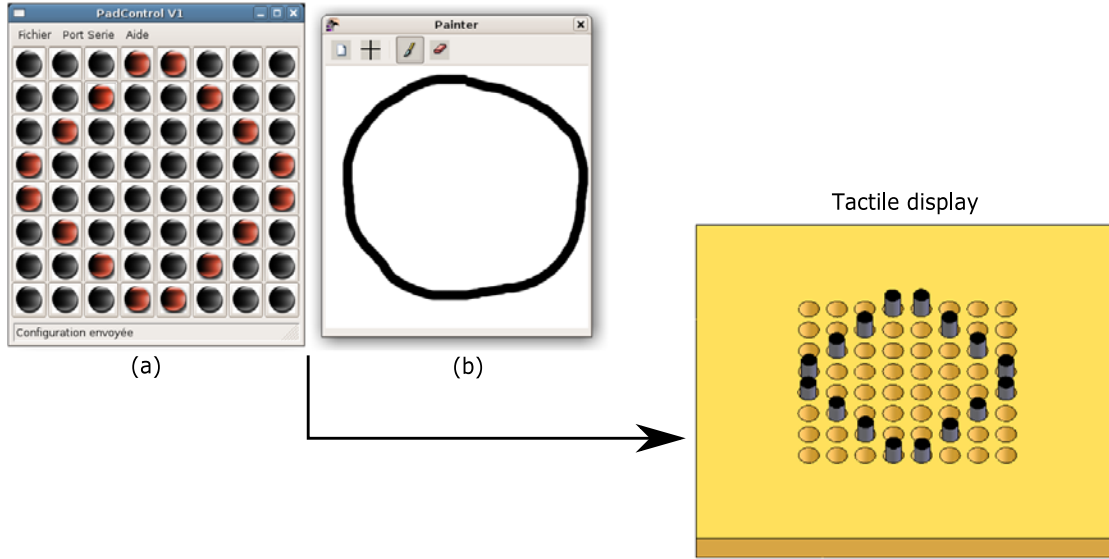


Figure 4.16: User interfaces.

### 4.3 A thermal array structure

As aforementioned, the tactile display is basically an array structure. The information displayed by the taxels results from the thermally driven actuation of the SMA springs, which are triggered once they are heated enough to transform from martensite to austenite. The main problem in confined small spaces is that heat conduction through the air becomes significant. This implies that a thermal interaction between the actuators in the matrix is present and might cause an undesired actuation of the adjacent taxels. Since the array relies on the creation or modification of temperature gradients, it is useful to model its structure thermally in order to predict its performance.

Consider an SMA spring with a steady-state temperature of  $100^{\circ}\text{C}$ . As the distance to the neighboring SMAs is small, this temperature becomes a heat gradient that influences their thermal state.

Heat transfer within the SMA array is a two dimensional conduction problem that can be defined using Fourier's steady-state heat flow rate equation:

$$Q(t) = kS\nabla T \quad (4.1)$$

where  $Q$  is the flow rate of the heat convected away from the SMA,  $k$  is the thermal conductivity of the air ( $k=0.025 \text{ W/m}\cdot\text{K}$ ) and  $\nabla T$  is the temperature gradient at the location of interest.

Under the assumption that  $Q$  is uniformly distributed within the SMA area  $S$ , it can be considered that an active SMA spring at  $100^{\circ}\text{C}$  is a 275 mW heat source.

Figure 4.17 shows the 1D stationary heat flow distribution connecting the active SMA with its passive neighbor located at 2.6 mm. Note that this last is actually thermally influenced with an approximately 25 mW heat flow.

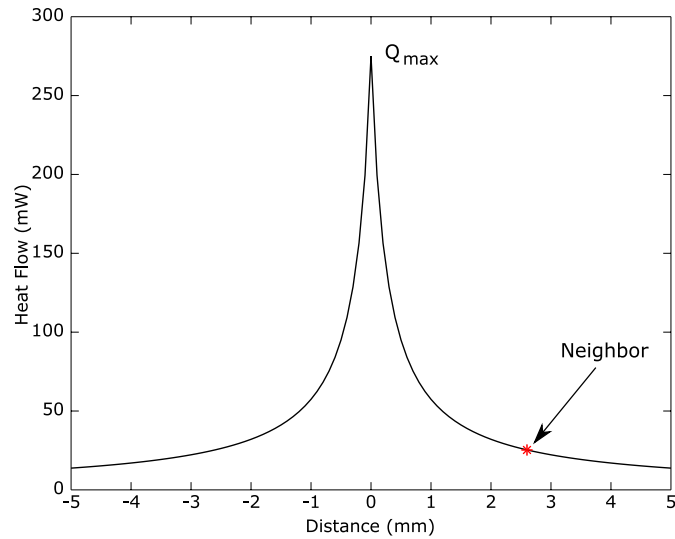


Figure 4.17: The SMA's heat flow distribution as a function of distance.

Thermal interaction becomes more problematic when the number of active elements increases. Recall that all conduction problems in which thermal conductivity is an invariant follow the superposition principle.

Figure 4.18 simulates the combined impact of several heat sources on the array for 2, 4 and 8 adjacency configurations. Naturally, heat flow in the entire array increases in proportion to the number of heating sources. Note that the passive SMA is thermally influenced by an increasing thermal flow (50, 102 and 176 mW). An important remark on the simulation is that the conduction problem is one-dimensional for the 1 and 2 adjacency configurations but becomes bi-dimensional for the 4 and 8 adjacency ones as heat flow is generated in two directions.

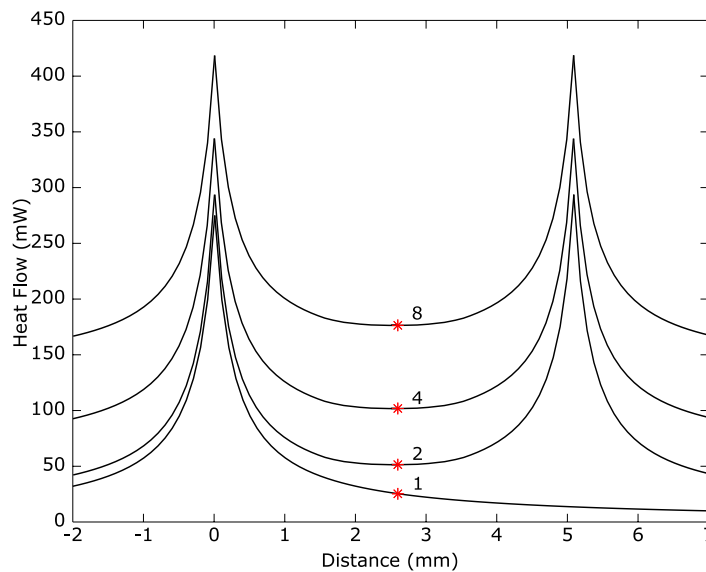


Figure 4.18: Superposition used to simulate the impact of several heat sources.

Figures 4.19(a)-(d) show the steady-state 2D heat distribution in the array while the temperature plots in figure 4.20 demonstrate the impact of thermal interaction in the passive and active actuators for each one of the configurations.

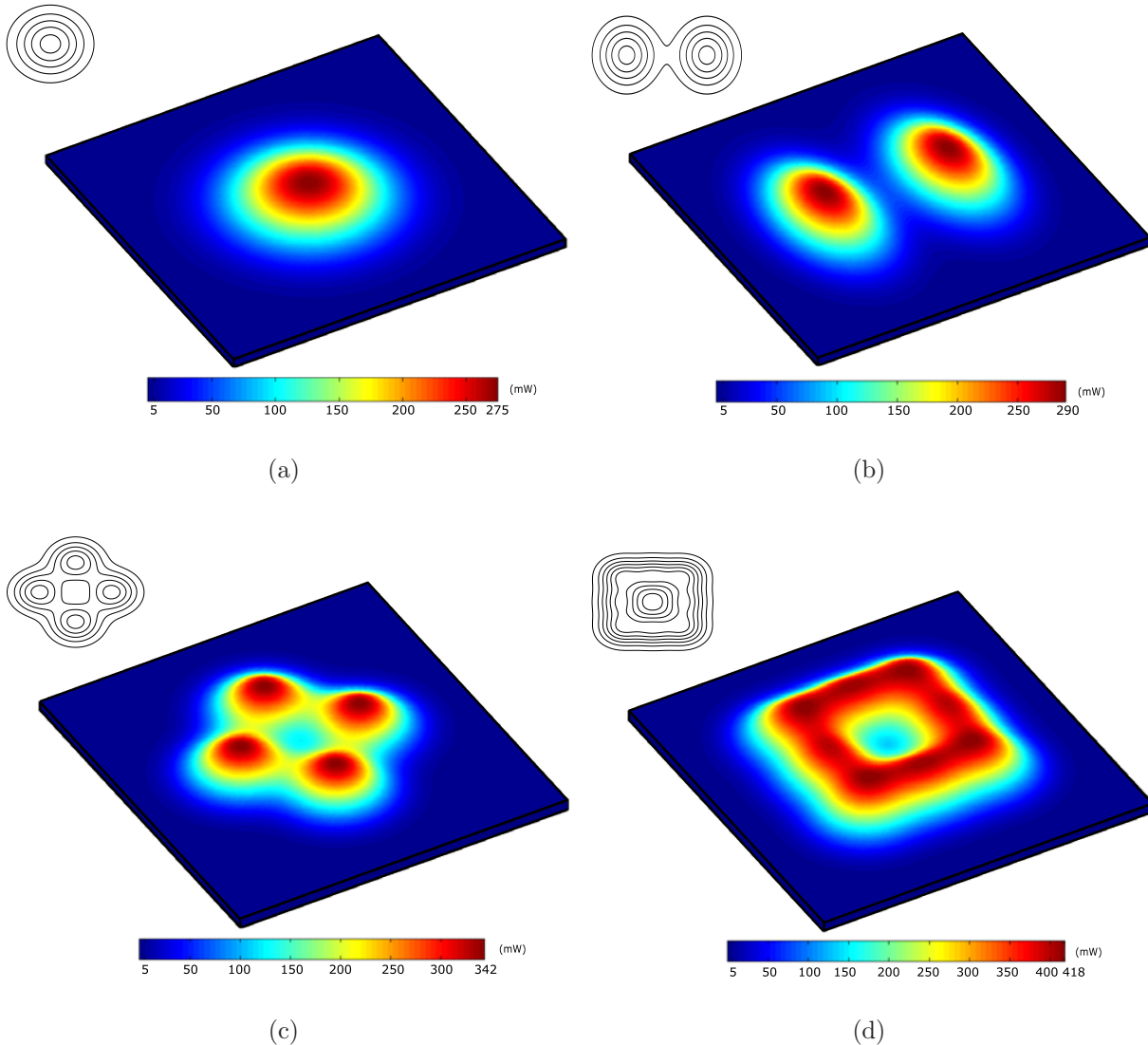


Figure 4.19: Steady-state solution of the 3 x 3 array (surface and contour plots) with (a) one, (b) two, (c) four and (d) eight heat sources.

Figure 4.20(b) shows the step response simulated in a single actuator point when 1, 2, 4 and 8 SMAs are switched on. Note that its steady temperature increases according to the number of heating sources: 100, 106, 121 and 136°C for the 1, 2, 4 and 8 adjacencies, respectively.

Figure 4.20(a) shows the temperature evolution of the passive actuator. Note that the 1, 2 and 4-adjacencies do not reach to activate the SMA. However, the 8-adjacency quickly increases the SMA's temperature to its set point.

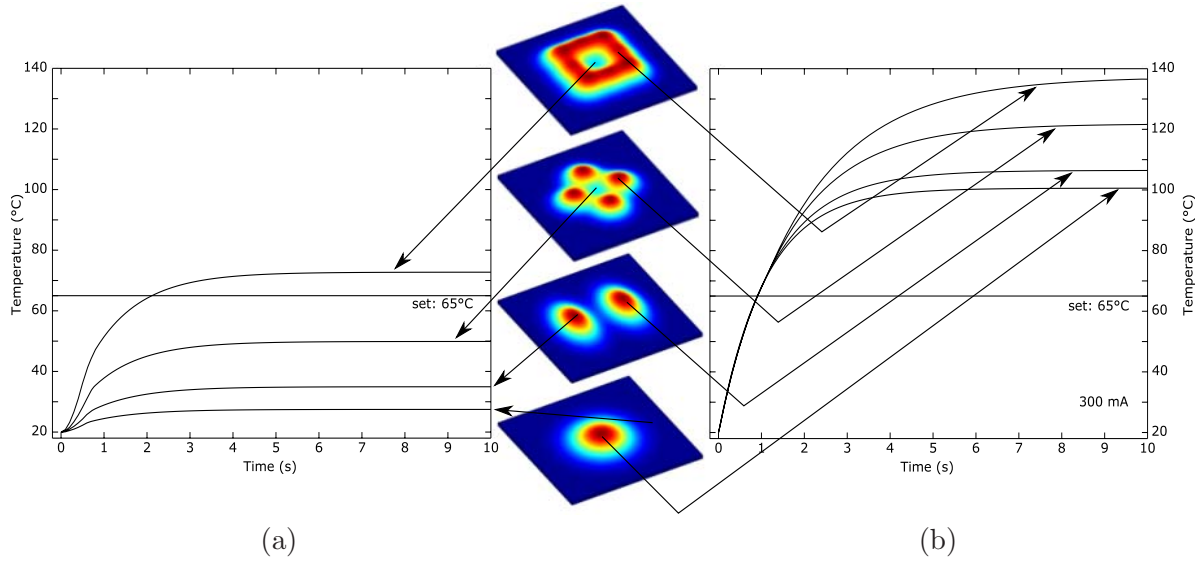


Figure 4.20: Simulated temperature-time responses for the 1, 2, 4 and 8-adjacency configurations: (a) passive and (b) active SMA.

Table 4.1 compares the simulated and experimentally observed triggering times of the passive SMA. Each configuration was tested by setting the corresponding SMAs with 300 mA and measuring the time in which the passive SMA started to present deformation. Recall from theory that this time corresponds to the one needed to reach  $A_f$ . Note that simulation reproduces acceptably the physical behavior [Velazquez06g].

Adjacency	Set time (s)	
	Simulated	Experimental
1	-	-*
2	-	-*
4	-	130
8	2.1	3

\* No deformation was observed for 20 min.

Table 4.1: Comparison of analytical/experimental actuation times (passive SMA).

Denser arrays can be simulated using the same principle. Naturally, thermal interaction can be considerably reduced using a cooling system such as the miniature fan shown in figure 4.5(a), which cooling flow rate was estimated in 1 m/s (see Appendix C).



## 4.4 Conclusion

This chapter has presented the design and implementation of a new concept for low-cost, lightweight, compact and highly-portable tactile display devices. Using SMAs, it intends to make possible highly-portable Braille-like displays for 200 € or less.

A first prototype of 64 SMA based taxels has been introduced together with its electronic drive, control method and software interface. This system offers high spatial resolution and good performance in addition to being robust, maintainable and simple to fabricate. Both mechanical and electronic drive designs are easily scalable to larger devices while still being price attractive.

Next chapter will evaluate its performance on information transmission through basic psychophysics experiments, especially those concerned with shape recognition and spatial organization (spatial cognitive maps).

---

## Chapter 5

# Preliminary Psychophysical Evaluation of the Tactile Display

---

This chapter presents preliminary results from a set of tactile perception experiments using the 8 x 8 SMA based tactile display. Nine tasks involving healthy blindfolded sighted voluntary subjects were performed to evaluate (1) tactile acuity, (2) shape recognition and (3) space interaction/navigation abilities. Experimental results show an overall acceptable recognition performance that validates the appropriateness of the information displayed and demonstrates initial feasibility of the system.

## 5.1 First evaluation of the tactile display

Preliminary psychophysical experiments were carried out to evaluate whether the SMA based prototype display generates tactile stimulation that is appropriate for the sensitivity of human touch and tactile perception.

For this purpose, a set of 9 tactile tasks was conducted within the following areas:

1. Tactile acuity and Braille
2. Shape recognition
3. Space interaction and navigation

### 5.1.1 Experimental procedure

Twenty-five graduate students (24 men and 1 woman) at Paris 6 University participated voluntarily in a set of 5 tests. No special criteria were used to select them. They were randomly divided into 5 groups of 5 subjects.

All participants were healthy sighted with no known impairments in tactile sensory or cognitive functions and with absolutely no previous experience in Braille or tactile display usage. Their ages ranged from 24 to 28 years old with an average age of 26. All were right-handed.

During the experiments, the subjects were seated blindfolded in front of the tactile display, so that no cue from sight could be obtained (Figure 5.1). Before each session, they were totally naive about all aspects of the test and were given general instructions concerning the task. No familiarization time was granted prior to the tests. Unless indicated, the subjects explored the tactile surface freely with no time restriction and no specific finger/hand imposed.

## 5.2 Experiment 1: tactile acuity and Braille

This test aimed to explore the tactile acuity in the first group of 5 subjects. Acuity means the capacity to discriminate certain simple and basic spatial features of stimulation [Stevens96]. We focused on evaluating the subjects' TPDT (two-point detection threshold) and their ability to distinguish differences in location of tactile stimuli. For this purpose, eight taxels of the tactile display were used simulating a Braille cell.

The study was divided in three sessions: location of a tactile stimulus, location of tactile stimuli and bimodal perception.

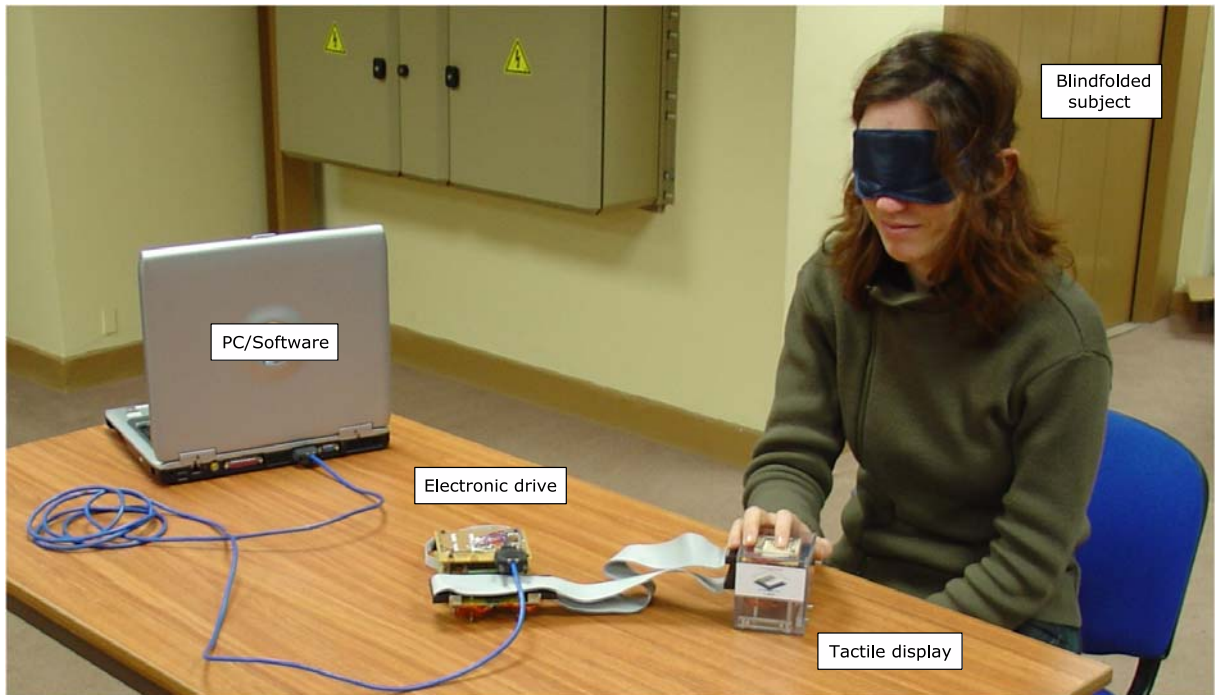


Figure 5.1: The experimental platform.

### 5.2.1 Session 1 - Location of a tactile stimulus

#### *Method:*

In the first session, the subjects were asked to place a finger on the tactile display and to keep it immobile throughout the test (passive touch). It was noted that all of them used the index finger.

The sequence in figure 5.2 was then presented. The subjects were asked to verbally report the location of the contact point (or points) perceived at each time. The subject was allowed one guess.

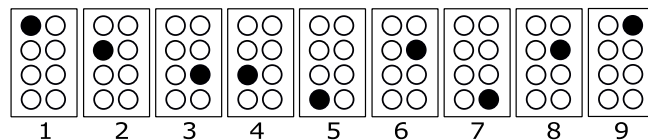


Figure 5.2: Single stimulus point configurations to evaluate the subjects' tactile acuity (location of a tactile stimulus).

#### *Results and discussion:*

Figure 5.3 shows the results obtained from this session. Note that an overall good performance (64.4%) is obtained in locating a tactile stimulus. Inspection of figure 5.3 clearly shows that the stimuli closer to the fingertip (configurations 1 and 9) are easier to identify than those placed deeper in the finger.

It was also observed that 87.5% of the errors were of the same type: the subject always pointed to the correct column but a row above the actual stimulus point.

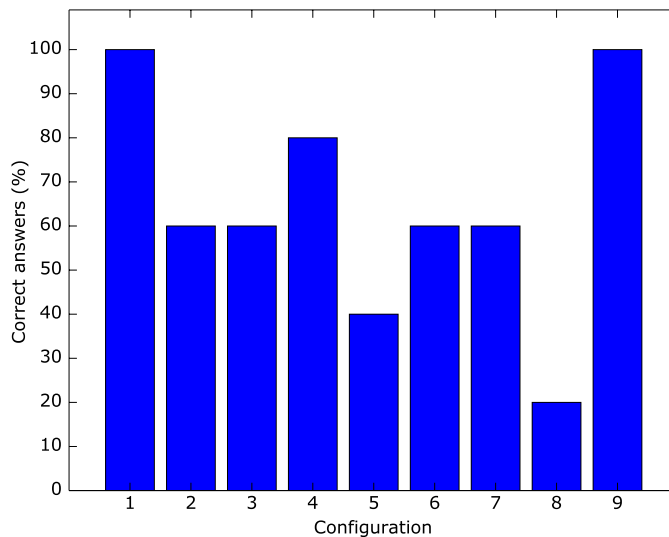


Figure 5.3: The subjects’ performance for each of the nine configurations (passive touch).

### 5.2.2 Session 2 - Location of tactile stimuli

*Method:*

The nine configurations in figure 5.4 were used for the second session. They correspond to Braille characters in the French language. As seen, for each of the configurations, one or several contact points are presented to the subjects, who were asked to identify them. Naturally, the subjects were naive about the number of contact points. It was stated that, in contrast to the previous session, it was allowed to move the finger and freely explore the tactile display (active touch). Again, one guess was allowed for each configuration.

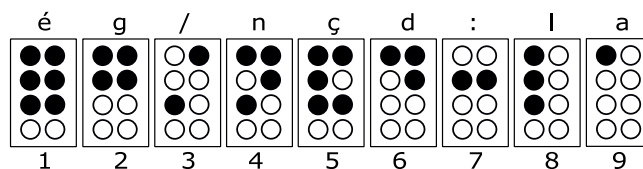


Figure 5.4: Braille characters to evaluate the subjects’ tactile acuity (location of simultaneous tactile stimuli).

*Results and discussion:*

Figure 5.5 (black bars) shows the results obtained from the Braille character identification. This task is much more complicated than the first one and poorer scores were obtained

(an overall recognition rate of 26.7%). An analysis performed on the errors revealed that in 60.6%, the subjects were not able to identify the correct number of contact points and in 65% of these cases, the number of contact points was underestimated. However, the points identified corresponded to the ones actually presented. The remaining 39.4% of the errors were as in session 1: the subject pointed to the correct column but wrong row. In conclusion, the subjects were more likely to miss a contact point than to misplace it.

### 5.2.3 Session 3 - Bimodal perception

#### *Method:*

The third session presented again the configurations in figure 5.4 to the subjects. However, this time the subjects were not blindfolded; they were asked to explore the tactile display (active touch) while watching a sheet of paper containing figure 5.4 (the tactile display was not seen at any time). Their task was to match what they felt tactually with what they were seeing. Again, one guess was allowed for each configuration.

#### *Results and discussion:*

Figure 5.5 (yellow bars) shows the results obtained from this session. Note that the overall recognition performance increases significantly with vision (to 86.7%). It has been well documented [Newell03] that the visual modality, generally dominant over the tactile one in sighted people, enhances tactile perception.

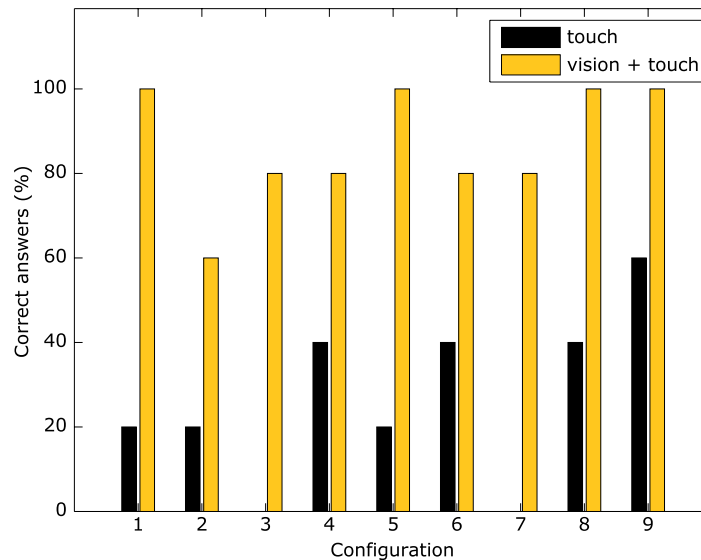


Figure 5.5: The subjects' performance in the Braille character recognition task (active touch): touch (black bars) and vision+touch (yellow bars). Bimodal perception led to a better recognition performance.

## 5.3 Experiment 2: shape recognition

The goal of the second test was to determine whether the subjects could use the tactile display to identify several geometric and various simple shapes. The study was divided in two sessions: primitive and various shapes.

### 5.3.1 Session 1 - Primitive shapes

#### *Method:*

The six basic geometric shapes shown in figure 5.6 were used for the first session. The second group of 5 participants was previously instructed about the 3 possible shapes (square, circle and triangle) but not about their dimensions or characteristics (edged or filled). Then, they were asked to freely explore the tactile display (active touch). When finished, they verbally reported the shape perceived. Each shape was presented once during the experiment and only one guess was allowed to the subject. The exploration time was recorded for each shape and for each participant.

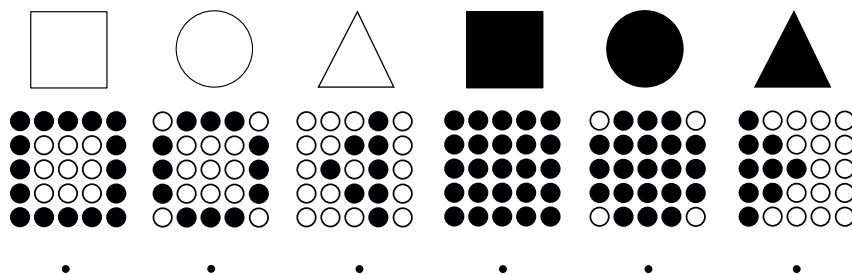


Figure 5.6: The six basic shapes used in experiment 2. All shapes were displayed in a 5 x 5 taxel area (40% of the active space on the display). The black dot represents the subject's related position to the shape.

#### *Results and discussion:*

The mean percent correct for discriminating each of the six shapes averaged across the participants is shown in figure 5.7. Note that an overall acceptable recognition rate is observed except for the filled circle, which was taken for the square in all cases. This shape, with less evident curved boundaries, is more difficult to detect than the polygonal ones. This might be due to the linear scraping motion of the finger during exploration. When asked about the characteristics of the shapes, none of the subjects realized that some shapes were filled. All of them stated that they focused mainly on exploring the borders.

Figure 5.8 shows the subjects' exploration times by shape (maximum, minimum and average time). Note that the difficulty of the recognition task appears to be different from edged shapes to filled shapes: the subjects' understanding time increases when exploring filled shapes. Finally, there was no evidence that longer exploration times led to better discrimination performances.

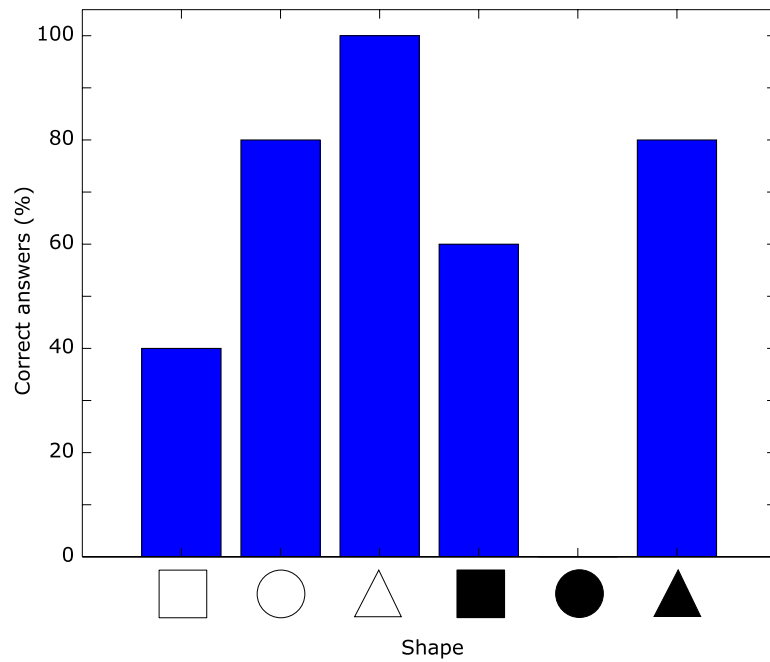


Figure 5.7: The mean percent correct discrimination performance for each of the six basic shapes (active touch).

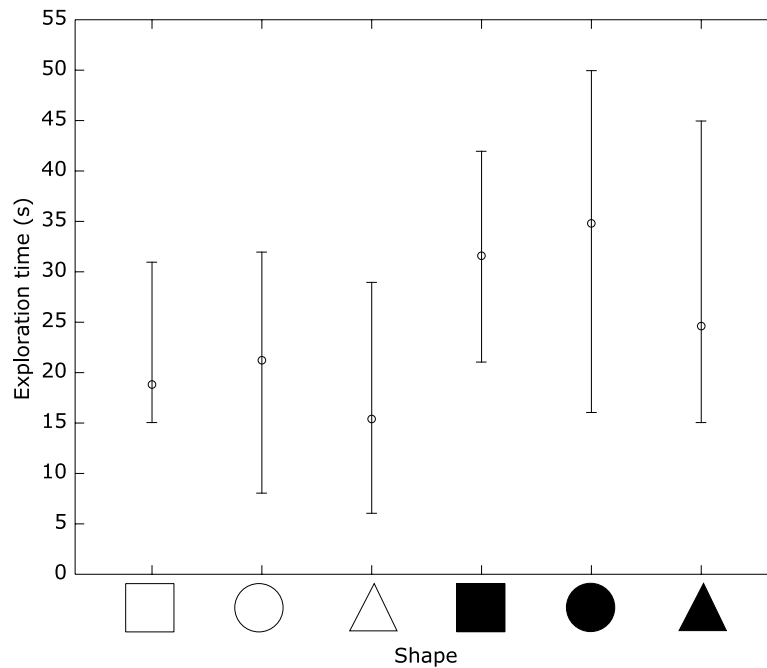


Figure 5.8: Exploration times by shape. Filled shapes appear to be more difficult to identify.



### 5.3.2 Session 2 - Various shapes

*Method:*

A second shape recognition session was performed with the same group of 5 subjects. Four different shapes were presented this time. The subjects were asked to explore the tactile surface (active touch) and then asked to draw on a sheet of paper the shape perceived. Each recognition task was timed.

*Results and discussion:*

Figure 5.9 summarizes the results obtained: it shows the shape displayed on the tactile display and the shapes drawn by each subject. Note that the shapes recognized are quite close to the displayed ones [Velazquez06g].

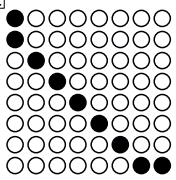




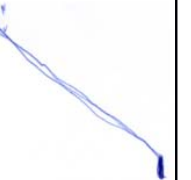
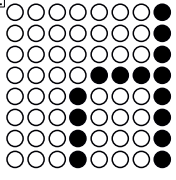
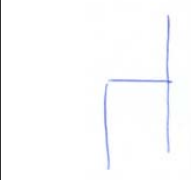

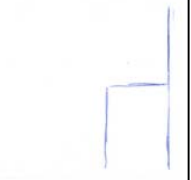
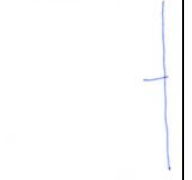
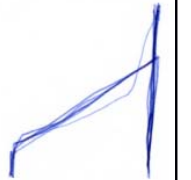
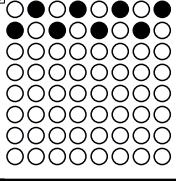



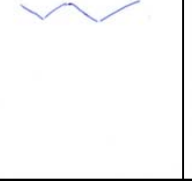
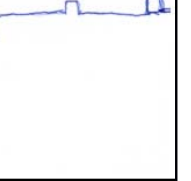
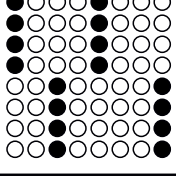
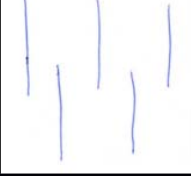


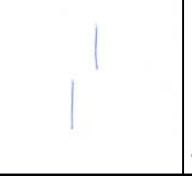
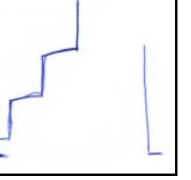
Shape Displayed	Shape Recognized				
	Subject-1	Subject-2	Subject-3	Subject-4	Subject-5
1 					
2 					
3 					
4 					

Figure 5.9: Results of the 5 subjects in the 2D tactile shape recognition task.

Figure 5.10 shows the exploration times by shape (maximum, minimum and average time). Note that the time needed to recognize each shape is roughly the same for all subjects. Results suggest either a higher difficulty in recognizing the fourth shape or fatigue since two subjects took up to 40 s exploring the tactile display.

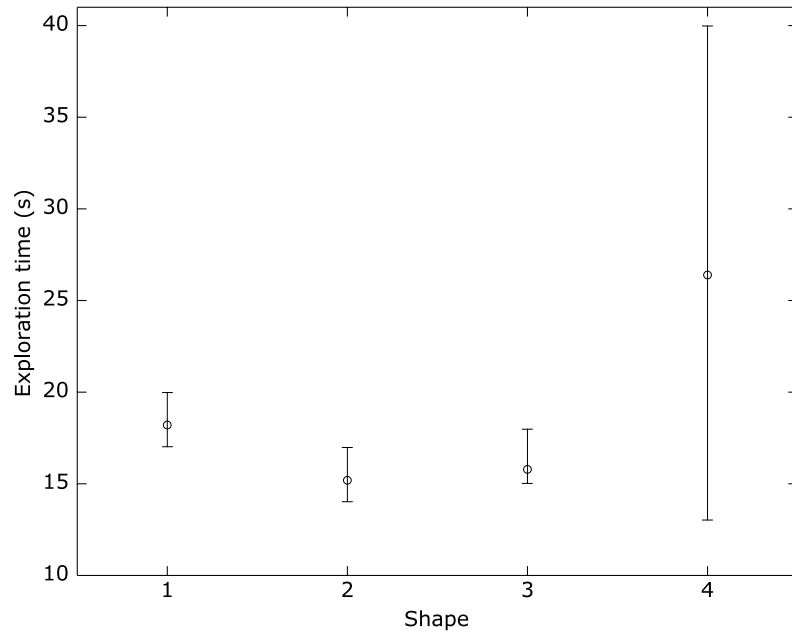


Figure 5.10: Exploration time by shape (drawing session).

## 5.4 Experiment 3: space interaction and navigation

This section intends to evaluate the subjects' ability to interact and navigate in a 3D environment using the 2D tactile information provided by the tactile display.

This study consists of three sessions: direction recognition, environment structure and navigation using tactile maps.

### 5.4.1 Session 1 - Direction recognition

The purpose of this session was to determine whether the subjects could recognize the direction of motion of dynamic information. The session consisted of two trials.

#### *Method (Trial-1):*

The four sequences in figure 5.11 were presented to the third group of 5 subjects. The subjects were asked to explore the tactile display and to verbally report the direction perceived. Each task was timed. Again, one guess was allowed for each configuration. All subjects chose passive exploration, i.e. they preferred to keep the fingers static on the display. It was noted that all of them used the index and middle fingers of the right hand to cover the tactile surface.

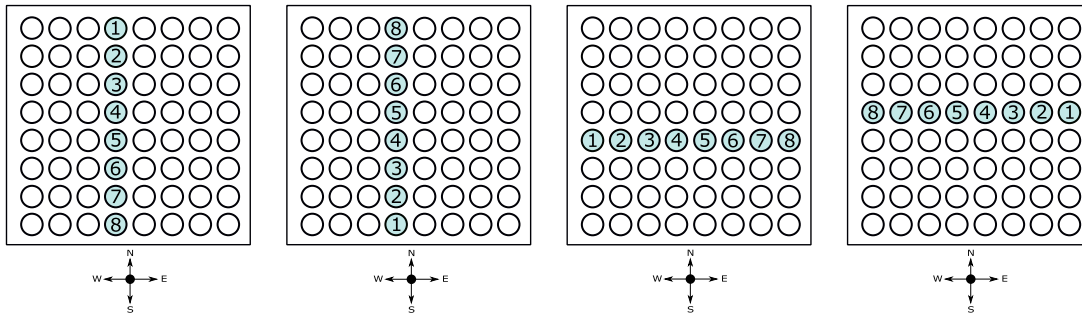


Figure 5.11: Configurations used in the direction recognition task. The four basic directions (North, South, Est, West) were presented to the subjects as straight lines. The number inside the contact pin indicates its schedule of activation and the black dot the subject’s related position to the moving sequence.

*Results and discussion (Trial-1):*

Results obtained were very satisfying: all subjects recognized all directions (a 100% recognition rate). It has to be recalled that the display’s refreshable rate is limited to 1.5 Hz due to the shape memory alloy technology used for actuation of the pins. It has been reported that the direction recognition task becomes more difficult as frequency increases, such as in the case of vibratory tactile displays [Benali-Khoudja04].

*Method (Trial-2):*

To confirm these results, another set of directions (Figure 5.12) was presented to the same group. Note that this time the patterns are more complex. The same conditions were respected: one guess and passive exploration. Each task was timed.

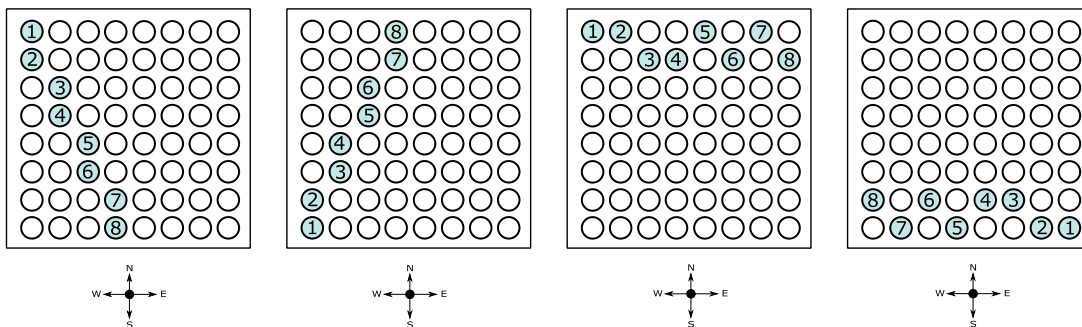


Figure 5.12: The second set of configurations used in the direction recognition task.

*Results and discussion (Trial-2):*

Results obtained were again very satisfying: all subjects recognized all directions (a 100% recognition rate). Figure 5.13 compares the recognition times by direction recorded from both trials. Note that, in general, the subjects were able to recognize the directions of trial-1 faster than those of trial-2. In some cases, they were able to recognize the direction even before the sequence display finished (8 s).

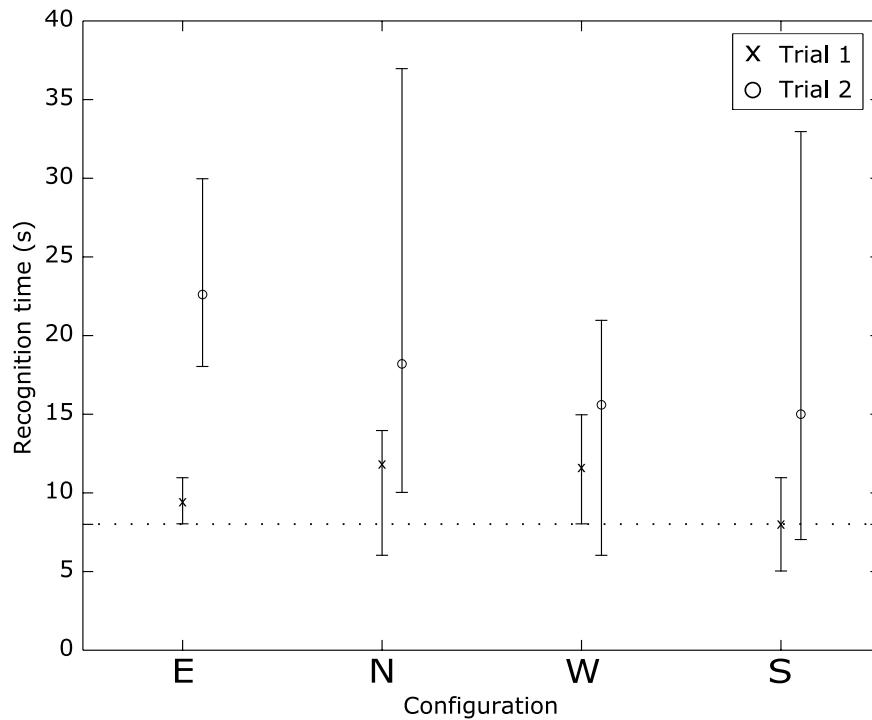


Figure 5.13: Comparison between trial-1/trial-2 direction recognition times. The broken line represents the end of sequence display (8 s).

### 5.4.2 Session 2 - Environment structure

This session aimed to obtain a preliminary feedback on the effectiveness of the Intelligent Glasses (IG) environment representation concept. Recall from chapter 1 that the IG system intends to provide a simplified version of the near environment through an edge-like tactile representation of its structure.

#### *Method:*

For this purpose, the configurations in figure 5.14(a) were presented to the fourth group of participants. They represent 6 different kinds of obstacles (walls). The black dot represents the subject's related position to the wall. So, as shown in figure 5.14(b), the subject is facing the wall and has in the tactile display a tactile representation of that view.

During the exploration task, the subjects were not blindfolded and they explored the tactile display at will (active touch) while watching a sheet of paper containing the 6 configurations in figure 5.14(a). Again, their task was to match what they understand tactually with one of the possible configurations. Each exploration task was timed and one guess was allowed to the subject.

Two trials were conducted. In the first one, the 6 configurations were represented with the minimum possible contact points: 3. In the second trial the line segments were each extended 1 contact point in length for a total of 5 contact points.

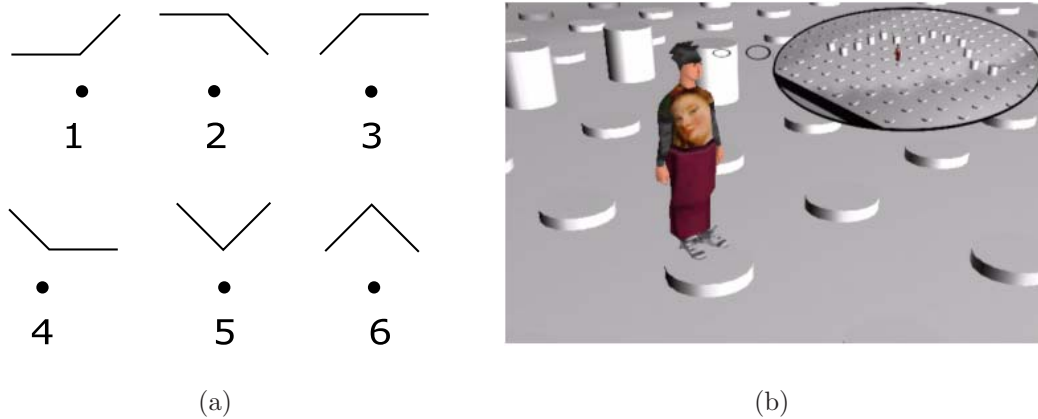


Figure 5.14: (a) Configurations used in the environment structure understanding task and (b) the subject in the environment.

*Results and discussion:*

Figure 5.15 compares the results obtained in both sessions. Note that an overall good recognition performance is observed in both and that the recognition rate obtained with 5 contact points (90%) is generally better than the one obtained with 3 (86.7%). During the tests, the subjects realized themselves that the configurations with 5 contact points were bigger and when asked about their preferences, they stated that these latter were easier to recognize.

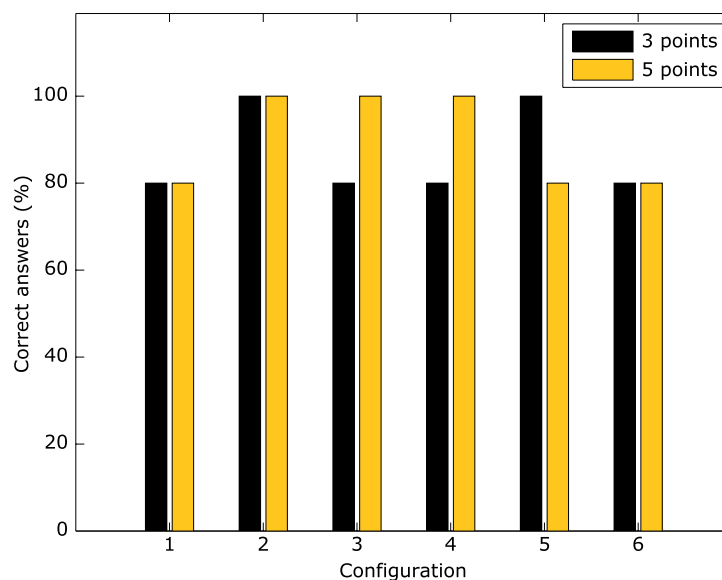


Figure 5.15: Comparison between the subjects' average recognition performance in trials 1 and 2.

Figure 5.16(a) shows the exploration times per subject during the first trial. Note that the subjects take less time and become more efficient in exploring the display as the test progresses. Figure 5.16(b) shows the exploration times per subject during the second trial. Note that a more uniform exploration time is observed as trial progresses which suggests a learning/habituation to the task/device.

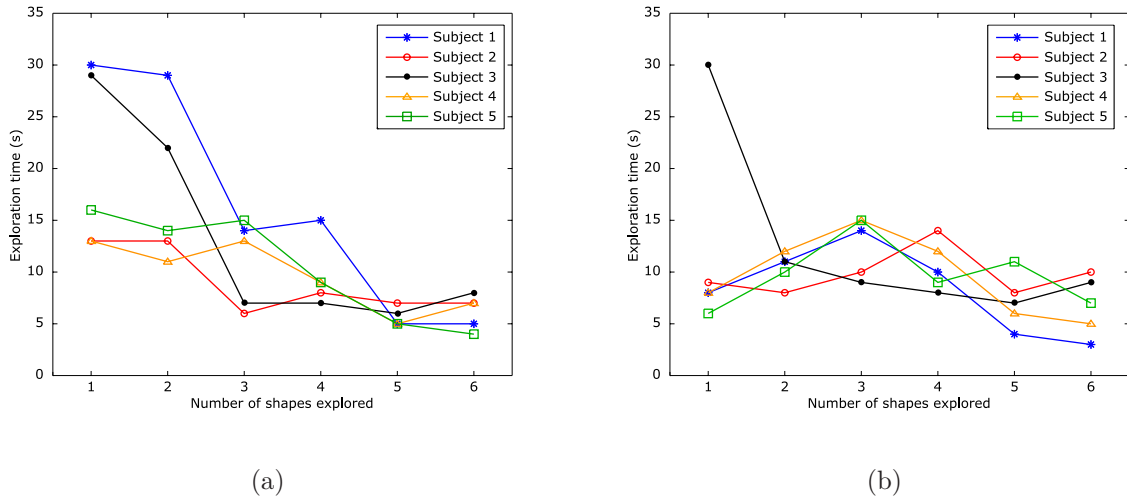


Figure 5.16: Exploration times per subject in the environment structure understanding task: (a) trial 1 and (b) trial 2.

### 5.4.3 Session 3 - Navigation and tactile maps

This session takes a step forward in the environment structure understanding task. Its goal is to evaluate the subjects' ability to understand multiple tactile representations and to integrate them to generate space maps [Fontaine06].

#### *Method:*

The virtual environment in figure 5.17(a) was presented to the fifth and last group of 5 subjects. It is composed of four spaces (rooms). In each room, the subject is placed at the entrance and from that point, he/she has a view of the room. Figure 5.17(b) shows these four subject-related views as well as their tactile coding in the 8 x 8 display.

Each participant was asked to explore the tactile display (active touch) and, once the current tactile map had been fully understood, to report it as a drawing. At the end, the four tactile maps had to be concatenated to establish a navigation environment. The four choices in figure 5.18 were then proposed to the subject. Based on the drawings and knowing that the free-from-obstacles space leads to the "door" to the next room, the subject was required to identify the one that appeared to him/her the correct navigation environment. One guess was given to the subject in every stage of the session and each task was timed.

First attempts did not involve any drawings, however it was realized that the cognitive task required was too complex: the subjects were capable of remembering only the last tactile map explored and just for a short period of time (about 20 s).

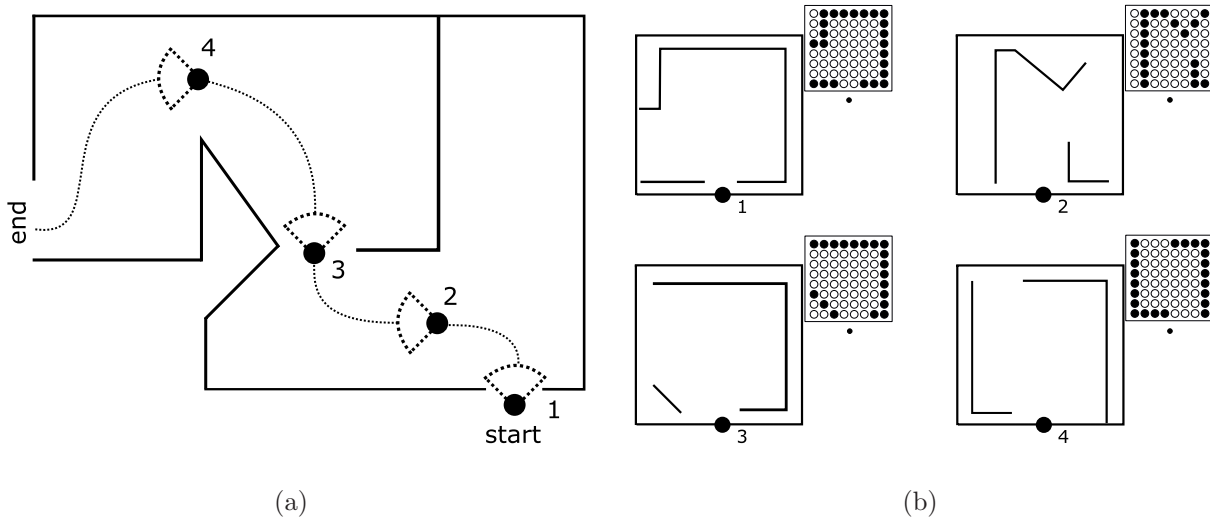


Figure 5.17: (a) The virtual environment used in session 3. The subject progresses in the environment according to the schedule indicated. (b) The subject's views and the corresponding tactile representations. The subject's position in the environment/tactile display is represented by the black dot.

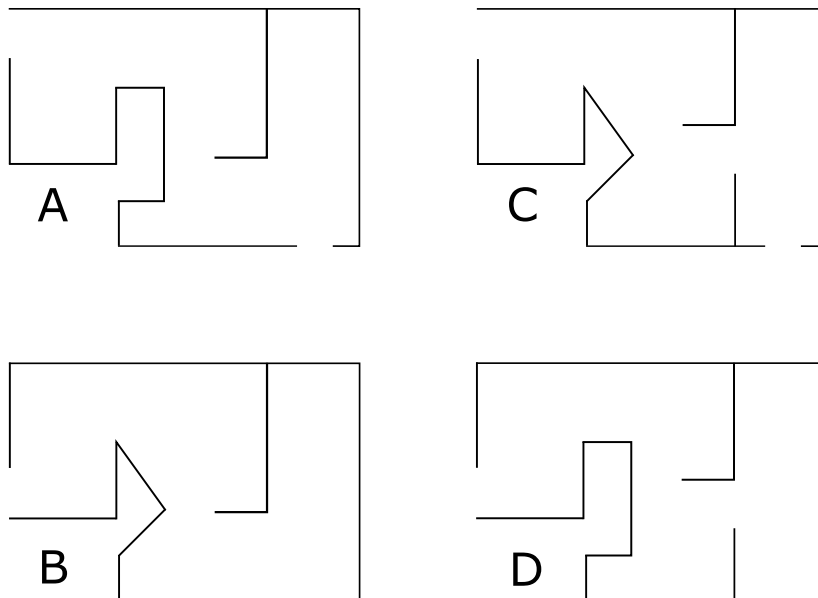


Figure 5.18: The four environments proposed to the subjects. The correct answer is **B**. Note that shape recognition (square/rectangle, triangle and straight lines) and spatial sense (dimension and location) abilities are evaluated as well.

*Results and discussion:*

Results obtained are analyzed in detail for each subject to illustrate the individual procedures and performances during the task.

Figure 5.19 shows the four representations drawn by subject-1. Note that in room (1), subject-1 appears to have translated both entrance parallel-to-him/her lines into perpendicular lines. Subject-1 does not detect the triangle in room (2) but represents acceptably rooms (3) and (4).

When reconstructing the navigation environment it was observed that, based on the first drawing, subject-1 first discards environments **A** and **B**. From the second drawing, subject-1 points to **D** but the third drawing suggests him/her that he/she missed the triangle in the second drawing: subject-1 points then to **C**. The door's position in the fourth drawing indicates that there is an error in **C** and subject-1 reconsiders **B**. From **C** and **B**, subject-1 is more persuaded by the first drawing and finally chooses **C**.

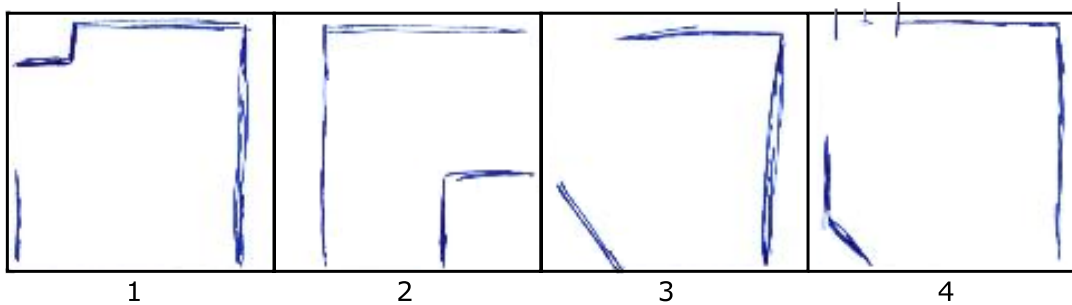


Figure 5.19: The four views recognized by subject-1.

The four views drawn by subject-2 are presented in figure 5.20. Note in room (1), that subject-2 does not recognize either of the entrance parallel lines and that the right wall is perceived to be discontinuous. In room (2), subject-2 appears to have essentially recognized the triangle but not the walls. Room (3) shows a good understanding while room (4) suggests an overall good shape recognition but with dimensional errors.

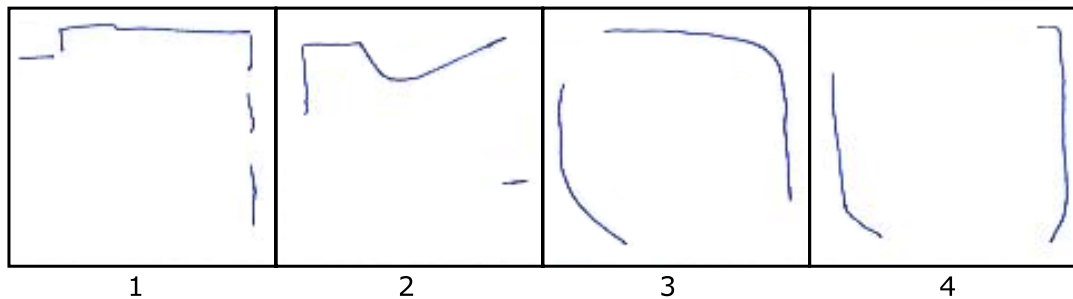


Figure 5.20: The four views recognized by subject-2.

Based on the first drawing, subject-2 first discards environments **C** and **D**. Even though the second and third drawings strongly suggest a triangular form, subject-2 points to **A**.



The fourth drawing with dimensional problems does not allow subject-2 to realize the position of the exit door and finally subject-2 chooses **A**.

Figure 5.21 shows the four views drawn by subject-3. Note that rooms (1), (3) and (4) are well recognized in both shape and dimension. Room (2) suggests that the triangle was perceived as a rectangle and translated from the bottom of the display to one of the sides.

When reconstructing the navigation environment, subject-3 discards environments **C** and **D** based on the first drawing. Then, subject-3 obtains no information from the second drawing and skips to the third one, where he/she realizes the triangle and points to **B**. Finally, the fourth drawing, correct in shape and dimension, confirms the **B** choice.

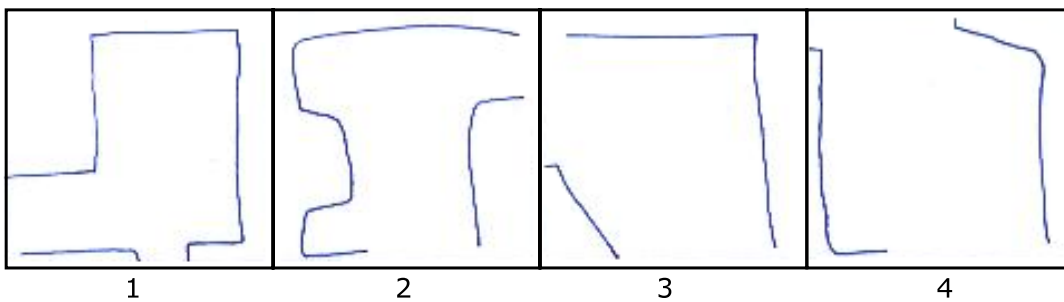


Figure 5.21: The four views recognized by subject-3.

The four views drawn by subject-4 are shown in figure 5.22. Note that an overall good recognition performance (both shape and dimension) is observed in all 4 rooms.

Based on his/her first drawing, subject-4 first discards environments **C** and **D**. From the second drawing, subject-4 is able to recognize the triangle and points to **B**, drawing (3) confirms the triangle and drawing (4) the door's position. Finally, subject-4 chooses **B**.

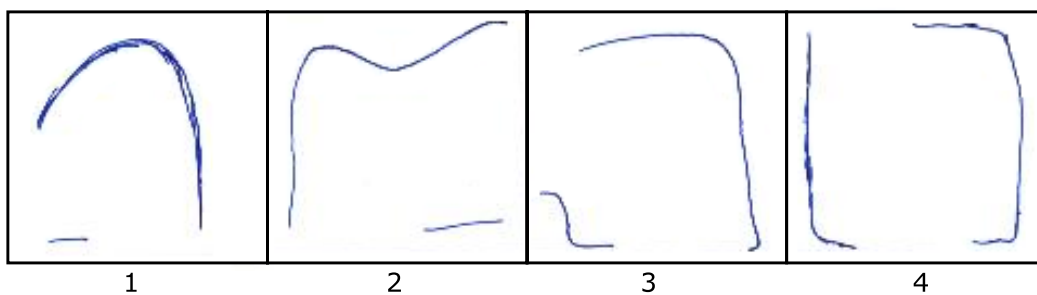


Figure 5.22: The four views recognized by subject-4.

Figure 5.23 presents the four views drawn by subject-5. An overall good recognition performance (both shape and dimension) is observed in all 4 rooms. Note that the triangle in room (2) was perfectly recognized.

As subject-4, subject-5 first discards environments **C** and **D**. From the second drawing, subject-5 easily recognizes the triangle and points to **B**, drawing (3) quickly confirms the triangle and drawing (4) the door's position. Environment **B** is finally chosen.

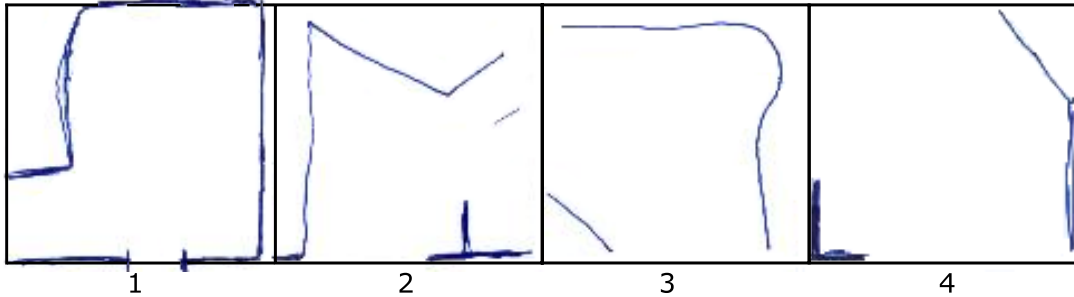


Figure 5.23: The four views recognized by subject-5.

In conclusion, 3 out of 5 subjects (60%) were able to recognize successfully their navigation environment. What we consider important is that navigational information presented to the sense of touch via the tactile display seems feasible: all subjects demonstrated to have acquired the notion of tactile obstacle and tactile map. However the spatial representation (shape and dimension) does not seem to be clear and uniform for everybody, a result that can be anticipated if we consider that there are undoubtedly subjects more skillful than others [Fontaine06].

Figure 5.24 shows the exploration times per subject during the room recognizing test. From the shape recognition results presented in section 5.3, we expected exploration times within one minute but as shown, this was rarely observed in this group. It was also observed (and later confirmed by the subjects themselves) that the faster subjects tried to obtain a global idea of the shape explored while the slower ones sought to understand everything in detail. Curiously, the global idea was more effective and accurate in all cases.

Note that almost all the subjects (except subject-2) take less time and become more efficient in exploring the display as the test progresses. Again, this suggests a learning/habituation to the task/device.

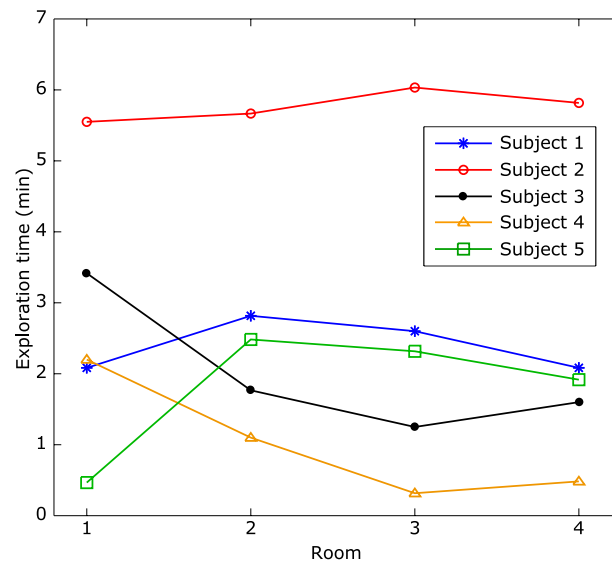


Figure 5.24: Exploration times per subject in the tactile map task.

## 5.5 Conclusion

This chapter has presented a set of tactile perception experiments to show the effectiveness of the tactile information transmitted through the display in sighted people.

Three studies were conducted: (1) tactile acuity, (2) shape recognition and (3) space interaction/navigation. Main results are summarized as follows:

1. Experiment 1 confirmed that the location of a point tactile stimulus can be recognized with an overall acceptable rate. However, multiple point stimuli recognition, as in Braille, is less discriminable especially for sighted people who are not used to it. When aided by a visual reference, this performance can be improved significantly.
2. Experiment 2 demonstrated that basic and regular geometric shapes can be successfully recognized by all subjects in times up to one minute.
3. Experiment 3 attempted to evaluate and understand how participants applied the tactile information to represent an environment through single and multiple maps. Results show that the proposed edge-like representation of the environment is simple and relatively fast to understand and that, upon learning, subjects become more efficient and used to the task.

Future work will involve more formal psychophysics experiments especially those concerned with spatial organization and spatial cognitive mapping. However, these preliminary results obtained from healthy sighted totally naive in Braille/tactile display usage are undoubtedly encouraging for testing the system with blind people.

# Conclusions

This thesis has presented the design of a low-cost highly-portable tactile display implemented with shape memory alloys, which is intended to be integrated in a novel electronic aid for mobility assistance of the blind. The main research topics presented in this work were SMA technology, SMA based miniature actuators, tactile displays, tactile perception and electronic aids for mobility assistance of the blind.

This section concludes summarizing the main achievements, the limitations/improvements and future perspectives of our work.

The main achievements are summarized as follows.

1) *Shape memory alloys.* The thermomechanical behavior of a NiTi-Flexinol SMA helical spring was analytically and experimentally investigated. Two existing constitutive models were used to predict its actuation speed and load-displacement behavior. Experimental tests, including thermal response under stress-free and constant stress and isothermal tensile tests, were carried out to validate both simulations. First attempts revealed the need for a parameter re-identification. DSC and electrical resistance measurements were then performed to determine the exact value of the properties involved in modeling and to predict a more accurate behavior. A fatigue life analysis based on strain rate permitted establishing the specimen's operating stroke consistent with obtaining the maximum number of cycles. Finally, some micro-structural observations were presented to illustrate the effects of heat treatment and fatigue on SMAs.

2) *SMA based actuators.* Three SMA based miniature actuators or taxels have been designed and tested for touch stimulation applications. The behavior of these taxels has been simulated by using the load-displacement characteristic of the NiTi-Flexinol SMA helical spring developed. The first taxel is a biased actuator with a pen-like blocking structure, an attractive design that provides a tensile and compressive force using a single SMA element but with difficulties in bandwidth. The second taxel is an antagonist configuration with blocking structures with improved bandwidth and controllable reversible motion, but with additional mechanisms that complicate the design. The third taxel is still an antagonist configuration but with no blocking structures, an optimal, simple and extremely low-cost design that relies on the pre-strain of the antagonist pair of SMAs to ensure bistability. This last design was retained and fully characterized in terms of force and bandwidth performance.

3) *Tactile displays.* Based on the miniature antagonist taxel developed, a 64 element tactile display has been designed and prototyped. This Braille-like tactile display is a compact, lightweight, portable and low-cost device that can be easily scaled while still being price attractive. The display uses an electronic controller based on a crossbar architecture that simplifies the addressing problem of the antagonist taxels. Two software graphic interfaces make its operation friendly to the user.

4) *Tactile perception.* The performance of the tactile display and the appropriateness of the information displayed were evaluated through a set of tactile perception tests. Twenty-five voluntary subjects participated in nine tasks involving tactile acuity and Braille, shape recognition and environment structure for navigation purposes. Results obtained are very encouraging: recognition rates in all tasks were satisfying. Particularly, those dealing with the environment structure. Results strongly suggest that the *Intelligent Glasses* edge-like tactile representation of the environment is simple and relatively fast to understand and that, upon learning, subjects become more efficient and familiar to the task.

This work concludes stating that SMAs are a good actuation option for binary tactile displays. The 1.5 Hz bandwidth achieved, which appeared at first to be the major limitation, has proved to be suitable. Results obtained show that people explore the tactile display and understand the tactile information much slower.

The main limitations identified and improvements to pursue are summarized as follows.

Two main limitations are found in the system:

1) Setting a uniform and exactly identical pre-strain in the antagonist pair of SMAs for the large number of taxels is not evident. Very fine SMAs are difficult to manipulate and more in confined small spaces like the tactile display. Patience and effort that slows down the assembling process is required. Bistability is not compromised but the consequence of this non-uniformity is that taxels raise to slightly different heights, which is visually and tactually noticeable.

2) The crossbar electronic controller offers remarkable advantages already discussed but it will never perform as fast as the independent addressing controller because taxels must be activated in separate time slices. Setting a number of taxels at the same time, i.e all in one step, can only be achieved using the controller presented in chapter 4 figure 4.9. This is not a significant drawback in the 8 x 8 display but it will become less negligible as the size of the matrix increases.

Two technological improvements can be pursued in the prototype:

1) The spring's mechanical hysteresis due to the R-phase can be eliminated by a simple thermal treatment when fixing the helical shape. The experimental work presented in [Khelifaoui03] suggests that heat treating the NiTi alloy at 500°C for more than an hour (the time used in this work was 5 minutes) superimposes both M and R-phases producing one single stable martensitic phase (Figure 5.25).

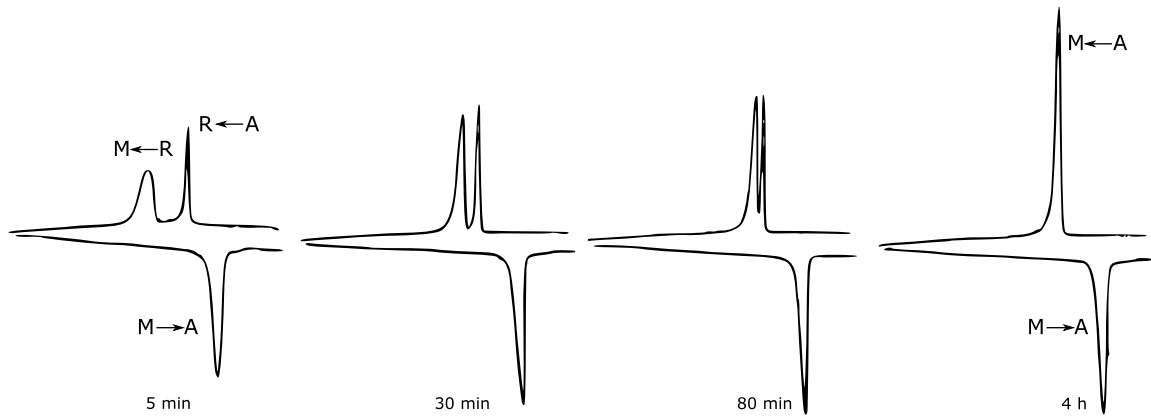


Figure 5.25: Evolution of DSC thermograms of NiTi alloy at 500°C.

2) The crossbar activation method that iterates over each and every row of the matrix can be improved by using PWM (pulse width modulation). Using PWM, the SMAs can be heated sequentially at high frequency to simulate the independent addressing controller and thus produce the effect of a quasi uniform raise and retraction. Figure 5.26 illustrates this concept. Consider two SMA actuators that cannot be actuated at the same time. The heating method currently used actuates one SMA first and then the other one (Figure 5.26(a)). Using PWM, both are progressively heated, still sequentially and their set point is achieved almost simultaneously (Figure 5.26(b)).

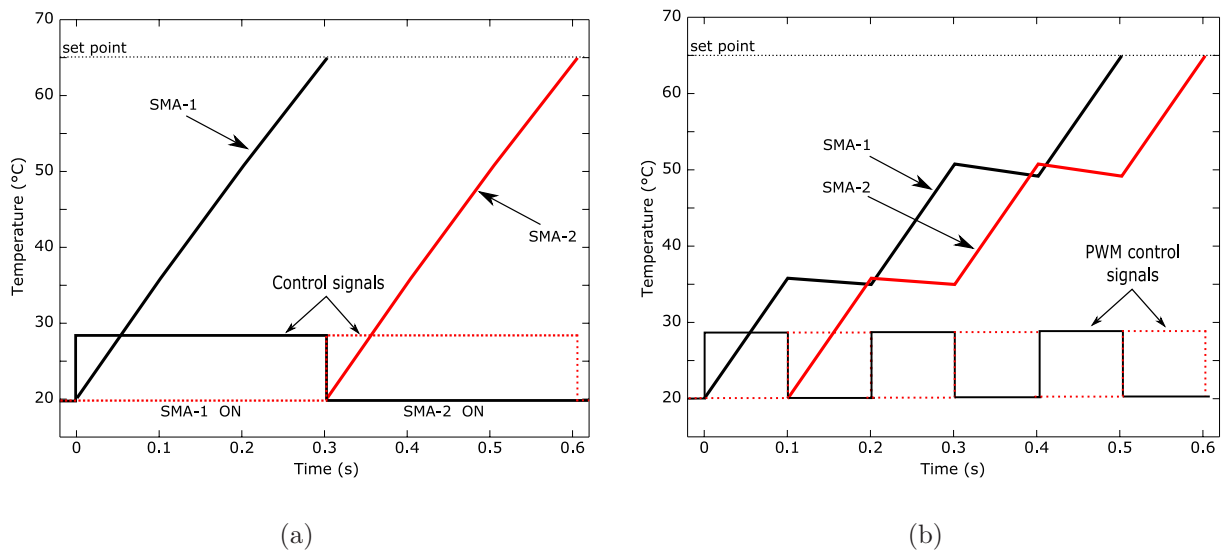


Figure 5.26: Heating drive methods among rows in the matrix. Signals and temporal evolution of temperature using a (a) one by one (currently used) and (b) PWM method.

In terms of immediate future work it is currently considered:

- 1) The design and implementation of an on-board lightweight power supply.

- 2) The cables connecting the computer/processing unit and the tactile display are envisaged to be replaced by a wireless radio connection.
- 3) More formal psychophysics experiments will be designed and performed, especially those concerned with spatial organization and spatial cognitive maps. Once the tactile system is coupled with the vision module, it will be possible to actually navigate within an environment and to evaluate the relation between vision, touch, perception and motion.
- 4) The system will be tested with blind people, which is our final goal and is expected to open new research directions.

# Bibliography

- [Bach-Rita98] P. Bach-Rita, K. Kaczmarek, M. Tyler and J. Garcia-Lara. *From perception with a 49-point electrotactile stimulus array on the tongue: a technical note*. Journal of Rehabilitation Research and Development, vol. 35, no. 4, pages 427–430, 1998.
- [BAT] BAT. Bay Advanced Technologies Ltd. Updated information available at: [www.batforblind.co.nz](http://www.batforblind.co.nz).
- [Bellouard00] Y. Bellouard. *Conception de dispositifs en alliage à mémoire de forme en microtechnique*. PhD Thesis, Swiss Federal Institute of Technology (EPFL), 2000.
- [Benali-Khoudja04] M. Benali-Khoudja. *VITAL: Un nouveau système de communication tactile*. PhD Thesis, Evry-Val d’Essonne University, 2004.
- [Benjamin73] J. Benjamin, N. Ali and A. Schepis. *A laser cane for the blind*. In Proc. of San Diego Biomedical Symposium, pages 53–57, San Diego, CA, USA, 1973.
- [Berveiller91] M. Berveiller, E. Patoor and M. Buisson. *Thermomechanical constitutive equations for shape memory alloys*. Journal de Physique IV, vol. 1, C.4, pages 387–393, 1991.
- [Birman97] V. Birman. *Review of mechanics of shape memory alloy structures*. Applied Mechanics Reviews, vol. 50, no. 11, pages 629–645, 1997.
- [Bissit80] D. Bissit and D. Heyes. *Application of biofeedback in the rehabilitation of the blind*. Ergonomics, vol. 11, no. 1, pages 31–33, 1980.
- [Borenstein90] J. Borenstein. *The NavBelt - A computerized multi-sensor travel aid for active guidance of the blind*. In Proc. of CSUN’s 5th Annual Conference on Technology and Persons with Visual Disabilities, pages 107–116, Los Angeles, CA, USA, 1990.
- [Boyd96a] J. Boyd and D. Lagoudas. *A thermodynamic constitutive model for the shape memory materials. Part I. The monolithic shape memory alloys*. International Journal of Plasticity, vol. 12, no. 7, pages 805–842, 1996.



- [Boyd96b] J. Boyd and D. Lagoudas. *A thermodynamic constitutive model for the shape memory materials. Part II. The SMA composite materials*. International Journal of Plasticity, vol. 12, no. 7, pages 843–873, 1996.
- [Brinson93] L. Brinson. *One-dimensional constitutive behavior of shape memory alloys: Thermomechanical derivation with non-constant material functions and redefined martensite internal variable*. Journal of Intelligent Materials, Systems and Structures, vol. 4, pages 229–242, 1993.
- [Chaillet99] N. Chaillet. *Contribution à la modélisation, la commande et la réalisation de microactionneurs et de composants pour la microrobotique*. HDR Thesis, Franche-Comté University, 1999.
- [de Sars05] V. de Sars. *Conception et commande d'une micro-structure active à haut mobilité. Application à la chirurgie mini-invasive*. PhD Thesis, Paris 6 University, 2005.
- [Dobelle00] H. Dobelle. *Artificial vision for the blind by connecting a television camera to the visual cortex*. ASAIO Journal (American Society for Artificial Internal Organs), vol. 46, pages 3–9, 2000.
- [Dubbel95] H. Dubbel, W. Beitz and K. Küttner. DUBBEL handbook of mechanical engineering. Springer-Verlag Berlin, 1995.
- [Dynalloy] Dynalloy. *Flexinol data sheet*. Updated information available at: [www.dynalloy.com](http://www.dynalloy.com).
- [Falk89] F. Falk. *Pseudoelastic stress strain curves of polycrystalline shape memory alloys calculated from single crystal data*. International Journal of Engineering Science, vol. 27, pages 277–284, 1989.
- [Farcy97] R. Farcy and R. Damaschini. *Triangulating laser profilometer as a three-dimensional space perception system for the blind*. Applied Optics, vol. 36, pages 8227–8232, 1997.
- [Fischer95] H. Fischer, B. Neisius and R. Trapp. *Tactile feedback for endoscopic surgery*. Chapter 19 in Interactive Technology and the New Paradigm for Healthcare, IOS Press, pages 114–117, 1995.
- [Fontaine06] E. Fontaine, R. Velazquez, M. Wiertelwski and E. Pissaloux. *Experimental evaluation of a new touch stimulating interface dedicated to information display for the visually impaired*. In Proc. of the 4th Conference and Workshop on Assistive Technologies for Vision and Hearing Impairment, Kufstein, Austria, 2006.
- [GDA] GDA. Guide Dogs of America. Updated information available at: [www.guidedogsofamerica.org](http://www.guidedogsofamerica.org).
- [GDP] GDP. GDP Research Australia. Updated information available at: [www.gdp-research.com.au](http://www.gdp-research.com.au).

- [Geiger84] S. Geiger. Handbook of physiology section 1: the nervous system. American Physiological Society, 1984.
- [Gill02] J. Gill, K. Ho and G. Carman. *Three-dimensional thin-film shape memory alloy microactuator with two-way effect*. Journal of Microelectromechanical Systems, vol. 11, no. 1, pages 68–77, 2002.
- [Graesser94] E. Graesser and F. Cozzarelli. *A proposed three-dimensional constitutive model for shape memory alloys*. Journal of Intelligent Materials, Systems and Structures, vol. 5, pages 78–89, 1994.
- [Grant99] D. Grant. *Accurate and rapid control of shape memory alloy actuators*. PhD Thesis, McGill University, 1999.
- [Hafez04] M. Hafez and M. Benali-Khoudja. *3D Tactile rendering based on bi (multi) stable SMA monolithic systems*. In Proc. of IEEE International Symposium on Micromechatronics and Human Science, Nagoya, Japan, 2004.
- [Hakkinen02] J. Hakkinen, T. Vuori and M. Paakka. *Postural stability and sickness symptoms after HMD use*. In Proc. of 2002 IEEE International Conference on Systems, Man and Cybernetics, pages 147–152, Hammamet, Tunisia, 2002.
- [HumanWare] HumanWare. Updated information available at: [www.humanware.com](http://www.humanware.com).
- [Ikuta90] K. Ikuta. *Micro/Miniature shape memory alloy actuator*. In Proc. of IEEE International Conference on Robotics and Automation, pages 2156–2161, Cincinnati, OH, USA, 1990.
- [Ivshin94] Y. Ivshin and J. Pence. *A constitutive model for hysteretic phase transition behaviour*. International Journal of Engineering Science, vol. 32, no. 6, pages 681–704, 1994.
- [Johansson83] R. Johansson and A. Vallbo. *Tactile sensory coding in the glabrous skin of the human hand*. Trends in Neurosciences, Elsevier Biomedical Press, vol. 6, no. 1, pages 27–32, 1983.
- [Kafka94] V. Kafka. *Shape Memory: A new concept of explanation and of mathematical modeling. Part 1: Micromechanical explanation of the causality in the SM process*. Journal of Intelligent Materials, Systems and Structures, vol. 5, no. 6, pages 809–814, 1994.
- [Kay64a] L. Kay. *An ultrasonic sensing probe as a mobility aid for the blind*. Ultrasonics, vol. 2, pages 53–59, 1964.
- [Kay74b] L. Kay. *A sonar aid to enhance spatial perception of the blind: engineering design and evaluation*. Radio and Electronic Engineer, vol. 44, no. 11, pages 605–627, 1974.
- [Khelfaoui03] F. Khelfaoui and G. Guenin. *Influence of the recovery and recrystallization processes on the martensitic transformation of cold worked equiatomic Ti-Ni alloy*. Materials Science and Engineering, vol. 355, no. 1, pages 292–298, 2003.

- [Konyo00] M. Konyo, S. Tadokoro and T. Takamori. *Artificial tactile feel display using soft gel actuators*. In Proc. of IEEE International Conference on Robotics and Automation, pages 3416–3421, San Francisco, CA, USA, 2000.
- [Lenay03] C. Lenay, O. Gapenne, S. Hanneton, C. Marque and C. Genou elle. *Sensory substitution: limits and perspectives*. Chapter 16 in Touching for Knowing, pages 275–292, 2003.
- [LExcellent96] C. LExcellent, B. Goo, Q. Sun and J. Bernardini. *Characterization, thermo-mechanical behavior and micromechanical-based constitutive model of shape-memory Cu-Zn-Al single crystals*. Acta Metall. Mater., vol. 44, no. 9, pages 3773–3780, 1996.
- [Liang90] C. Liang and C. Roger. *One-dimensional thermomechanical constitutive relations for shape memory materials*. Journal of Intelligent Materials, Systems and Structures, vol. 1, no. 2, pages 207–234, 1990.
- [Loomis81] J. Loomis. *On the tangibility of letters and Braille*. Perception and Psychophysics, vol. 29, no. 1, pages 37–46, 1981.
- [Maingreaud05] F. Maingreaud. *Une contribution   la perception de l’espace et son int gration dans une aide pour la navigation des d ficients visuels*. PhD Thesis, Paris 6 University, 2005.
- [Maucher00] T. Maucher, J. Schemmel and K. Meier. *The Heidelberg tactile vision substitution system*. In Proc. of 6th International Conference on Tactile Aids, Hearing Aids and Cochlear Implants, Exeter, England, 2000.
- [Meijer92] P. Meijer. *An experimental system for auditory image representations*. IEEE Transactions on Biomedical Engineering, vol. 39, no. 2, pages 112–121, 1992.
- [Miller00] D. Miller and D. Lagoudas. *Thermomechanical characterization of NiTiCu and NiTi SMA actuators: influence of plastic strains*. Smart Materials and Structures, vol. 9, pages 640–652, 2000.
- [Moy00] G. Moy, C. Wagner and R. Fearing. *A compliant tactile display for teletactation*. In Proc. of IEEE International Conference on Robotics and Automation, pages 3409–3415, San Francisco, CA, USA, 2000.
- [Nae03] F. Nae, Y. Matsuzaki and T. Ikeda. *Micromechanical modeling of polycrystalline shape memory alloys including thermo-mechanical coupling*. Smart Materials and Structures, vol. 12, pages 6–17, 2003.
- [Nakatani03] M. Nakatani, H. Kajimoto, D. Sekiguchi, N. Kawakami and S. Tachi. *3D form display with shape memory alloy*. In Proc. of 13th International Conference on Artificial Reality and Telexistence, pages 179–184, Tokyo, Japan, 2003.
- [Newell03] F. Newell, H. B lthoff and M. Ernst. *Cross-modal perception of actively explored objects*. In Proc. of EuroHaptics 2003, pages 291–299, Dublin, Ireland, 2003.

- [Nurion-Raycal] Nurion-Raycal. Updated information available at: [www.nurion.net](http://www.nurion.net).
- [Ortin89a] J. Ortin and A. Planes. *Thermodynamics of thermoelastic martensitic transformations*. Acta Metallurgica, vol. 37, no. 5, pages 1433–1441, 1989.
- [Ortin91b] J. Ortin and A. Planes. *Thermodynamics and hysteresis behavior of thermoelastic martensitic transformations*. Journal de Physique IV, vol. 1, C.4, pages 13–23, 1991.
- [Otsuka99] K. Otsuka and C. Wayman. Shape memory materials. Cambridge University Press, 1999.
- [Pasquero03] J. Pasquero and V. Hayward. *STReSS: A practical tactile display system with one millimeter spatial resolution and 700 Hz refresh rate*. In Proc. of EuroHaptics 2003, pages 94–110, Dublin, Ireland, 2003.
- [Patoor87] E. Patoor, A. Eberhardt and M. Berveiller. *Potentiel pseudo-élastique et plasticité de transformation martensitique dans les mono et polycristaux métalliques*. Acta Metallurgica, vol. 35, pages 2779–2789, 1987.
- [Peirs98] J. Peirs, D. Reynaerts and H. Van-Brussel. *A micro robotic arm for a self propelling colonoscope*. In Proc. of 6th International Conference on New Actuators, pages 576–579, Bremen, Germany, 1998.
- [Pissaloux02] E. Pissaloux. *A vision system design for blind mobility assistance*. In Proc. of the 24th Annual International Conference of the IEEE Engineering in Medicine and Biology Society, pages 2349–2350, Houston, TX, USA, 2002.
- [Polidori98] G. Polidori, M. Lachi and J. Pader. *Unsteady convective heat transfer on a semi-infinite flat surface impulsively heated*. International Communication in Heat and Mass Transfer, vol. 25, pages 33–42, 1998.
- [Potapov00] P. Potapov and E. da Silva. *Time response of shape memory actuators*. Journal of Intelligent Materials, Systems and Structures, vol. 11, pages 125–134, 2000.
- [Pressey77] N. Pressey. *Mowat sensor*. Focus, vol. 11, no. 3, pages 35–39, 1977.
- [RNIB] RNIB. Royal National Institute of the Blind. Updated information available at: [www.rnib.org.uk](http://www.rnib.org.uk).
- [Russell66a] L. Russell. *Travel pathsounder and evaluation*. In Proc. of Conference on the Evaluation of Sensory Devices for the Blind, pages 293–297, London, England, 1966.
- [Russell95b] R. Russell and R. Gorbet. *Improving the response of SMA actuators*. In Proc. of IEEE International Conference on Robotics and Automation, pages 2299–2304, Nagoya, Japan, 1995.
- [Sekuler02] R. Sekuler and R. Blake. Perception. McGraw-Hill Education, New York, USA, 2002.

- [SFS] SFS. Sound Foresight Ltd. Updated information available at: [www.soundforesight.co.uk](http://www.soundforesight.co.uk).
- [Shinohara98] M. Shinohara, Y. Shimizu and A. Mochizuki. *Three-dimensional tactile display for the blind*. IEEE Transactions on Rehabilitation Engineering, vol. 6, no. 3, pages 249–256, 1998.
- [SonicVision] SonicVision. Updated information available at: [www.sonicvision.co.nz](http://www.sonicvision.co.nz).
- [Stevens96] J. Stevens, E. Foulke and M. Patterson. *Tactile acuity, aging, and Braille reading in long-term blindness*. Journal of Experimental Psychology: Applied, vol. 2, no. 2, pages 91–106, 1996.
- [Stone00] R. Stone. *Haptic feedback: A potted history, from telepresence to virtual reality*. In Proc. of the 1st International Workshop on Haptic Human-Computer Interaction, Glasgow, UK, 2000.
- [Summers02] I. Summers and C. Chanter. *A broadband tactile array on the fingertip*. Journal of the Acoustical Society of America, vol. 112, pages 2118–2126, 2002.
- [Sutou05] Y. Sutou, T. Omori, K. Yamauchi, N. Ono, R. Kainuma and K. Ishida. *Effect of grain size and texture on pseudoelasticity in Cu-Al-Mn based shape memory wire*. Acta Materialia, vol. 53, pages 4121–4133, 2005.
- [Tanaka86] K. Tanaka. *A thermomechanical sketch of shape memory effect: one-dimensional tensile behaviour*. Res Mechanica, vol. 18, pages 251–263, 1986.
- [Taylor97a] P. Taylor, A. Moser and A. Creed. *The design and control of a tactile display based on shape memory alloys*. In Proc. of IEEE International Conference on Robotics and Automation, pages 1318–1323, Albuquerque, NM, USA, 1997.
- [Taylor98b] P. Taylor, D. Pollet, A. Hosseini and C. Varley. *Advances in an electrorheological fluid based tactile array*. Displays, vol. 18, pages 135–141, 1998.
- [TiNi-Alloy90] TiNi-Alloy. *Tactile display driven by shape memory wires*. US Patent: 5,718,588, 1990.
- [Tobushi00a] H. Tobushi, T. Nakahara, Y. Shimeno and T. Hashimoto. *Low-cycle fatigue of TiNi shape memory alloy and formulation of fatigue life*. Journal of Engineering Materials and Technology, vol. 122, no. 2, pages 186–191, 2000.
- [Tobushi91b] H. Tobushi and K. Tanaka. *Deformation of a shape memory alloy helical spring*. JSME International Journal, Series I, vol. 34, no. 1, pages 83–89, 1991.
- [Ulrich01] I. Ulrich and J. Borenstein. *The GuideCane - Applying mobile robot technologies to assist the visually impaired*. IEEE Transactions on System, Man and Cybernetics. Part A: Systems and Humans, vol. 31, no. 2, pages 131–136, 2001.

- [Velazquez06a] R. Velazquez, M. Hafez, E. Pissaloux and J. Szewczyk. *A computational-experimental thermomechanical study of shape memory alloy microcoils and its application to the design of actuators*. Journal of Computational and Theoretical Nanoscience. American Scientific Publishers, vol. 3, no. 4, pages 1–13, 2006.
- [Velazquez05b] R. Velazquez, M. Hafez, J. Szewczyk and E. Pissaloux. *Experimental and computational thermomechanical study of a shape memory alloy micro-actuator: aspects of antagonist type behavior*. In Proc. of 3rd MIT Conference on Computational Fluid and Solid Mechanics, pages 1026–1030, Cambridge, MA, USA, 2005.
- [Velazquez05c] R. Velazquez, E. Pissaloux, M. Hafez and J. Szewczyk. *A low-cost highly-portable tactile display based on shape memory alloy micro-actuators*. In Proc. of IEEE International Conference on Virtual Environments, Human-Computer Interfaces and Measurement Systems, pages 121–126, Giardini Naxos, Italy, 2005.
- [Velazquez05d] R. Velazquez, E. Pissaloux, M. Hafez and J. Szewczyk. *Miniature shape memory alloy actuator for tactile binary information display*. In Proc. of IEEE International Conference on Robotics and Automation, pages 1356–1361, Barcelona, Spain 2005.
- [Velazquez04e] R. Velazquez, E. Pissaloux, J. Szewczyk and M. Hafez. *Design and characterization of a shape memory alloy based micro-actuator for tactile stimulation*. In Proc. of IEEE International Symposium on Industrial Electronics, pages 3–8, Ajaccio, France, 2004.
- [Velazquez04f] R. Velazquez, E. Pissaloux, J. Szewczyk and M. Hafez. *Système visuo-tactile d'aide à la mobilité indépendante des déficients visuels dans des environnements 3D non-coopérants*. Journal J3eA, EDP Sciences, vol. 3, no. 1, 2004.
- [Velazquez06g] R. Velazquez, E. Pissaloux and M. Wiertelwski. *A compact tactile display for the blind with shape memory alloys*. In Proc. of IEEE International Conference on Robotics and Automation, pages 3905–3910, Orlando, FL, USA, 2006.
- [Velazquez04h] R. Velazquez, J. Szewczyk, E. Pissaloux and M. Hafez. *Touch stimulation through a SMA actuated micro-mechanism*. In Proc. of 14th IEEE-SPIE Symposium on Electronics for High Energy Physics, Photonics and Web Engineering, pages 586–597, Wilga, Poland, 2004.
- [Wagner02] C. Wagner, S. Lederman and R. Howe. *Design and performance of a tactile shape display using RC servomotors*. In Proc. of the 10th Symposium on Haptic Interfaces for Virtual Environment and Teleoperator Systems, pages 354–355, Orlando, FL, USA, 2002.
- [Waram93] T. Waram. Actuator design using shape memory alloys. T.C. Waram Publishing, Ontario, 1993.

- 
- [Wellman97] P. Wellman, W. Peine, G. Favalora and R. Howe. *Mechanical design and control of a high bandwidth SMA tactile display*. In Proc. of International Symposium on Experimental Robotics, pages 56–66, Barcelona, Spain, 1997.
- [WHO02] WHO. World Health Organization. The World Health Report 2002 : Reducing Risks, Promoting Healthy Life. Geneva, Switzerland, 2002.
- [Wiertlewski06] M. Wiertlewski. *Conception d'outils pour une interface tactile*. Rapport de stage d'ingénieur de l'Ecole Nationale d'Ingénieurs de Saint-Etienne, 2006.
- [Ziegler02] M. Ziegler and M. Stan. *Design and analysis of crossbar circuits for molecular nanoelectronics*. In Proc. of 2nd IEEE Conference on Nanotechnology, pages 323–327, Washington D.C., USA, 2002.

# Publications

(Only first authored papers)

## Journal papers

1. R. Velazquez, M. Hafez, E. Pissaloux and J. Szewczyk, *A Computational-Experimental Thermomechanical Study of Shape Memory Alloy Microcoils and its Application to the Design of Actuators*. Journal of Computational and Theoretical Nanoscience, American Scientific Publishers, Vol. 3, No. 4, 2006.
2. R. Velazquez, E. Pissaloux, J. Szewczyk et M. Hafez, *Système Visuo-Tactile d'Aide à la Mobilité Indépendante des Déficients Visuels dans des Environnements 3D Non-Coopérants*. Journal J3eA, EDP Sciences, Vol. 3, Hors-Série 1, 2004.

## International conference proceedings

1. R. Velazquez, E. Pissaloux and M. Wiertelowski, *A Compact Tactile Display for the Blind with Shape Memory Alloys*. In Proc. of 2006 IEEE International Conference on Robotics and Automation, Orlando, FL, USA, May 2006.
2. R. Velazquez, E. Pissaloux, M. Hafez and J. Szewczyk, *Measurement of SMA Thermal Properties in the Design/Evaluation of Actuators*. In Proc. of the 15<sup>th</sup> International Symposium on Measurement and Control in Robotics, Brussels, Belgium, November 2005.
3. R. Velazquez, E. Pissaloux, J-C. Guinot and F. Maingreud, *Walking Using Touch: Design and Preliminary Prototype of a Non-Invasive ETA for the Visually Impaired*. In Proc. of the 27<sup>th</sup> Annual International Conference of the IEEE Engineering in Medicine and Biology Society, Shanghai, China, September 2005. (poster)
4. R. Velazquez, E. Pissaloux, M. Hafez and J. Szewczyk, *A Low-Cost Highly-Portable Tactile Display Based on Shape Memory Alloy Micro-Actuators*. In Proc. of 2005 IEEE International Conference on Virtual Environments, Human-Computer Interfaces and Measurement Systems, Giardini Naxos, Italy, July 2005.
5. R. Velazquez, M. Hafez, J. Szewczyk and E. Pissaloux, *Experimental and Computational Thermomechanical Study of a Shape Memory Alloy Micro-Actuator: Aspects of Antagonist Type Behavior*. In Proc. of the 3<sup>rd</sup> MIT Conference on Computational Fluid and Solid Mechanics, MIT Campus, Cambridge, MA, USA, June 2005.



6. R. Velazquez, E. Pissaloux, M. Hafez and J. Szewczyk, *Miniature Shape Memory Alloy Actuator for Tactile Binary Information Display*. In Proc. of 2005 IEEE International Conference on Robotics and Automation, Barcelona, Spain, April 2005.
7. R. Velazquez and E. Pissaloux, *Design of Shape Memory Alloy Helical Springs Using Force and Time Response Criteria*. In Proc. of Mechatronics & Robotics 2004 (Student Session), Aachen, Germany, September 2004.
8. R. Velazquez, E. Pissaloux and P. Le Polotec, *Towards a Local Spatial Representation System for Mobility Assistance of the Blind*. In Proc. of the 3<sup>rd</sup> Conference and Workshop on Assistive Technologies for Vision and Hearing Impairment, Granada, Spain, July 2004.
9. R. Velazquez, J. Szewczyk, E. Pissaloux and M. Hafez, *Touch Stimulation through a SMA Actuated Micro-Mechanism*. In Proc. of the 14<sup>th</sup> IEEE-SPIE Symposium on Electronics for High Energy Physics, Photonics and Web Engineering, Wilga, Poland, May 2004.
10. R. Velazquez, E. Pissaloux, J. Szewczyk and M. Hafez, *Design and Characterization of a Shape Memory Alloy Based Micro-Actuator for Tactile Stimulation*. In Proc. of 2004 IEEE International Symposium on Industrial Electronics, Ajaccio, France, May 2004.
11. R. Velazquez, F. Maingreud and E. Pissaloux, *Intelligent Glasses: A New Man-Machine Interface Concept Integrating Computer Vision and Human Tactile Perception*. In Proc. of EuroHaptics 2003, Dublin, Ireland, July 2003. (poster)

## National conference proceedings

1. R. Velazquez, J. Szewczyk, M. Hafez et E. Pissaloux, *Une Interface Tactile Portable à Bas Coût pour le Handicap Visuel*. Dans Actes des 5<sup>èmes</sup> Journées Nationales de la Recherche en Robotique, Guidel, France, octobre 2005. (poster)
2. R. Velazquez, M. Hafez, J. Szewczyk et E. Pissaloux, *Etude Théorique et Expérimentale des Propriétés Thermomécaniques des Alliages à Mémoire de Forme : Application à la Conception des Actionneurs du Type Antagoniste*. Dans Actes du 17<sup>ème</sup> Congrès Français de Mécanique, Troyes, France, septembre 2005.
3. R. Velazquez, E. Pissaloux, M. Hafez et J. Szewczyk, *Actionneur Miniature en Alliages à Mémoire de Forme pour l’Affichage Tactile d’Informations*. Dans Actes des 3<sup>èmes</sup> Journées du RTP Microrobotique, Lausanne, Suisse, décembre 2004.
4. R. Velazquez, E. Pissaloux, J. Szewczyk et M. Hafez, *Modélisation et Validation Expérimentale d’un Micro-Actionneur en AMF : Application à la Réalisation d’Interfaces à Affichage Tactile pour les Déficients Visuels*. Dans Actes des 2<sup>èmes</sup> Journées du RTP Microrobotique, Bourges, France, décembre 2003.
5. R. Velazquez, F. Maingreud et E. Pissaloux, *Conception d’un Système Electronique d’Aide à la Mobilité des Non-voyants Basé sur des Principes Visio-Tactiles*. Dans Actes des 17<sup>èmes</sup> Journées des Jeunes Chercheurs en Robotique, Versailles, France, avril 2003.

---

## Appendix A

# SMA Helical Spring Design Parameters

---

To design an actuator given a desired force and stroke, equation (2.28) has to be solved for the design variables: wire diameter  $d$ , mean spring diameter  $D$  and the number of active coils  $N$  as a function of given parameters:

- $d$  is related to the force that can be developed. In practice, it is determined taking into account the closest-to-design commercially available diameter.
- $D$  is related to both parameters: force and stroke. A useful design indicator is the spring index  $c$  defined as  $c=D/d$ . Typical range for  $c$  is about 4 to 9, with an optimum value of 6. Another key design parameter for  $D$  is the available space for placing the actuator.
- $N$  is related to the stroke.

All these parameters are interrelated leading to a mechanical problem for which an acceptable trade-off must be found within the following set of constraints:

1. According to touch applications (see chapter 1, section "Guidelines for tactile displays: a psychophysiology approach"), the spring should be able to produce a minimum tensile force of 100 mN and a stroke of 1 mm. A delivered force of 200 mN was fixed as the design goal, while a 2 mm stroke was considered a more flexible value to work with (unexpected implementations, possibility of adjustable stroke, etc.).

2. The spring's maximum external diameter was fixed in 2 mm. This value allows the desired actuator inter-spacing (2.54 mm).
3. The spring should always operate within its elastic zone to guarantee linear behavior and to obtain a maximum number of operating cycles.

According to equation (2.28), the tensile force  $F$  exerted by a SMA helical spring in the elastic region is defined by:

$$F = \frac{\pi d^3 \tau_p}{8D} \quad (\text{A.1})$$

In addition to torsional stress, there are two other sources of stress: the direct shear stress and the curvature stress. The stress due to curvature comes from the spring being unable to twist as load is applied, thus contributing to the torsional stress in the wire. To account for these additional sources of stress, the uncorrected torsional stress is multiplied by the *Wahl correction factor*  $K_w$ , which is a function of the spring index  $c$ .  $K_w$  can be calculated as follows:

$$K_w = \frac{4c - 1}{4c - 4} + \frac{0.615}{c} \quad (\text{A.2})$$

Equation (A.1) with the corrected torsional stress can be expressed as:

$$F = \frac{\pi d^3 \tau_p}{8DK_w} \quad (\text{A.3})$$

On the other hand, the temperature-dependent torsional stress  $\tau_p$  of interest in a SMA helical spring occurs during loading at high temperature or austenite phase, so:

$$\tau_p = c_m (A_f - M_s) \quad (\text{A.4})$$

The parameters of the NiTi spring are then:  $\tau_p=127$  MPa (using the values of tables 2.1 and 2.2) and  $K_w=1.2525$  with  $c=6$ .

Figure A.1(a) shows the tensile force  $F$  exerted as a function of the mean spring diameter  $D$  and the wire's diameter  $d$  according to equation (A.3). Note the trade-off between parameters. Figure A.1(b) shows a zoom of the region of interest. Note that a 200  $\mu\text{m}$  diameter wire is capable of delivering the desired 200 mN force. Determination of the mean spring diameter  $D$  is immediate:  $D=1.2$  mm.

Concerning the calculation of the number of active coils  $N$ : The spring's stroke  $\delta$  is equal to the difference between the deflections at high and low temperatures ( $\delta=\delta_m - \delta_a$ ), so according to equation (2.20), the strain  $\gamma$  induced by  $\delta$  is given by:

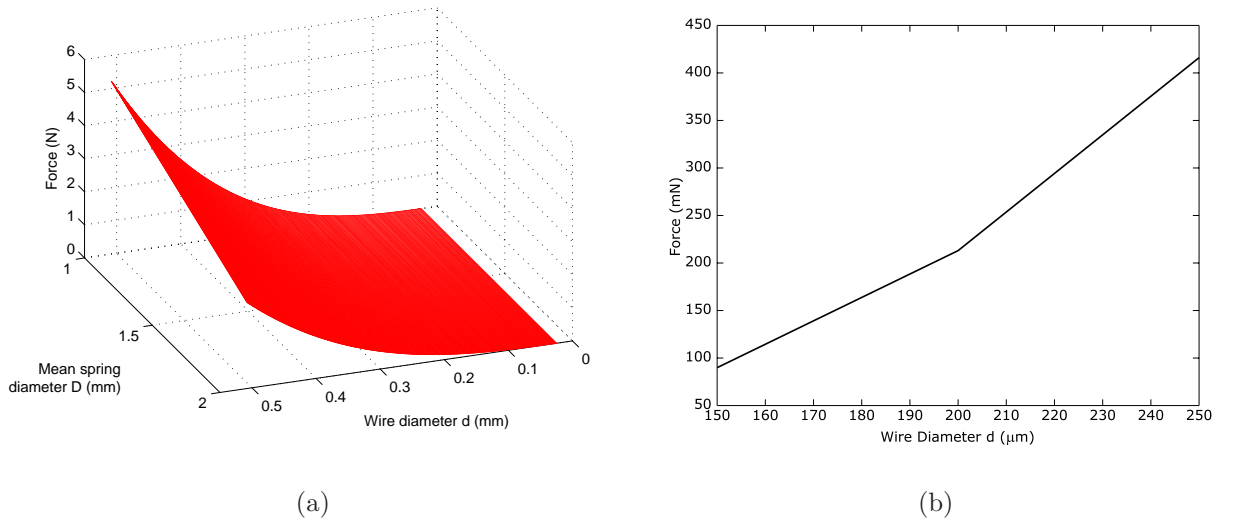


Figure A.1: (a) Tensile force exerted as a function of geometrical parameters  $D$  and  $d$  and (b) 2D representation of the region of interest.

$$\gamma_a = \frac{\tau_p}{G_a} = \frac{127}{28200} = 0.0045$$

$$\gamma_m = \frac{\tau_p}{G_m} = \frac{127}{10500} = 0.0121 \quad (\text{A.5})$$

$$\gamma_\delta = \gamma_a - \gamma_m = 0.0076$$

The number of active coils is obtained for the desired stroke ( $\delta=2$  mm) as follows:

$$N = \frac{Gd\delta}{\pi D^2 \tau_p} = \frac{d\delta}{\pi D^2 \gamma_\delta} = 11.63 \quad (\text{A.6})$$

Therefore, the dimensions of the spring which will deliver the required force and stroke for our application are:  $d=200 \mu\text{m}$ ,  $D=1.2$  mm and  $N=12$ .

**Note:** Implementation procedures required to modify slightly the value of  $D$  to 1.3 mm. Dimensions of the actual prototype are:  $d=200 \mu\text{m}$ ,  $D=1.3$  mm and  $N=12$ .



---

# Appendix B

## Experimental Platforms

---

### B.1 Measurement of electrical resistance

The experimental setups used to measure the spring's electrical resistance  $R$  are shown in figure B.1. The platforms simply consist of an XYZ translation table, a multimeter, a DC power source and a thermocouple.

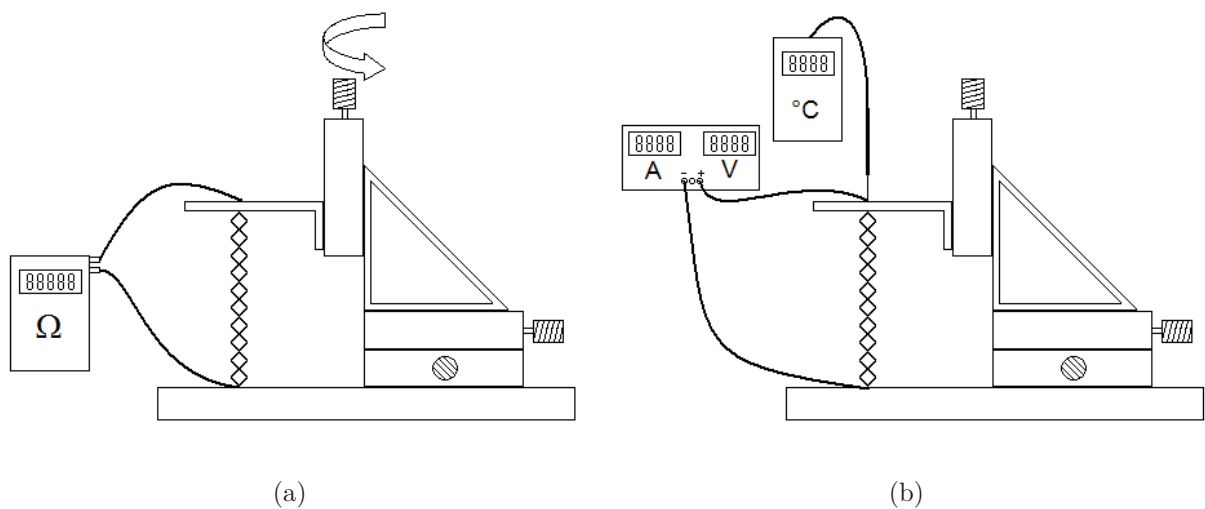


Figure B.1: Schematic representation of the experimental setups used to measure the spring's electrical resistance.

Two kinds of tests were performed:

- 1) Measurement of  $R$  as a function of deflection (Figure B.1(a)).
- 2) Measurement of  $R$  as a function of temperature (Figure B.1(b)).

For the first case, measurements were simply performed using the multimeter and manually increasing the spring's deflection with the XYZ table. Samples were taken every millimeter.

For the second case, a DC power source was used to induce the Joule heating effect and gradually increase the spring's temperature, which was monitored by the thermocouple. Samples were taken every  $5^{\circ}\text{C}$ . Being impossible to measure  $R$  with a multimeter (remember a current flows through the spring),  $R$  was obtained by Ohm's law from the voltage/current values displayed on the power source.

To guarantee the repeatability in the results, the following precautions were taken:

- 1) Practically identical environment conditions (air flow and ambient temperature).
- 2) Identical pre-strain: "erasing" the deformed shape before any measurement by means of thermal cycling without load.
- 3) Careful mechanical and electrical fixation of the SMA and instrumentation to avoid external perturbations in the measurements.

## B.2 Measurement of SMA thermal properties

Figure B.2 shows the testing system used to evaluate the spring's thermal behavior. The platform consists of an XYZ translation table, a DC power source, a thermocouple and an LVDT (linear variable differential transformer).

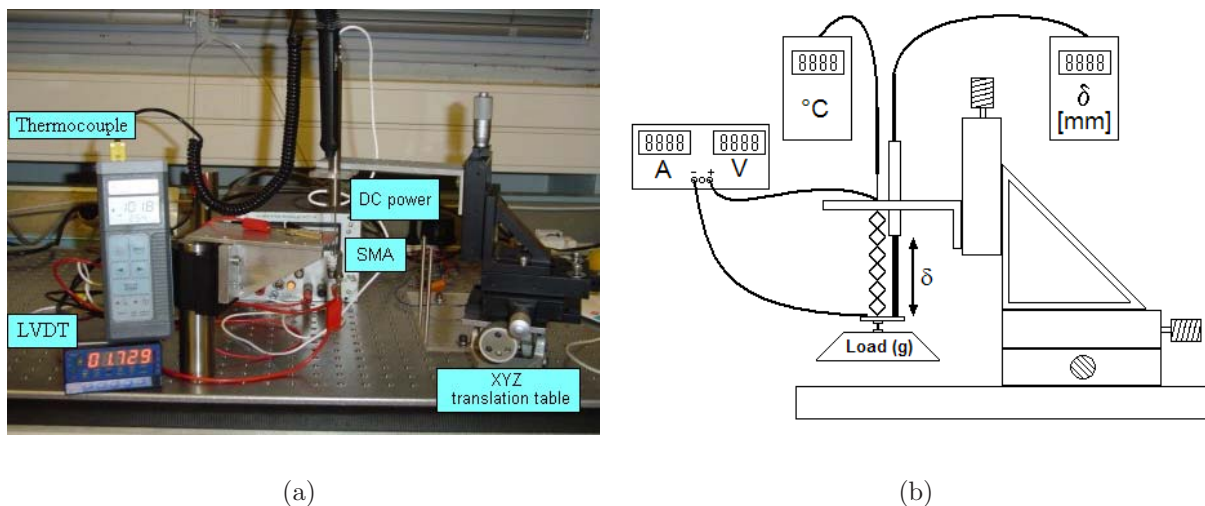


Figure B.2: Experimental setup used to measure the spring's thermal behavior: (a) photo and (b) schematic representation.

This platform allows the measurement of the spring's deflection and temperature (using the LVDT and thermocouple, respectively) as a function of the input current and stress applied (using the DC power source and a load).

The thermocouple has a sampling rate of 0.6 s while the LVDT samples data every 20 ms.

Both LVDT and thermocouple are equipped with serial ports for communication with a PC. Results were finally processed with MATLAB<sup>1</sup>.

As seen from figure B.2, these experiments involve deflection of the spring. This implies that, while one spring end is mechanically fixed, the other one moves carrying the LVDT and the power cable that closes the electric circuit to provide energy. Careful mechanical fixation of these three elements had to be implemented. The total mass of this fixation was estimated at 4 g (or a 1.24 MPa stress), which had to be taken into account for all measurements.

### B.3 Measurement of SMA mechanical properties

Figure B.3 shows the experimental platform, a tensile-like machine, that was implemented to measure the spring's mechanical properties. The platform consists of an XYZ translation table, a DC power source, a thermocouple and a load cell (force sensor).

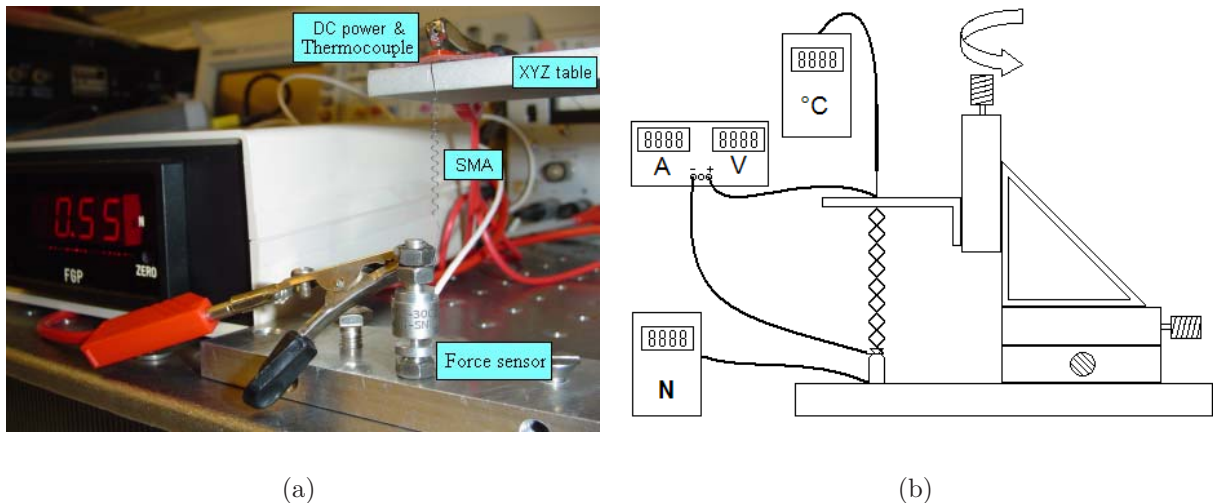


Figure B.3: Experimental platform used to measure the spring's tensile behavior: (a) photo and (b) schematic representation.

This platform allows the measurement of the force developed by the spring as a function of temperature and deflection.

<sup>1</sup>The MathWorks Inc.



The force was monitored by the load cell while the temperature induced by an input current was measured with the thermocouple. Tests performed at room temperature did not need thermocouple nor power source. Deflection was manually induced with the XYZ table. Samples were taken at different deflection values according to the experiment.

Table B.1 summarizes the equipment used in this section.

<b>Equipment</b>	<b>Supplier</b>	<b>Model</b>
Thermocouple	Impac	Tastotherm MP2001 (Type K)
LVDT	Sensorex	LVDT sensor Alpha-LSE 6510
Load cell	FPG Sensors	M210 ABS
XYZ translation table	Mitutoyo	-
DC power source	HQ Power	PS-23023
Multimeter	Tenma	Precision series 72-7745

Table B.1: Equipment used in the experimental platforms.

---

## Appendix C

# Cooling Flow Rate

---

The miniature fan used as cooling system is a 12 V DC axial fan from PAPST Inc. (400F series). Its compact dimensions and weight (40 x 40 x 10 mm, 17 g) allow an easy integration into the tactile display. According to the manufacturer's data sheets, it provides a volumetric flow rate estimated in 8 m<sup>3</sup>/h.

Air velocity  $\omega$  (or flow rate in m/s) can be calculated by dividing the volumetric flow rate by the cross-sectional area of the air flow passage or duct. Figure C.1 shows the miniature fan installed in the tactile display's rectangular enclosure.

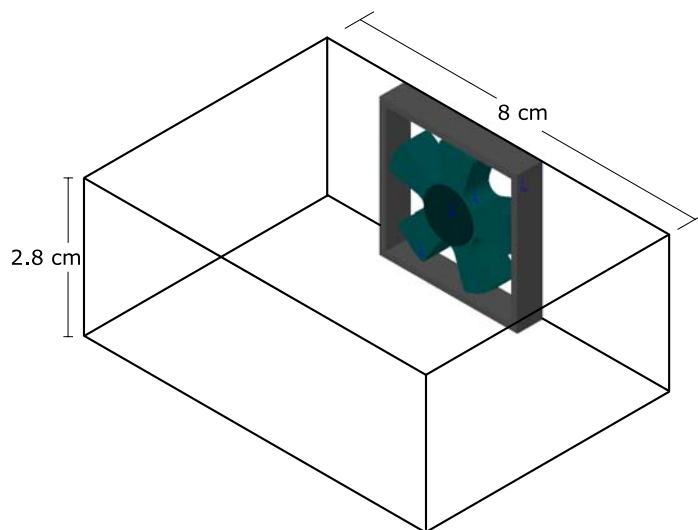


Figure C.1: Fan in a rectangular duct.

Thus, the cross-sectional area of the display's enclosure is 0.0022 m<sup>2</sup>.

Calculation of  $\omega$  is immediate: 1 m/s.

---

# Appendix D

## Résumé des travaux

---

Ce travail de thèse s'inscrit dans le cadre du projet *Lunettes Intelligentes*, qui a pour ambition la réalisation d'un système électronique d'aide aux déplacements indépendants en toute sécurité des déficients visuels. Ce projet vise à concevoir et à réaliser un système fournissant aux utilisateurs (les aveugles, les mal-voyants et les personnes âgées) une information sur la disposition spatiale des obstacles localisés dans leur environnement immédiat. Le prototype se compose d'un système de vision stéréoscopique et d'une surface à stimulation tactile. Deux mini-caméras montées sur l'armature des lunettes de l'utilisateur détectent les obstacles et transmettent ces informations à une interface tactile, qui représentent leurs positions sur la scène telle une carte. L'utilisateur explore librement la carte tactile et est capable de reconstruire et de comprendre la structure de l'environnement.

### D.1 Le système Lunettes Intelligentes

Le système *Lunettes Intelligentes (LI)* est une nouvelle aide à la mobilité basée sur la substitution/suppléance sensorielle qui tente de redonner les informations visuelles essentielles pour la navigation (dont on se sert habituellement pour percevoir l'espace extra-personnel), et de les communiquer aux déficients visuels via le sens de toucher.

Le système LI se compose de deux modules: un module de vision et une interface tactile [Pissaloux02]. La figure D.1 montre le concept de navigation proposé par les LI et résume son mode opératoire. Le module de vision est conçu pour l'analyse, l'optimisation et la

retranscription d'informations sur les obstacles se trouvant dans l'environnement 3D le plus proche du déficient visuel. Deux images stéréo sont à la base de l'acquisition de l'information visuelle (Figure D.1(b.1)). Différents algorithmes de vision permettent de localiser les obstacles dans l'environnement 3D et de retranscrire cette information en une représentation tactile (Figure D.1(b.2)); cette dernière est affichée sur l'interface à stimulation tactile pour une exploration rapide avec la main (Figure D.1(b.3)). Soulignons que ce mode d'exploitation de l'information est assez intuitif pour les déficients visuels et semble être facilement et rapidement compris.

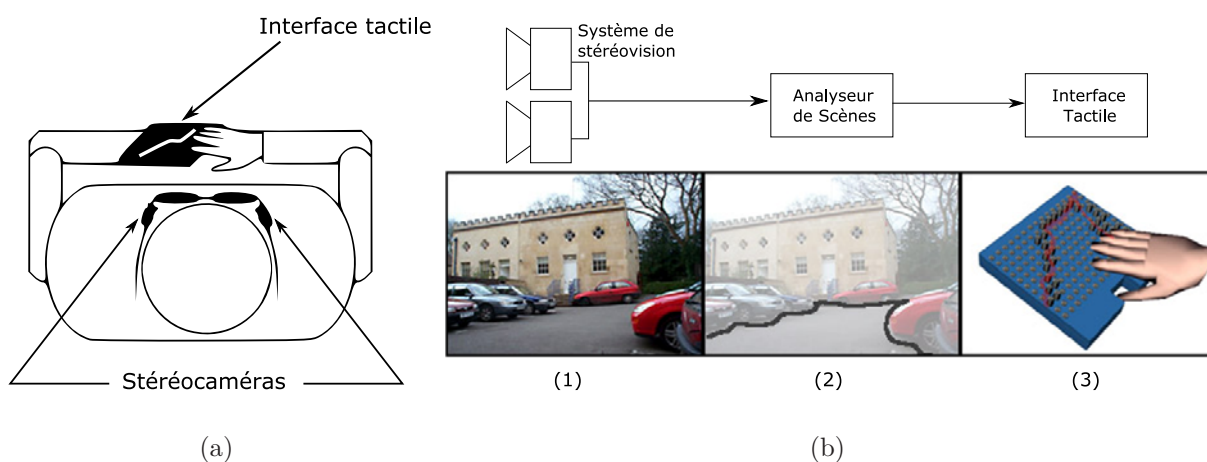


Figure D.1: (a) Concept de navigation avec le système Lunettes Intelligentes et (b) son mode opératoire: (1) l'image mosaïque obtenue avec le système de stéréovision, représentant l'environnement immédiat, (2) les obstacles dans la scène sont localisés par l'intermédiaire des algorithmes de vision et sont affichés via leur contour (3) sur l'interface tactile, l'identification de leur position permet alors d'en déduire la trajectoire à suivre.

Ce travail de thèse se concentre sur la conception et le prototypage de l'interface tactile. Les travaux concernant le module de vision sont détaillés dans [Maingreud05].

### D.1.1 Interface tactile

Les interfaces tactiles et leurs dispositifs associés sont dédiés à stimuler la peau, en particulier le bout des doigts, pour générer des sensations de contact via le toucher. Typiquement, les interfaces tactiles se composent d'une matrice 2D dont le relief est commandé par des actionneurs mécaniques appelés *taxels* (éléments tactiles de l'interface).

Depuis des décennies, les interfaces tactiles ont principalement été utilisées pour la transmission de l'information aux déficients visuels. Mais leurs vraies possibilités n'ont été révélées que récemment, lorsque le sens du toucher est devenu l'une des possibilités d'interaction à travers les ordinateurs: réalité virtuelle, robotique, télémanipulation, jeux et divertissements; depuis peu, la réhabilitation (pour le traitement des maladies cognitives et comportementales) envisage leur utilisation à des fins thérapeutiques.

Les systèmes de lecture utilisant le code Braille sont les outils à stimulation tactile les plus populaires. Ces interfaces sont souvent basées sur la technologie piézoélectrique. Actuellement, l'inconvénient principal de ces dispositifs est leurs prix (leur coût varie entre 3000 et 16000 €). Par ailleurs, l'affichage de l'information graphique en 2D est pratiquement impossible dû à l'encombrement de ces actionneurs piézoélectriques. De plus, la portabilité des interfaces de Braille est limitée (systèmes de 1 kg pour des dimensions de: 25 x 15.5 x 5 cm<sup>3</sup>) [HumanWare].

Plusieurs équipes de recherche ont développé des prototypes d'interface à stimulation tactile en cherchant une mise en oeuvre plus efficace, tant au niveau de l'encombrement et des performances temporelles que du coût. Elles explorent les différentes technologies d'actionnement: électromagnétique ([Wagner02], [Benali-Khoudja04], [Fischer95]), piézoélectrique ([Pasquero03], [Summers02]), pneumatique ([Moy00]), alliages à mémoire de forme (AMF) ([Taylor97a], [Wellman97]), polymères électroactifs ([Konyo00]) et fluides électrorhéologiques ([Taylor98b]). Chacune de ces technologies a ses propres avantages et inconvénients (cf. tableau 1.1 du chapitre 1) et, en raison du compromis entre contraintes temporelles, spatiales, force d'actionnement, capacité d'intégration et coût, aucune n'est optimale pour la réalisation des interfaces tactiles.

### D.1.2 Critères de conception d'une interface tactile pour le système LI

L'objectif fondamental de cette recherche est de concevoir et de réaliser une interface à stimulation tactile qui restitue avec précision l'information provenant de l'extérieur (l'information fournie par le système de vision stéréoscopique) pour la transmettre à l'utilisateur en vue d'assister son interaction avec l'espace.

Aussi, l'acceptation (l'appropriation) du système LI par les utilisateurs dépendra principalement de la nature de l'interface tactile; si sa manipulation est suffisamment aisée et fiable, et l'information fournie est pertinente pour la tâche visée, le système LI sera évidemment plus facilement adopté. Afin de réaliser une interface tactile optimale, nous considérerons les critères globaux de conception suivants [Velazquez04f]:

1. Le système tactile doit être facile à manier et exiger peu ou pas d'apprentissage spécifique. Cela implique que l'utilisateur doit pouvoir l'employer de manière quasi-intuitive.
2. Le dispositif doit être portable. L'interface tactile doit être légère et de petites dimensions. Une petite surface tactile permettra un balayage rapide. Ceci est essentiel afin de pouvoir prendre des décisions rapides au moment des déplacements. Il est également important que le dispositif soit d'un encombrement réduit et très discret (facteurs essentiels pour les déficients visuels et personnes âgées).
3. Il est aussi souhaitable que l'interface soit à bas coût, afin qu'elle puisse avoir un avantage certain sur les dispositifs disponibles dans le commerce et dans le but d'une production industrielle future.

Concernant les spécifications fonctionnelles et physiques des interfaces tactiles, quatre paramètres doivent être pris en compte selon l'application visée: résolution spatiale, bande passante, force et débattement d'actionnement.

La psychophysiologie du sens du toucher impose des contraintes qui guident le choix de ces paramètres pour l'application des LI:

1. Résolution spatiale. Plusieurs études physiologiques du sens du toucher ont été faites afin de mieux comprendre les différents récepteurs de la peau humaine ([Geiger84], [Sekuler02], [Johansson83]). Ces études prouvent que les sensations perçues lors d'un contact mécanique passent principalement par les *mécanorécepteurs* et plus particulièrement lors de l'exploration fine d'un objet par les corpuscules de Meissner. Au bout des doigts, la densité des corpuscules de Meissner peut atteindre les 140 unités/cm<sup>2</sup>. Cela correspond à un espacement de centre en centre, entre deux unités adjacentes de 0,9 mm. Cependant, le sens du toucher humain ne peut pas atteindre cette résolution. Notre sens du toucher ne peut discriminer deux points qu'à partir d'un seuil de 2 à 3 mm (2,54 mm est le seuil standard adopté par les interfaces de Braille). Ainsi, pour bien stimuler les corpuscules de Meissner du bout des doigt, la distance entre 2 points de contact de l'interface, et donc sa résolution, doit être de l'ordre de 2,54 mm.
2. Force d'actionnement. Chaque actionneur doit pouvoir résister à la force de contact des doigts ou de la paume pendant le processus exploratoire. Plusieurs études sur la force de contact entre le doigt et la surface d'exploration indiquent qu'une force d'entre 50 et 100 mN s'applique en exploration normale. Au delà, il s'agit d'une force de contact intentionnellement violente [Loomis81]. En conséquence, la force minimale délivrée par l'actionneur doit être de 100 mN.
3. Bande passante et débattement d'actionnement. La figure D.2 montre la relation entre fréquence et amplitude de déformation subie par la peau pour la détection de stimuli mécaniques dans les récepteurs de Meissner.

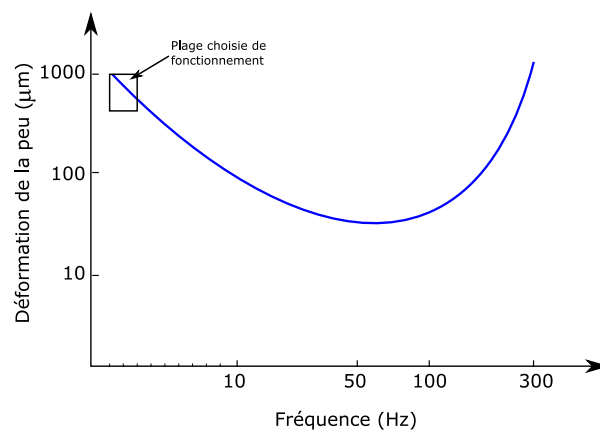


Figure D.2: Seuil de détection minimal de déformation de la peau en fonction de la fréquence dans les corpuscules de Meissner, d'après [Sekuler02].

La plage de fonctionnement choisie pour l'interface est: fréquences de 1 à 3 Hz et amplitudes de déformation de la peau, et donc d'actionnement, de 0,7 à 1 mm.

## D.2 Les alliages à mémoire de forme

Le tableau 1.2 du chapitre 1 suggère que les alliages à mémoire de forme peuvent constituer une approche appropriée pour répondre aux exigences d'actionnement du problème posé.

La famille des *alliages à mémoire de forme (AMF)* désigne une classe de matériaux qui, après déformation permanente à basse température, retrouvent leur forme initiale non déformée par simple élévation de température. Cette propriété, désignée par le terme *effet à mémoire de forme (EMF)*, est illustrée par la figure D.3. Les AMF ont deux états structuraux principaux, l'un à haute température, appelé *austénite*, et l'autre à basse température, appelé *martensite*. C'est lors du retour à son état austénitique que l'AMF est capable de générer un travail mécanique et donc d'entraîner une charge. C'est l'EMF des AMF que l'on exploite pour l'actionnement.

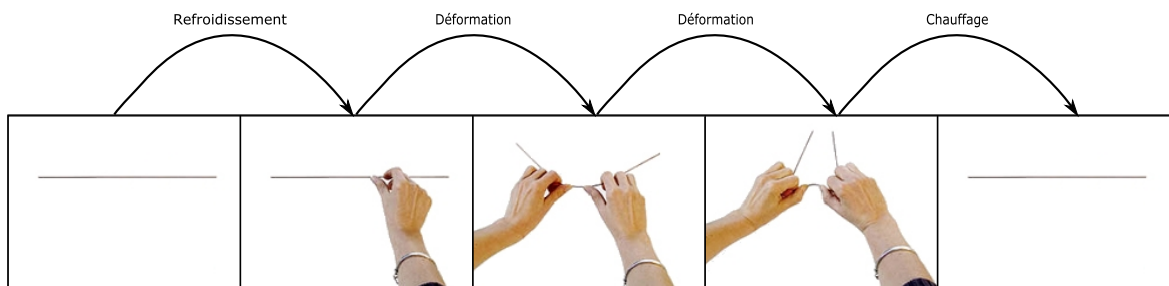


Figure D.3: Effet mémoire de forme.

Les AMF offrent plusieurs caractéristiques remarquables pour des applications telles que les micro-actionneurs ou les structures actives: simplicité, dimensions compactes, rapport poids/puissance, activation propre et silencieuse, haute résistance à la fatigue et faible coût [Ikuta90].

Mais les AMF présentent aussi quelques inconvénients potentiels pour la réalisation d'interfaces tactiles: faibles débattements liés à une déformation relative de 4 à 5 %, faibles bandes passantes liées au processus de refroidissement (autour de 0,1 Hz), comportement fortement non linéaire rendant sa commande complexe, et le besoin de structures de blocage pour maintenir la position active de l'AMF sans énergie.

Ce travail propose un concept d'actionnement à base d'AMF aux grandes performances qui sera la base de l'interface tactile du système LI:

1. Nous proposons d'utiliser un ressort hélicoïdal en AMF comme l'élément actif d'un actionneur à stimulation tactile. Comparés avec les fils AMF, les ressorts ont un débattement beaucoup plus important. Des courses de 300% peuvent facilement être obtenues en utilisant des ressorts. Cependant, comme ils opèrent en torsion plutôt qu'en traction, ils ne peuvent pas développer la même force. On démontrera que les ressorts en AMF peuvent être conçus pour développer des forces appropriées



pour les applications tactiles, et en même temps offrir une course et une compacité que l'on ne peut pas obtenir avec des fils.

2. Nous proposons un système simple et à faible coût de convection forcée pour accélérer le processus de refroidissement et améliorer la bande passante des AMF par l'utilisation d'un mini-ventilateur intégré au dispositif de l'interface tactile.
3. Nous proposons une conception d'actionneurs tactiles qui assurent le maintien des positions actives des AMF en utilisant leurs propres propriétés mécaniques, évitant l'utilisation de structures de blocage et ne nécessitant ainsi qu'une simple commande binaire.

## D.2.1 Élément actif en AMF

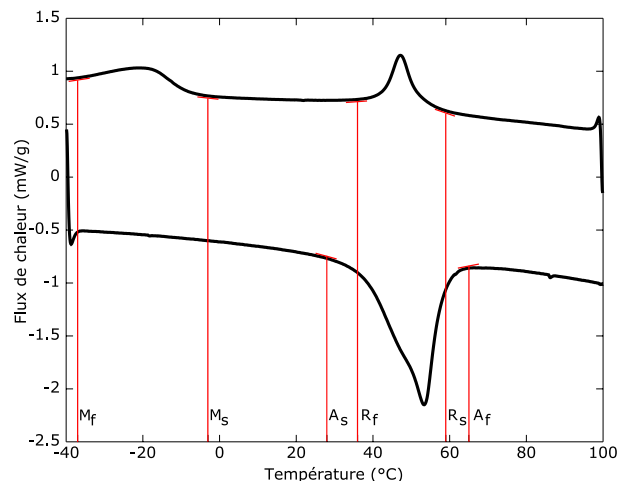
### D.2.1.1 Matériaux

Un ressort hélicoïdal en AMF a été fabriqué en utilisant un fil Flexinol-200 (de composition  $\text{Ni}_{52}\text{Ti}_{48}$ ) ayant les caractéristiques géométriques suivantes: fil de  $200\ \mu\text{m}$  de diamètre,  $1,5\ \text{mm}$  de diamètre externe d'enroulement et 12 spires actives. Sa longueur est de  $7\ \text{mm}$  et son poids est de  $30\ \text{mg}$  (Figure D.4(a)).

La forme hélicoïdale a été fixée par un traitement thermique de recristallisation dans lequel le matériau a été soumis à  $500^\circ\text{C}$  pendant 5 min. Les températures stables de transition déterminées par mesure calorifique différentielle (DSC) sont  $65, 28, 59, 36, -3$  et  $-37^\circ\text{C}$  pour  $A_f, A_s, R_s, R_f, M_s$  et  $M_f$ , respectivement (Figure D.4(b)) [Velazquez06a].



(a)



(b)

Figure D.4: (a) Ressort NiTi et (b) températures de transition déterminées par analyse DSC.

### D.2.1.2 Évaluation analytique et expérimentale du comportement thermo-mécanique du ressort en AMF

Le comportement en torsion des matériaux en AMF a fait l'objet de recherches, notamment pour modéliser le comportement des ressorts. Un modèle élasto-plastique a été proposé par Tobushi et Tanaka [Tobushi91b] pour modéliser la force et la course envisageables avec un ressort hélicoïdal en AMF. En considérant simplement les paramètres géométriques du ressort, ce modèle donne une relation force-déformation-température (D.1) comme suit:

$$F = \begin{cases} \frac{G\delta^4}{8ND^3}\delta & \delta < \delta_e \\ \frac{\pi\tau_p d^3}{6D} \left[ 1 - \frac{1}{4} \left( \frac{\pi ND^2 \tau_p}{dG\delta} \right)^3 \right] & \delta \geq \delta_e \end{cases} \quad (\text{D.1})$$

avec:  $\delta_e = \frac{\pi D^2 N \tau_p}{Gd}$  et:  $\tau_p = \begin{cases} c_m (T - R_s) & \text{charge} \\ c_a (T - A_s) & \text{décharge} \end{cases}$

où  $F$  est la force en traction développée par le ressort en AMF, fonction de la déformation  $\delta$ ,  $d$  est le diamètre de fil,  $D$  le diamètre d'enroulement du ressort,  $N$  le nombre de spires actives,  $G$  le module de cisaillement,  $\tau_p$  la contrainte maximale en torsion,  $\delta_e$  la limite des régions élastique et plastique, et  $c_m$  et  $c_a$  sont des constantes propres au matériau correspondant aux conditions de transformation.

Pour le matériau NiTi, les résultats expérimentaux en [Tobushi91b] indiquent 28.2 GPa et 10.5 GPa pour le module austénitique et martensitique de cisaillement  $G$  respectivement et estiment  $c_m=6.3$  MPA/K et  $c_a=4.9$  MPA/K.

La figure D.5(a) compare les performances analytiques (trait continue) et expérimentales (trait pointillé) du ressort proposé pour une déformation maximale de 10 mm. Dans les deux cas, simulation et expérimentation, on considère que l'ensemble de ce matériau est dans une phase unique, i.e. austénite et martensite pures (20, 85 et 105°C).

On peut observer que la simulation donne de bons résultats quant à la prédiction du comportement force-déformation. On remarque que la force développée par le ressort augmente avec la température: 180 mN à 20°C, 410 mN à 85°C et 720 mN à 98°C. Par ailleurs, les courbes de décharge indiquent l'hystérésis mécanique de l'AMF lorsque celui-ci est en train de récupérer sa forme initialement mémorisée. On remarque que, pour les températures austénitiques (85 et 105°C), la forme mémorisée est parfaitement retrouvée, ce qui n'est pas le cas pour les températures martensitiques (20°C).

La figure D.5(b) présente une représentation phénoménologique du comportement du ressort dans l'espace force-déformation-température. Nos observations expérimentales ont montré qu'au delà de 105°C, le comportement force-déformation du ressort était pratiquement constant [Velazquez06a]. Ces observations sont intégrées dans la représentation 3D.

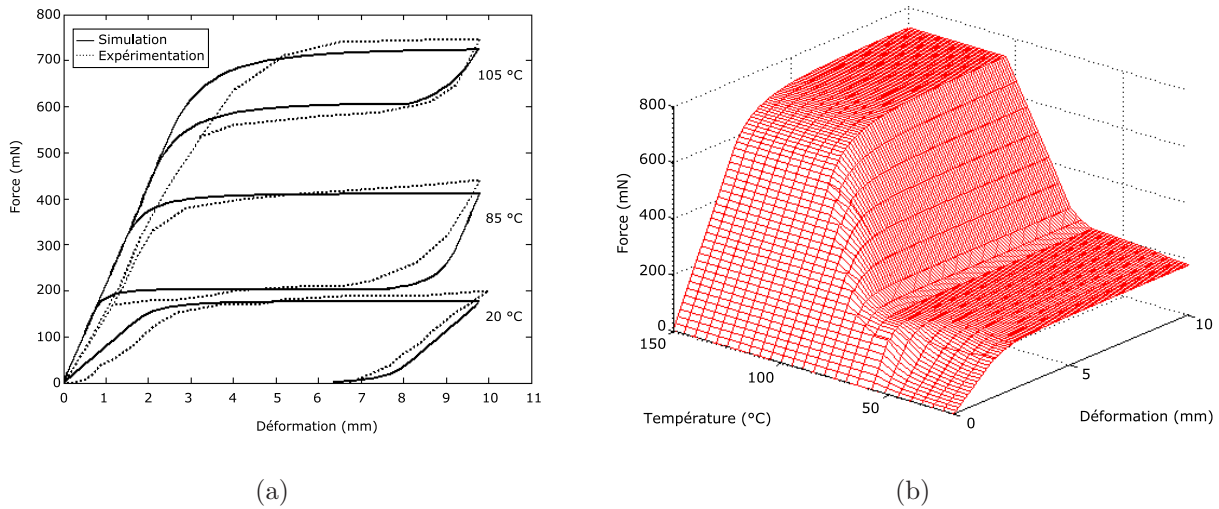


Figure D.5: Relations force-déformation du ressort NiTi : (a) Confrontation des mesures expérimentales et de simulation à températures constantes (20, 85 et 105°C) et (b) représentation dans l'espace force-déformation-température du comportement en charge.

On remarque que le ressort pesant 30 mg est capable de développer des forces de l'ordre de 410 mN lorsqu'il est activé dans sa phase austénitique (85°C), soit 1360 fois son propre poids et 4 fois la force nécessaire pour l'application visée.

### D.3 Actionneur tactile

Ce ressort est à la base d'un actionneur miniature pour l'affichage tactile d'informations. Nous proposons un actionneur tactile ou *taxel* basé sur le principe d'un montage antagoniste des AMF. La figure D.6 montre le prototype d'actionneur construit avec une paire de ressorts en AMF. Cet actionneur mesure 1,5 mm de diamètre, 45 mm de longueur et son poids est de 150 mg. Son coût de réalisation est de 2 € [Velazquez05d].

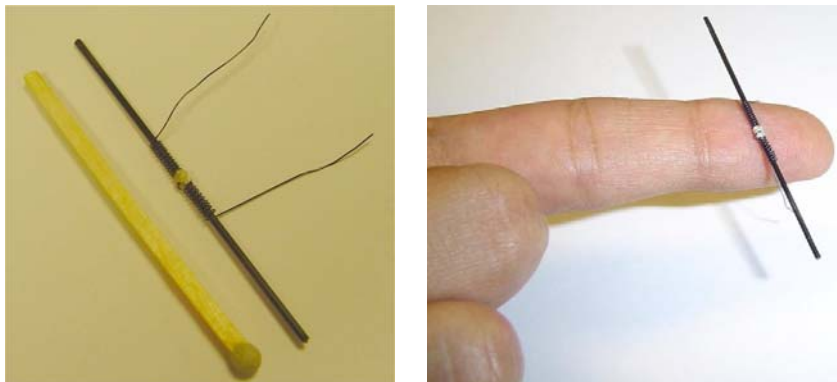


Figure D.6: Actionneur miniature basé sur le principe de montage antagoniste de deux ressorts en AMF.

Son principe d'opération est montré sur la figure D.7. En position initiale (1) le taxel est sorti. Les deux ressorts en AMF sont identiquement précontraints et en état martensitique. (2) Quand l'AMF-1 est chauffé de manière électrique, il récupère sa forme initiale comprimée, et allonge l'AMF-2 faisant descendre le taxel. Le taxel est maintenant dans la position rentrée. (3) Quand le courant électrique est désactivé, la température de l'AMF-1 commence à descendre et donc sa force de compression diminue. En conséquence, le taxel tend à remonter. Cependant, il sera démontré qu'il ne reviendra pas à sa position initiale (taxel sorti). La position basse (taxel rentré) est toujours assurée. (4) Pour remonter le taxel, l'AMF-2 est activé. Lors du refroidissement, la position initiale sera atteinte.

Considérons que la surface soit explorée avec le bout des doigts. Sur la figure (5), comme il a été montré en (1), la configuration par défaut du taxel est celle où les deux ressorts en AMF sont en état martensitique et le taxel est en position sorti. Cette configuration doit au moins être capable de résister aux forces de contact ( $F_e$ ) développées lors d'une exploration normale (100 mN). (6) Si une force supérieure est appliquée (une exploration intentionnellement violente), la tête du taxel descendra au niveau de la surface. (7) Lorsque la force redeviendra nulle, le taxel remontera naturellement pour récupérer sa configuration initiale (taxel sorti).

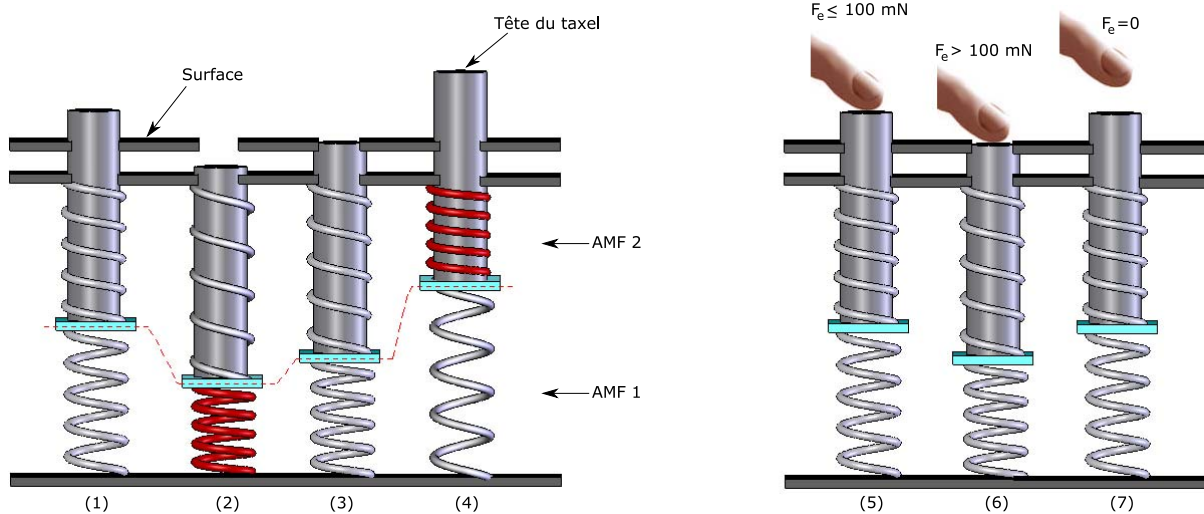


Figure D.7: Principe d'opération du taxel proposé.

Les trois avantages principaux de ce concept d'actionnement sont :

1. Le taxel est un actionneur bistable dont les deux états d'équilibre sont parfaitement stables.
2. L'actionneur n'a pas besoin des structures mécaniques de blocage pour maintenir sa position active. Les positions haute et basse sont assurées par les propres caractéristiques mécaniques des ressorts.
3. Le comportement dynamique est symétrique (les deux ressorts en AMF sont identiques).

4. Le problème de commande est réduit à une opération binaire: taxel totalement sorti ou taxel totalement rentré. Chaque ressort ne peut prendre que deux états: austénitique (haute température et comprimé) ou martensitique (basse température et allongé) et aucune forme intermédiaire.
5. Son faible coût et sa simplicité de réalisation sont des atouts importants.

Pour se convaincre de l'efficacité de ce principe, considérons les deux ressorts montés en série puis identiquement précontraints (distance  $O-\delta_0$  et  $O'-\delta_0$  sur la figure D.8 en équilibre martensitique en point  $\delta_0$  (Figure D.8(1)). Lors de l'échauffement du ressort inférieur, le nouveau point d'équilibre atteint  $B$  est défini par l'intersection de la courbe austénitique et de la courbe martensitique du ressort supérieur (Figure D.8(2)). Lors du refroidissement, les sollicitations mécaniques exercées sur le ressort inférieur vont diminuer progressivement. En conséquence, le point d'équilibre ne suivra pas la trajectoire  $B-\delta_0$  mais plutôt la trajectoire  $B-D$  (Figure D.8(3)). Le même phénomène est observé lors du chauffage du ressort supérieur; il va suivre la trajectoire  $\delta_0/D-A-C$  au lieu de  $\delta_0/D-A-\delta_0$  (Figures D.8(4) et D.8(5)).

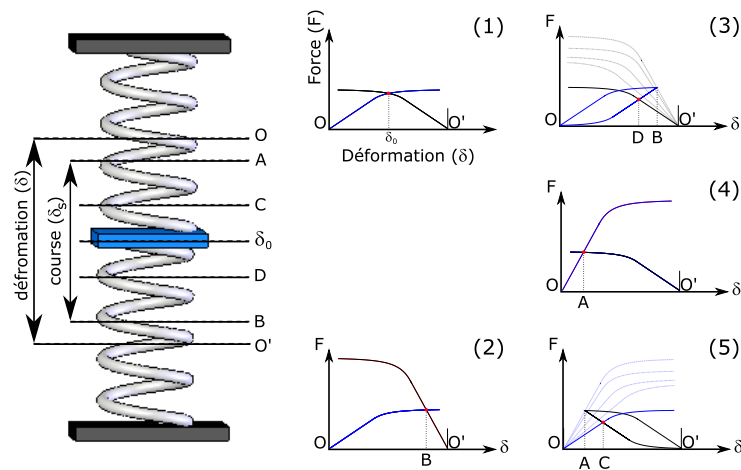


Figure D.8: Principe de fonctionnement antagoniste des AMF: représentation conceptuelle et relations force-déformation pour un cycle d'opération.

Une idée plus complète de la trajectoire thermomécanique suivie par le point d'équilibre est montrée sur la figure D.9. On remarque que le point initial  $\delta_0$  n'est pas retrouvé en raison de la caractéristique martensitique du ressort.

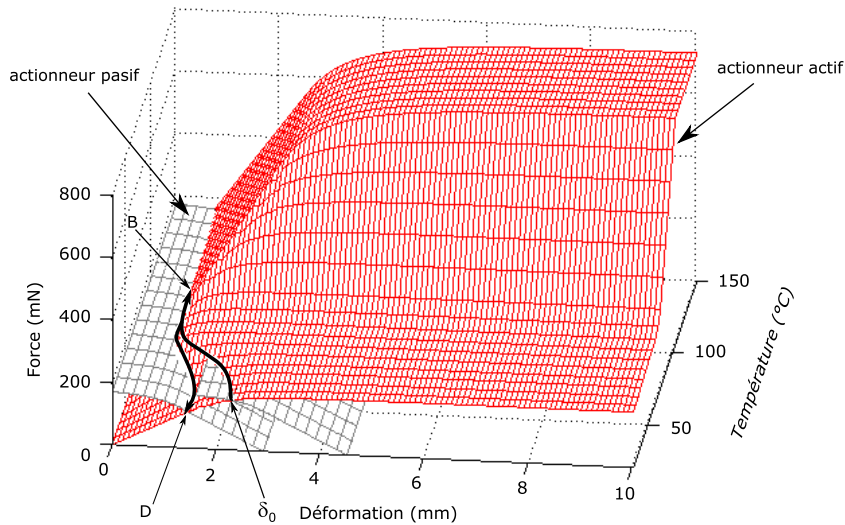


Figure D.9: Principe de fonctionnement antagoniste des AMF: trajectoire thermomécanique dans l'espace force-déformation-température.

La figure D.10 montre la relation entre la force externe  $F_e$  et le déplacement du taxel lors du processus d'exploration de l'utilisateur avec ses doigts. On remarque qu'une force de 102 mN est nécessaire pour faire descendre la tête du taxel au niveau de la surface.

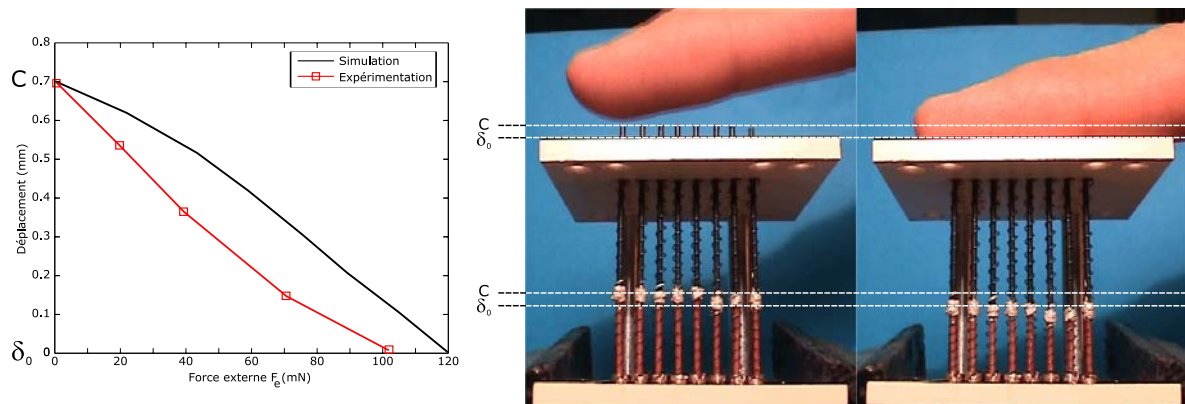


Figure D.10: Performance du taxel lors de l'application d'une force externe  $F_e$  : concept bistable sans structures additionnelles de blocage.

Afin d'évaluer la bande passante du taxel, la plate-forme expérimentale de la figure D.11 a été implantée. Rappelons que l'une des contraintes de l'actionneur antagoniste est que à aucun moment les deux ressorts ne doivent être activés en même temps. A cet effet, un interrupteur inverseur a été utilisé pour activer alternativement les ressorts 1 et 2.

Les courbes D.11(a.1) et (a.2) montrent la réponse en position du taxel aux fréquences respectives de 0,27 et 0,37 Hz. On remarque que si la fréquence augmente, la réponse du taxel devient problématique: le temps disponible pour le refroidissement diminue jusqu'au moment où le système n'a plus suffisamment de temps pour dissiper la chaleur. L'actionneur est alors en état de saturation (Figure D.11(a.2)).

Cet effet de saturation nécessite le développement de stratégies pour augmenter le taux de refroidissement des AMF. Afin de respecter le critère de simplicité et de portabilité de l'interface tactile, un simple mini-ventilateur léger et à bas coût a été utilisé comme système de refroidissement. Les courbes D.11(b.1), (b.2) et (b.3) montrent les réponses de l'actionneur respectivement à 0,5, 1 et 1,5 Hz. On remarque que la bande passante de l'actionneur augmente pour atteindre 1,5 Hz sans saturation en conditions de convection forcée. Cependant, la puissance délivrée au taxel augmente afin d'accélérer le temps de chauffage et assurer la course totale du taxel (distance  $A-B$  sur la figure D.11(a)).

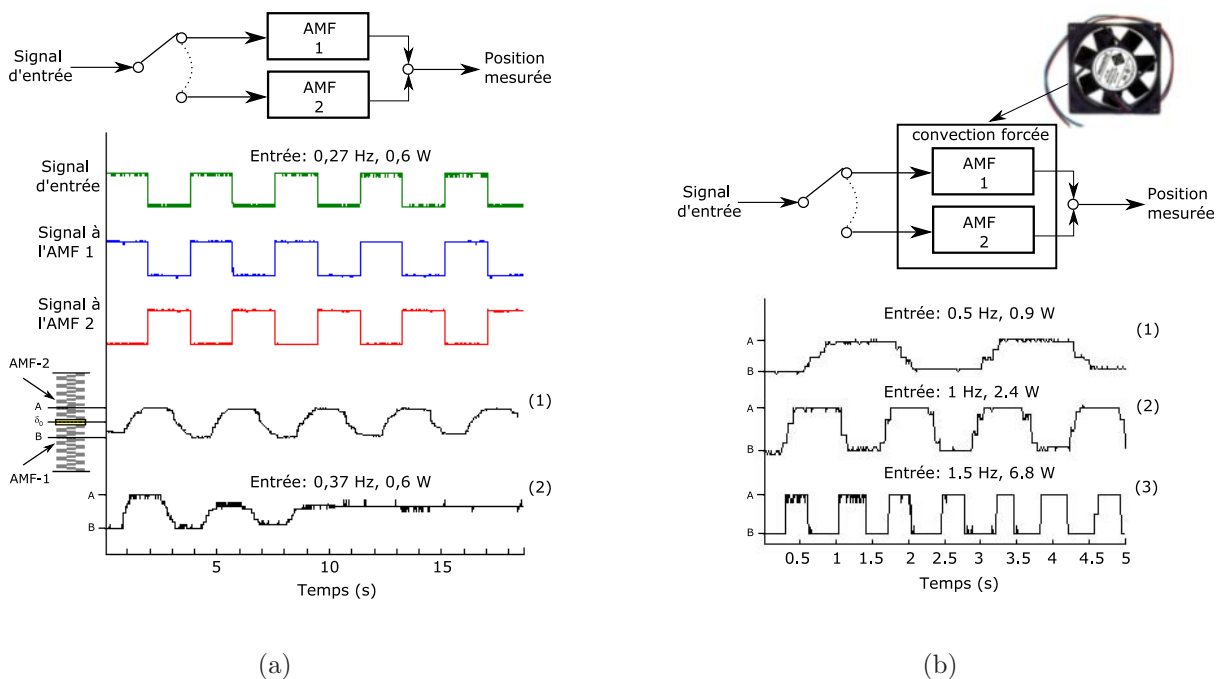


Figure D.11: (a) Le contrôleur antagoniste et ses réponses en position aux fréquences d'entrée de 0,27 et 0,37 Hz. (b) Réponses en position aux fréquences de 0,5, 1 et 1,5 Hz sous conditions de convection forcée.

## D.4 Interface tactile

### D.4.1 Surface à stimulation tactile

Cet actionneur est l'élément de base de l'interface tactile du système LI. Un premier prototype de 8 x 8 taxels a été envisagé. La figure D.12(a) montre la structure de l'interface tactile. Le prototype se compose de 3 plaques qui regroupent l'ensemble de 64 taxels antagonistes. Les taxels seront commandés indépendamment, chauffés électriquement et refroidis en utilisant la convection forcée du mini-ventilateur placé juste à côté des actionneurs [Velazquez05c].

La figure D.12(b) montre le prototype complètement assemblé. L'espacement des micro-actionneurs est de 2,6 mm (le standard de Braille) et permettra d'intégrer les 64 taxels dans un espace équivalent à la surface d'une pièce d'un euro. Le système offre une haute résolution spatiale, en plus d'être robuste et simple à réaliser. Sa conception permettra d'être facilement redimensionné pour un nombre supérieur de taxels tout en conservant un faible coût.

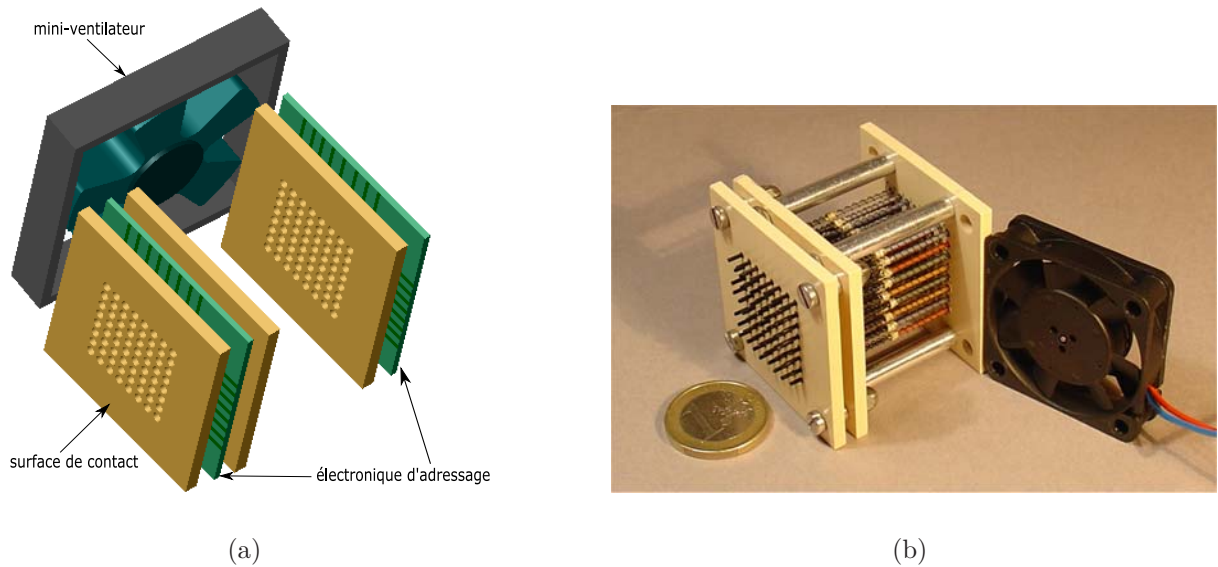


Figure D.12: (a) Concept de l'interface tactile et (b) prototype (64 taxels).

Le dispositif entier pèse 200 g et est compact, ses faibles dimensions (un cube de 8 cm de côté) le rendent facilement portable par l'utilisateur (Figure D.13). Son coût de réalisation est d'approximativement 200 € [Velazquez05c].



Figure D.13: Première version d'une interface tactile portable à bas coût pour les déficients visuels basée sur des micro-actionneurs en alliages à mémoire de forme (AMF).



## D.4.2 Système électronique de commande

La figure D.14 schématise le système électronique utilisé pour commander la surface à stimulation tactile. Le système se compose d'une interface graphique logicielle capable de générer des données tactiles (des formes, figures, séquences, etc). Deux fonctionnalités ont été développées: l'utilisateur peut choisir directement les taxels à activer ou il peut dessiner la forme à afficher. Une carte électronique reçoit via le port série de l'ordinateur la matrice des taxels à activer et traite cette information. Enfin, la surface tactile affiche l'information grâce à des signaux analogiques envoyés par la carte électronique.

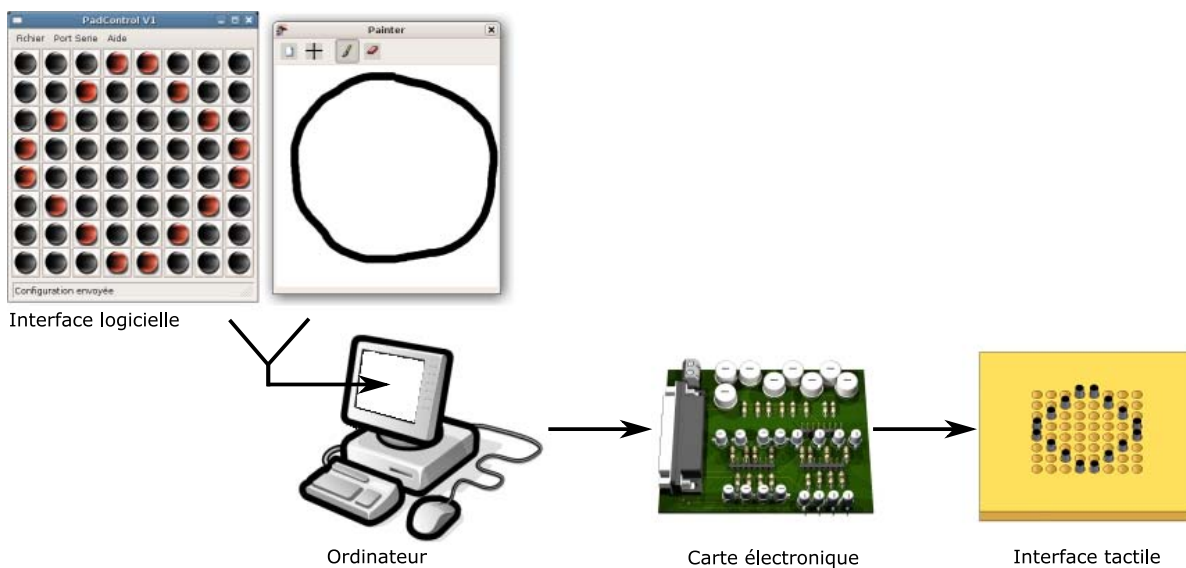


Figure D.14: Système électronique de commande.

Un facteur important à prendre en compte lors de la conception de systèmes électroniques de commande pour dispositifs de type matriciels comme le notre est le problème du redimensionnement à un nombre supérieur d'éléments. Dans une matrice de  $N \times N$  éléments dans laquelle chaque élément est commandé indépendamment, on obtient  $N^2$  éléments électroniques de pilotage. Ce type de contrôleurs est tout à fait envisageable si  $N$  est petit. Cependant, lorsque la taille de la matrice augmente, le nombre d'éléments de pilotage augmente de la même manière. Dans notre cas, la surface tactile est composée de 64 taxels antagonistes, soit 128 éléments en AMF à commander: le schéma de contrôle de taille  $2N^2$  est assez encombrant et coûteux.

Une méthode plus efficace en termes d'encombrement, de simplicité et de coût est la méthode d'actionnement *crossbar* (méthode ligne-colonne). La figure D.15 montre cette méthode d'activation, qui a été adoptée pour piloter la surface à stimulation tactile. On remarque que pour activer un ressort en AMF, il suffit de commander la ligne et la colonne de celui-ci. La taille du schéma de commande est ainsi réduit de  $2N^2$  à  $3N$  [Velazquez06g].

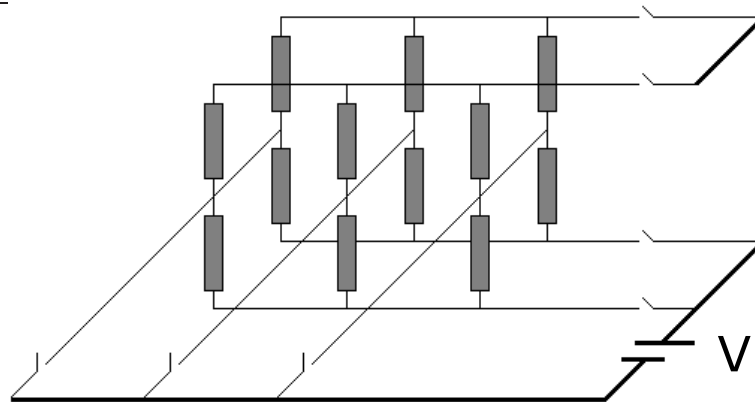


Figure D.15: Contrôleur électronique 3N.

## D.5 Évaluation expérimentale de l'interface tactile et du concept de représentation de l'espace des LI

Des études préliminaires ont été conduites afin d'évaluer les performances de l'interface tactile et de vérifier la pertinence de l'information affichée sur la surface pour la sensibilité et la perception tactile.

Dans ce but, un ensemble de 9 tâches de reconnaissance tactile a été réalisé. L'une d'entre elles est détaillée dans ce résumé. Cette tâche permet d'obtenir un premier retour sur l'efficacité du concept Lunettes Intelligentes et sur sa représentation tactile de l'espace.

Cinq sujets (4 hommes et une femme), étudiants à Paris 6, ont participé volontairement à ce test. Tous les participants étaient des sujets sains, droitiers, sans maladies cognitives connues et sans déficit connu du sens du toucher.

Pendant les tests, les sujets étaient assis, les yeux bandés, devant la surface à stimulation tactile (aucune information visuelle ne pouvait être obtenue) (Figure D.16). Pour l'exploration de la surface, les sujets étaient libres d'utiliser leur main droite ou leur main gauche et aucune limite de temps n'était imposée. Aucun temps d'entraînement ni de familiarisation avec l'interface n'a été accordé aux sujets.

Sous ces conditions l'environnement virtuel de la figure D.17(a) a été proposé aux 5 sujets. Cet environnement était composé de 4 espaces différents (chambres). Les sujets étaient placés à l'entrée de chaque chambre et de ce point, en avaient une certaine vue. La figure D.17(b) montre ces 4 vues ainsi que leur codage tactile affiché sur la matrice 8 x 8 [Fontaine06].

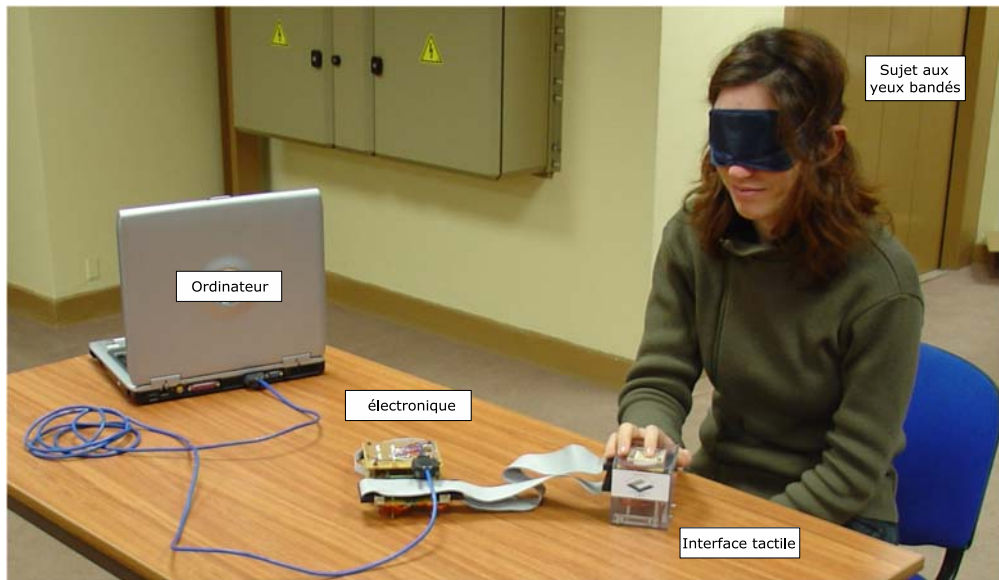


Figure D.16: La plate-forme expérimentale.

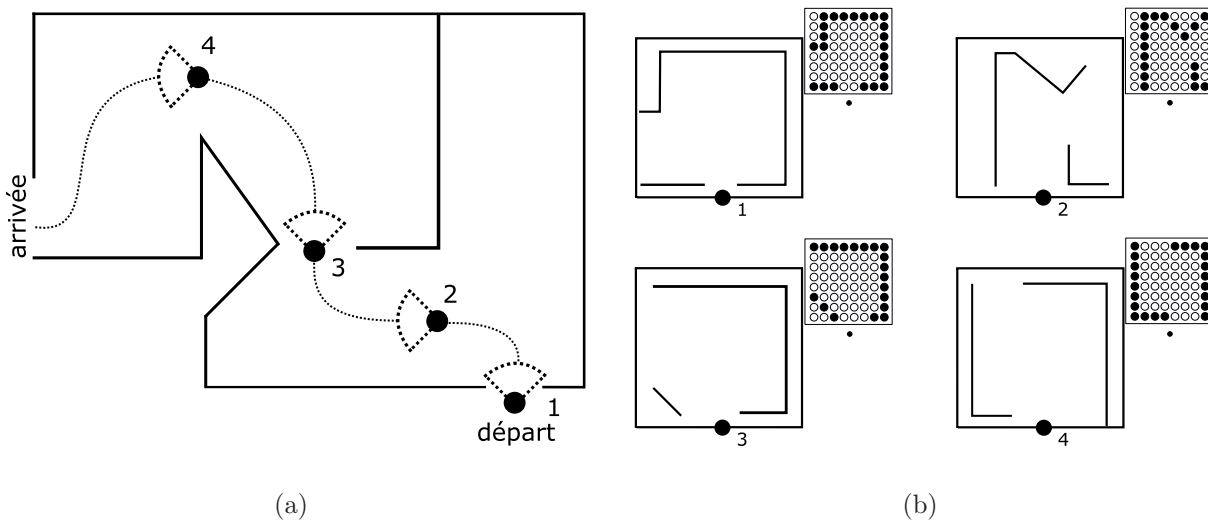


Figure D.17: (a) L'environnement virtuel proposé aux sujets. Le sujet progresse dans l'environnement selon la numérotation indiquée. (b) Les vues du sujet et les représentations tactiles correspondantes. La position du sujet dans l'environnement et sur la surface tactile est indiquée par le point noir.

Il était demandé à chaque sujet d'explorer la surface et, lorsqu'il avait compris complètement la carte tactile affichée, de la dessiner sur une feuille de papier. Une fois les 4 cartes tactiles dessinées, les sujets devaient les assembler pour reconstruire l'environnement de navigation et les 4 choix présentés sur la figure D.18 leur étaient proposés afin de les guider dans cette tâche. Ainsi, en se basant sur les dessins et en sachant qu'une ouverture dans la représentation correspond au point de vue que le sujet aura dans la chambre suivante, il lui était demandé d'identifier l'environnement qui lui semblait être correct.

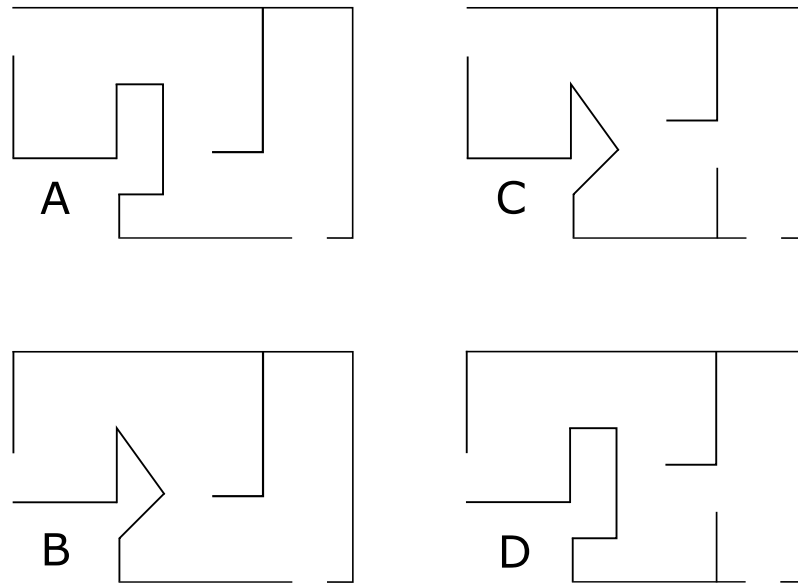


Figure D.18: Les 4 environnements proposés aux sujets. La réponse correcte est la **B**. Deux capacités sont simultanément testées: la reconnaissance de formes (carré/rectangle, triangle et ligne droite) et la spatialisation (dimension et placement).

Lors des premiers tests mis en oeuvre il n'était pas demandé de réaliser les dessins mais il est rapidement apparu que la tâche cognitive demandée était trop importante: les sujets étaient seulement capables de se souvenir de la dernière carte tactile explorée et ce pendant un temps assez court (environ 20 s).

La figure D.19 présente les résultats obtenus par les cinq sujets. Les résultats ont été brièvement analysés pour chaque sujet afin d'illustrer leurs performances et les procédés individuels qu'ils ont utilisés lors de la reconstruction et de la reconnaissance de la structure de l'environnement.

**Sujet 1:** Dans la chambre (1), le sujet 1 perçoit les deux lignes de l'entrée comme perpendiculaires à lui alors qu'elles sont parallèles et il ne détecte pas le triangle de la chambre (2). En revanche, il représente correctement les chambres (3) et (4).

Lors de la re-construction de l'environnement, le sujet 1 en se basant sur son premier dessin et en procédant par élimination, écarte les environnements **A** et **B**. En utilisant son 2ème dessin, le sujet 1 envisage la solution **D**, mais lors de l'examen de son 3ème dessin, il réalise alors qu'il n'a pas perçu le triangle dans son 2ème dessin. Il change donc son choix et s'oriente vers la solution **C**. La position de la porte de sortie dans son 4ème dessin lui indique que la solution **C** n'est pas forcément la plus adéquate et il reconsidère le choix **B**. Enfin étant plus convaincu par son 1er dessin que par le 4ème il arrête son choix sur la solution **C**.

	Chambre 1	Chambre 2	Chambre 3	Chambre 4	Décision finale
Sujet 1					C
Sujet 2					A
Sujet 3					B
Sujet 4					B
Sujet 5					B

Figure D.19: Les quatre vues dessinées par les 5 sujets et leur décision finale.

**Sujet 2:** Dans la chambre (1), le sujet 2 ne reconnaît aucune des lignes parallèles et le mur à sa droite lui semble discontinu. Dans la chambre (2), il semble essentiellement avoir reconnu le triangle mais pas les murs. Dans la chambre (3) il montre une bonne perception tandis que dans la chambre (4) il montre une bonne perception mais avec des problèmes dimensionnels.

En se basant sur son 1er dessin, le sujet 2 élimine tout d'abord les environnements C et D. Bien que les 2ème et 3ème dessins suggèrent fortement une forme triangulaire, le sujet 2 s'oriente vers le choix A. Le 4ème dessin, qui comporte des problèmes de dimensions ne lui permet pas de se rendre compte de la position de la porte de sortie et finalement le sujet 2 confirme le choix de A.

**Sujet 3:** On remarque que les chambres (1), (3) et (4) ont été perçues correctement en formes et en dimensions. En revanche, la forme et la position du triangle dans la chambre (2) ont été mal perçues.

Lors de la re-construction de l'environnement et en se basant sur son 1er dessin, le sujet 3 élimine tout d'abord les environnements **C** et **D**. Il n'obtient aucune information utile à partir de son 2ème dessin, passe au 3ème dessin et se rend compte de la présence du triangle, c'est à ce moment qu'il oriente son choix vers **B**. Finalement, le 4ème dessin, correctement représenté en formes et dimensions, lui permet de confirmer le choix **B**.

**Sujet 4:** De manière générale, dans les 4 chambres, le sujet 4 reconnaît correctement (formes et dimensions) les représentations.

En se basant sur son 1er dessin, le sujet 3 écarte tout d'abord les environnements **C** et **D**. La reconnaissance du triangle sur son 2ème dessin, l'oriente vers **B**, choix qu'il confirme ensuite en analysant les dessins 3 et 4.

**Sujet 5:** Une bonne reconnaissance générale dans les 4 chambres est observée. Le triangle dans la chambre (2) a également été parfaitement reconnu.

Comme le sujet 4, le sujet 5 écarte tout d'abord **C** et **D**. A partir de son 2ème dessin, le sujet 5 reconnaît rapidement le triangle et s'oriente vers **B**, le dessin 3 confirme la présence du triangle et le dessin 4 la position de la porte. L'environnement **B** est finalement choisi.

En conclusion, 3 sujets sur 5 (soit 60%) ont été capables de reconnaître avec succès leur environnement de navigation. Il est important de souligner que l'information tactile présentée semble appropriée pour la navigation: tous les sujets ont démontré avoir acquis la notion d'obstacle. En revanche la représentation spatiale ne semble pas être claire et uniforme pour tous, ce qui est évident si l'on considère les différences inter-individuelles en termes de capacité et d'habileté tactile [Fontaine06].

## D.6 Conclusion

Ce résumé a présenté un système appelé *Lunettes Intelligentes*, une aide à la mobilité et à la navigation indépendante et en sécurité des personnes aveugles ou malvoyantes dans un environnement 3D non coopérant. Ce système permet la détection et la localisation des obstacles en associant un système de vision stéréoscopique et une interface tactile.

Dans le cadre de ce projet, un nouveau concept d'interface tactile compacte, portable, légère et à faible coût pour les déficients visuels a été présenté. Un premier prototype de 64 actionneurs en technologie AMF a été réalisé. Ce système offre une haute résolution spatiale et de bonnes performances en plus d'être robuste et simple à implanter. Ses conceptions mécanique et électronique permettent facilement de le redimensionner à un nombre supérieur d'éléments tout en conservant un coût relativement faible.

Des expériences préliminaires ont été conduites pour évaluer les performances de l'interface tactile et le concept de représentation de l'espace proposé par le système Lunettes Intelligentes. Les résultats montrent que la représentation tactile de la topologie de l'environnement peut être facilement comprise et utilisée par les utilisateurs, ce qui confirme l'utilité et la pertinence du système.

## Résumé

Ce travail de thèse porte sur la conception et la réalisation d'un nouveau concept d'interface tactile compacte, portable, légère, à faible coût et à haute résolution. Cette interface, dédiée aux personnes aveugles et malvoyantes, est à la base d'une nouvelle approche d'aide à la mobilité basée sur la substitution/suppléance visuo-tactile.

En s'appuyant sur la psychophysiologie du sens du toucher associée à une technologie d'actionnement de type Alliages à Mémoire de Forme (AMF), un dispositif mécatronique a été conçu et réalisé pour générer, via le toucher, des sensations de contact à l'extrémité des doigts. Le prototype est constitué d'une matrice de 64 micro-actionneurs en AMF de 1,5 mm de diamètre offrant des courses maximales de 1,4 mm chacun. L'espacement entre les actionneurs est de 2,6 mm. Les efforts développés par chaque actionneur sont de l'ordre de 300 mN. Enfin, la bande passante maximale sans dégradation des performances est de 1,5 Hz. Le dispositif réalisé est compact et ne pèse que 200 g. Ses faibles dimensions (un cube de 8 cm de côté) le rendent facilement portable par l'utilisateur. L'interface est en mesure d'afficher un grand nombre d'informations binaires sur sa matrice 8 x 8. Par ailleurs, ses conceptions mécanique et électronique de commande peuvent être facilement redimensionnées pour un nombre supérieur d'actionneurs tout en conservant un faible coût.

Des études psychophysiques conduites sur des sujets voyants montrent la pertinence de l'information transmise via l'interface et démontrent l'intérêt du dispositif réalisé pour l'assistance aux personnes aveugles et malvoyantes.

**Mots-clés:** Aides électroniques à la mobilité, interfaces homme-machine, interfaces tactiles, micro-actionneurs, Alliages à Mémoire de Forme (AMF), ressorts hélicoïdaux en alliage NiTi.

---

## Abstract

This thesis explores the design, implementation and performance of a new concept for a low-cost, high-resolution, lightweight, compact and highly-portable tactile display. This tactile device is intended to be used in a novel visuo-tactile sensory substitution/supplementation electronic travel aid (ETA) for the blind/visually impaired.

Based on the psychophysiology of touch and using Shape Memory Alloys (SMAs) as the actuation technology, a mechatronic device was designed and prototyped to stimulate the sense of touch by creating sensations of contact on the fingertips.

The prototype consists of an array of 64 elements spaced 2.6 mm apart that vertically actuates SMA based miniature actuators of 1.5 mm diameter to a height range of 1.4 mm with a pull force of 300 mN up to a 1.5 Hz bandwidth. The full display weights 200 g and its compact dimensions (a cube of 8 cm side-length) make it easy for the user to carry. The display is capable of presenting a wide range of tactile binary information on its 8 x 8 matrix. Moreover, both mechanical and electronic drive designs are easily scalable to larger devices while still being price attractive.

Human psychophysics experiments demonstrate the effectiveness of the tactile information transmitted by the display to sighted people and show feasibility in principle of the system as an assistive technology for the blind/visually impaired.

**Keywords:** Electronic travel aids (ETAs), man-machine interfaces, tactile displays, micro/miniature actuators, Shape Memory Alloys (SMAs), NiTi helical springs.